AD-A265 750

3

AEOSR-TR· 93 0086

**Department of Mechanical and
Industrial Engineering
University of Illinois at
Urbana-Champaign
Urbana, IL 61801**

UILU-ENG 93-4015

ANNUAL TECHNICAL REPORT

Two Temperature Modeling and Experimental Measurements of Laser Sustained Hydrogen Plasmas

H. Krier and A. E. Mertogul

DTIC
ELECTE
JUN 14 1993
S E D

93-13130

REPORT DOCUMENTATION PAGE

1. AGENCY USE ONLY (Leave blank)	2. REPORT DATE 01 May 1993	3. REPORT TYPE AND DATES COVERED Annual Technical, 16June1992-01May1993

4. TITLE AND SUBTITLE Two Temperature Modeling and Experimental Measurements of Laser Sustained Hydrogen Plasmas	5. FUNDING NUMBERS AFOSR Contract No. F49620-92-J-0448

6. AUTHOR(S)

Herman Krier and Ayhan E. Mertogul

7. PERFORMING ORGANIZATION NAME(S) AND ADDRESS(ES) University of Illinois at Urbana-Champaign Department of Mechanical and Industrial Engineering 140 MEB, 1206 W. Green Street Urbana, Illinois 61801	8. PERFORMING ORGANIZATION REPORT NUMBER UILU-ENG 93-4015

9. SPONSORING/MONITORING AGENCY NAME(S) AND ADDRESS(ES) AFOSR/NA 110 Duncan Avebue Suite B115 Bolling AFB DC 20332-0001	10. SPONSORING/MONITORING AGENCY REPORT NUMBER

11. SUPPLEMENTARY NOTES

12a. DISTRIBUTION/AVAILABILITY STATEMENT Approved for Public Release; Distribution is Unlimited	12b. DISTRIBUTION CODE

13. ABSTRACT (Maximum 200 words)

Experiments have been performed which measured the global absorption and thermal efficiency of laser sustained hydrogen plasmas for the first time. Results include global absorption as high as 90% and thermal efficiency as high as 80%. These results validate laser propulsion as a feasible orbital transfer technology.

A kinetic nonequilibrium model of laser sustained hydrogen plasmas has been formulated and solved. This model is the first of its kind and includes a discretized beam raytrace with a variable index of refraction based upon plasma electron number density. Model results have compared favorably with experimental results and the model has been used to provide predictions of LSP performance well outside the realm of experiments. Multiple model solutions have been obtained which are dependent upon initial conditions. No significant kinetic nonequilibrium was observed in LSP core regions for incident powers up to 700 kW. Beam refraction by the LSP has been observed to have a major effect on LSP performance.

The methodology formulated in this document has direct applicability to two temperature modeling of arcjet plasmas, work which is currently underway at UIUC.

14. SUBJECT TERMS Beamed Energy Propulsion, Two Temperature Modeling, Laser Sustained Hydrogen Plasmas		15. NUMBER OF PAGES 244
		16. PRICE CODE

17. SECURITY CLASSIFICATION OF REPORT Unclassified	18. SECURITY CLASSIFICATION OF THIS PAGE Unclassified	19. SECURITY CLASSIFICATION OF ABSTRACT Unclassified	20. LIMITATION OF ABSTRACT UL

ANNUAL TECHNICAL REPORT

No. UILU-ENG 93-4015

TWO TEMPERATURE MODELING AND EXPERIMENTAL MEASUREMENTS OF LASER SUSTAINED HYDROGEN PLASMAS

prepared by

Herman Krier[1] and Ayhan E. Mertogul[2]

Department of Mechanical and Industrial Engineering
University of Illinois at Urbana-Champaign
1206 West Green Street
Urbana, IL 61801

Accesion For		
NTIS CRA&I		☒
DTIC TAB		☐
U..announced		☐
Justification		
By		
Dist.ibution /		
Availability Codes		
Dist	Avail and / or Special	
A-1		

[1] Co-Principal Investigator
[2] Post Doctoral Research Associate

APPROVED FOR PUBLIC RELEASE; DISTRIBUTION UNLIMITED

Abstract

Experiments have been performed which measured global absorption and thermal efficiency of laser sustained hydrogen plasmas for the first time. Results include global absorption as high as 90% and thermal efficiency as high as 80%. These results validate laser propulsion as a feasible orbital transfer technology.

A kinetic nonequilibrium model of laser sustained hydrogen plasmas has been formulated and solved. This model is the first of its kind and includes a discretized beam raytrace with a variable index of refraction based upon plasma electron number density. Model results have compared favorably with experimental results and the model has been used to provide predictions of LSP performance well outside the realm of experiments. Multiple model solutions have been obtained which are dependent upon initial conditions. No significant kinetic nonequilibrium was observed in LSP core regions for incident powers up to 700 kW. Beam refraction by the LSP has been observed to have a major effect on LSP performance.

The methodology formulated in this document has direct applicability to two temperature modeling of arcjet plasmas, work which is currently underway at UIUC.

Acknowledgements

Table of Contents

List of Tables

List of Figures

1. Introduction

This work is presented as a two part study of hydrogen laser sustained plasmas. Following the introductory chapter in which the fundamentals of laser propulsion and laser sustained plasma (LSP) behavior are explained, the results of experiments measuring LSP performance are presented. The rest of the work is comprised of the formulation of the generalized non-LTE model, and the formulation and solution of the simplified kinetic nonequilibrium model which were subsequently developed to extend the realm of possible operating conditions beyond those possible in the laboratory.

The main text has been written to allow the reader to assimilate the main ideas presented without getting bogged down in the details. However, for completeness, all the details of the experiments and the model have been presented as a series of appendices after the main text.

1.1 Laser Propulsion

The basic premise of all rocket propulsion systems is to heat a propellant which can then be expanded from a pressurized chamber through a nozzle to produce thrust. Variations of the method used to heat the propellant are what constitute the different categories of rockets. Regardless of the type of rocket being considered, certain relations between performance parameters are generally valid. Using these relations as reference, the relative advantages and disadvantages of rocket systems can be compared.

The thrust produced by a rocket of any type can be written in terms of the propellant mass flow rate, $\dot{m}$, and the propellant effective exhaust velocity, C, as:

$$\text{Thrust} = \dot{m}\, C \qquad \text{(Newtons)} \qquad (1.1)$$

where C is defined by:

$$C = U_e + \frac{(P_e - P_a)A_e}{\dot{m}} \qquad \text{(m/s)} \qquad (1.2)$$

in which U_e is the propellant exhaust velocity, P_e is the nozzle exit pressure, P_a is the ambient pressure of the nozzle surroundings, and A_e is the nozzle exit area.

If the specific impulse, I_{sp}, is defined as a constant times thrust per unit mass flow, given by:

$$I_{sp} = \frac{C}{g_0} \qquad \text{(seconds)} \qquad (1.3)$$

where g_0 is the acceleration of gravity at sea level, the thrust may be written:

$$\text{Thrust} = \dot{m} \, g_0 \, I_{sp} \qquad \text{(Newtons)} \qquad (1.4)$$

Specific impulse is a measure of the efficiency of the thrust produced (thrust force per unit weight flow) and is directly related to the vehicle velocity increment during thruster operation. Neglecting the effect of ambient pressure, it is easy to show that the specific impulse (or normalized exhaust velocity) can be calculated from the change in enthalpy from the rocket chamber to the exhaust exit plane as:

$$I_{sp} \approx \frac{1}{g_0} \sqrt{ \frac{2\gamma \bar{R} T_0 \left(1 - \left(\frac{P_e}{P_0}\right)^{(\gamma-1)/\gamma} \right)}{(\gamma-1) \, MW} } \qquad \text{(seconds)} \qquad (1.5)$$

where MW is the propellant molecular weight, $\bar{R}$ is the universal gas constant, T_0 is the chamber stagnation temperature, P_0 is the chamber stagnation pressure, and γ is the ratio of specific heats. It is obvious that a high chamber propellant temperature and a low propellant molecular weight are desirable to maximize specific impulse.

If a conversion efficiency η is defined as the efficiency between the power input (whether in the form of chemical energy or an external power source) to the system and the kinetic energy of the exhaust propellant, it can be shown that the relation between thrust, specific impulse and input power is given by:

$$\text{Thrust} = \frac{2 \, \eta \, P_{input}}{g_0 \, I_{sp}} \qquad \text{(Newtons)} \qquad (1.6)$$

For the purpose of this discussion rocket propulsion systems can be broadly classified as either chemical or electric. Chemical rockets operate by burning a fuel, either solid or liquid, which is then used as propellant. These systems are capable of producing tremendous amounts of thrust limited only by the amount of propellant that can be passed through the system, however they typically produce low specific impulses with an upper limit of approximately 450 seconds. The theoretical chamber temperature in such a system can be as great as 4400 K, and the molecular weight of the propellant ranges between 8.9 and 29.3 kg/kg-mole depending on the fuel (Sutton,

1986, p. 140). Despite their limited specific impulse, chemical rockets are the system of choice for the purpose of boosting payloads from the earth's surface.

Electric thrusters generally utilize the energy of an external field to heat a propellant. Although low molecular weight propellants can be used to maximize the specific impulse, electric propulsion systems are thrust limited as is evident from equation (1.6). This is because the power source for an electric propulsion system would necessarily be a lightweight generator carried onboard the vehicle.

Laser rocket propulsion is a concept wherein propellant is heated through absorption of a remotely based laser beam. The motivation for the development of such a system was to utilize the best aspects of both chemical and electric propulsive systems. Some advantages inherent to such a system become immediately apparent. First, the power source is not carried onboard the vehicle so the power input to the propellant is not limited to the output of a given class of generator. Second, the propellant can be chosen to minimize molecular weight (hydrogen) and thereby maximize the specific impulse. With the combination of these two factors, laser propulsion systems are theoretically capable of producing moderate thrusts (> 1 kN) with specific impulses in excess of 1000 seconds for 10 MW input power. This type of performance makes laser propulsion an excellent choice for orbital transfer missions.

However, problems exist in the coupling of the beamed energy and the propellant. The primary mechanism for laser absorption is inverse bremsstrahlung in which a photon is absorbed by an electron in the presence of a third particle which carries off excess momentum. Without some initial source of electrons the beam would not be absorbed and would pass through the propellant unattenuated. If electrons are somehow supplied to the region of the laser beam focus, absorption will occur and the electrons will quickly become extremely hot. Collisions of the heated electrons with gas molecules then heats them and further causes molecular dissociation and ionization which produces more absorbers and heated heavy species. The mixture of charged and neutral species which results is called a plasma. Throughout these events, the electrons and the excited heavy species also radiate energy which may be reabsorbed or lost to the surroundings. If the rate of

ionization is sufficiently high to balance recombination, radiation, and diffusion losses, then the absorption of power is self-sustaining.

1.2 Effects of Control Parameters

On a macroscopic level, a laser beam is focused into a flow chamber from the upstream to downstream direction, or in other words in the same direction as the propellant flow. The plasma that forms in the beam will physically adjust its position in the propellant flow and the focused beam where a balance exists between power absorbed from the beam and power lost to the propellant. Unfortunately, this power balance cannot always be maintained, and the plasma may not always be stable.

Physically, the LSP acts much like a very hot semi-porous bluff body within the propellant flow (Eguiguren, 1989). Propellant approaching the plasma from upstream undergoes a drastic reduction in density accompanied by an acceleration through and around the plasma. For the purpose of this discussion, the plasma wave front may be simply defined as the leading edge of the plasma, although where the plasma begins is not always clear. Although a stable LSP is stationary in the laboratory frame with respect to an external observer, the LSP wave speed is a useful concept which may be used to describe the speed of the incident propellant for which the LSP is stable. All stable LSPs must exist with the plasma wave front upstream of the laser focus, and the plasma wave speed matching the incident propellant speed. If, for any reason, the LSP wave front is downstream of the laser focus, it will either propagate forward upstream of the focus and stabilize or propagate further downstream and extinguish.

Based on this simple explanation, many aspects of LSP behavior may now be explained. Supposing that a stable LSP exists, there are five parameters which may be varied to alter the LSP condition. These parameters are the incident laser power, the incident propellant mass flux, the chamber ambient gas pressure, the beam focusing geometry, and the beam wavelength. A perturbation of any of these parameters may cause the LSP power balance to be momentarily upset, and the wave speed of the LSP wave front to not match the incident propellant speed. However,

whenever possible, the LSP will shift position to reestablish the power balance and match wave speed with propellant speed.

As an illustrative example, consider the effect of a variation of incident beam power on a stable LSP. An increase in incident laser power will cause an increase in power absorbed by the LSP which will cause in increase in the LSP wave speed. In order to reestablish a power balance, and because the LSP wave speed is higher than the incident propellant speed, the LSP will move upstream. The LSP wave front will stabilize at a position upstream where the incident beam is less focused, the local power absorption is less, and the LSP wave speed again matches the incident propellant speed. A decrease in incident power would cause a decrease in the LSP wave speed. The LSP will therefore be pushed downstream by the propellant. The LSP wave front will stabilize at a position downstream closer to the focus where the local power absorption is higher, and once again the power balance is restored. If the power flux at the focus is insufficient to maintain the LSP power balance, then the LSP will continue through to the downstream side of the focus where no position in the beam has sufficient power flux to stabilize it. The net effect is that the plasma extinguishes, and the phenomenon is commonly referred to as blowout.

Following the arguments above, the effects of the other parameters may be briefly summarized. An increase in gas pressure has the effect of raising the local absorption coefficient by raising the local number density of electrons, and therefore raising the incident power absorbed. The result would be an increase in LSP wave speed and a shift upstream to reestablish a power balance. A decrease of gas pressure has the opposite effect, causing the LSP wave front to shift downstream toward the laser focus to reestablish a balance. Once again, if the maximum power flux at the focus is insufficient to stabilize the LSP wave front, it will be pushed downstream of the focus where it will extinguish. Variation of the laser wavelength also has the effect of altering the local absorption coefficients so the effect is analogous to variation in the chamber gas pressure.

Variation in the gas flow rate also has a predictable result. A decrease in gas flow rate would decrease convective loss from the LSP to the propellant and cause the LSP wave speed to be higher than the propellant speed. The LSP wave front would shift upstream to reestablish a power

balance. Conversely, an increase in gas flow rate would increase convective loss to the propellant and force the LSP to shift closer to the focus to reestablish the power balance. This is where the origin of the term blowout comes from, because if the mass flow rate is too high for stability, the LSP wave front is pushed through to the downstream side of the focus and is effectively blown out.

Variation of beam focusing geometry has a measurable effect on LSP stability. The beam f-number is defined as the ratio of the laser beam outer diameter to the focal length of the focusing lens. Therefore, a high f-number system has a more gradual focusing of the incident beam than does a low f-number system. This means that to maintain a power balance, an LSP must shift a greater distance in a high f-number system than in a low f-number system. If perturbations existed in one or more of the other control parameters, and the system was close to the edge of stability, the high f-number LSP would be observed to continually shift position more than the low f-number LSP. This phenomenon has been observed experimentally and is commonly referred to as plasma bounce. Should the LSP bounce amplitude be so great as to cause the LSP wave front to momentarily shift downstream, it may recover and return to a stable position upstream of the focus, or it may extinguish.

For conditions in which the LSP front is far upstream of the focus, such as a combination of high f-number with high pressure and low mole flux, it has been well documented by Fowler and Smith (1975), Kozlov, Kuznetsov, and Masyukov (1979), Mertogul (1989), and Keefer, Welle, and Peters (1985) that there exists an LSP instability which is not the same as a blowout. This type of instability has been commonly referred to as a shockout because it occurs for combinations of control parameters that are at the opposite end of the LSP stability regime from the parameters required for a blowout to occur. Shockouts are briefly discussed in Chapter 2.

Assuming the LSP is stable, there are two global quantities which are used to describe its performance. The global absorption is defined as the fraction of incident laser power absorbed by the LSP, and the thermal efficiency is defined as the fraction of incident laser power retained by the

propellant as thermal energy. The difference between these two quantities represents the power lost to the surroundings mostly due to LSP radiation.

In order to design a practical laser thruster, the designers must be fully aware of the plasma stability limits and performance values. However, since practical thrusters will be powered by lasers having megawatts of power, and experiments can currently be conducted only up to 10 kW (due to maximum power output of the UIUC laser), it has become clear that a model of the plasma physics is necessary to make predictions of performance at high power levels. This model must include as much of the plasma physics on the microscopic level as possible, as well as the macroscopic flow problem of a gas which is suddenly severely heated while flowing through a duct.

It was with these goals in mind that this work was started. Experiments provided a measure of plasma performance and stability limits which were to serve as a database for comparison of the model results at low powers. Model operating parameters could then be changed to make predictions for cases not possible in the laboratory.

1.3 Theoretical Background

The study of a laser sustained plasma requires a knowledge of the fundamental physical phenomena which may be present within the plasma. In order to facilitate a better understanding of the material to be presented, several of these phenomena and the associated jargon will be briefly summarized.

Hydrogen plasma is a mixture of seven species which are electrons (e^-), protons (H^+), neutral molecules (H_2), neutral atoms (H), negative ions (H^-), diatomic positive ions (H_2^+), and triatomic positive ions (H_3^+). The last three species listed are sometimes referred to as the minor species due to their lower relative number densities compared to the others. All species except for electrons and protons also have internal energy modes which allow them to be internally excited. Specifically, the atomic species may become electronically excited, and the molecular species may become vibrationally, rotationally, and electronically excited. The nature of the interactions

between the species is quite complex but may be broken down to involve only a few fundamental phenomena which will now be discussed.

Particles within a plasma interact with one another through collisions and radiation. There exist three broad classifications for the radiation present within a plasma. These classifications are line radiation (bound-bound), free-bound continuum radiation and free-free continuum radiation (Venugopalan, 1971a, p.14-17).

Line radiation is the result of atoms and molecules undergoing transitions between internal energy states. When an atom or molecule makes a transition between two internal energy levels, the quantity of energy involved in the transition is simply the energy difference between the two levels. If the levels had exact values for their energies, then the transition would have a single discrete energy value. The energy of a released photon would then have this value and would correspond to a single discrete frequency. However the values of the energy levels are not exact but instead are somewhat blurred due to various effects normally referred to as broadening (Griem, 1974). The result of these blurred energy levels is that emitted photons are not of a single discrete frequency but instead consist of a distribution of frequencies commonly referred to as the lineshape. The central frequency of the lineshape is the nominal frequency of the transition and the width of the frequency spread depends upon the type and severity of broadening mechanism present which is a result of the local plasma conditions (Venugopalan, 1971a, p.14).

The three main types of line radiation interaction with particles are spontaneous emission, absorption and stimulated emission. An excited particle may spontaneously make a transition to a lower energy state and release a photon to carry off the transition energy. This is called spontaneous emission. Similarly, a particle may absorb a photon with energy equal to the energy of an internal transition and thereby transition to an excited level. This phenomenon is called induced absorption. Finally, a photon with energy equal to an internal transition may stimulate a particle in an excited state to transition to a lower state. In this process the incident photon stimulates the excited particle which releases a photon identical to the incident photon and transitions to a lower state. This process is called stimulated emission and is one of the key

processes in the function of a laser. It should be stressed that regardless of the process, all line photons have some degree of broadening associated with them. More will be said regarding line radiation in Appendix F on the collisional-radiative (C-R) model.

Free-bound continuum radiation is the result of a transition between end states in which one of the states has a continuous distribution of energies. A good example is the radiative recombination reaction wherein a free electron recombines with a proton to produce a neutral atom and a photon. The photons produced by this reaction have a distribution of energy which is a result of the distribution of energy of the recombining electrons. The frequency spectrum for this type of radiation would not be a broadened line, but rather a continuum with no upper frequency limit and a discrete broadened lower limit corresponding to the lowest possible energy of the radiated photon. Although there would be no theoretical upper frequency limit, in actuality the intensity of the radiation would decrease to zero as frequency is increased.

Transitions which occur between free states must also produce photons with a continuous energy distribution, since both end states have continuous energy distributions. The frequency spectrum for this type of radiation is therefore continuous with no discrete limits on either the low or high energy ends. Of course the intensity of radiation once again would approach zero with increasing frequency. A good example of this type of transition is bremsstrahlung radiation wherein a free electron loses energy through radiation. This reaction is only possible in the presence of a third body (an atom, ion, or molecule) to conserve momentum. The actual process is a type of inelastic collision which is discussed in the next section.

Energy transfer between the species within a plasma occurs through collisions. With the exception of spontaneous emission, all radiative processes may also be described as a collisional process wherein one of the particles is a photon. For the purpose of this work, all collisions may be classified as either elastic or inelastic. Elastic collisions are those in which the kinetic energy of the colliding particles is conserved. Inelastic collisions are those in which total energy is conserved but kinetic energy is not (Uman, 1964, p.118).

If the species in a plasma were simple spherical balls of varying mass with no internal degrees of freedom, all the collisions could be adequately described as elastic. The existence of charged species with Coulomb fields and species with internal degrees of freedom necessitate the existence of inelastic collisions. Because an accelerated charged particle must radiate, a charged species approaching another with a Coulomb field will radiate energy. Even though the charged species may never collide in the sense of two billiard balls, the interaction of their electric fields is referred to as a collision (Uman, 1964, p. 118).

Species with internal degrees of freedom may undergo an internal energy transition as a result of a collision. For example, an electron may collide with a ground state hydrogen atom and recoil with a loss of kinetic energy which reappears as the excitation energy of the resultant excited atom. More will be said regarding inelastic collisions in Appendix F on the C-R model.

1.4 Thermodynamic State

The assumed thermodynamic state of a plasma will determine the approach to modeling the plasma. The number of equations included in the model as well as the inclusion or neglect of terms which describe physical phenomena will be effected by assumptions regarding the thermodynamic state. As a basis for further discussion, the designations for the various possible levels of thermodynamic equilibrium within a plasma are summarized in this section.

Thermodynamic equilibrium (TE) is the idealized state wherein there are no temperature or concentration gradients and the system in question is in thermal, mechanical, chemical and radiative equilibrium. In such a system the radiation field is black body at the temperature of the system (Cho, 1988 and van der Mullen, 1990). In an actual system there are always temperature and concentration gradients under which the assumption of thermodynamic equilibrium breaks down (van der Mullen, 1990). If the rate of collisional energy transfer is high, the energy of particles will equilibrate within a small volume faster than the particles can travel out of the volume. In other words the length scale for temperature and concentration changes will be longer than the length scale for energy exchange. Therefore, within a local volume, thermal equilibrium will be

valid even though the radiation field may not be Planckian. The resulting condition is referred to as local thermal equilibrium (LTE) (Dresvin, 1977, p. 76).

If the system is in LTE, one temperature describes the kinetic energy of free electrons and heavy particles, and can be used to determine excited state populations through a Boltzmann distribution, and ionization fractions through a Saha equation (Griem, 1964, p. 134). However, because collisional cross sections increase with excited energy level, but radiative rates of decay decrease, it is possible that all excited levels higher than the level where the two rates are roughly the same order of magnitude are in equilibrium with each other and with the kinetic energy of the free electrons, but not with the population distribution of lower lying states (Griem, 1964, p. 130, and Burton and Blades, 1990). This condition is referred to as partial local thermal equilibrium (PLTE).

More recently, van der Mullen (1990) has defined LTE to be the state wherein the system is in local Maxwell equilibrium (LME), local isothermal (kinetic) equilibrium (LIE), local Saha equilibrium (LSE), and local Boltzmann equilibrium (LBE).

In the most general case no form of thermal equilibrium is assumed (non-LTE), and there may be several temperatures necessary to describe the LSP thermodynamic state including separate electron and heavy species kinetic temperatures. Although the assumption of LTE may not always be correct, the simplification it provides to the analysis of plasmas has made it a common practice. This assumption of LTE has been widely used in several previous investigations, both theoretical and experimental, including Beddini and Owano (1987), Beddini, Owano, and Kuo (1987), Eguiguren (1989), Glumb and Krier (1986), Grier (1962, 1966), Jeng and Keefer (1986, 1987a, 1987b, 1988), Kemp and Krech (1980), Kemp and Root (1979), Kemp, et al. (1977), Mazumder, Rockstroh, and Krier (1987), Merkle, Molvik, and Shaw (1985), Moder (1990), Molvik, Choi, and Merkle (1984), Muller and Uhlenbusch (1982), Patch (1969, 1971), Raizer (1970), and Yos (1963).

1.5 Plasma Composition

This section has been included to point out the different methods necessary in order to compute the plasma composition assuming LTE and without assuming LTE. The basic method for the calculation of equilibrium number densities is to first identify the reactants and products for each equilibrium reaction taking place. As an example, consider the ionization of the hydrogen atom represented by the reaction:

$$H \Leftrightarrow H^+ + e^- \tag{1.7}$$

where the double arrow indicates the reaction to be in chemical equilibrium. Setting the chemical potential of the reactants equal to that of the products then yields:

$$\mu_H = \mu_{H^+} + \mu_{e^-} \tag{1.8}$$

Writing the chemical potentials as functions of temperature, volume, particle number densities, and particle partition functions yields:

$$- (R_u T) \ln\left(\frac{Z_H}{n_H V}\right) = - (R_u T) \ln\left(\frac{Z_{H^+}}{n_{H^+} V}\right) - (R_u T) \ln\left(\frac{Z_{e^-}}{n_{e^-} V}\right) \tag{1.9}$$

where R_u is the universal gas constant, and Z is the particle partition function.

Equation (1.9) may be rearranged as:

$$\frac{n_{H^+} n_{e^-}}{n_H} = \frac{1}{V} \frac{Z_{H^+} Z_{e^-}}{Z_H} \tag{1.10}$$

With the computation of the particle partition functions, equation (1.10) takes the form usually referred to as a Saha equation. Calculation of the partition function for hydrogen atoms requires the choice of an upper excited level at which to truncate an otherwise infinite series. This is traditionally done through a calculation of the lowering of the ionization potential due to the interaction with other particles in the LSP. Two methods, the Debye-Hückel and Bethe methods, are generally applied and the method resulting in the maximum lowering of the ionization potential is used (Patch, 1969). Equations for each of the reactions, supplemented by the appropriate equation of state, and the assumption of quasineutrality can then be used to solve for all the species number densities. A variation of this approach for a system in kinetic nonequilibrium is presented in detail in Appendix J.

The case of non-LTE species number densities may require a different approach. If the kinetic and excitation temperatures are known or assumed, a Saha type equation can be written for each reaction which takes the form of that given by Potapov (1966) who assumed that electron temperature was equal to atomic excitation temperature, or Cho (1988) who assumed electron excitational noneqr ilirium. If more than one excitational temperature is necessary, an analytical model which uses four temperatures including two excitation temperatures can be used to determine population densities (Cho and Eddy, 1989). In all these cases, the temperatures would be supplied by other portions of the overall solution algorithm (or through experiments), and the equations can be solved iteratively.

If however, no knowledge of the excited state populations is known, and therefore excitation temperature is not well defined, the approach to determining species densities becomes more involved. The species densities are solved as a result of the species continuity equations for the entire flowfield with source terms for the production of species provided by the C-R rate equations.

The simplified model assumes the approach of Potapov (1966) for the computation of the number densities of the four major hydrogen species, H_2, H^+, H and e^-. Details of the simplified species computation appear in Appendix J, and its effect on the overall algorithm are described in Appendix F on the C-R model, Appendix G on diffusion fluxes, and Chapter 4 on the simplified model.

1.6 Causes of Non-Local Thermal Equilibrium

In real laboratory situations there may exist all of the four classifications of thermal non-equilibrium defined by van der Mullen (1990), which include Maxwellian, kinetic, populational (Boltzmann), and ionizational (Saha). A summary comparison of LTE and non-LTE LSPs can be seen in Figure 1.1.

There are several contributing factors that are likely to drive plasmas away from equilibrium. These include intense electric fields, diffusion of excited species, severe temperature gradients, and non-local radiation. A non-Maxwellian electron velocity distribution would result if electron-

electron collisions were not rapid enough to overcome the effect of some external mechanism. In the case of an LSP, electron-ion IB absorption is the external mechanism that would be responsible for causing a non-Maxwellian distribution.

LTE
* Thermodynamic state is completely described by a single temperature and pressure.
* Excited species populations determined through Boltzmann factors.
* Ionization fraction determined through Saha equation.

non-LTE
* Maxwellian non-LTE: Species have non-Maxwellian velocity distributions due to some external driving force and a lack of collisional relaxation.
* kinetic non-LTE: Electrons and heavy species each governed by a Maxwellian distribution, but at different kinetic temperatures.
* Boltzmann non-LTE: Boltzmann excitation temperature is not be well defined due to a non-Boltzmann excited state distribution.
* Saha non-LTE: Multitemperature Saha equation no longer valid for prediction of species populations due to local excess or deficient populations of electrons due to diffusion.
* Population of excited states and ions must be determined through the use of species continuity equations and a collisional-radiative rate model.

Figure 1.1   A summary comparison of LTE and non-LTE conditions in an LSP.

If the rate of energy absorption by the electrons exceeds the rate at which the electrons equilibrate through collisions, then the electron velocity distribution may become non-Maxwellian (Gamalii, et al., 1990, and Langdon, 1980). Langdon (1980) asserts the following criterion for singly charged ions for the electron velocity distribution to be non-Maxwellian:

$$I \geq \frac{T_e}{(4 \times 10^{-16}) \lambda^2} \tag{1.11}$$

where I is the incident beam irradiance in W/cm^2, T_e is the electron temperature in keV, and λ is the laser wavelength in microns. Based on equation (1.11), a beam irradiance of 2.2×10^{10} W/cm^2 would be necessary to cause a non-Maxwellian distribution for an electron temperature of 1 eV and at 10.6 μm. Assuming that the incident beam is not attenuated at all before if becomes fully focused, and based on a 1 mm focal spot diameter, this irradiance corresponds to an incident power of 175 MW. The actual required beam irradiance would

probably be much higher since the beam is most definitely attenuated before reaching the focal spot. Also, it is obvious that the hotter the LSP gets, the greater the necessary beam irradiance becomes. Therefore it can be safely assumed that LSP free electrons have a Maxwellian velocity distribution.

Kinetic non-equilibrium occurs when electrons and heavy particles are each governed by their own kinetic temperature. This may occur in plasmas in which different forces act upon different species, as pointed out by van der Mullen (1990). Because the collision cross section for momentum transfer between like particles is high with respect to that for particles of greatly differing masses, it is possible that electrons and heavy particles may be each governed by a Maxwellian distribution at different temperatures (Griem, 1964, p. 130, and van der Mullen, 1990). In the case of an LSP, the energy from the incident beam is initially absorbed by free electrons which then undergo relaxation through collisions and radiation. Based on this, Griem (1964, p. 157) has proposed the following criterion for the validity of kinetic equilibrium between electrons and heavy particles for the case of an inhomogeneous stationary (with a net zero rate of ionization) plasma:

$$E^2 << \left(5.5 \times 10^{-12} \, n_e \, \frac{E_H \, jev}{k_b T}\right)^2 \frac{m_e}{M} \tag{1.12}$$

where E is the applied electric field in V/m, n_e is the electron number density in cm^{-3}, E_H is the ionization energy of the heavy particle in question in eV, jev is the conversion factor from eV to Joules with a value of 1.60219×10^{-19}, m_e is the electron mass, and M is the heavy particle mass. Using a beam irradiance of 10^5 watts/cm^2, which is two orders of magnitude smaller than the laboratory beam irradiance at 7 kW incident power as estimated by Mertogul, Zerkle, and Krier (1992), results in an electric field magnitude of 8.7×10^5 V/m. The maximum electron number density for one atmosphere LTE hydrogen plasma is 1.8×10^{17} cm^{-3} at approximately 18000K following the analysis of Moder (1990). Using these values in equation (1.12) with the unlowered ionization potential for hydrogen yields a right hand side of 4.1×10^{10} which is an order of magnitude *smaller* than the left hand side. This result indicates that equal electron and heavy

particle kinetic temperatures would not be a good assumption in this case. Clearly if the incident beam power is increased, the criterion is driven further from being satisfied. Depending on the wavelength of the incident beam, both populational and ionizational equilibrium may also be upset through photoionization.

Populational, or Boltzmann, non-equilibrium is the condition wherein the excited state populations cannot be fit to a Boltzmann distribution at any one temperature. In the case of PLTE, the upper excited levels could be fit to an excitation temperature, but in the general non-LTE case the excitation temperature is not well defined. In a plasma that is not collisionally dominated, diffusion of excited neutrals from one region into another at a different temperature could drive the distribution of excited states in both regions away from Boltzmann distributions at given temperatures (van der Mullen, 1990). Collisional relaxation would drive the distributions back toward equilibrium, but if the diffusion rate was high, populational non-equilibrium would result.

Ionizational, or Saha, non-equilibrium is the condition wherein the fraction of ionized free electrons does not match that predicted by the Saha equation. Clearly, diffusion of electrons or ions could cause a local imbalance in ionizational equilibrium. Inelastic collisional processes including recombination and ionization would drive the species densities towards equilibrium, but once again, if the diffusion rate of species was high enough, ionizational nonequilibrium would result.

Another possibility is the diffusion of excited species which then radiate before collisional relaxation can occur, thereby biasing the local radiation field (Siegel and Howell, 1981, p. 447). Clearly, this type of non-equilibrium would be further enhanced by severe temperature gradients between the regions.

The loss of optically thin line radiation through spontaneous emission has the effect of underpopulating upper bound atomic levels and overpopulating the lower levels (Burton and Blades, 1990, and Venugopalan, 1971a, p. 168). Optically thin radiation may also contribute to nonequilibrium through non-local radiation effects. Radiation (line and continuum) originating in an extremely hot region may be only partially absorbed by an adjacent cooler region and travel

across a large portion of the plasma before it is absorbed. If this were the case, populations of excited neutrals in the absorbing regions could be skewed toward the upper excited states through line absorption. In addition, photoionization by the continuum radiation could cause ionizational nonequilibrium.

All of these effects point to the conclusion that plasmas that are not collisionally dominated are likely to have some aspect of non-equilibrium. In addition, the presence of an intense laser beam which is absorbed by the electrons makes the existence of kinetic non-equilibrium not only possible but likely. The existence of any one of the classifications of non-equilibrium may cause the existence of the others (Dresvin, 1977, p. 79, and van der Mullen, 1990). Therefore any analysis of the LSP should include the possibility of kinetic, Boltzmann, and Saha non-LTE as well as both local and non-local phenomena.

2. Experimental Investigation

The experimental investigation of laser sustained hydrogen plasmas had two main purposes. The first was to measure global absorption and thermal efficiency under a variety of conditions. The second purpose was to establish a database for comparison with a generalized non-LTE model which was to be produced at a later date.

Continuous wave laser sustained plasmas in forced convective flow had been studied previously both at the University of Illinois at Urbana-Champaign (UIUC) and at the University of Tennessee Space Institute (UTSI). The majority of this previous work involved the use of argon as the propellant gas. Keefer and co-workers at UTSI have studied argon LSPs at less than 1 kW input laser power, up to 4.5 m/s gas flow velocity, up to 4 atm gas pressure and several beam geometries (Jeng and Keefer, 1987c, Keefer, Welle, and Peters, 1985, and Welle, Keefer, and Peters, 1986 and 1987). Their results include global absorption as high as 86% and thermal efficiency of 38% for a 2.5 atm argon LSP. Work done by Krier, Mazumder, and colleagues here at UIUC using single argon LSPs has produced global absorption as high as 97% and thermal efficiency as high as 46% at 2.5 atm gas pressure (Mertogul, 1989, and Zerkle, et al., 1990).

Having exhausted the possibilities for single argon plasmas, work at UIUC turned to dual (two plasmas side by side) LSPs with variable focal separation distance. The dual LSP work produced thermal efficiencies as high as 58% and showed that there was a slight advantage of using dual LSPs each at a given power over a single LSP at that power (Schwartz et al., 1989). There also followed some work involving mixtures of helium and argon to observe the effect of the addition of the lower molecular weight gas (Schwartz et al., 1989).

There have been very few works involving hydrogen laser sustained plasmas. Here the distinction between a pulsed plasma and a steady state plasma should be made. Pulsed plasmas are produced using a high power short duration pulsed laser. Pulsed plasmas have been produced in hydrogen to study breakdown intensity (Eskridge, McCay, and VanZandt, 1987, McCay, Eskridge, and VanZandt, 1988, and VanZandt, McCay, and Eskridge, 1984), as well as electron recombination rate (Litvak and Edwards, 1966). Kozlov, Kuznetsov, and Masyukov (1979)

studied the effect of pressure and power variations on steady state hydrogen plasma stability using a 1 kW continuous wave CO_2 laser at pressures from 1 to 10 atm. They found that the primary loss mechanism of hydrogen plasmas in the regime of conditions of their experiments was thermal conductivity in contrast to monatomic gases in which the dominant loss mechanism was radiative emission. They also noted that the shape of the hydrogen plasma was spherical rather than conical following the beam like in monatomic gases, and that the hydrogen plasma was smaller than monatomic plasmas at the same power.

2.1 Experimental Facility

The experimental facility used in this work was essentially the same as that used since the project's inception with a few important modifications. This work utilized an AVCO Everett 10 kW CW CO_2 10.6 μm laser that was part of the UIUC Materials Engineering Research Lab (MERL). The laser functioned in an annular TEM 01* mode with the inner diameter of the annulus being approximately 50 mm and the outer diameter being 70 mm. This laser was used for both initiation and sustainment of the plasmas.

The second main component in the experimental facility was the absorption chamber within which plasmas were sustained. This 127 mm inside diameter cylindrical chamber consisted of an inlet section, the main section, and the exit section. The exit section was made of aluminum with the rest being made of stainless steel. The parts were bolted together with custom cut neoprene sheets and vacuum grease used to provide a seal. The chamber was aligned such that propellant gas entered at the bottom and flowed vertically upward before exiting through four ports at the top. Within the absorption chamber was mounted a convergent quartz tube with a terminal ID of 48 mm and a wall thickness of 3 mm which served to accelerate the flow without blocking spectroscopic access to the plasma. The exit ports were connected to a manifold made of stainless steel pipe fittings which led to a microprocessor controlled valve and th n ultimately outside the building where the gas was exhausted above the roof line for safety. The inlet section of the chamber has a porous sintered steel filter insert through which propellant gas was forced. The purpose of this

insert was to quiet inlet flow turbulence before the flow entered the bottom of the convergent quartz tube.

The collimated annular beam exited the laser horizontally and was steered with three watercooled copper mirrors to be vertical immediately beneath the absorption chamber. The beam was focused into the absorption chamber with a plano-convex zinc selenide (ZnSe) lens mounted in a lens holder on a motor driven translation stage. The bottom of the absorption chamber was sealed with a ZnSe window. Rectangular quartz windows on either side of the chamber permitted visual access to the plasma.

A tungsten rod was used to supply the free electrons necessary for plasma initiation. The tungsten insertion location was approximately 17 mm above the lip of the quartz tube. To initiate a plasma the lens translation stage was positioned such that the plasma focus was at the same vertical position as the tungsten rod insertion position. Assuming the optical system was aligned correctly with the beam centered within the quartz tube and focused on the tungsten rod, plasma initiation could then proceed. Electrons released by the tungsten rod in the presence of hydrogen molecules rapidly absorb power from the incident laser and heat up. Collisions with molecules then result in hot molecules which dissociate to produce atoms which further enhance the absorption process. Further collisions with atoms produce protons and more electrons which further enhance beam absorption. Initiation would not be guaranteed unless the operating conditions were within the realm of plasma stability. The initiation procedure is practically instantaneous, and the tungsten rod was retracted immediately following initiation. Assuming the test conditions are within stability limits, the plasma is self-sustaining. However, a drop in incident power or gas pressure, or an increase in gas flow rate could cause the plasma to become unstable and extinguish as was discussed in Chapter 1. The test stand can be seen in the diagram of Figure 2.1.

The absorption chamber has several basic diagnostic features which were used to gather temperature and beam absorption data. To monitor chamber wall temperature, a type T thermocouple is embedded in the chamber wall. This thermocouple was used primarily as a safety precaution to prevent damage to neoprene seals due to excessive temperatures. A single type K

thermocouple mounted within a three inch section of PVC pipe just upstream of the inlet was used to measure inlet gas temperature. Exhaust gas temperatures were measured by millisecond response, type K thermocouples in each of the four two inch insulated exit ports. A watercooled copper cone calorimeter used both as a beam dump and to measure the amount of energy passing through the chamber is mounted to the chamber directly above the exit section. An array of thermocouples within the calorimeter measure the temperature difference of the cooling water between the outlet and inlet. This temperature difference is used to calculate the amount of power incident on the calorimeter. A failsafe system connected to the calorimeter cooling water control valve prevented plasma initiation (prevented target insertion) if the cooling water was not flowing at a minimum rate of 4 liters per minute to protect the calorimeter. A pressure transducer mounted in the chamber wall provided the chamber pressure for a feedback control system which controlled the chamber pressure. The methods used for the calibration of the laser power and the calorimeter are irrelevant to this work. However, this information can be found in Zerkle (1988) and Mertogul (1989).

There are four variable parameters which could be controlled using the facility just described. These parameters are laser power, beam focusing f-number, gas pressure, and gas flow rate. The laser output could be changed simply by adjusting its power settings. The beam f-number, which is defined as the ratio of the beam outer diameter to the lens focal length, could be switched to be either 4.1 or 7.1 simply by changing the focusing lens employed. The chamber gas pressure and flow rates were controlled by the hydrogen handling system which is fully described in Appendix A.

Data from the thermocouples, the calorimeter, and the chamber pressure transducer were scanned once every second by a Fluke 2240A datalogger. The data was immediately transferred to a Macintosh Plus and stored for later analysis. The errors inherent in the data reduction are fully discussed in Appendix B.
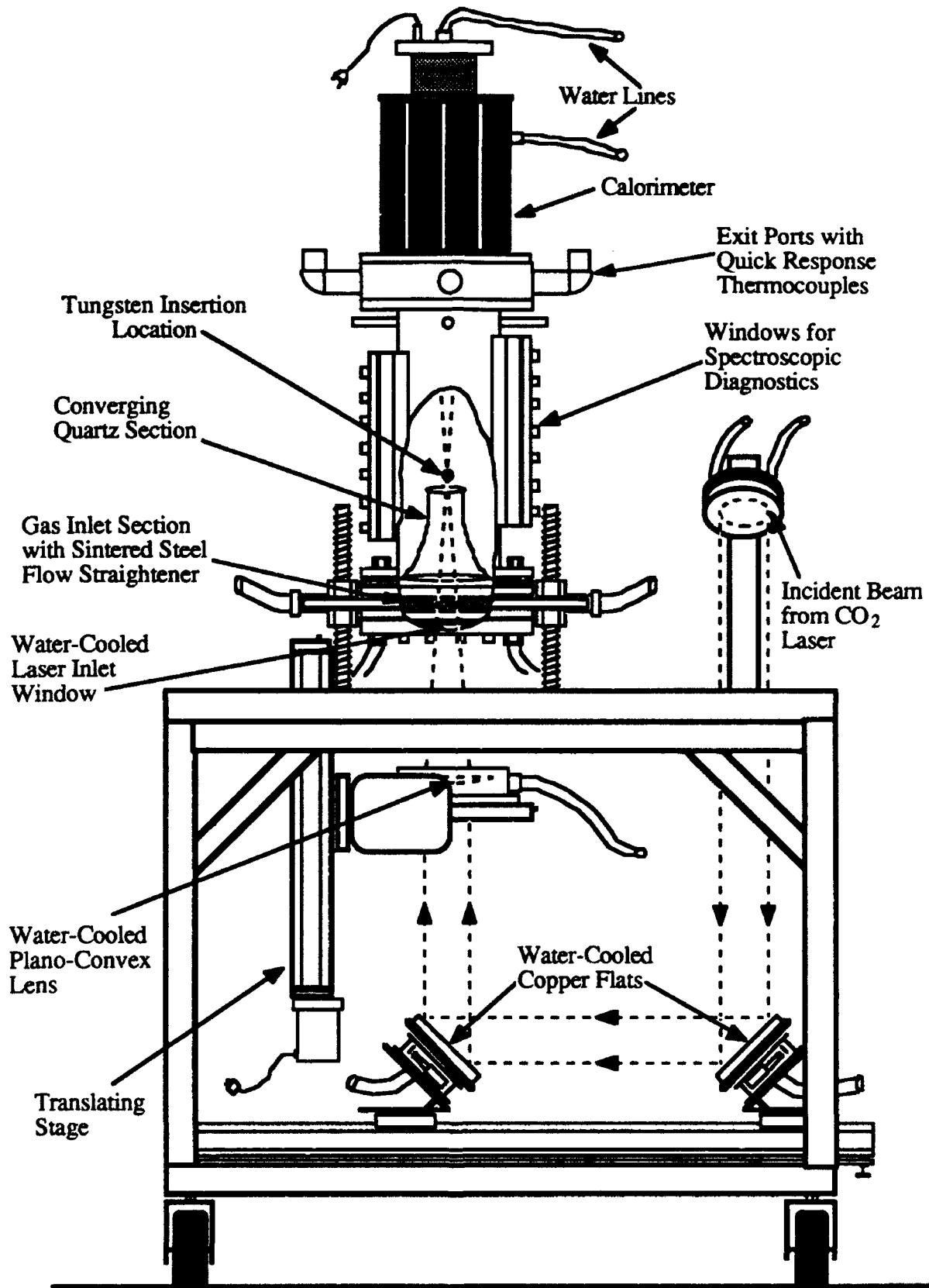
Figure 2.1   Test stand used in hydrogen plasma experiments.

2.2 Global Absorption and Thermal Efficiency

The two measured performance quantities in this work are global absorption and thermal efficiency. Global absorption was computed using the measured transmitted energy as determined from calorimeter measurements. The global absorption was determined by the simple relation:

$$\alpha = \frac{P_{input} - P_{measured}}{P_{input}} \qquad (2.1)$$

where P_{input} is the input laser power, and $P_{measured}$ is the measured transmitted laser power. The global absorption is expressed as a percentage by simply multiplying α by 100. The total error in the measured global absorption varies with the experimental conditions, and has been computed in Appendix B for all test cases. A good representative value for this absolute error is less than $\pm 2\%$.

Thermal efficiency was computed using the stagnation temperature increase between the chamber inlet and exit as measured by the inlet and exit thermocouples. Thermal efficiency was then determined by the simple relation:

$$\eta = \frac{\dot{m} C_p \Delta T}{P_{input}} \qquad (2.2)$$

where $\dot{m}$ is the mass flow rate, C_p is the constant pressure specific heat, ΔT is the stagnation temperature increase, and P_{input} is the input laser power. The total absolute error in the measured thermal efficiency has been computed in Appendix B for every test case, and a good representative value is less than $\pm 6\%$.

Global absorption and thermal efficiency for mixture experiments involving argon and hydrogen are also computed using equations (2.1) and (2.2) as explained in Appendix B, and as listed in Appendix C. Based on that listing, representative values for absolute error for global absorption and thermal efficiency for the mixtures are less than $\pm 2\%$ and $\pm 6\%$ respectively.

2.3 Experimental Results

Similar to the qualitative results of Kozlov, Kuznetsov, and Masyukov (1979), the results of UIUC experiments also indicated hydrogen plasmas to be smaller and to radiate less than argon plasmas at similar conditions. In addition, hydrogen plasmas had a distinct pink coloration which is a result of Balmer line emission. Based on photographic evidence, the LSPs were shaped

roughly like elongated ellipses with the long axis aligned with the gas flow direction. The LSPs typically varied between 4 and 6 mm in diameter and 11 and 19 mm in length over the range of operating conditions tested. Operating conditions appeared to have a predictable effect on plasma size and shape. Again based on photographic evidence, increased incident laser power resulted in an LSP with slightly increased length and width. Also, f-7.1 LSPs had a distinctively pointier downstream end (more teardrop shaped) than f-4.1 LSPs.

The results reported below and appearing in Mertogul, Zerkle, and Krier (1992) represent the first quantitative study of global absorption and thermal efficiency conducted for continuous wave laser sustained plasmas using hydrogen as the propellant gas. However, as a precursor to testing pure hydrogen plasmas, experiments were conducted using argon and hydrogen mixtures. Argon plasmas were a known quantity with regard to stability and performance. Therefore it was felt that the best way to achieve stable hydrogen plasmas was to start with stable argon plasmas and transition to pure hydrogen. The effect of hydrogen addition on the performance of argon plasmas was also of interest.

Mixture experiments were conducted at 7 kW, approximately 2.5 atm, f-4.1 focusing geometry, and fixed mole fluxes of 345 moles/m²s and 690 moles/m²s. Results of the mixture experiments can be seen in the plot of Figure 2.2.

Note that global absorption (as denoted by the square symbols in Figure 2.2) is essentially constant versus the hydrogen mixture percentage, but is approximately 13% greater for the higher mole flux case. Therefore the addition of hydrogen does not appreciably alter the local absorption coefficients by altering the number density of absorbers. The greater total mole flux would cause the plasma to be positioned closer to the beam focus than the lesser total mole flux. The greater beam intensity closer to the focus may be the reason global absorption is higher for the 690 moles/m²s case.

The addition of hydrogen has a significant effect on thermal efficiency. Note that the thermal efficiency (as denoted by the circular symbols in Figure 2.2) increases with the increased addition of hydrogen. A possible explanation for this result is that hydrogen has greater thermal

conductivity and specific heat than does argon. Therefore the hydrogen plasma would be expected to be cooler than the argon plasma, thereby radiating less energy. Since a major portion of the difference between measured global absorption and measured thermal efficiency is lost radiation, the addition of hydrogen causes an increase in thermal efficiency. Due to the molecular weight of hydrogen, it was originally proposed as a propellant to maximize specific impulse. However, now the additional advantage of better performing LSPs has also been demonstrated.
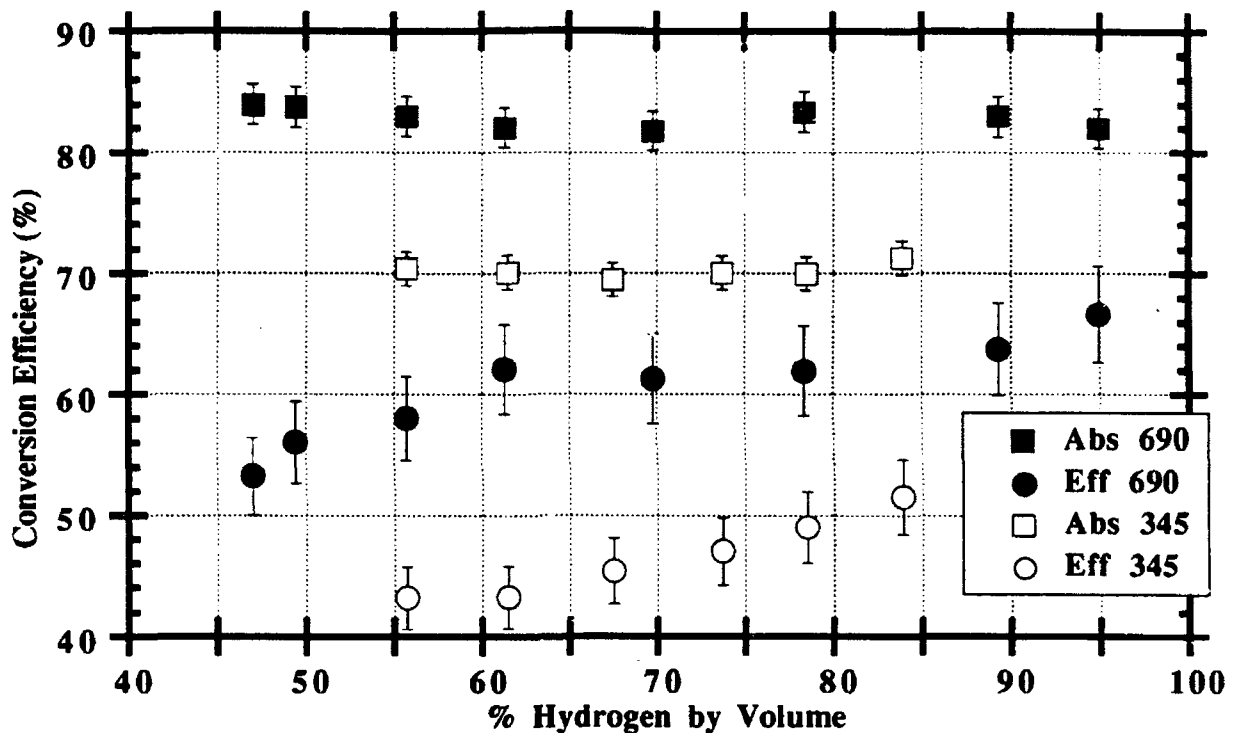
Figure 2.2   Global Absorption and Thermal Efficiency for mixtures of argon
            and hydrogen at fixed total mole fluxes of 345 moles/m²s and 690 moles/m²s, 7kW,
            f-4.1, and approximately 2.5 atm.

The successful measurement of global absorption and thermal efficiency of pure hydrogen LSPs depended upon whether or not the operating conditions were within the limits of LSP stability. Blindly choosing a set of operating conditions and attempting to ignite an LSP in pure hydrogen is a hit or miss approach. The mixture experiments provided not only performance data but also an indication of stable operating conditions for pure LSPs.

The range of allowable mole fluxes which could be used to sustain pure hydrogen LSPs was limited on the high end by LSP blowouts and on the low end by the inability of the hydrogen handling system to maintain chamber pressure as discussed in Appendix A. Therefore experiments were not conducted in the low mole flux, high pressure regime. This was not considered significant since it was expected that optimal mole fluxes would be near to the blowout mole fluxes. There was however, a well known phenomenon associated with low mole flux, high f-number, and high pressure which is of interest to the discussion of LSP stability.

The phenomenon, which is commonly called a shockout, occurs in conditions of high pressure and low mole flux, or high f-numbers, or combinations of both whenever there is not enough propellant flux to force the LSP to remain close to the laser focus. Fowler and Smith (1975) reported that LSPs with f-numbers greater than approximately 10 typically would not remain stable because the LSP front was far from the beam focus. Therefore small perturbations in the system would cause a large amplitude LSP bounce as described in Chapter 1, and the LSPs were likely to extinguish. Kozlov, Kuznetsov, and Masyukov (1979) reported the same phenomenon, although they described it differently. LSPs in both monatomic and molecular gases (including H_2) were found to extinguish if the gas pressure was increased while holding the other parameters constant. Clearly this phenomenon is the same as that reported by Fowler and Smith (1975) since an increase in gas pressure would result in the LSP front moving upstream away from the focus. Kozlov, Kuznetsov, and Masyukov (1979) attribute the instability to an increase in laser absorption at the plasma front, coupled with a temperature decrease in the plasma core, which through an analysis of the plasma energy balance results in an instability. Keefer, Welle, and Peters (1985) report another strikingly similar phenomenon which appears to be caused by both high f-numbers and increased pressure. Argon LSPs sustained with a 12 inch focal length lens and a given power and mole flux were reported to be stable up to but not beyond 2 atm, while LSPs sustained with an 8 inch focal length lens with the same power and mole flux demonstrated no instability problems for the range of pressures investigated. Finally, the shockout instability was also reported by Mertogul (1989) for 2.5 kW, f-7.1, 2.5 atm argon LSPs at mass fluxes below 15.5 kg/m^{2}s.

Although the shockout phenomenon was not of direct interest in this work, it has important implications for the construction of laser thrusters, in which focusing geometry, chamber pressure and gas mole flux are necessarily linked. Pressure and mole flux conditions for stable f-8.5, 7 kW LSPs were mapped in both Black, et al. (1992), and Black, Krier, and Glumb (1992). Although the authors mistakenly claimed that a new low-velocity LSP instability had been discovered, both papers illustrate the importance of the phenomenon to design and construction of a laser thruster.

Blowouts of hydrogen LSPs were recorded for a variety of powers and pressures. The method in which the blowout conditions were determined varied. In some cases a series of mole fluxes were run at a given power, pressure and beam geometry until the LSP could no longer be maintained. Then the mole flux for which the LSP was no longer stable was recorded as the blowout mole flux for that power, pressure and f-number. Alternately, the chamber pressure and mole flux were held constant and the laser power was gradually reduced until the LSP became unstable. In this case the power for which the LSP became unstable was recorded along with the mole flux, pressure and f-number. In another variation, chamber pressure was decreased until the LSP blew out. In all cases, the exact conditions for blowout were difficult to determine without some error. Nevertheless the recorded blowouts should provide a meaningful description of hydrogen LSP blowout stability limits. The recorded values for blowout conditions are listed in Table 2.1 and plotted in Figure 2.3.

In addition to the 14 mixture data points, there were 98 pure hydrogen data points acquired. The global absorption and thermal efficiency results for pure hydrogen LSPs will be presented in the following sections. For reference purposes, 2000 moles/m^{2}s of hydrogen corresponds to 7.296 g/s which at 3.5 atm corresponds to an average flow speed of 14.1 m/s upstream of the LSP.

The global absorption of a hydrogen LSP has been found to be strongly influenced by the laser power. It is evident from the plot in Figure 2.4 that for a given gas pressure, global absorption is determined by the incident power and is relatively independent of the mole flux. In addition the LSP blowout limit was observed to increase with incident power. Note that at 3.5 kW incident

power no plasmas could be held stable at mole fluxes beyond approximately 2023 moles/m^{2}s. None of the 5 or 7 kW LSPs was observed to become unstable at this pressure at the mole fluxes investigated.

Table 2.1 Hydrogen LSP Blowout Conditions

Power (kW)	Pressure (atm)	F-number	Mole Flux (moles/m^{2}s)
7.00	1.39	4.1	499
7.00	1.53	4.1	699
7.00	1.70	4.1	704
7.00	1.80	4.1	1011
7.00	1.84	4.1	1198
7.00	2.11	4.1	1244
6.42	2.04	4.1	1096
6.42	2.15	4.1	1203
6.42	2.51	4.1	1664
5.15	2.13	4.1	1075
5.00	2.13	4.1	842
4.41	2.11	4.1	696
4.41	2.17	4.1	872
3.56	3.57	4.1	2248
3.56	3.55	4.1	2023
3.06	4.05	4.1	1982
2.93	3.54	4.1	1483
2.93	4.02	4.1	1823
7.00	1.84	7.1	882
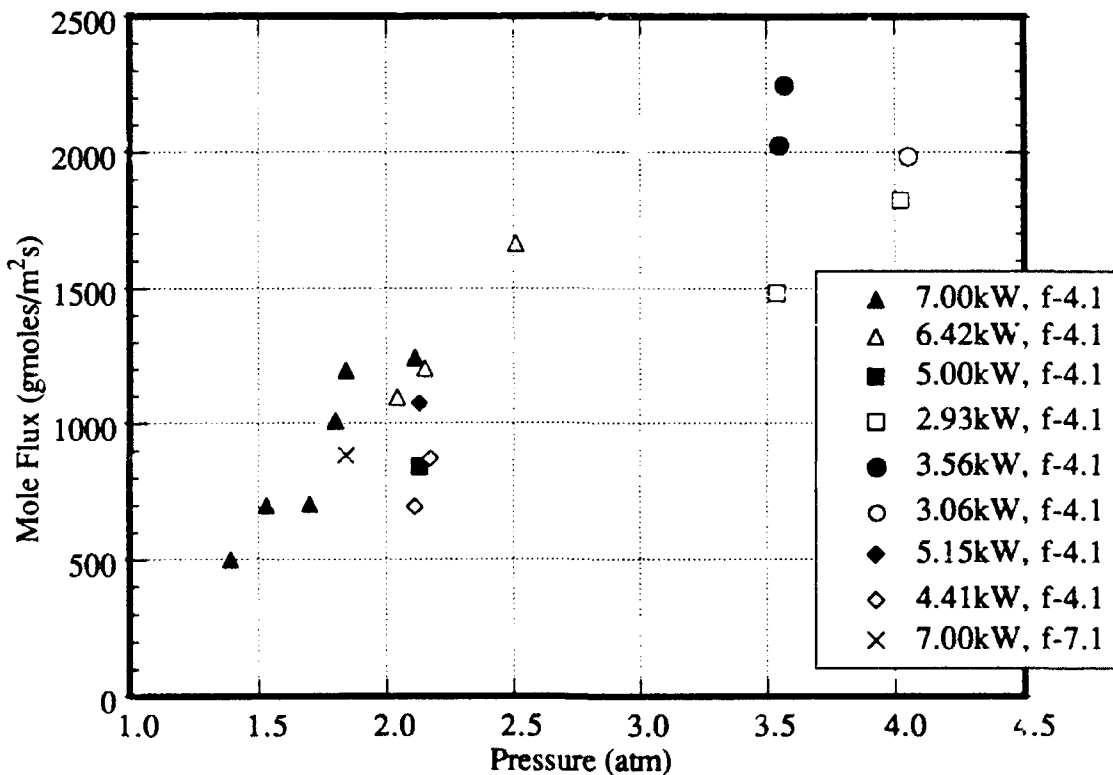
Figure 2.3   Plot of blowout conditions for hydrogen LSPs
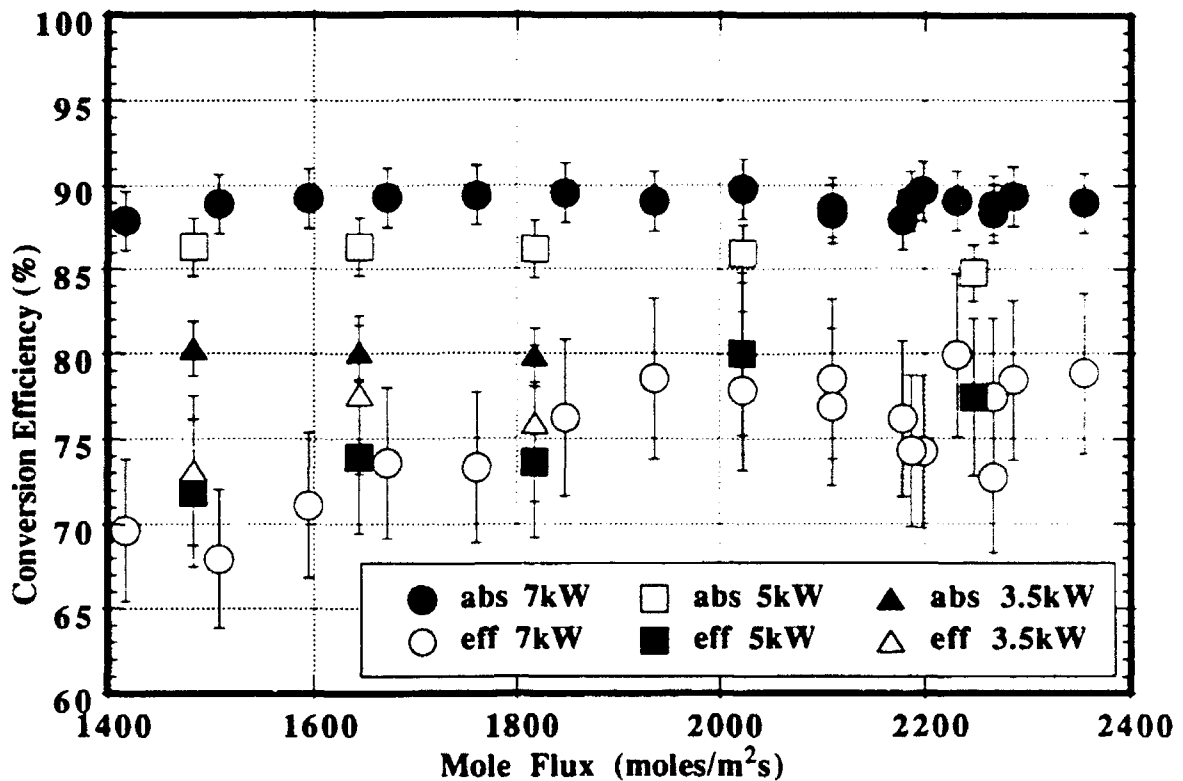
Figure 2.4   Global Absorption and Thermal Efficiency of f-4.1 hydrogen LSPs
plotted vs mole flux for incident laser powers of 3.5, 5, and 7 kW, at 3.53±0.11 atm
gas pressure.

Although for a given mole flux and gas pressure greater absorption is achieved at greater power, the LSP thermal efficiency does not follow such a simple relation. For a given mole flux and pressure, the thermal efficiency depends on how close the conditions are to the optimal mole flux. Due to the shift in upstream position of the LSP with increased power, an increase in mole flux is required to force the LSP back downstream to its optimal position. It is evident from the previous discussion that because increased incident power results in increased absorption and an increased mole flux stability limit, greater thermal efficiencies are possible at increased incident power and mole fluxes beyond the stability limit of low powers.

Gas pressure variation affects global absorption and thermal efficiency in a way analogous with incident power variation. An increase in gas pressure results in an increase in the mole flux stability limit. At 7 kW incident power, and f-4.1 focusing geometry, LSPs at 1.80 atm are not stable beyond 1011 moles/m^{2}s. However at the same conditions and 3.52 atm, the LSPs exhibit

no instabilities and are stable at the maximum mole flux tested, 2355 moles/m^2s. Similarly LSPs at 5 kW, f-4.1, 2.13 atm are not stable at mole fluxes greater than 842 moles/m^2s, but at the same conditions and 3.55 atm the LSPs again exhibit no instabilities and are stable at the maximum mole flux tested at 5 kW, 2247 moles/m^2s.

Increases in gas pressure also result in increases in global absorption, although present evidence indicates that absorption levels off at the highest pressures tested, 3.53 and 4.08 atm, as indicated by the plot in Figure 2.5. More data at higher pressure and possibly at a different power level are required to verify this absorption plateau.

As is the case with increased incident power, increased gas pressure causes an increase in optimal mole flux. As indicated by the data in Figure 2.5, increased global absorption from increased gas pressure allows for the possibility of increased thermal efficiency assuming the mole flux can be optimized. Referring to the data in Figure 2.5 the thermal efficiency at 4.08 atm was not at the optimal mole flux and therefore appears slightly low.

In order to observe the effects of varying focusing geometry, 7 kW, f-7.1 LSP experiments were conducted at 2.52, 3.05 and 3.54 atm for comparison with 7 kW, f-4.1 experiments at those pressures. In all cases f-7.1 LSPs produced lower global absorption and thermal efficiency than f-4.1 LSPs. A comparison of f-4.1 and f-7.1 LSP performance can be seen in Figure 2.6. In addition it was observed that the f-4.1 geometry produced LSPs which were stable at greater mole fluxes than the f-7.1 geometry. At 7 kW incident power and f-4.1 focusing geometry, LSPs at 1.84 atm extinguished due to blowout at approximately 1198 moles/m^2s, however 7 kW, 1.84 atm, f-7.1 LSPs were not stable at mole fluxes greater than 882 moles/m^2s.

The effect of mole flux variation was briefly touched upon above. It is important to have a physical understanding of what the variation of mole flux does to LSP behavior. A stable LSP exists in a state of balance where energy gained through absorption of the incident beam equals energy lost through plasma radiation as well as convection and conduction to the propellant gas. A stable LSP will occupy a position such that the LSP leading edge is upstream of the beam focus. An increase in the mole flux results in an increase in the LSP convective transfer to the propellant

and causes the LSP front to shift position downstream (closer to the focus) to a position in the focused beam with a higher power flux. The LSP will restabilize at a position where the energy absorbed once again balances the energy lost. However if the incident beam power is insufficient, the LSP front will be forced downstream of the beam focus where the LSP extinguishes.
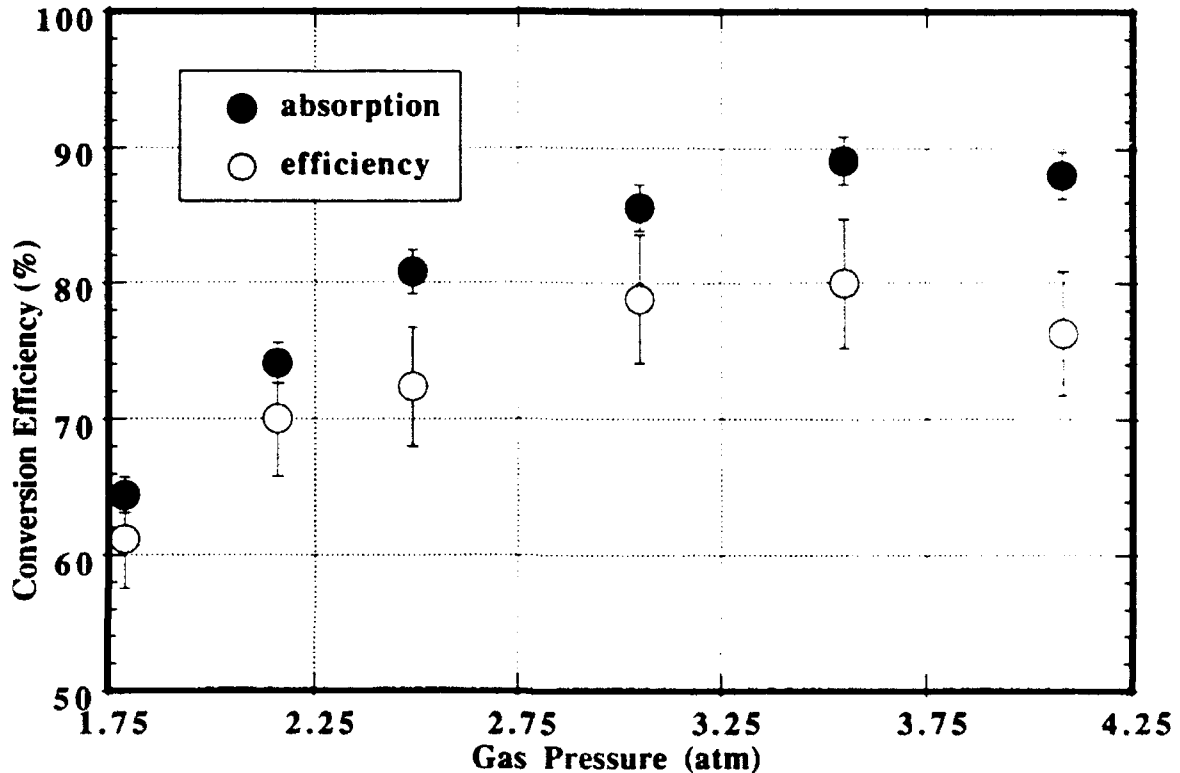
Figure 2.5   Maximum measured thermal efficiency and corresponding global absorption for 7 kW, f-4.1 hydrogen LSPs at the indicated pressures.

Following this reasoning it is apparent why the mole flux for optimum thermal efficiency increases with both incident power and gas pressure. An increase in laser power causes an increase in incident power flux and causes the LSP to reposition upstream where the beam is less focused and where power absorbed balances power lost. Similarly an increase in gas pressure increases the local absorption coefficient (due to an overall increase in electron number density) causing the LSP to again reposition upstream to a beam position with a lower power flux where the energy balance is again reestablished. Optimally the LSP is positioned where the losses to the propellant (conductive and convective) are maximized while the radiative losses to the chamber

walls are minimized. Increased incident laser power and gas pressure both cause the LSP to shift upstream requiring increased mole fluxes to force the LSP back downstream to optimal position.
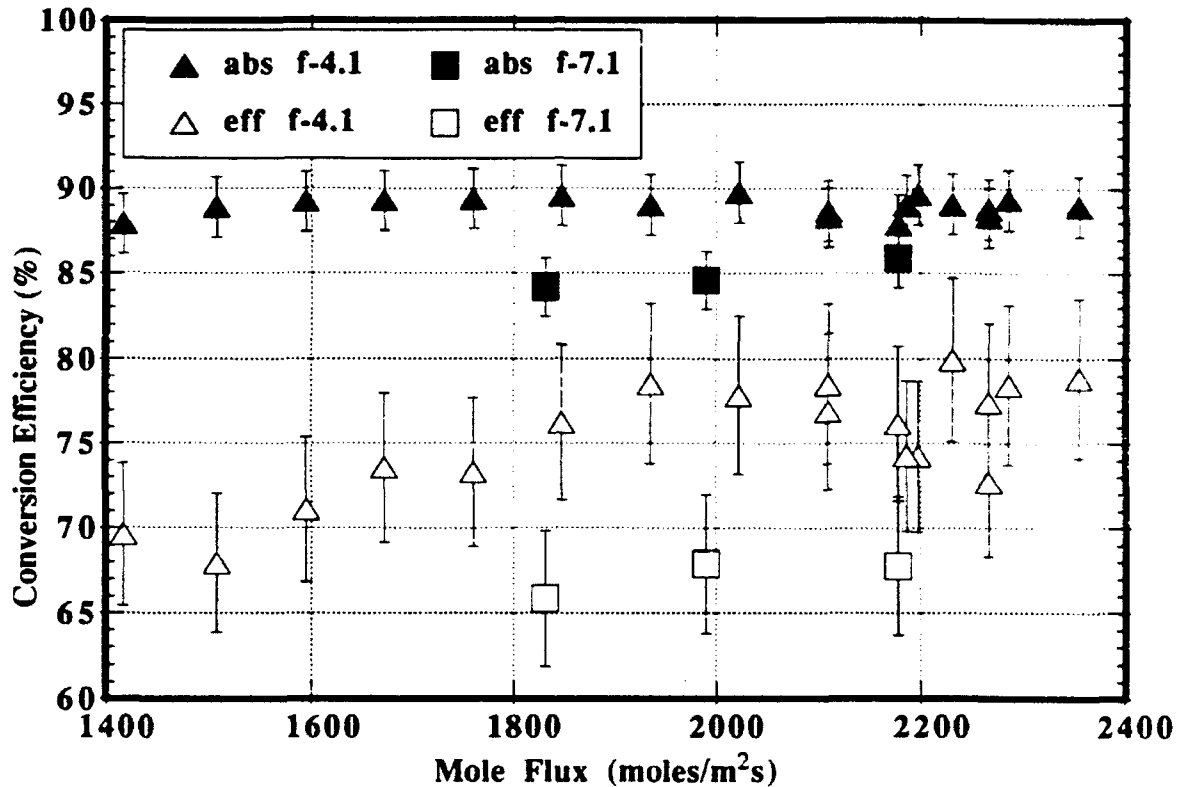
Figure 2.6   Global absorption and thermal efficiency of 7 kW, f-4.1, hydrogen LSPs at 3.52±0.10 atm, and 7 kW, f-7.1, hydrogen LSPs at 3.54±0.01 atm.

2.4 Experimental Conclusions

It has been experimentally demonstrated that pure hydrogen LSPs have better thermal efficiencies than argon-hydrogen mixture LSPs for conditions of identical power, pressure, f-number and total mole flux.

Measurements of global absorption and thermal efficiency of pure hydrogen LSPs have been presented. Global absorption of the incident laser power was observed to increase with increases in both incident power and gas pressure. Although the highest measured value for global absorption was 89.8% it is expected that 100% absorption is possible with higher incident laser powers. The optimal mole flux for thermal efficiency was also observed to increase with increased incident power and gas pressure. Higher global absorption and thermal efficiency as well as an

extended blowout stability limit can be expected from lower f-number focusing geometry as compared to higher f-number focusing geometry.

The minimum overall efficiency required for the feasibility of laser propulsion as an orbital transfer technology was determined to be 30% by Frisbee, Horvath and Sercel (1985). Although it cannot be guaranteed that laboratory results will scale to the power levels in excess of 1 MW required in an actual laser thruster, the results for thermal efficiency presented in this work indicate that laser propulsion is a feasible orbital transfer technology.

3. Generalized Non-LTE Model Formulation

The key to producing LSPs with high thermal efficiencies is to maximize global absorption and minimize radiation loss from the LSP. It has been proposed that a minimum total conversion efficiency of 30% is necessary for laser propulsion to be a feasible concept (Frisbee, Horvath, and Sercel, 1985). Measurements have demonstrated global absorption as high as 89.8% and thermal efficiency as high as 80.2% using hydrogen as the propellant gas. These global measurements provide meaningful information regarding the effects of the control parameters on overall system performance but give no information on the detailed structure of the LSP and the actual energy transfer mechanisms. The goal of this work was to formulate a model for the prediction of global absorption and thermal efficiency at very high input laser powers as would be used in an actual thruster. However the accurate prediction of these quantities depends completely on the accurate modeling of the LSP physics on a microscopic level, including species reactions, transport coefficients and radiation.

The problem to be solved is that of an axisymmetric hydrogen laser sustained plasma. The control parameters are the gas mole flux (determined by mass flow rate and duct cross section), incident laser power, incident beam focusing geometry, gas pressure, and laser wavelength (now set at 10.6 microns but may be varied). A variable number of species (minimum of 12) will be included in the analysis depending upon the highest neutral level of hydrogen computed. These species include the neutral electronically excited levels of hydrogen, electrons, protons, H_2, H^-, H_2^+, and H_3^+. The model will produce predictions for global absorption fraction, and thermal efficiency which are the fraction of laser power absorbed by the propellant gas and the fraction of laser power retained by the gas as thermal energy. In addition the model will also provide axisymmetric fields for electron temperature, heavy species temperature, gas velocity, all the species number densities, rates of production of species, and local beam absorption. The rates of species production and local beam absorption are useful in determining which portions of the plasma are ionizing and which portions are recombining. The species temperatures and number

densities may be analyzed to determine the extent of kinetic, Boltzmann, and Saha non-equilibrium.

3.1 Literature Review

All previous models of LSPs, regardless of the type of propellant considered, the method of calculating energy absorbed, or the numerical solution scheme *have assumed LTE to be a valid assumption*. Early attempts include the one dimensional constant pressure model of Raizer (1970) which used an absorption coefficient that was a function of temperature and pressure, a variable intensity input beam, and tabulated values of thermal conductivity. The model was for air at one atm and included a term for radiation loss that was also a function of temperature and pressure. Kemp and Root (1979) also formulated a one dimensional constant pressure model which calculated equilibrium concentrations and thermodynamic properties using a method similar to Patch (1971). The Kemp and Root (1979) model included both electron ion (e-i) and electron neutral (e-n) IB absorption coefficients taken from Caledonia, Wu, and Pirri (1975), and values for thermal conductivity which combined the calculations of Yos (1963) with a radiative thermal conductivity which was a function of temperature. The Kemp and Root (1979) model was for hydrogen at pressures from 1 to 30 atm and laser intensities from 10^4 to 10^6 W/cm^2, and included a term for radiation loss as a function of temperature and pressure.

The earliest attempt at a two dimensional model was that of Muller and Uhlenbusch (1982) which was for argon at 5 bar pressure. This model included a focused input beam, an IB absorption coefficient, and values for thermal conductivity including radiation taken from experimental data. In addition, the model assumed that the ratio of specific heat at constant pressure to thermal conductivity was a constant, and that convection in the radial direction could be neglected. This second assumption reduced the problem to one of a single energy balance equation.

The first fully two dimensional model was that of Molvik, Choi, and Merkle (1984), which solved the problem of a focused laser beam in unchoked hydrogen flow through a converging diverging nozzle. Real gas properties and the ideal gas law were used, with separate grids for the

fluid dynamics and radiation equations. A constant absorption coefficient was assumed allowing the source term appearing in the energy equation to be treated explicitly which simplified the numerical solution. Actual calculations were done with a stagnation pressure of 1.04×10^6 N/m², a downstream static pressure of 1×10^6 N/m², and a stagnation temperature of 6250 K. Although the effect of laser input power on peak temperature was discussed, no calculations of global absorption or thermal efficiency were presented. The model of Glumb and Krier (1986) was the first to calculate these quantities. This model was for axisymmetric steady flow and neglected radial velocities, like Muller and Uhlenbusch (1982), but included real gas properties for argon at 1 atm including expressions for IB absorption and radiation loss. A variable focused beam intensity and variable propellant velocity were included. Argon was chosen for the analysis for comparison with existing experimental data. Results from the model included predictions for temperature fields, global absorption, thermal efficiency and blowout flow velocity.

Presented at roughly the same time as the Glumb and Krier (1986) model, the model of Merkle, Molvik, and Shaw (1985) again solved the fully two dimensional problem of a 10.6 μm laser beam focused into a propellant in a converging diverging nozzle. Parametric studies of laser power, beam focal length, gas velocity, inlet temperature and gas pressure were made. The input beam was split into a series of individual rays which were tracked through the LSP with both diffraction and refraction effects ignored. The propellant was hydrogen seeded with 1% cesium to boost low temperature absorptivities. This was done to lower the peak temperatures encountered and thereby minimize the numerical problems associated with extreme temperature gradients. Real gas properties for pure hydrogen (neglecting the cesium) as well as the perfect gas law were used. Unlike the earlier model of this group, Molvik, Choi, and Merkle (1984), a variable absorption coefficient was used for the propellant mixture taken from Kemp and Krech (1980). Results included temperature contours but no information on global absorption or thermal efficiency.

The first fully two dimensional model to predict global absorption and thermal efficiency was that of Jeng and Keefer (1987b). Hydrogen was used as the propellant gas in an axisymmetric flowfield. As was done by Merkle, Molvik, and Shaw (1985), the input beam was split into a

finite number of rays which were then tracked through the LSP. The effects of beam diffraction through the focusing lens and refraction within the LSP were neglected as minor. As was done in the Glumb and Krier (1986) model, radiation was divided into an optically thin portion which was assumed lost to the surroundings and an optically thick portion which was accounted for through a radiative conductivity term. The flow was assumed to be laminar so that the kinetic energy and viscous dissipation terms in the energy equation were neglected. Thermodynamic properties were interpolated from various tabulated sources (Patch, 1971, and Grier, 1962 and 1966), radiative conductivity was taken from the work of Kemp and Root (1979), expressions for e-i and e-n IB absorption from Caledonia, Wu, and Pirri (1975), and radiation loss from the LSP was taken from the work of Kemp et al. (1977). The SIMPLE algorithm as found in the work of Patankar (1980) was used to solve for velocity, temperature and pressure fields. Results include velocity and temperature contours, as well predictions for global absorption and thermal efficiency versus variations in laser power, inlet velocity, optical f-number, and gas pressure. Jeng and Keefer (1987a) also presented an analysis of a converging-diverging thruster geometry using the same model.

Beddini, Owano, and Kuo (1987) have presented an alternative formulation to the problem of laser beam and flowfield interaction. Their model assumes an axisymmetric flowfield using argon as the propellant. Although the exact technique used to implement a focused beam is unclear, Beddini states that ray tracing is not used. In another work, Beddini and Owano (1987) solved the problem of energy addition to an axisymmetric flow of both argon and hydrogen with and without wall injection. This effort uses quasi-ellipsoidal energy addition zones to heat the gas, thereby avoiding the necessity of dealing with the calculation of absorption coefficients and reality in general.

The latest LSP model was that of Eguiguren (1989) which was similar in many ways to the earlier model of Jeng and Keefer (1987b). The most useful aspect of Eguiguren's model were the predictions of global absorption and thermal efficiency as well as temperature and stream function contours for argon and hydrogen at one atm gas pressure. Results for global absorption and

thermal efficiency from the Eguiguren (1989) model are presented with experimental data from Mertogul (1989) and Zerkle, et al. (1990) in Figure 3.1. Trends for absorption and efficiency appear to agree with a slight discrepancy in the actual thermal efficiency values which may be due to two assumptions of the model. First the model assumed that the system was adiabatic which may not have been the experimental reality. Energy lost to the absorption chamber would result in model overprediction of thermal efficiencies. The other assumption was that of LTE, which has since been proven to be incorrect by Zerkle (1992a). The presence of non-LTE means that the electrons are hotter than the heavy species and hotter than they would be in LTE. The hotter non-LTE electrons radiate more than would be predicted by the model, again causing an overprediction for thermal efficiency.
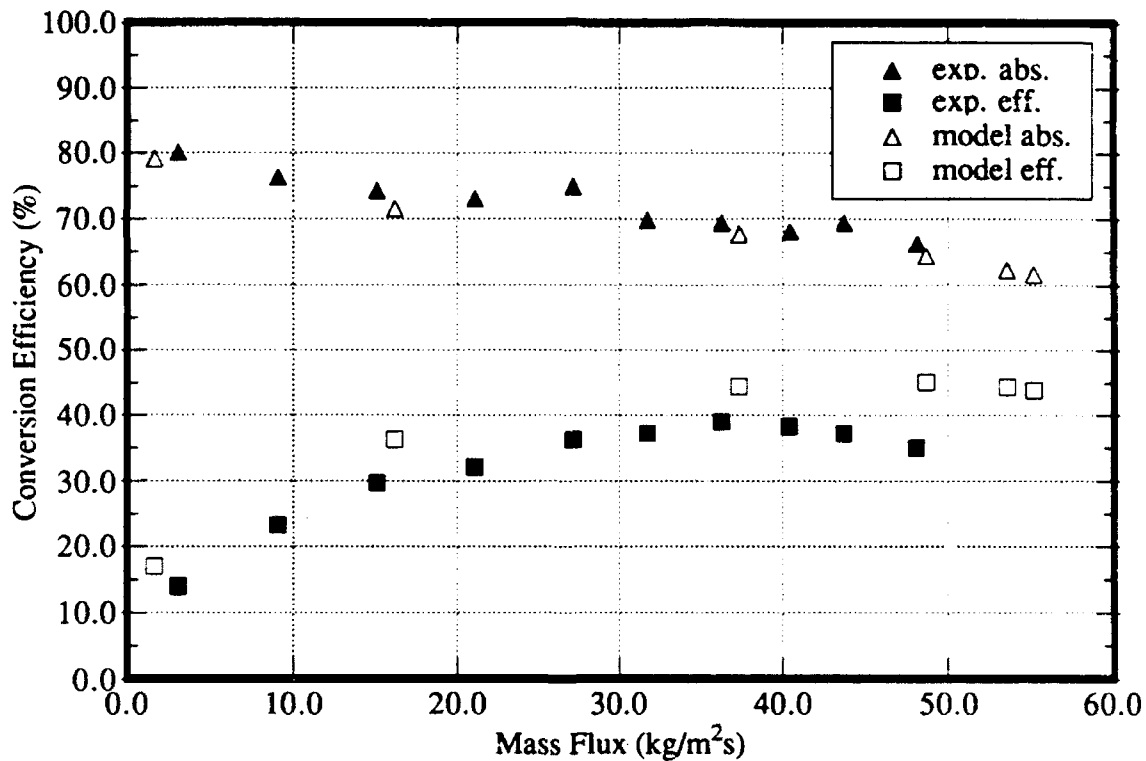
Figure 3.1   Comparison of results from the Eguiguren (1989) LTE model for argon 5kW, f-4, 1 atm LSPs, and experimental results from Mertogul (1989) and Zerkle, et al. (1990) for argon 5kW, f-4.1, 1 atm LSPs

Thermodynamic and transport data were acquired from interpolation of tables, which limited the range of applicability of the model. The core of the program used the SIMPLE algorithm described

by Patankar (1980) to solve the axisymmetric momentum, energy and continuity (through the pressure correction equation) equations.

Although there have been no attempts at non-LTE LSP modeling, electric arcs and other plasmas have been modeled with and without the assumption of LTE (Butler, Kashiwa, and King, 1990, Rhodes and Keefer, 1990 and 1991, Langerman and Lemmon, 1991, Edwards and Fleck, 1979, Donskoi, Klubnikin, and Salangin, 1985, Miller and Martinez-Sanchez, 1990, Niewood and Martinez-Sanchez, 1990, Lelevkin et al., 1986, Incropera, 1973, Chen and Pfender, 1981, Dix, 1964, Scott and Incropera, 1973, Vriens, 1973 and 1974, Kruger, 1970, Kruger and Mitchner, 1967, Watanabe, et al., 1991, Chang and Pfender, 1990, and Kroesen, et al., 1990).

These models often follow a hierarchy of complexity starting with those that assume LTE. The next step in the progression is to assume a two kinetic temperature model. At this level the species densities may be computed through a thermodynamic analysis using the law of mass action and an equation of state as done by Chen and Pfender (1981). The next level of sophistication is the introduction of species equations and diffusion. Electron species equations have been included by Lelevkin, et al. (1986), and Chang and Pfender (1990), whose models include an electron production term which accounts for electron collisional ionization and electron three body recombination.

3.2 Generalized Non-LTE Model Assumptions

The goal of a generalized non-LTE model is to predict results for global absorption and thermal efficiency of hydrogen laser sustained plasmas (LSPs) at any given pressure, and at very high powers. The approach taken to such a prediction can depend on apriori knowledge of the thermodynamic state of the LSP. If it is known that the LSP is in LTE, collisions are the dominant relaxation mechanism and only one temperature is necessary for a complete thermodynamic description. As discussed in Chapter 1, there are several factors which may be present in a high power LSP which tend to drive the LSP out of equilibrium. These effects include strong electric fields (the incident laser beam), severe temperature gradients, diffusion of excited species, optically thin radiation, and non-local radiation (radiation originating in a remote part of the LSP).

Therefore LSPs cannot in general be assumed to be in local thermal equilibrium, especially at high input beam powers, and a fully general model should include the effects of ionizational, kinetic and populational non-equilibrium. In the general non-LTE case, a separate temperature could be assigned to each energy mode of each species. Excited neutral species populations and ionization fractions may or may not be described by Boltzmann factors and the Saha equation respectively. The non-LTE case greatly complicates the solution process with the introduction of these new temperatures.

The generalized model assumptions include laminar and axisymmetric flow, and steady state conditions. No assumption is made with regard to thermodynamic state except that all heavy species share a common heavy temperature, T_g. Radiation has been split into a number of discrete bands and lines as described in Appendix F.

3.3 Conservation Equations

The problem to be solved is one of axisymmetric duct flow with a variable number of species, two temperatures, and an assortment of energy and species sources. The variables in question are: T_e (electron kinetic temperature), T_g (heavy species temperature), u (axial velocity component), v (radial velocity component), p (local static pressure), X_s (mole fraction for species s), and n_{tot} (the total number density). These variables represent a total of 6+kslast equations, where kslast represents the number of species considered. As in any closed system, there must be an equation for every variable. The derivation of all the conservation equations, (3.1) to (3.7), can be found in Appendix D. The equations will be briefly presented here in their final form.

The axisymmetric electron energy equation for variable electron thermal conductivity is:

$$\frac{\partial}{\partial x}\left(\left(\frac{3}{2}\,k_b\left(unflx+n_eu\right)\right)T_e\right)+\frac{1}{r}\frac{\partial}{\partial r}\left(\left(\frac{3}{2}\,rk_b\left(vnflx+n_ev\right)\right)T_e\right)=\frac{\partial}{\partial x}\left(\lambda_e\frac{\partial T_e}{\partial x}\right)+\frac{1}{r}\frac{\partial}{\partial r}\left(r\lambda_e\frac{\partial T_e}{\partial r}\right)$$

$$-\left(n_ek_b\frac{\partial u}{\partial x}\right)T_e-\left(\frac{n_ek_b}{r}\frac{\partial}{\partial r}(rv)\right)T_e + BABS - ELST + INSTE - RADLS + CONRAD \quad (3.1)$$

where the last five terms represent sources as described in Appendix F and Appendix H.

The axisymmetric heavy species energy equation for variable heavy species thermal conductivity is:

$$\frac{\partial}{\partial x}\left(\left(\frac{3}{2}k_b\left(hunflx+n_hu\right)\right)T_g\right) + \frac{1}{r}\frac{\partial}{\partial r}\left(\left(\frac{3}{2}k_br\left(hvnflx+n_hv\right)\right)T_g\right) = \frac{\partial}{\partial x}\left(\lambda_h\frac{\partial T_g}{\partial x}\right) + \frac{1}{r}\frac{\partial}{\partial r}\left(r\lambda_h\frac{\partial T_g}{\partial r}\right)$$
$$-\left(n_hk_b\frac{\partial u}{\partial x}\right)T_g - \left(\frac{n_hk_b}{r}\frac{\partial}{\partial r}(rv)\right)T_g + ELST + INSTH \qquad (3.2)$$

where, again, the last two terms are sources as described in Appendix F.

The axisymmetric axial momentum equation for variable density and viscosity is:

$$\frac{\partial}{\partial x}(\rho uu) + \frac{1}{r}\frac{\partial}{\partial r}(r\rho uv) =$$
$$\frac{4}{3}\frac{\partial}{\partial x}\left(\mu\frac{\partial u}{\partial x}\right) + \frac{1}{r}\frac{\partial}{\partial r}\left(\mu r\frac{\partial u}{\partial r}\right) - \frac{2}{3}\frac{\partial}{\partial x}\left(\mu\frac{\partial v}{\partial r}\right) - \frac{2}{3r}\frac{\partial}{\partial x}(\mu v) + \frac{1}{r}\frac{\partial}{\partial r}\left(\mu r\frac{\partial v}{\partial x}\right) - \frac{\partial p}{\partial x} - \rho g \qquad (3.3)$$

The axisymmetric radial momentum equation for variable density and viscosity is:

$$\frac{\partial}{\partial x}(\rho uv) + \frac{1}{r\partial r}(r\rho vv) = \frac{\partial}{\partial x}\left(\mu\frac{\partial v}{\partial x}\right) + \frac{4}{3r}\frac{\partial}{\partial r}\left(\mu r\frac{\partial v}{\partial r}\right) + \frac{\partial}{\partial x}\left(\mu\frac{\partial u}{\partial r}\right)$$
$$-\frac{2}{3r}\frac{\partial}{\partial r}\left(\mu r\frac{\partial u}{\partial x}\right) + \frac{2\mu}{3r}\frac{\partial u}{\partial x} - \frac{\partial p}{\partial r} - \frac{4}{3}\frac{\mu v}{r^2} - \frac{2v}{3r}\frac{\partial\mu}{\partial r} \qquad (3.4)$$

The bulk continuity equation for a variable density axisymmetric cylindrical system is:

$$\frac{\partial}{\partial x}(\rho u) + \frac{1}{r\partial r}(r\rho v) = 0 \qquad (3.5)$$

which in the realm of the SIMPLE algorithm (Patankar, 1980) is used to solve for the local pressure, p.

The axisymmetric species continuity equation for any species, s, is:

$$\frac{\partial}{\partial x}(n_su) + \frac{1}{r\partial r}(vn_sr) = -\frac{\partial}{\partial x}(n_su_s) - \frac{1}{r\partial r}(v_sn_sr) + \left(\dot{n}_s\right)_{CR} \qquad (3.6)$$

where the uppermost bound atomic level included is determined by the magnitude of the lowering of the ionization potential which is determined by plasma conditions. If the diffusion fluxes are replaced by a mole fraction and effective diffusion coefficient formulation, then equation (3.6) may be equivalently written as:

$$\frac{\partial}{\partial x}(n_{tot}X_su) + \frac{1}{r}\frac{\partial}{\partial r}(n_{tot}X_srv) = \frac{\partial}{\partial x}\left(D_{effu}\frac{\partial X_s}{\partial x}\right) + \frac{1}{r}\frac{\partial}{\partial r}\left(rD_{effv}\frac{\partial X_s}{\partial r}\right) + \frac{\partial}{\partial x}\left(\frac{1}{m_s}D_s^T\frac{\partial}{\partial x}(\ln T_s)\right)$$
$$+ \frac{1}{r}\frac{\partial}{\partial r}\left(\frac{r}{m_s}D_s^T\frac{\partial}{\partial r}(\ln T_s)\right) + \left(\dot{n}_s\right)_{CR} \qquad (3.7)$$

where D_{effu} and D_{effv} represent the effective axial and radial diffusion coefficients for species s which are described in Appendix G, and D_s^T is the thermal diffusion coefficient which is described in Appendix E.

The equation of state necessary to relate total number density to system pressure and the electron and gas temperatures is:

$$P = n_{tot}\left(X_e k_b T_e + X_h k_b T_g\right)\left(1 - P_c^{DH}\right) \tag{3.8}$$

where P is the system pressure, and P_c^{DH} is the Debye-Hückel pressure correction which is (Cho, 1988):

$$P_c^{DH} = \left(24\pi\left(n_e + n_h\right)\left(\frac{4\pi e^2 k_c}{k_b}\left(\frac{n_e}{T_e} + \frac{(n_{H^+}) + (n_{H^-}) + (n_{H_2^+}) + (n_{H_3^+})}{T_g}\right)\right)^{1.5}\right)^{-1} \tag{3.9}$$

3.4 Transport Coefficients and Source Terms

The prediction of global absorption and thermal efficiency can be considered to be a macroscopic prediction that requires the accurate prediction of LSP thermodynamic properties and transport coefficients including all the species number densities at each point within the LSP. Once the species number densities and kinetic temperatures are known, the transport coefficients can be calculated.

The transport coefficients for the set of conservation equations (3.1) to (3.7) include the global viscosity, μ, and the thermal conductivity for electrons and heavy particles, λ_e, and λ_h. In addition, the multicomponent diffusion coefficient, D_{ij}, and the thermal diffusion coefficient, D_s^T, are necessary to compute species diffusion fluxes. A summary of the transport coefficients required by the conservation equations may be seen in Table 3.1.

Table 3.1 Transport Coefficients Appearing in Conservation Equations

Transport Coefficient	Required by
electron thermal conductivity, λ_e	electron energy equation
heavy species thermal conductivity, λ_h	heavy species energy equation
global viscosity, μ	axial and radial momentum equations
multicomponent species diffusion, D_{ij}	computation of diffusion fluxes
thermal species diffusion, D_s^T	computation of diffusion fluxes

The computation of the transport coefficients are presented in detail in Appendix E and will not be discussed further in this section.

There are several source terms which appear in the conservation equations (3.1) to (3.7). A summary of these source terms may be seen in Table 3.2. Although each is described in full detail in the appropriate appendix, a brief description is given here.

Table 3.2 Source Terms Appearing in Conservation Equations

Source Term	Appearing in Equation
BABS	electron energy
$(\dot{n}_s)_{CR}$	species continuity
ELST	electron and heavy energy
INSTE	electron energy
INSTH	heavy energy
RADLS	electron energy
CONRAD	electron energy

The first term listed in Table 3.2, BABS, represents the amount of power absorbed by the electron from the incident beam. The details of the computation of BABS appear in Appendix H. The details of the computation of all the other terms listed in Table 3.2 appear in Appendix F. The term $(\dot{n}_s)_{CR}$ represents the net volumetric production rate of species s. The term ELST represents the rate of energy transfer from electrons to heavy species due to elastic collisions. The term INSTE represents the net rate of energy gain or loss of the electrons, due to inelastic collisions between the electrons and the heavy species. The term INSTH represents the net rate of energy gain or loss of the heavy species due to inelastic collisions involving electrons, heavy species, and radiation. The term RADLS represents the power lost by the electrons due to optically thin continuum radiation. Finally, the term CONRAD represents the power lost or gained by electrons due to non-optically thin continuum radiation exchange.

The conservation equations (3.1) to (3.7) also contain terms which include the diffusion fluxes of each species, or of the heavy species as a whole as in the heavy energy equation. The details of the computation of these diffusion fluxes appear in Appendix G.

3.5 Solution Algorithm

This section describes the general approach of the overall solution algorithm as can be seen in the block diagram of Figure 3.2. Following initialization of the computational grid, the variable fields, the source terms, and the transport coefficients, the discretized raytrace is initialized up to the computational domain inlet. The iteration loop then begins.
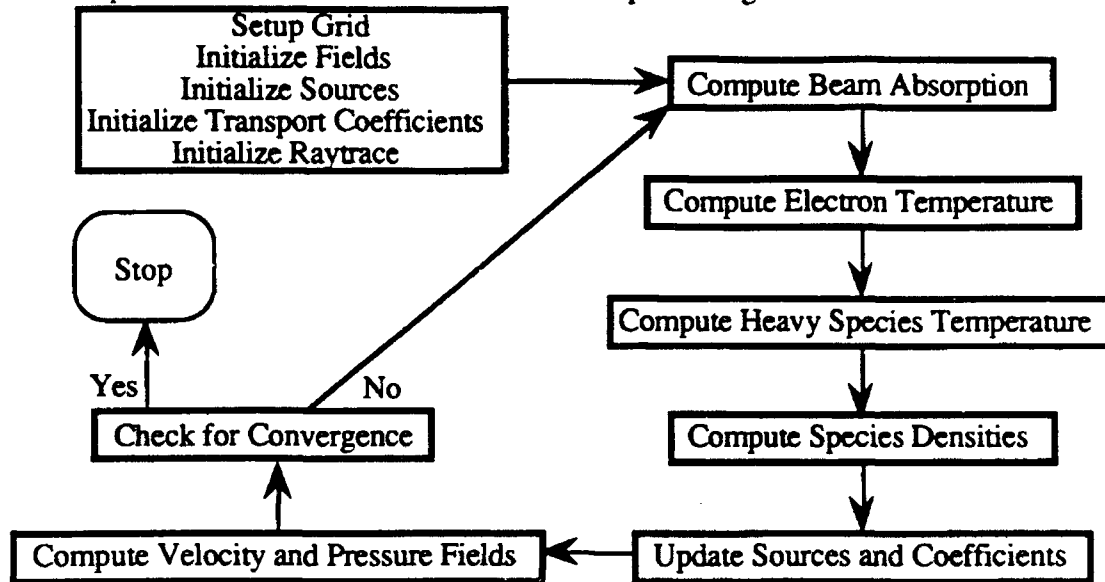
Figure 3.2   Block diagram of solution algorithm

The first step in each iteration is the computational domain raytrace which computes the power absorbed by the electrons. Using locally updated values for power absorption, the electron and heavy species energy equations are iterated to get updated values for electron and heavy species temperatures. Depending on the form of the algorithm being used, the species densities are computed next. If the complete model is being used, species conservation equations along with the multitemperature equation of state are used to compute all the species number densities. If the simplified model is being used, two laws of mass action and the multitemperature equation of state are used to compute the major species number densities as described fully in Appendix J. Following the computation of species densities, the sources and transport coefficients are updated. Next the diffusion fluxes are computed using the multicomponent and thermal diffusion coefficients and the ambipolar assumption. In the case of the full model, the diffusion fluxes are also used to compute effective diffusion coefficients for each species which are then used in the

species conservation equations. Following the update of global mass density, the velocity and pressure fields are iterated and convergence of all variables is checked. Should the variables be found to have converged, the algorithm writes all fields to files for analysis and stops.

The method of solution employed for the conservation equations is one of successive approximation through iterative underrelaxation. The algorithm starts with initial guesses for all the variables which are then iterated, or allowed to relax, toward the solution. Details of the computational grid, discretization of the conservation equations, underrelaxation, boundary conditions, interface computations, and convergence, can be found in Appendix I.

In each iteration, each of the variables is updated using the latest available values for the other variables, the transport coefficients, the source terms, and the variable itself. If the overall algorithm is stable, all the variables will gradually assume values which no longer change appreciably if further iterations are applied. This lack of further change of the variables, which is linked to the solution of the discretized conservation equations, is termed convergence and can be treated quantitatively as discussed in Appendix I. However, for many cases, due to an inconsistent algorithm, or possibly a physically impossible case, the variable values will not converge but will rather take on nonphysical values. It is the greatest flaw of the iterative solution method that non-physical answers from one conservation equation can then be fed into the next conservation equation, along with the accompanying non-physical source terms. The non-physical input often perpetuates itself and the variables diverge from an answer causing the code to blow up. Precautions have been taken in the formulation of this problem to assure stability in the realm of the SIMPLE algorithm as explained in Appendix I.

The next section describes in detail the generalized non-LTE model solution algorithm from the point of view of the actual computer code. The solution flowchart as can be seen in Figure 3.3 is described including the nature of each of the subroutines.

3.6 Description of Subroutines of Generalized Model

The double arrows in Figure 3.3 have the meaning of a subroutine call followed by a return to the calling program upon execution. The core of the program controls the subroutine calls and is

where all the necessary constants and common blocks are assigned. The initial portion of the overall program consists of six subroutines, four of which are only ever called once.
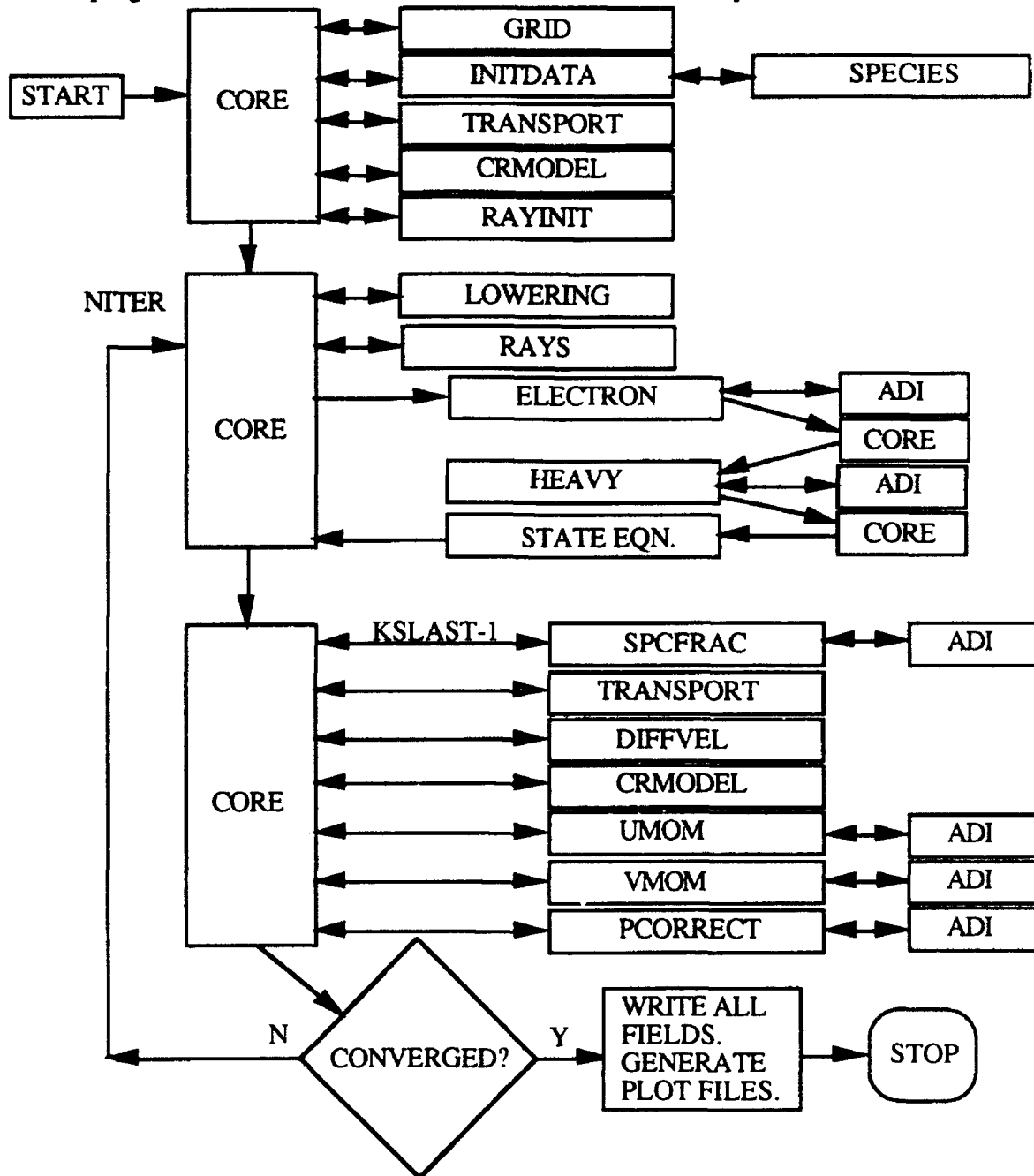
Figure 3.3   Flowchart of solution algorithm for generalized non-LTE model

The subroutine GRID is called only once and computes the flowfield mesh sizes as well as cell areas and weighting factors which are discussed in Appendix I. It also allows for user choice of a uniform or non-uniform grid spacing. In the case of non-uniform grid spacing, the mesh

arrangement is determined based upon user input integer values for axial and radial non-uniformity. Axially the grid is split into thirds, with each third assigned a third of the overall domain length. The user input number for axial non-uniformity represents the ratio of the number of axial grid points in the first third of the axial domain to the number of grid points in each of the second and third thirds of the domain.

Similarly, the radial grid is split in half with each half assigned half of the overall radial domain distance. The user input for radial non-uniformity represents the ratio of grid points in the first radial half of the domain (near the axis) to the number of grid points in the second radial half. In this way, more grids may be clustered near the axis of symmetry and in the first axial third of the domain.

As an example, consider a domain that is 304.8 mm axially by 63.5 mm radially, with the total grid size being 100 by 50 and the axial and radial grid numbers being 3 and 4. Axially there would be 60 scalar grid nodes in the first 101.6 mm, followed by 20 scalar grid nodes in each of the second and third 101.6 mm. Radially there would be 40 scalar grid nodes in the first 31.75 mm near the axis, and 10 scalar grid nodes in the 31.75 mm near the wall.

Subroutine INITDATA is also called only once for the purpose of assigning the initial flowfield variables. Within INITDATA there are three choices for the format of input files as selected by the user. A complete non-LTE set of variables (T_e, T_g, u, v, p, ρ, and all n_s) may be input, an LTE set consisting of temperature, pressure, and axial and radial velocities may be input, or the flowfields may be generated from scratch. In the generalized version of the model, the subroutine SPECIES is called only in the cases where either an LTE or scratch temperature field has been input and the species densities are to be computed. Subroutine SPECIES contains an algorithm which computes major species densities based on T_e, T_g, and system pressure neglecting the minor species (H_2^+, H_3^+, H^-). In the LTE case, $T_e = T_g$, and the minor species are simply assigned arbitrary low number densities.

Subroutine TRANSPORT has the function of computing the transport coefficients for the entire flowfield which is discussed in detail in Appendix E. This subroutine is the most computationally intensive of any of the subroutines.

Subroutine CRMODEL uses a set of rate equations (a collisional-radiative model) to compute the rates of creation or destruction of all species as well as the corresponding energy transfer. Subroutine CRMODEL is discussed in Appendix F.

The final subroutine of the initialization set is RAYINIT which computes the geometry and intensity of the incident beam rays based on user input of lens and beam specifications as well as the number of discrete rays to be used, the total incident power, and the optics to domain distance. The ray quantities are computed physically to the inlet (start of the flowfield computational domain). Details of the ray trace, from the lens through the computational domain appear in Appendix H. At this point all the necessary precomputations are completed and the iteration algorithm may begin.

The total number of equations can vary from iteration to iteration depending upon the uppermost neutral level used. In order to determine the number of excited states to include in the system of equations, and therefore the number of excited neutral continuity equations, the non-LTE lowering of the ionization potential of hydrogen is computed in subroutine LOWERING using slightly modified versions of the Debye-Hückel and Bethe methods which account for more than one temperature (Cho, 1988). Therefore, the first step of every iteration is the computation of the maximum value for lowering of the ionization potential over the entire computational domain, and therefore the highest possible bound state for neutral hydrogen. If there has been a change in the highest bound state, species densities are adjusted and the iteration continues with the new total number of species. The minimum uppermost bound atomic hydrogen level has been constrained to be 6 (5th excited level) to be consistent with tracking of line radiation. It should be noted that in the generalized model, due to a need for consistency in the species conservation equations, the maximum computed value for ionization lowering anywhere in the computational domain is used as the lowering value over the entire domain. However in the simplified model, the lowering may

be different across the domain because the computation of species densities is self contained in subroutine SPECIES.

The second subroutine of every iteration is RAYS which computes the passage and attenuation of the discrete rays (from RAYINIT) through the flowfield domain. The rays are attenuated through Beer's law with absorption coefficients computed based on inverse bremsstrahlung absorption coefficients. A variable index of refraction and Snell's law are used to trace the ray paths. The net results of RAYS are the global absorption (through the total beam attenuation) as well as the exact amount of energy deposited into each flowfield computational cell. This energy appears as a source term in the electron energy equation. The function of subroutine RAYS is fully described in Appendix H.

The next section of the program flowchart consists of the energy equations and the state equation. The energy equations yield latest values for electron and gas temperatures and the state equation yields the latest values for total number density, n_{tot}. The pressure correction, P_c^{DH} is computed from the latest values of the species number densities and temperatures. Subroutine SPCFRAC is called in its appropriate version for each species (except for species number 3) to compute species number densities based on the latest values of all the other variables as well as the species source term provided by subroutine CRMODEL. Species number 3, which is molecular hydrogen, is computed from summing the mole fractions of all the species to unity. If the species mole fractions sum to greater than unity, then species number 3 is assigned some arbitrarily low mole fraction, and all the species mole fractions are readjusted to sum to unity. At this point, the latest number densities are computed by simply multiplying the computed mole fractions by the total number density, n_{tot}.

If, compared to the previous iteration, the electron or heavy temperatures have changed by a specified percentage, then subroutine TRANSPORT is called at this point to update all of the transport coefficients. Subroutine TRANSPORT is only called in this way because it is an exceedingly complex subroutine which readily consumes computing time. Accurate transport coefficient values are necessary for ultimate convergence, however it would be highly inefficient to

continuously update the coefficients based upon only partially converged flowfield values. Therefore the compromise has been chosen of updating the coefficient values when progress toward convergence has been made. The details of subroutine TRANSPORT depend upon whether the full generalized model or the simplified model is being used.

Subroutine DIFFVEL uses the latest values of the transport coefficients, the species densities, and temperatures to compute the diffusion number fluxes of all the species based on ordinary species gradient diffusion and thermal diffusion as explained in Appendix E. The details of the actual diffusion computations are discussed in Appendix G. Key to the current discussion however is that DIFFVEL produces diffusion flux terms for use in the electron and heavy species energy equations, as well as effective diffusion coefficients for use in the species conservation equations.

Based upon the latest values of all the flowfield variables, the subroutine CRMODEL next computes the rates of production or destruction of all the species and of photons of selected wavelength bands and lines. The version of the CR model necessary for the fully generalized model is described in detail in Appendix F.

Finally, the momentum equations for axisymmetric flow in the axial and radial directions are solved for their respective velocity components through the subroutines UMOM and VMOM. The essence of the SIMPLE algorithm (which is the basis of all the conservation equation solutions) is then the update of the local pressure field in order to satisfy the bulk continuity equation which is accomplished through the subroutine PCORRECT. One iteration of the entire solution algorithm has now been described. If the residuals from the conservation equations and the state equation have converged to preset values, the algorithm quits and writes all the variable fields to files or generates plot files for analysis. Of course if convergence has not been achieved, the algorithm loops back to the computation of the ionization potential lowering and continues.

3.7 Solution Strategies

Although formulation of the problem was a formidable task, the vast majority of time and frustration has been spent on trying to get a non-trivial converged solution. Countless variations of

the solution algorithm were tried with little success. In most cases the conservation equation residuals would decrease to a point and then merely fluctuate or explosively increase resulting in a program bomb. In order to quantify some of these attempts at solution, some of the techniques used are summarized in this section.

Since the conservation equations are linked, it would be advantageous to the overall convergence if one or more of the equations was converged almost immediately. The most immediately obvious technique for advancing convergence of the conservation equations individually was repeated looping of certain subroutines within each overall iteration. For instance, the energy and raytrace subroutines were put into a loop that was executed a number times for every complete single overall iteration. The number of times the loop was executed was determined by the energy residuals. The energy loop would execute a given number of times or until the energy residuals were less than a predetermined value. Repeated looping was also applied to the momentum and bulk continuity equations in the same fashion.

The problem with repeated looping is that if the equations are far from convergence, prolonged iterations of a single equation or group of equations in the absence of the other equations would tend to perpetuate any nonphysical answers. Then when the algorithm switched to the iteration of the other equations, these non-physical answers would be perpetuated further. In other words, repeated looping has the effect of unlinking the equations which may result in perpetuation of error that causes the code to blow up.

It was noted that in most cases of interest the conservation equations were source dominated. This means that the time scale for change due to local processes (sources) was much smaller than that due to the other processes (convection and diffusion). Therefore if a solution technique could be devised to take advantage of this aspect of the equations, it was thought that it might be successful.

The alternating direction implicit routine (ADI) used to solve the conservation equations is a line solution method. This means that a set of algebraic equations, one for each point in a line of points, is solved simultaneously. Physically this means that for a slice of constant x, all points in

the radial direction are assembled and solved. The routine then increments to the next x value and solves the next line using the previous answers. After sweeping across all x (from the inlet to the exit in the computational domain), the method then switches to lines of constant r and sweeps the domain in that direction.

A point solution method would solve for each point within the domain explicitly. Furthermore, the point solution could be repeated with updated sources. This was the essence of the point solution technique as suggested by Professor Vanka for the source dominated equations. The computational domain would be looped through a point at a time for each equation. At each point, the equation would be solved with updated sources a number of times. Although this technique also appeared to be promising, it also failed to produce a converged solution.

The concept of inertia is analogous to underrelaxation and is described in Patankar (1980). It is also analogous to adding an unsteady term to the equations and then adjusting the time steps. Although it was thought that adding inertia to the discretized conservation equations might help the convergence of the solutions, it was found that this was not the case and that inertia merely slowed down the rate of convergence.

Other techniques that were tried included source term underrelaxation and source dominated value limiting, both of which are described by Patankar (1980). Unfortunately, neither of these produced a satisfactory result either, and a non-trivial solution to the generalized model was not achieved. However, in hindsight, based on the knowledge and experience gained throughout this effort, given additional time, and with a bit of reworking, a solution algorithm can be developed which will yield non-trivial results for the generalized model.

Unfortunately, since the generalized model failed to produce results, a simplified model was formulated which retained some aspects of complexity, yet discarded others. This simplified model is described in Chapter 4.

4. Simplified Kinetic Non-Equilibrium Model

Due to problems in trying to get the full generalized non-LTE model as described in Chapter 3 to produce non-trivial results, the generalized non-LTE mc..el was simplified. The types of simplifications that were made were based on a combination of knowledge of the physical processes and computational complexities involved. Since the physical processes in an LSP are linked, care was taken in what was neglected and what was retained to insure that the simplified model had a physical basis.

4.1 Assumptions

The first assumption of the simplified model is that kinetic nonequilibrium is possible. This aspect of non-LTE was retained based upon the arguments presented in Chapter 1 and also due to the experimental results of Zerkle (1992) which demonstrated kinetic nonequilibrium in argon LSPs. Therefore, the simplified model retains two energy equations.

Chemical equilibrium is assumed, and the major species number densities are computed using the algorithm presented in Appendix J. Therefore the species mole fraction equations become redundant and are dropped from the algorithm. In the absence of the species equations, the species diffusion fluxes have also been dropped, thereby neglecting species diffusion. The assumption of chemical equilibrium also eliminates the need for the computation of species source terms and inelastic energy transfer terms from a collisional-radiative model.

Although the generalized model implicitly included both line and continuum radiation as described in Appendix F, the simplified model retains only the continuum radiation of the electrons, which is assumed to be optically thin. The collisional-radiative model is therefore reduced to the computation of optically thin continuum radiation loss and the elastic collisional transfer term.

There was some question as to whether the flow work terms appearing in the energy equations (3.1) and (3.2) were correctly formulated. The total flow work should be represented by the local static pressure multiplied by the divergence of the local velocity field. However, since the generalized model required two energy equations, the local pressure had two components.

Therefore the electron energy equation had a term for flow work involving electron pressure, and the heavy species energy equation had a term for flow work involving heavy species pressure. The sum of the two separate flow work terms however does not yield the total flow work described above, due to two discrepancies.

The pressure field which drives the flow results from the pressure correction equation and can be described as the system reference pressure plus a relatively small pressure correction. In the computation of species number densities for the simplified model, the system pressure is used without the small correction. In addition, the pressure terms in the energy equations, given by equations (D.46) and (D.57) neglect the Debye-Hückel pressure correction. The error due to these two factors was considered to be negligible, however the energy equations were slightly altered for the simplified model to assure consistency. The flow work term was dropped in the electron energy equation, and the flow work term was altered in the heavy energy equation to represent all of the flow work as the local static pressure multiplied by the divergence of the velocity field.

4.2 Conservation Equations

Based upon the above simplifications and assumptions, the conservation equations for the simplified model will now be presented. In the absence of flow work, electron diffusive heat flux, and inelastic collisional transfer, the electron energy equation becomes:

$$\frac{\partial}{\partial x}\left(\left(\frac{3}{2}k_b n_e u\right)T_e\right) + \frac{1}{r}\frac{\partial}{\partial r}\left(\left(\frac{3}{2}r k_b n_e v\right)T_e\right) = \frac{\partial}{\partial x}\left(\lambda_e\frac{\partial T_e}{\partial x}\right) + \frac{1}{r}\frac{\partial}{\partial r}\left(r\lambda_e\frac{\partial T_e}{\partial r}\right)$$

$$+ \text{BABS} - \text{ELST} - \text{RADLS} + \text{CONRAD} \qquad (4.1)$$

where, as explained in Appendix F, RADLS represents the optically thin radiation loss for photon energies above 100 eV. In addition, the simplified version of CONRAD represents the optically thin radiation loss for photon energies below 100 eV and is therefore always negative.

The simplified model heavy energy equation is:

$$\frac{\partial}{\partial x}\left(\left(\frac{3}{2}n_h k_b u\right)T_g\right) + \frac{1}{r}\frac{\partial}{\partial r}\left(\left(\frac{3}{2}r n_h k_b v\right)T_g\right) = \frac{\partial}{\partial x}\left(\lambda_h\frac{\partial T_g}{\partial x}\right) + \frac{1}{r}\frac{\partial}{\partial r}\left(r\lambda_h\frac{\partial T_g}{\partial r}\right)$$

$$- P\left(\frac{\partial u}{\partial x} + \frac{1}{r}\frac{\partial}{\partial r}(rv)\right) + \text{ELST} \qquad (4.2)$$

where the last two terms represent the flow work and elastic collisional transfer.

The momentum equations and continuity equation are unchanged in the simplified model and equations (3.3), (3.4), and (3.5) are still valid. The computation of the major species number density requires four equations for the four unknowns. The first of these equations represents charge neutrality and is referred to as the condition of quasineutrality given by:

$$n_e = n_{H^+} \qquad (4.3)$$

The second equation required to compute the number densities is the equation of state, given by:

$$P = \left(n_e k_b T_e + n_h k_b T_g\right)\left(1 - P_c^{DH}\right) \qquad (4.4)$$

where P is the system pressure, and once again P_c^{DH} is the Debye-Hückel pressure correction which, neglecting the minor species, is:

$$P_c^{DH} = \left(24\pi(n_e + n_h)\left(\frac{4\pi e^2 k_c}{k_b}\left(\frac{n_e}{T_e} + \frac{n_{H^+}}{T_g}\right)\right)^{-1.5}\right)^{-1} \qquad (4.5)$$

The last two equations required to compute the number densities are the dissociation and ionization laws of mass action which are respectively given by:

$$\frac{(n_H)^2}{n_{H_2}} = \exp\left(\frac{-E_{H_2}d}{k_b T_g}\right)\left(\frac{\pi m_H k_b T_g}{h^2}\right)^{\frac{3}{2}}\left(\frac{(Z_{Hex})^{\frac{2T_e}{T_g}}}{(Z_{H_2rot})(Z_{H_2}vib)(Z_{H_2ex})}\right) \qquad (4.6)$$

$$n_e\left(\frac{n_{H^+}}{n_H}\right)^{\frac{T_g}{T_e}} = \left(\frac{2\exp\left(\frac{-E_i}{k_b T_e}\right)\left(\frac{2\pi m_e k_b T_e}{h^2}\right)^{\frac{3}{2}}}{Z_{Hex}}\right) \qquad (4.7)$$

in which the E terms in the exponents represent zero point energies and the Z terms represent partition functions. The derivations of equations (4.6) and (4.7) as well as a description of the algorithm which computes the major species number densities using equations (4.4) to (4.7) can be seen in Appendix J.

4.3 Transport Coefficients

The computation of transport coefficients has also been changed for the simplified model. Due to the neglect of species diffusion in the simplified model, the multicomponent and thermal diffusion coefficients are not computed. Also, instead of computing the other coefficients directly as described in Appendix E, the electron thermal conductivity is approximated by an algebraic

expression, and the heavy species thermal conductivity and viscosity have been curve fit against temperature and pressure using LTE data from Kovitya (1985) and Cebeci and Bradshaw (1984).

The data taken from Kovitya (1985) is valid from 5000K to 60000K gas temperature, and for pressures from 1 atm to 100 atm. The data taken from Cebeci and Bradshaw (1984) is valid for 1 atm and gas temperatures from 300 K to 1300K. Nevertheless, curve fits were constructed from 300K to 60000K gas temperature, and pressures of 1, 10, and 100 atm for viscosity and heavy species thermal conductivity. Values for the model were then interpolated between the curve fits as necessary. The error introduced by this type of primitive curve fitting cannot be avoided in the absence of actual transport coefficient computations as described in Appendix E.

Electron thermal conductivity is based roughly on the values used by Chen (1980) for electron thermal conductivity in an argon plasma, and is given by the expression:

$$\lambda_e = 5 \times 10^{-25} n_e \sqrt{T_e} \qquad (4.8)$$

This expression is admittedly heuristic in nature, and may be a poor representation of the electron thermal conductivity. However, the error introduced cannot be avoided in the absence of the computations described in Appendix E.

4.4 Solution Algorithm

The solution algorithm for the simplified model remains essentially unchanged from that for the generalized model except for the exclusion of the subroutines DIFFVEL and SPCFRAC, and the altered form of subroutines CRMODEL and TRANSPORT. In addition, due to an improved method for the solution of the energy equations, subroutines ELECTRON and HEAVY have been combined into subroutine ENERGY. The simplified model flowchart can be seen in Figure 4.1.

Early tests of the simplified algorithm did not produce satisfactory results. The problem was in the normalized energy equation residuals which were observed to decrease to typically a few per cent and then oscillate or stick and not decrease further. No sensible explanation could be found for this behavior, but it was thought to be caused by the fact that the two energy equations were linked by the elastic energy transfer term in each. If the term ELST appearing in equations (4.1)

and (4.2) is rewritten as an elastic transfer coefficient, elst, multiplied by the kinetic temperature difference, the discretized form of equation (4.1) may be written for every point in the domain as:

$$(a_{Pe} + elst)T_e = \sum a_{nbe}T_{enb} + Sources_e + elst\ (T_g) \qquad (4.9)$$

and the discretized form of equation (4.2) may be written for every point in the domain as:

$$(a_{Pg} + elst)T_g = \sum a_{nbg}T_{gnb} + Sources_g + elst\ (T_e) \qquad (4.10)$$

where the elastic transfer term has been linearized as per Patankar (1980, p. 143) since it is a function of the variable being solved for in both equations (4.9) and (4.10), and the Sources terms do not include ELST. The direct link between the energy equations can be seen clearly.
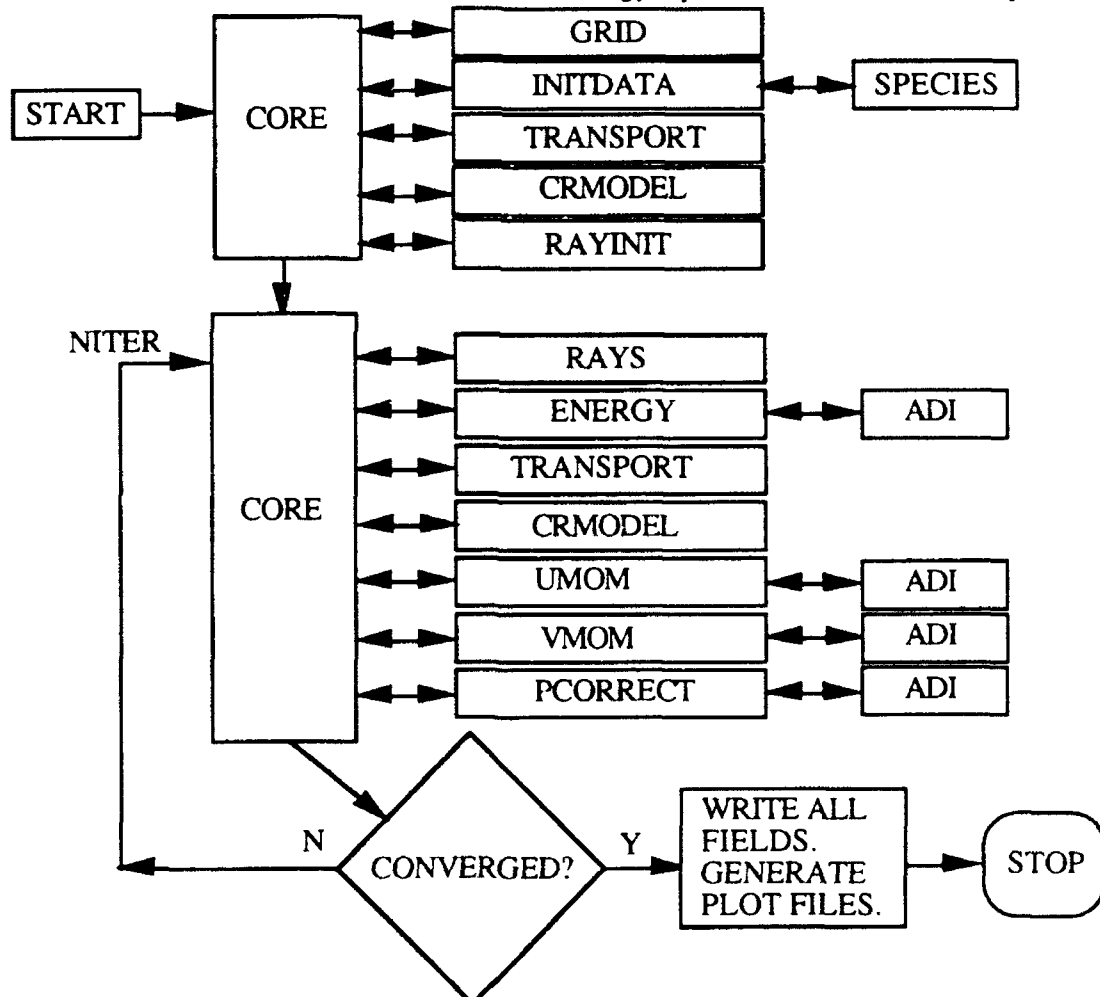
Figure 4.1   Flowchart of solution algorithm for simplified kinetic nonequilibrium model

Upon suggestion from Professor Vanka, equation (4.9) was solved for T_e and substituted into equation (4.10), and equation (4.10) was solved for T_g and substituted into equation (4.9). The

result is an equation for T_e which does not involve T_g at the solution point, and an equation for T_g which does not involve T_e at the solution point. The new discretized electron energy equation is:

$$\left(a_{Pe} + elst - \frac{elst^2}{a_{Pg} + elst}\right)T_e = \sum a_{nbe}T_{enb} + Sources_e + \frac{elst\left(\sum a_{nbg}T_{gnb} + Sources_g\right)}{a_{Pg} + elst} \quad (4.11)$$

and the new discretized heavy species energy equation is:

$$\left(a_{Pg} + elst - \frac{elst^2}{a_{Pe} + elst}\right)T_g = \sum a_{nbg}T_{gnb} + Sources_g + \frac{elst\left(\sum a_{nbe}T_{enb} + Sources_e\right)}{a_{Pe} + elst} \quad (4.12)$$

Equations (4.11) and (4.12) were incorporated into subroutine ENERGY to replace subroutines ELECTRON and HEAVY. Solutions were achieved for which the normalized energy residuals readily dropped to below values of 1×10^{-4}. Although the energy equations ultimately being solved for remain unchanged, a mathematical manipulation which increased the implicitness of the variables at the solution point was necessary for proper convergence. Results of the simplified model are discussed in Chapter 5.

5. Simplified Model Results

The simplified model was run for a variety of test cases to produce predictions versus variations in beam power, gas mole flux, gas pressure, and beam f-number. Results for global absorption and thermal efficiency are presented and compared with experimental results. Contour plots of selected quantities are also presented to illustrate physical phenomena and make case comparisons. In addition, it was discovered that model solutions are dependent upon initial conditions, as well as operating parameters.

Steady state solutions are defined by fields for which the normalized residuals for mass continuity, axial momentum, and radial momentum have decreased to or below 1×10^{-5}, and the normalized residuals for electron and heavy species energy have decreased to or below 1×10^{-4}. These levels were chosen to define convergence because it was observed that values for global absorption and thermal efficiency changed very little if further convergence was attempted.

Global absorption can be computed in two equivalent ways using the model. The first method is to compute the sum of BABS(i,j) multiplied by 2π over the entire domain and divide by the beam power. The second method is to compute the total power remaining in the incident beam rays upon exiting the computational domain, subtract this transmitted power from the incident power and once again divide by the incident power.

Following the first method, global absorption, α, may be written as:

$$\alpha = \frac{\sum_{domain} (2\pi)BABS(i,j)}{Beam\ Power} \tag{5.1}$$

Thermal efficiency is computed by summing the net enthalpy increase of the heavy species between exit and inlet, divided by the incident beam power. More precisely, thermal efficiency, η, may be written as:

$$\eta = \frac{\dot{m}\left(h_{exit} - h_{inlet}\right)}{Beam\ Power} \tag{5.2}$$

From the definition of enthalpy, equation (5.2) is equivalent to:

$$\eta = \frac{\sum_{exit}\left(\left(\frac{3}{2}n_h k_b T_g + P\right) u A\right)_{exit} - \sum_{inlet}\left(\left(\frac{3}{2}n_h k_b T_g + P\right) u A\right)_{inlet}}{\text{Beam Power}} \qquad (5.3)$$

If the fully generalized model were being used, the flow work in the energy equations would include a component due to electron pressure in the electron energy equation, and a component due to heavy species pressure in the heavy species energy equation. In that case, the pressure appearing in equation (5.3) would be given by the heavy species component, $n_h k_b T_g$. However, flow work was only included in the heavy species energy equation in the simplified model, and was based on the system pressure plus the small local correction. Since the local pressure correction is negligible with respect to the system pressure, it may be neglected in the computation of thermal efficiency. Therefore, the pressure appearing in equation (5.3) represents the system pressure.

5.1 Computational Domains

Several computational domains were used in this study depending upon the f-number and expected length of the plasma. The majority of runs were on computational domain D v iich is described below along with the other domains which are summarized in Table 5.1. The selection of the computational domain for a particular test case was based upon a balance between computational intensity and grid resolution. In addition, it is necessary that the exit of the domain be far enough downstream that the no derivative exit boundary condition does not affect the flowfield. In cases which produce elongated plasmas, it is also vital that the domain be long enough such that portions of the plasma tail which may still be radiating are included. Therefore, a long domain with a moderate number of grid nodes, but with a high resolution at the plasma core is desired. Referring to Table 5.1, the column headed Geometry refers to the axial and radial non-uniformity numbers described in Chapter 3, ROC refers to the radius of curvature of the focusing lens, ext is the lens extra thickness, and O.D.D. refers to the optics to domain distance necessary for the beam ray trace.

It is obvious from the description of the ray trace in Appendix H, that if the number of cells in the vicinity of the plasma core were changed, that the ray trace would have a different number of

turning points. If the grid in the plasma core region were too coarse, it is possible that the resulting abrupt changes in ray direction could represent a bad distortion of reality. Comparisons can therefore only be accurately made between cases for which the plasma core region has a similar grid resolution. That is why all of the domains share the same grid cell dimensions in the regions of the beam focus, regardless of the beam geometry or overall domain length.

Table 5.1 Computational Domains

Domain	Grid	Size(mm)	Geometry	ROC(mm)	ext(mm)	O.D.D.(mm)
D	100x50	304.8x63.5	3,4	426.77	5	260
F	100x50	304.8x63.5	3,4	850.00	7.5	562
G	100x50	304.8x63.5	3,4	222.00	5	112
H	100x50	406.4x63.5	8,4	426.77	5	260

5.2 Model Plasma Initiation

Once the desired grid and optical parameters are selected for a particular case, the next step is to initiate the plasma and allow the fields to relax to a steady state solution. Experimentally this was done by inserting a tungsten rod into the plasma focus as described in Chapter 2. The rod released free electrons which immediately began absorbing the incident laser beam and subsequently caused a plasma breakdown through continuous heating and collisions with heavy species. Although it qualitatively represents a point input of power at the beam focus, this phenomenon is not well described spatially or in the amount of energy initially distributed in the electrons ejected by the tungsten rod. Therefore, there is no definitive method in which the model plasma could be started which would exactly match experimental conditions. Before it was realized that initial conditions make a difference to the final solution, the question of how to start the model plasma was considered only from the standpoint of practicality and ease of achieving solutions.

The first few runs of the model were started assuming a cold flow of gas through the chamber and an unperturbed incident beam. This condition corresponds to the case of ltenum=0 in subroutine INITDATA. A small amount of energy was artificially placed near the focus of the unperturbed beam, which was known based upon the beam ray trace. Typically, for domain D and an f-4 beam geometry, one microwatt was added to the electron energy through setting the source term BABS(20,2) to a minimum of one microwatt for the first ten iterations. The result was a

spike in electron temperature which then gradually relaxed as plasma breakdown was simulated numerically by the species computation described in Appendix J. The fields then relaxed to steady state answers. This method of initiation was later labeled as the point spark method.

Cases which were to be run that were similar to cases for which answers already existed could be started in a different fashion. Since it was believed that giving the solution algorithm a set of converged fields for a case similar to the one to be run would result in faster convergence than starting from scratch, this is exactly what was done. This corresponds to the Itenum=1 case in subroutine INITDATA. This method was implemented by reading in the full set of six converged fields from a previous case and then allowing the algorithm to relax to a solution. Since this method of starting test cases was commonly used by Eguiguren (1989) in his LTE model, it was not thought to present any problems. A listing of model results appears in Table 5.2.

Table 5.2 Global Results of Test Cases

Case	Domain	Power (kW)	Pressure (atm)	Mole Flux	f#	input	# of iterations	abs (%)	eff (%)
tf45	D	70	3.5	2192.9	4	ps	1561	99.38	32.64
tf32	D	70	7	2192.9	4	ps	1514	99.93	23.77
tf37	D	70	3.5	2192.9	4	line	1527	99.83	39.85
f1	D	3.5	3.5	1507.6	4	ps	4530	82.93	73.19
f2	D	3.5	3.5	1781.8	4	ps	2202	85.30	74.56
f3	D	7	3.5	1644.7	4	ps	3556	94.09	72.80
f4	D	7	3.5	2192.9	4	ps	2436	94.38	79.72
f5	H	700	3.5	2192.9	4	ps	2338	99.95	13.19
f6	H	70	1	2192.9	4	ps	2430	89.63	58.65
f7	F	7	3.5	2192.9	8	ps	2930	94.50	75.27
f8	D	70	3.5	2192.9	4	f4	1919	99.38	32.64
f9	G	7	3.5	2192.9	2	ps	2279	94.36	76.48
f10	D	70	3.5	2192.9	4	tf32	1896	99.33	32.20
f11	D	7	3.5	1918.8	4	ps	1366	94.30	75.71
f12	D	3.5	3.5	2192.9	4	ps	2543	85.48	76.14
f13	D	3.5	3.5	1644.7	4	ps	1636	84.83	73.69
f14	D	3.5	3.5	2467.1	4	ps	1727	85.06	77.33
f15	D	3.5	3.5	3015.3	4	ps	2157	83.79	81.25

A variety of other methods could have been used to start the problem depending upon the distribution and magnitude of the initial sparks employed. Two other cases were actually used, which were a sequence of one microwatt sparks distributed along an axial line 11 scalar nodes long

in the domain just upstream of the beam focus, and a two dimensional box of one microwatt sparks 11 scalar nodes by 3 scalar nodes, again just upstream of the beam focus.

5.3 Initial Condition Dependent Multiple Solutions

Model solutions were dependent upon initial conditions as well as operating parameters. In order to eliminate any possibility that the multiple initial condition dependent solutions were the result of some inconsistency within the computational algorithm, or a function of the domain, two tests were conducted using a slightly different version of the heavy species energy equation which neglected the flow work term.

First, to insure that there were no errors associated with starting and stopping the code which would cause the spread of results, a case was started from a point spark on domain D and allowed to run for 500 iterations. The output was stored and the code was restarted using the stored output as input and allowed to run to convergence, taking an additional 615 iterations. The code was restarted a second time using the output after 500 iterations as input and allowed to run for another 500 iterations. The fields from this second case (1000 total iterations) were then used as input for another code run at the same conditions which converged to a solution in an additional 226 iterations. Finally, the same set of operating conditions were run from a point spark all the way to convergence in 1108 iterations. All three converged results were identical which proved that there was no problem in stopping and starting the code.

Second, to insure that the spread of results was not due to some problem with the computational grid, two cases at identical operating conditions both initiated with a point spark were run on different domains (D and H). The results for the two cases were negligibly different, thereby proving that the domain length was not a problem either.

Therefore, the conclusion is that the model solutions are indeed dependent upon initial conditions. The equations which govern the phenomenon studied constitute a set of 5 strongly nonlinear partial differential equations, coupled with 3 additional nonlinear algebraic equations (plus quasineutrality), as described in Chapter 4. This set of equations represents a nonlinear dynamical system with a phase space of infinite dimensions. In such systems, one *expects* to find

multiple stable and unstable coexisting attractors appearing in the phase space as equilibrium points, periodic motions, or quasi-periodic motions (Wiggins, 1990, Guckenheimer and Holmes, 1983, and Vakakis, 1993). Depending on the particular choice of initial conditions, one can end up in different domains of attraction and thus one can get *qualitatively* different stable solutions.

Numerical tests indicated that the obtained solutions were stable processes, i.e., if the solution field were perturbed, the dynamical process was found to be attracted back to the same solution. Using the version of the energy equations which neglected flow work, a set of solution fields was perturbed by multiplying all electron temperature nodes greater than 1000K by a factor of up to 10, and then allowing the solution to relax. All perturbed cases returned to the original solution, demonstrating it to be a stable solution. In addition, restarting the algorithm any number of times to produce plot files always resulted in a converged solution identical to the original solution. A comparison of global model results for the same parameters but four different initial conditions can be seen in Table 5.3.

Table 5.3 Comparison of Initial Condition Dependent Multiple Solutions

Case	Domain	Power (kW)	Pressure (atm)	Mole Flux	f#	input	# of iterations	abs (%)	eff (%)
tf45	D	70	3.5	2192.9	4	ps	1561	99.38	32.64
tf37	D	70	3.5	2192.9	4	line	1527	99.83	39.85
f8	D	70	3.5	2192.9	4	f4	1919	99.38	32.64
f10	D	70	3.5	2192.9	4	tf32	1896	99.33	32.20

Referring to Table 5.3, note that 4 different initial conditions yielded 3 different solutions. To summarize the results, case tf45 was initiated with a point spark, case tf37 was initiated with a line spark, case f8 was initiated with output from a 7 kW, 3.5 atm case (f4), and case f10 was initated with a 70 kW, 7 atm case (tf32). A comparison of temperature fields and ray traces reveals some interesting aspects about the physical structure of the multiple solutions and gives an indication of the effect of initial conditions. In the figures that follow, the darker lines starting at the domain inlet and reflecting at (passing through) the axis, represent the path of the incident beam as represented by a raytrace using 9 rays. Both the direction of beam travel and gas flow are bottom to top, and the left hand side of the domains represent an axis of symmetry.

The peak electron temperature for case tf45 as can be seen in Figure 5.1 was 40068 K, on the axis of symmetry, at location x=33.02, r=0 mm. The peak heavy species temperature for case tf45 was 39993 K. The outer portion of the beam has been refracted towards the axis, resulting in a tight ring focus.

The peak electron temperature for case tf37 as can be seen in Figure 5.2 was 30760 K, and is clearly off the axis of symmetry and further upstream, at location x=17.78, r=1.98 mm. The peak heavy species temperature for case tf37 was 30754 K. The off axis peak temperature location is due to the off axis beam focus which is due to refraction of the beam by the plasma. The plasma front for case tf37 is much further upstream than for case tf45, which causes the premature beam focus.

The peak electron temperature for case f10 as can be seen in Figure 5.3 was 39203 K, and is once again on the axis of symmetry at location x=33.02, r=0 mm. The peak heavy species temperature was 39140 K. Case f10 closely resembles case tf45 but has a lower peak electron temperature as well as a slightly lower thermal efficiency. The important difference, however, is that the plasma front is slightly shifted upstream for case f10 as compared with case tf45.

This shift of the plasma upstream can be clearly seen in the comparison of electron temperature contours presented in Figure 5.4. Note that the point spark case (tf45) is the furthest downstream, and the line spark case (tf37) is the furthest upstream. It should be stressed that the off axis temperature peak for case tf37 actually represents an annular region of peak temperature, and is caused by the premature focusing of the beam away from the axis, which is caused by the presence of the plasma in the first place.

It is interesting to note how the selection of initial conditions effects the steady state solution. The region of initial power input effects the final position of the steady state LSP. The line spark case introduced power (which resulted in a plasma) furthest upstream of the three cases considered, and therefore resulted in the most distorted incident beam, represented by an off axis focus. Intuitively, one would expect the off axis focus to move closer to the axis and end up in the

same position regardless of initial conditions. However , the model results clearly demonstrate that this does not occur.
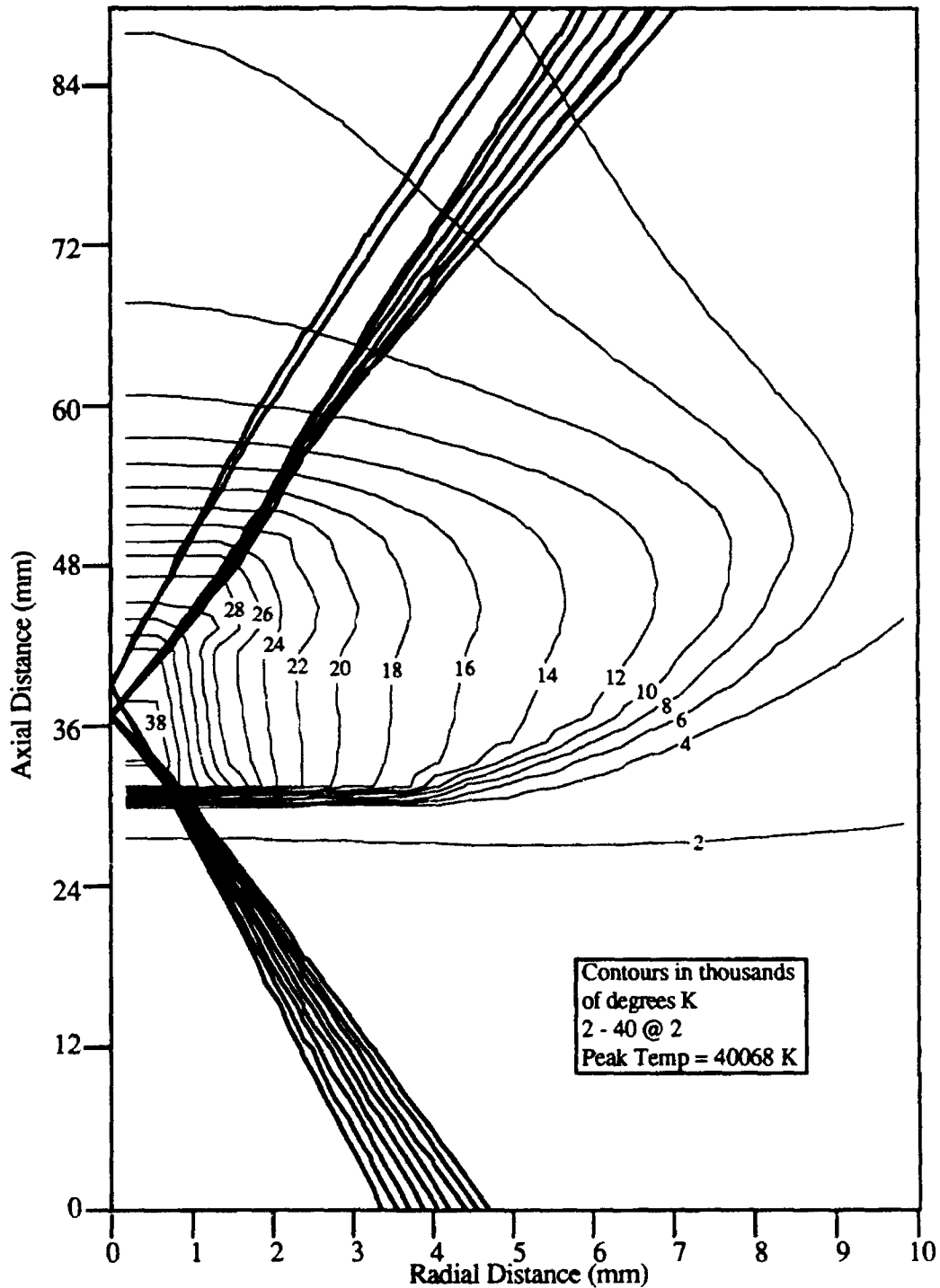
Figure 5.1   Electron temperature contours and beam ray trace for the core region of case tf45
which is a 70kW, f-4, 3.5 atm, 2192.9 moles/m^{2}s LSP from a point spark.
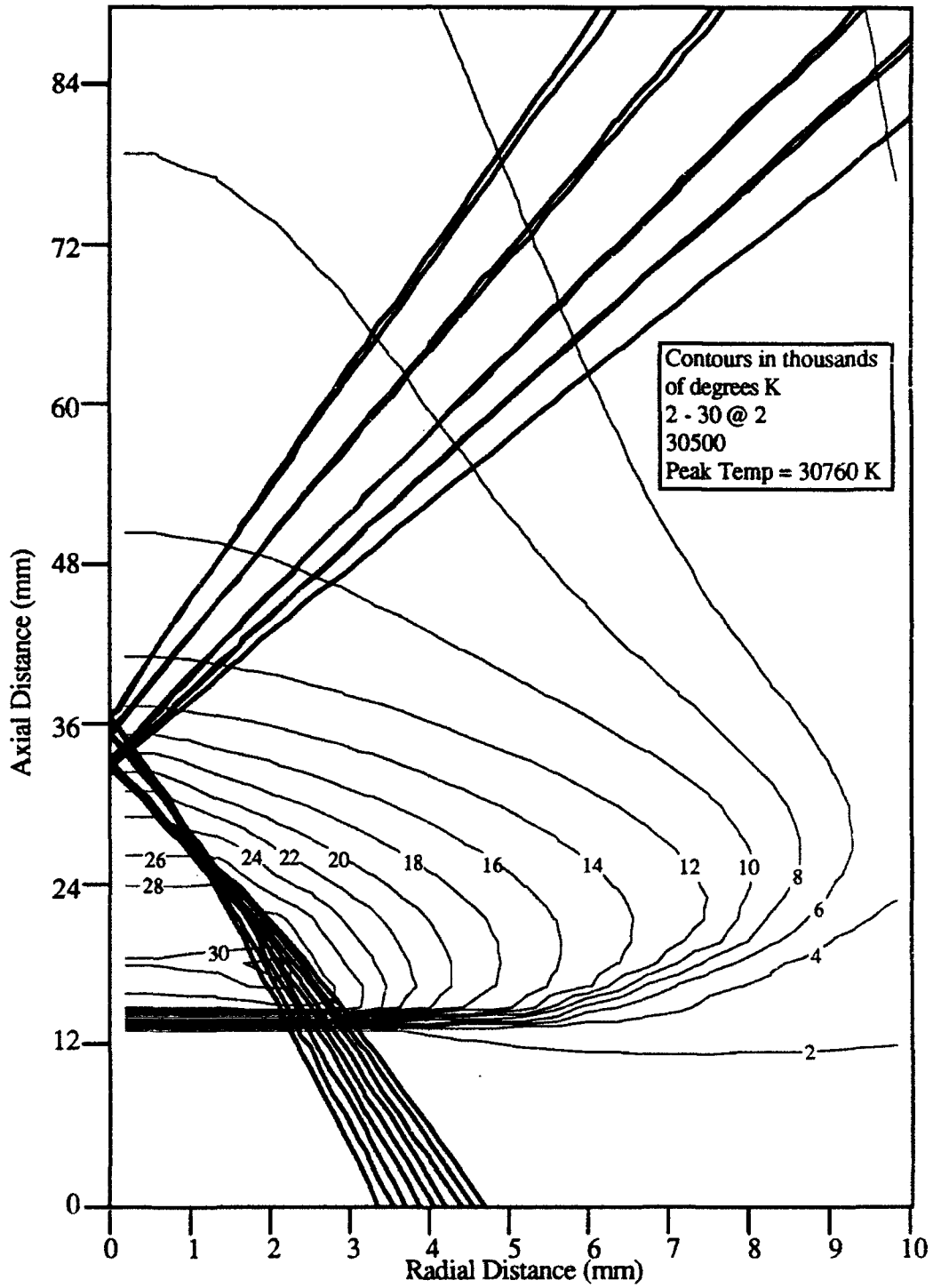
Figure 5.2   Electron temperature contours and beam ray trace for the core region of case tf37
which is a 70kW, f-4, 3.5 atm, 2192.9 moles/m²s LSP from a line spark.
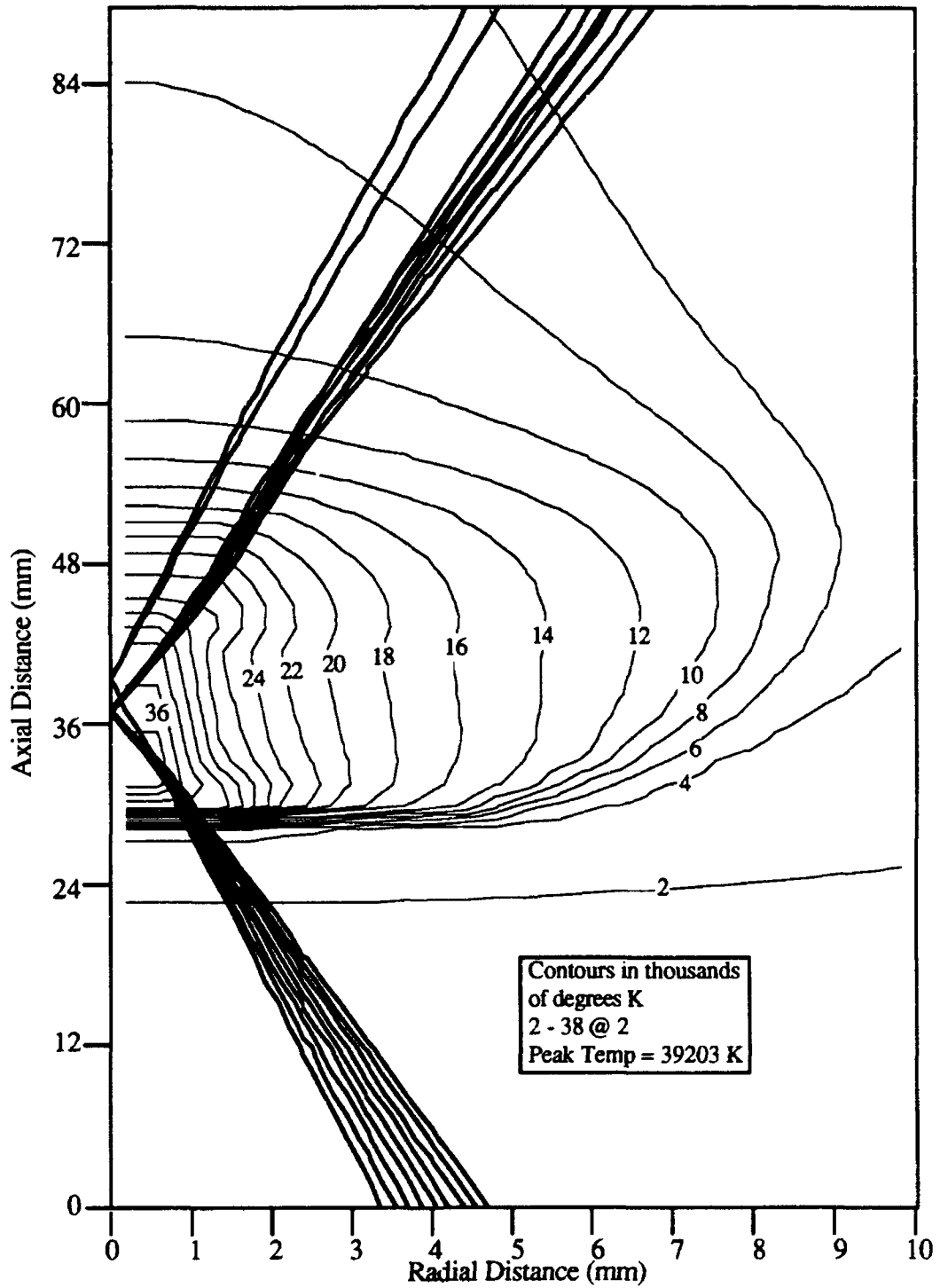
Figure 5.3   Electron temperature contours and beam ray trace for the core region of case f10 which is a 70kW, f-4, 3.5 atm, 2192.9 moles/m²s LSP from a 7 atm solution.
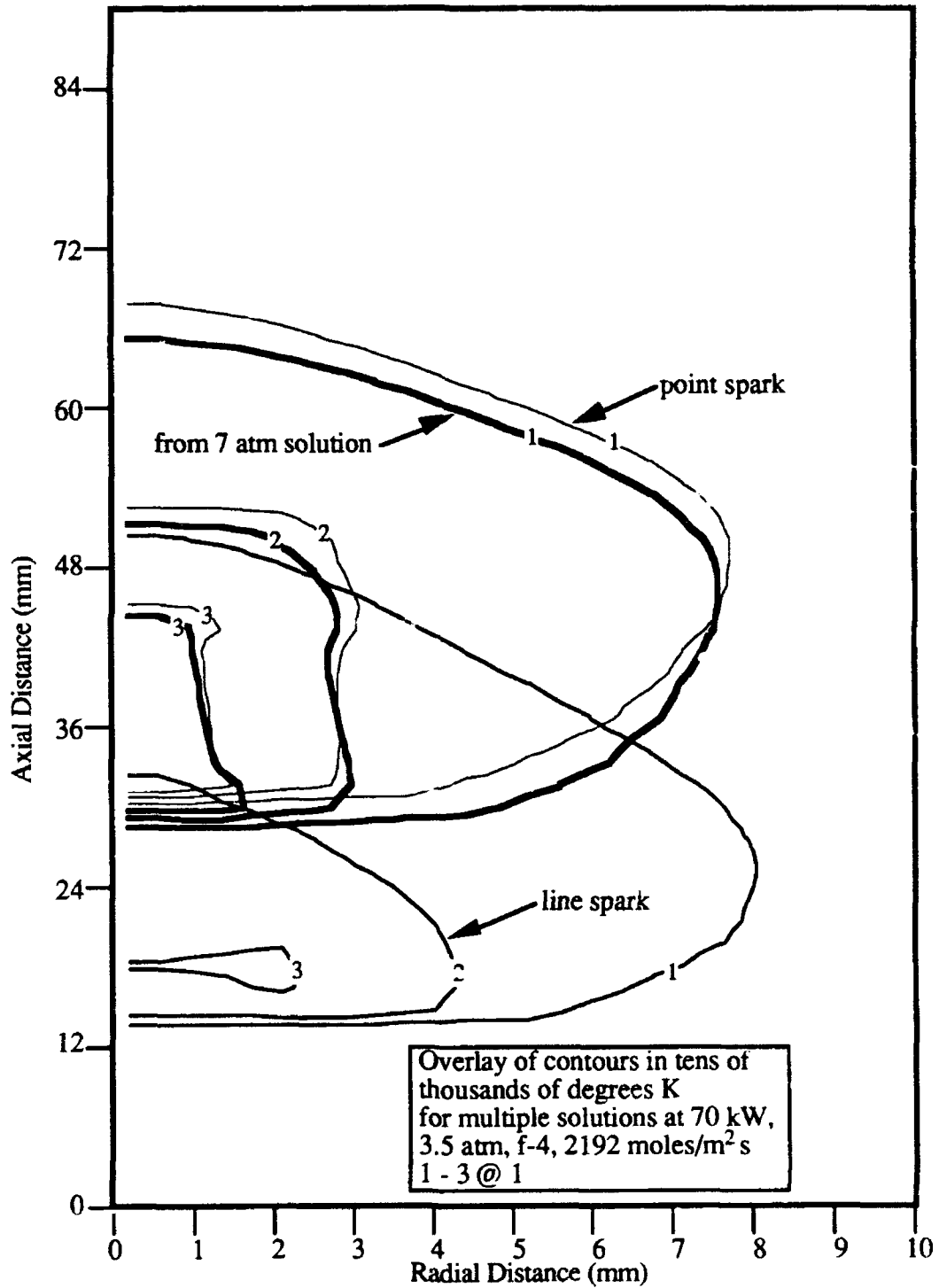
Figure 5.4   Comparison of electron temperature contours for the core regions of the multiple
solutions at 70 kW, 3.5 atm, f-4, and 2192.9 moles/m²s.

Based upon results from test cases in which the flow work term was neglected in the heavy species energy equation, it would appear that th ; multiple model solutions at 3.5 atm each represent a separate family of solutions. The same sort of spread in answers at 3.5 atm would be expected at other pressures for the same initial conditions. It is difficult to say exactly how many solutions there actually might be for a given set of parameters but different sets of initial conditions. It is known that not all initial conditions yield different answers as is evident from case f8, which yielded the exact same solution using a 7 kW set of fields as input, as did case tf45 from a point spark

5.4 Comparison with Experiments

Experimentally only one set of solutions has been detected. The fact that other solutions have not been observed experimentally does not eliminate the possibility of their existence. Similarly, despite the fact that the model has demonstrated multiple solutions dependent upon initial conditions, comparisons can still be made with the experimental results in terms of performance and stability. Model results generated with a point spark will be used for comparison purposes since the point spark most closely resembles experimental LSP initiation.

It should be noted, however that the model domain does not exactly match the experimental domain in one minor aspect. The model domain has uniform flow across the entire inlet. As described r Chapter 2, the experimental chamber consisted of a 127 mm i.d. cylindrical stainless steel chamber with a 48 mm i.d. quartz tube centered within it through which the gas flowed. Flow issuing from the tube therefore acted as a free jet into the larger chamber, with the corresponding recirculation eddies along the chamber walls. The SIMPLE algorithm can easily handle recirculation eddies as long as the eddies are contained within the computational domain and do not extend to the exit plane. If this were to happen, then there would be no appropriate exit boundary condition that could be applied. Because it was unknown apriori whether or not model plasma solutions would encounter problems with back flow at the exit plane, the inlet flow condition was slightly altered to eliminate the possibility of recirculation eddies. Model mole fluxes correspond to experimental mole fluxes through the 48 mm quartz tube However, because

of the expansion of the gas flow out of the tube, the model and experimental mole fluxes may not match precisely. In addition to possibly effecting predictions for global absorption and thermal efficiency, this would also be expected to effect blowout mole flux predictions. Model predictions for global absorption and thermal efficiency for a series of 7 kW, f-4, 3.5 atm LSPs can be seen compared with experimental results for similar conditions in Figure 5.5.
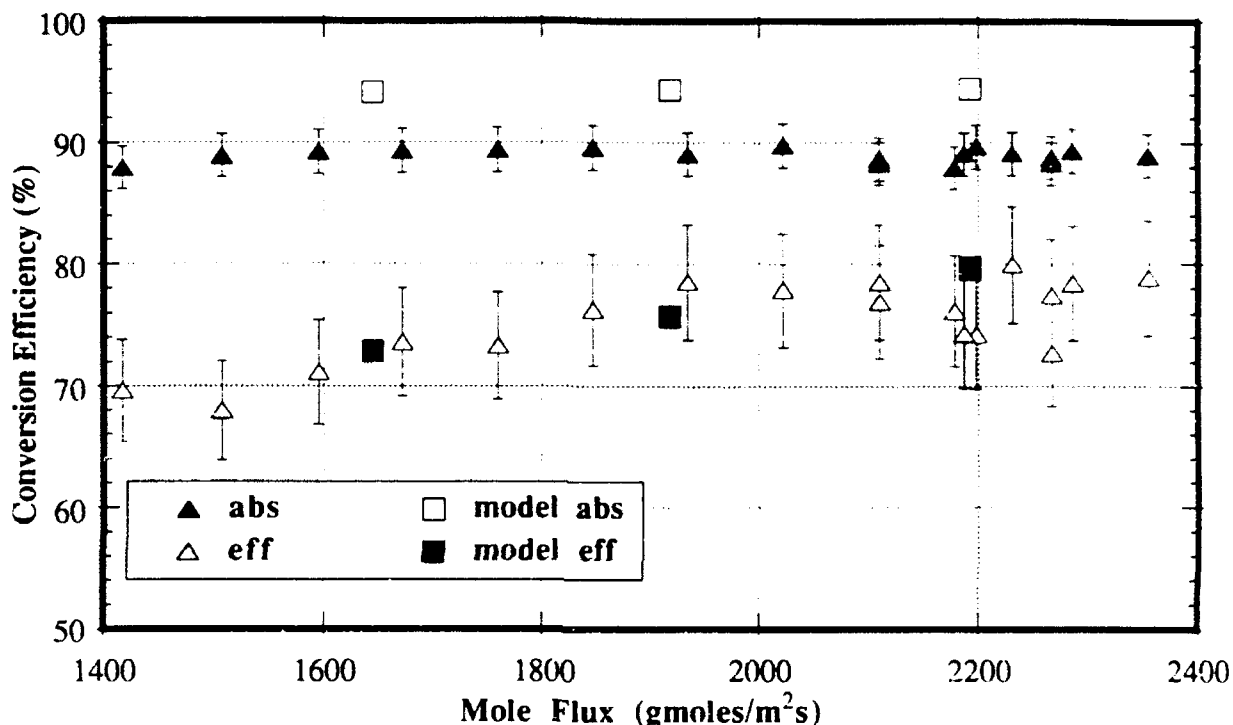
Figure 5.5   Comparison of model predictions for global absorption and thermal efficiency of 7 kW, f-4, 3.5 atm hydrogen LSPs and experimentally determined global absorption and thermal efficiency of 7 kW, f-4.1, hydrogen LSPs at 3.52±0.10 atm

Based upon the data in Figure 5.5, it would appear that at 7 kW, f-4, and 3.5 atm, the model slightly overpredicts global absorption. However it is also possible that the experimental global absorption data had a systematic error associated with it which caused the measurements to come out low. This error could have been due to plasma irradiation of the calorimeter cone on top of the absorption chamber which had been assumed to be negligible as described in Appendix B. The essentially constant model global absorption with increased mole flux agrees well with experimental results.

Model predictions for thermal efficiency at 7 kW, f-4, 3.5 atm appear to match experimental values both in magnitude and trend. No comparison can be made for blowout predictions at these conditions, however, because none of the 7 kW, 3.5 atm, f-4.1 experimental LSPs were blown out. Overall it would appear that there is fair agreement between model predictions and experimental results at 7 kW, f-4 and 3.5 atm.

Model predictions for global absorption and thermal efficiency for a series of 3.5 kW, f-4, 3.5 atm LSPs can be seen compared with experimental results for similar conditions in Figure 5.6. The experimental 3.5 kW LSPs did demonstrate a blowout as marked on the plot in Figure 5.6. Note that once again, the model slightly overpredicts global absorption compared with experimental values. The model results also indicate a slight variation in global absorption with increasing mole flux, but this effect is minor.
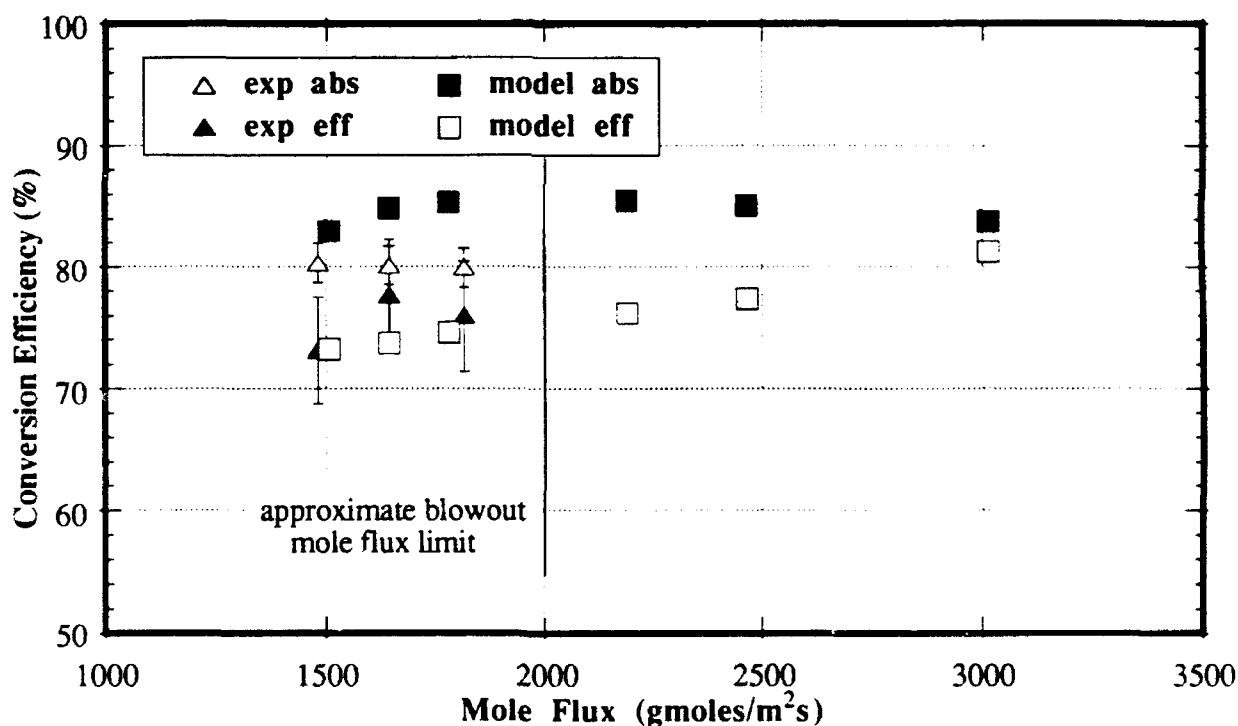
Figure 5.6   Comparison of model predictions for global absorption and thermal efficiency of 3.5 kW, f-4, 3.5 atm hydrogen LSPs and experimentally determined global absorption and thermal efficiency of 3.5 kW, f-4.1, hydrogen LSPs at 3.56±0.02 atm

Thermal efficiency as predicted by the model compares very well with the experimental results. However, a large discrepancy is visible in Figure 5.6 between the experimentally determined

blowout mole flux and the model blowout mole flux. It should be realized that experimentally, as LSPs approach the blowout limit, any small perturbations in the operating parameters can cause the plasma to prematurely extinguish. This is the major reason why blowout mole fluxes are difficult to exactly determine experimentally.

In addition, it has been observed experimentally as documented by Zerkle (1988) that the quality of the incident beam has an effect on the blowout mole flux. It was demonstrated that after a realignment of the laser optics which resulted in a more symmetrical beam that the blowout mole fluxes were observed to increase significantly. It is possible that since the model assumes a symmetrical beam that predictions for blowout mole flux would therefore be higher than what was observed experimentally due to possible laboratory beam asymmetries.

Theoretically, the blowout mole flux is reached when the value for thermal efficiency closely approaches the value for global absorption, representing a negligible radiation loss. Because there are no random perturbations in the model, a blowout prediction would be expected to correspond to the case where the values for global absorption and thermal efficiency come together. If one were to extrapolate the model data, this would occur at a mole flux near 3400 moles/m^{2}s. Therefore the model does only a fair job of predicting blow out mole flux, however this may be due to factors which are not even included in the model, such as beam asymmetries or experimental perturbation of control parameters.

5.5 Model Results Versus Control Parameters

As was done in Chapter 2, the effect of each of the four control parameters on model LSP performance will now be discussed. A discussion of model results has the advantage over global experimental results of a much fuller description of all the variable fields. Trends in global results will be summarized and compared with experimental observations. In addition, contour plots of variable fields will be presented to emphasize important points.

5.5.1 Effect of Mole Flux Variation

The variation of predicted global performance versus changes in mole flux have already been demonstrated in the plots of Figures 5.5 and 5.6. Model global absorption is essentially constant

versus mole flux, however model thermal efficiency increases with mole flux. Both these trends agree well with experimental results like those plotted in Figures 2.4 and 2.6.

A closer examination of LSP temperature and radiation fields clearly reveals that an increase in mole flux causes the LSP to slightly increase in length, and decrease in peak temperature. Contours of heavy species temperatures for a 1644.7 moles/m^2s, 7 kW, f-4, 3.5 atm (case f3) LSP may be seen in the plot in Figure 5.7. Note that the peak heavy species temperature was 21142 K (peak electron temperature was 21146 K). In contrast, contours of heavy species temperatures for a 2192.9 moles/m^2s, 7 kW, f-4, 3.5 atm (case f4) LSP may be seen in the plot in Figure 5.8. Note that the peak heavy species temperature of case f4 is slightly cooler than for case f3, with a value of 20434 K (peak electron temperature was 20439 K). In addition, the 3 and 5 thousand degree temperature contours for case f4 in Figure 5.8 clearly intersect the axis of symmetry further downstream than the corresponding contours for case f3 in Figure 5.7.

5.5.2 Effect of Power Variation

Model predictions for global absorption and thermal efficiency for three model cases (f4, tf45, and f5) at f-4, 3.5 atm, and 2192.9 moles/m^2s have been plotted against incident power in Figure 5.9. Predicted global absorption follows the experimentally observed trend of increasing with laser power, appearing to asymptote to 100%. For a fixed mole flux, thermal efficiency decreases with increased incident power, due to an increased fraction of the incident power lost as radiation from the LSP. The tremendous increase in radiating volume with incident power can be seen by comparing the radiation loss contours plotted in Figures 5.10, 5.11, and 5.12.

Referring to Figures 5.10 - 5.12, note that not only does the LSP radiating volume increase with power, but the region of maximum radiation loss moves farther from the axis as power is increased. This maximum radiation loss region corresponds to an electron temperature between 16000 K and 17000 K at 3.5 atm.
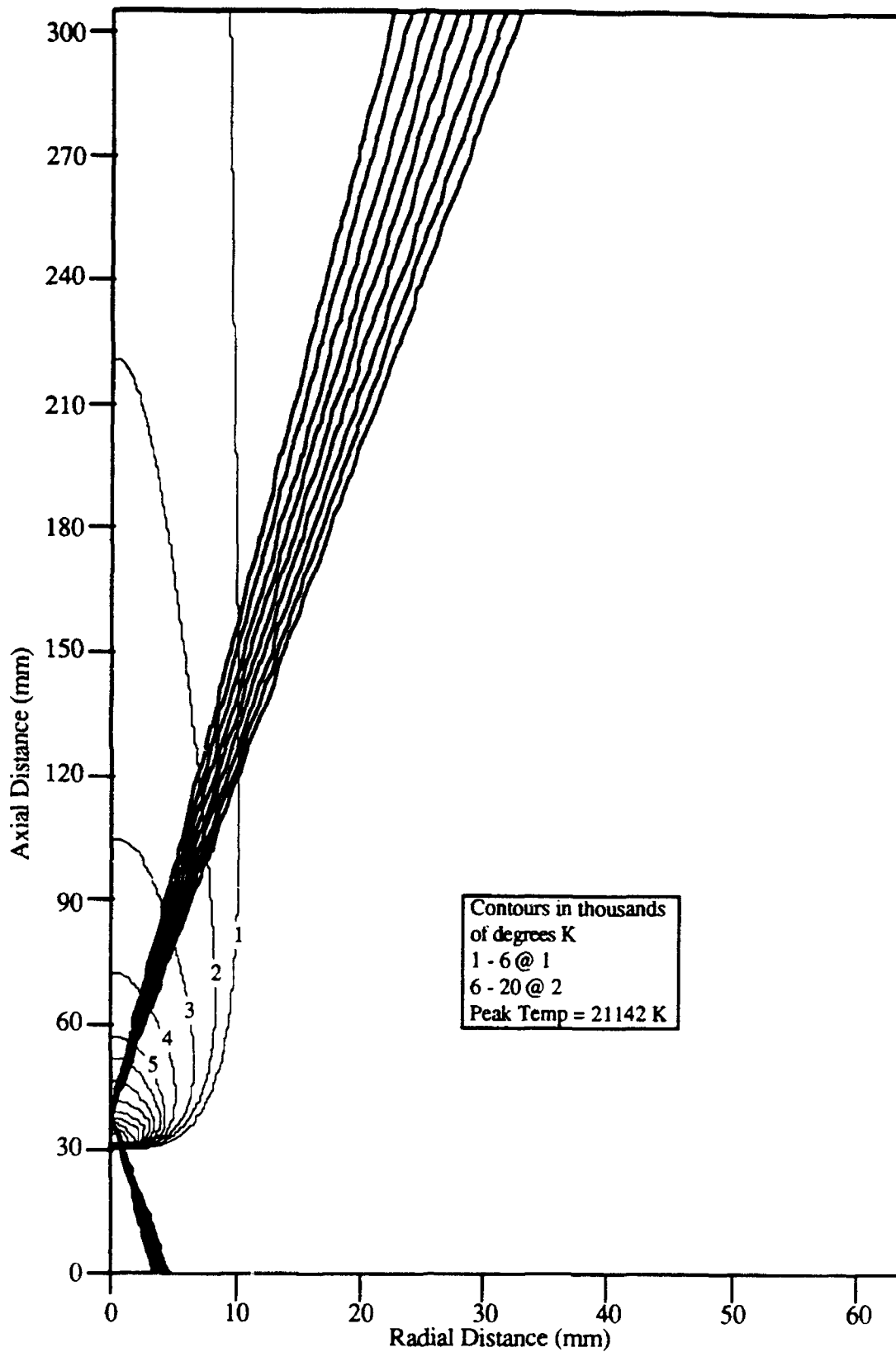
Figure 5.7 Heavy species temperature contours for a 7kW, 1644.7 moles/m²s, f-4, 3.5 atm (case f3) hydrogen LSP.
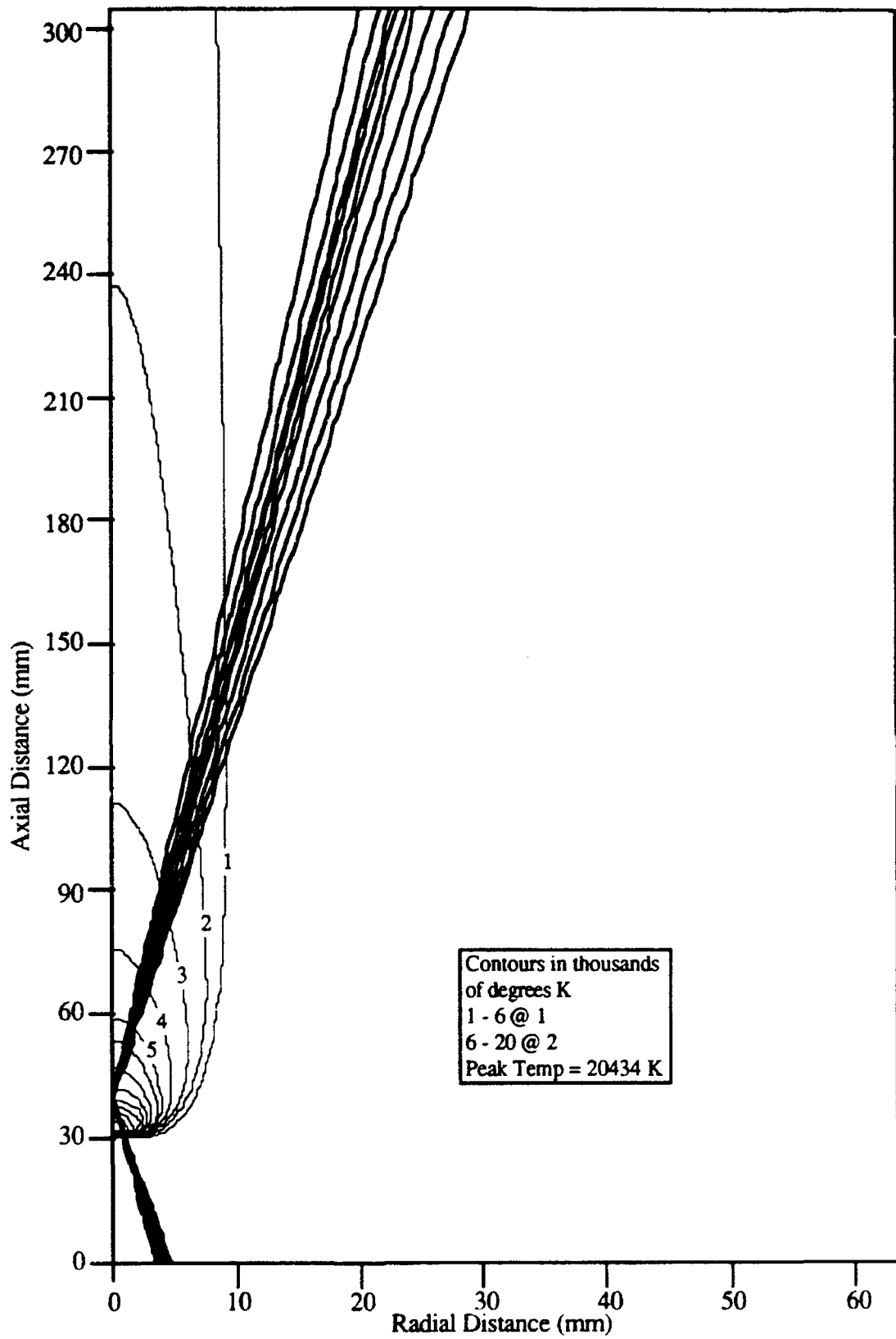
Figure 5.8   Heavy species temperature contours for a 7kW, 2192.9 moles/m^{2}s, f-4, 3.5 atm (case f4) hydrogen LSP.
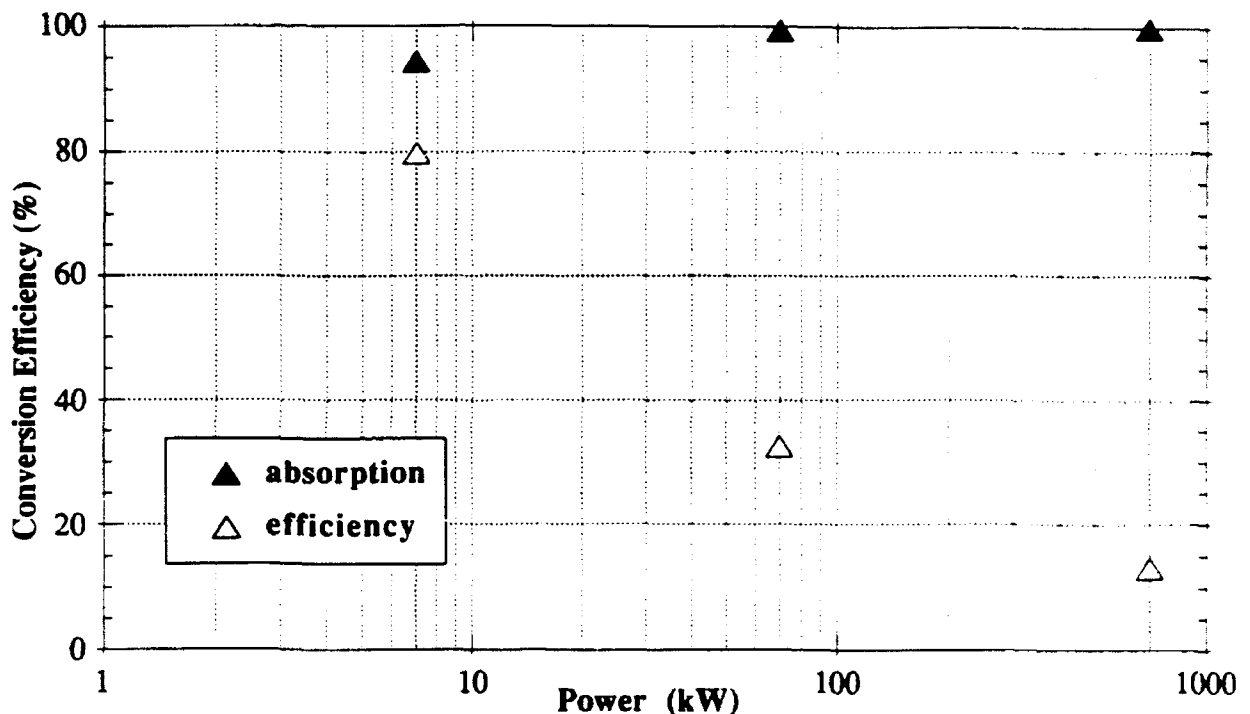
Figure 5.9   Model results for global absorption and thermal efficiency versus
            incident power for 3.5 atm, f-4, 2192 moles/m²s hydrogen LSPs. Cases f4, tf45,
            and f5 have been plotted.

Clearly, this temperature region moves away from the axis with increased power, because of

increased peak electron temperatures. Electron temperature contours for cases f4, tf45, and f5 can

be seen in the plots of Figures 5.13 - 5.15, respectively. Note the dramatic peak electron

temperature increase between 7 kW (20439 K),70 kW (40068 K), and 700 kW (69522 K).

The final comparison to be made with power variation is location of maximum beam absorption.

It would appear that as power is increased and peak temperature rises, the absorption coefficient

along the path of the beam is decreased. The vast majority of power is absorbed at or near the

focus in the 7kW case as can be seen in the plot of Figure 5.16. However, absorption of the beam

is far more gradual for the 700 kW case, with the region of maximum absorption actually occuring

just downstream of the laser focus as can be seen in the plot of Figure 5.17.
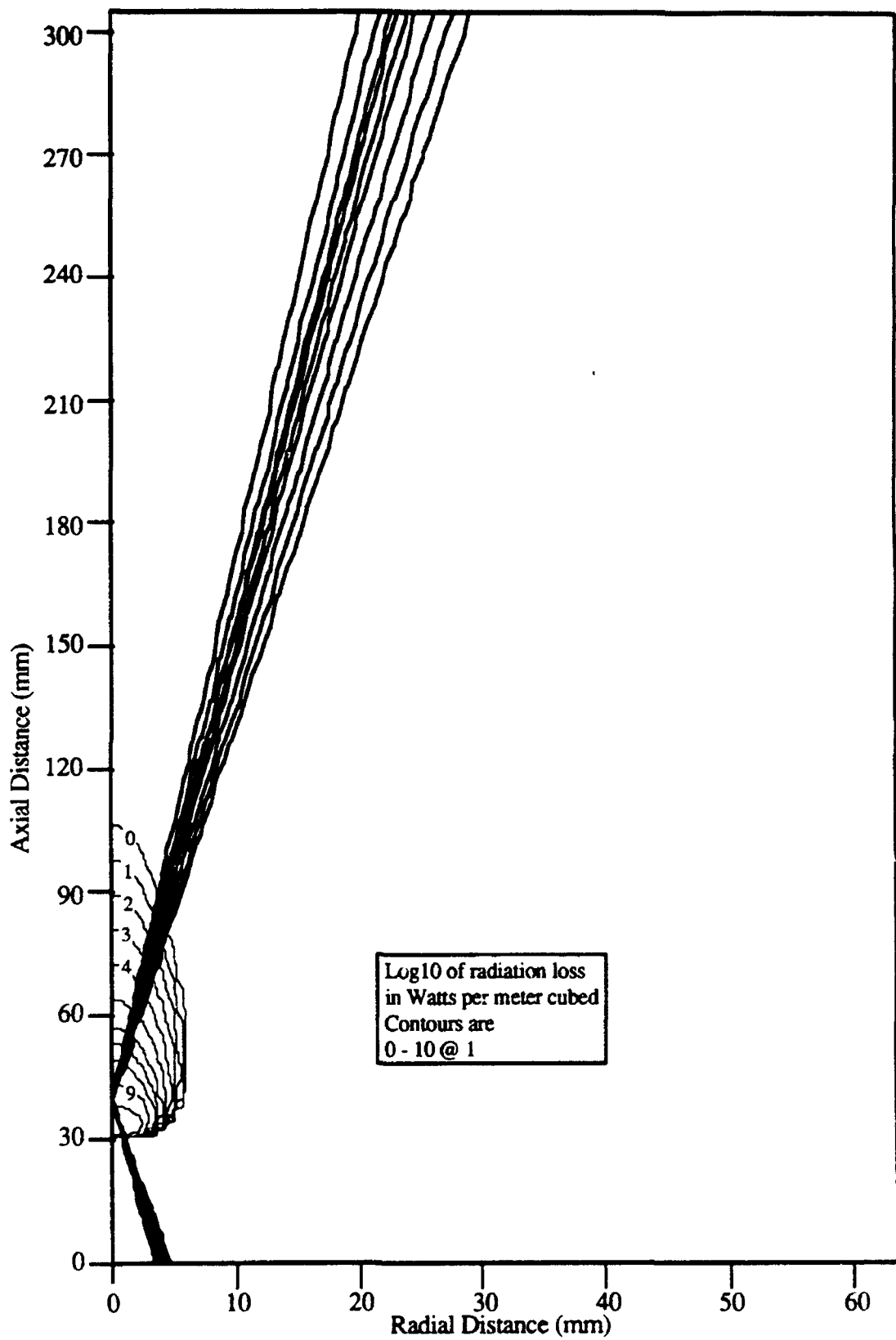
Figure 5.10   Contours of the base 10 log of radiation loss in Watts per meter cubed from case f4 which is a 7kW, 3.5 atm, f-4, 2192.9 gmoles/m²s hydrogen LSP.
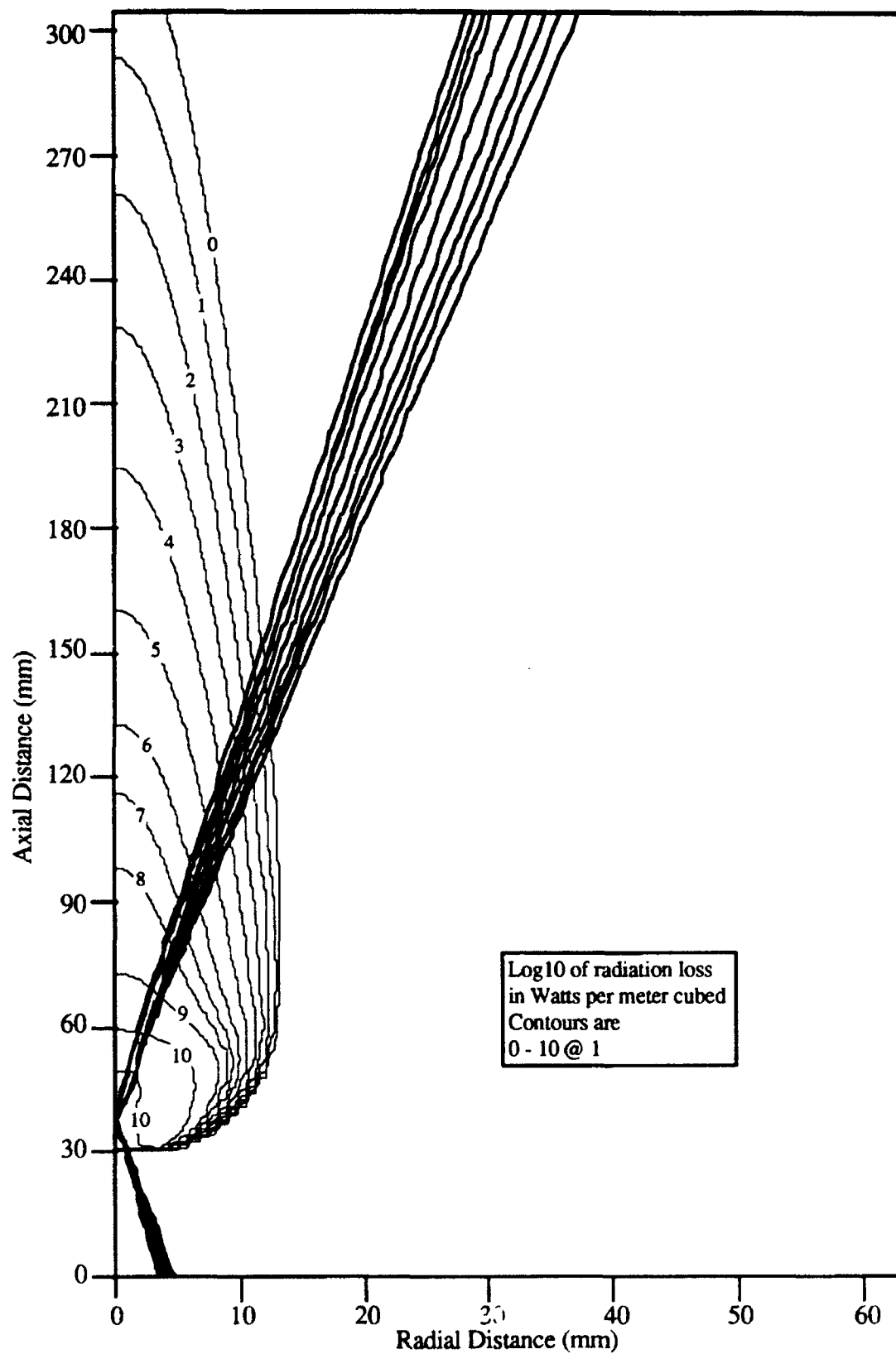
Figure 5.11   Contours of the base 10 log of radiation loss in Watts per meter cubed from case tf45 which is a 70kW, 3.5 atm, f-4, 2192.9 gmoles/m^{2}s hydrogen LSP.
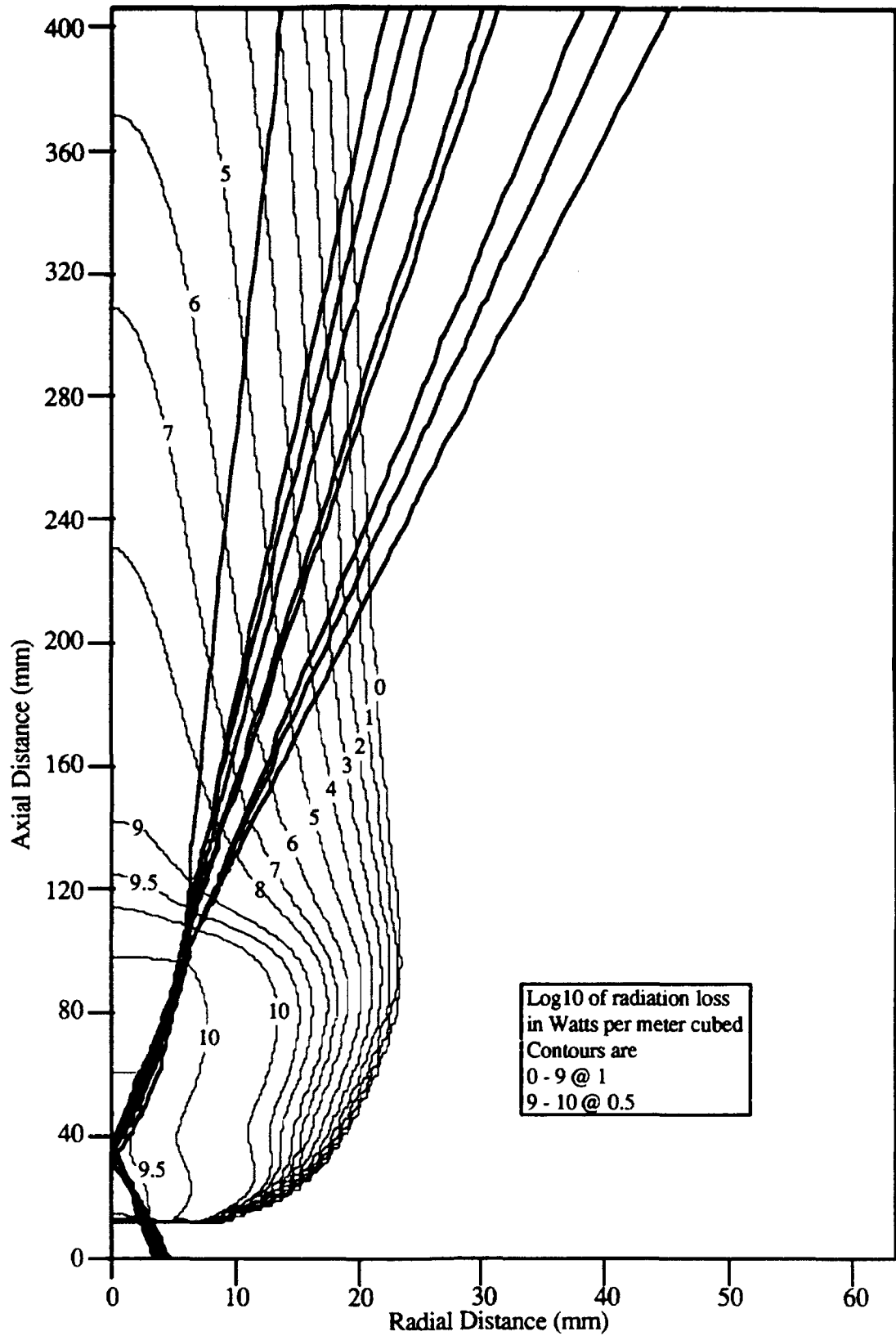
Figure 5.12   Contours of the base 10 log of radiation loss in Watts per meter cubed from case
f5 which is a 700kW, 3.5 atm, f-4, 2192.9 gmoles/m^{2}s hydrogen LSP.
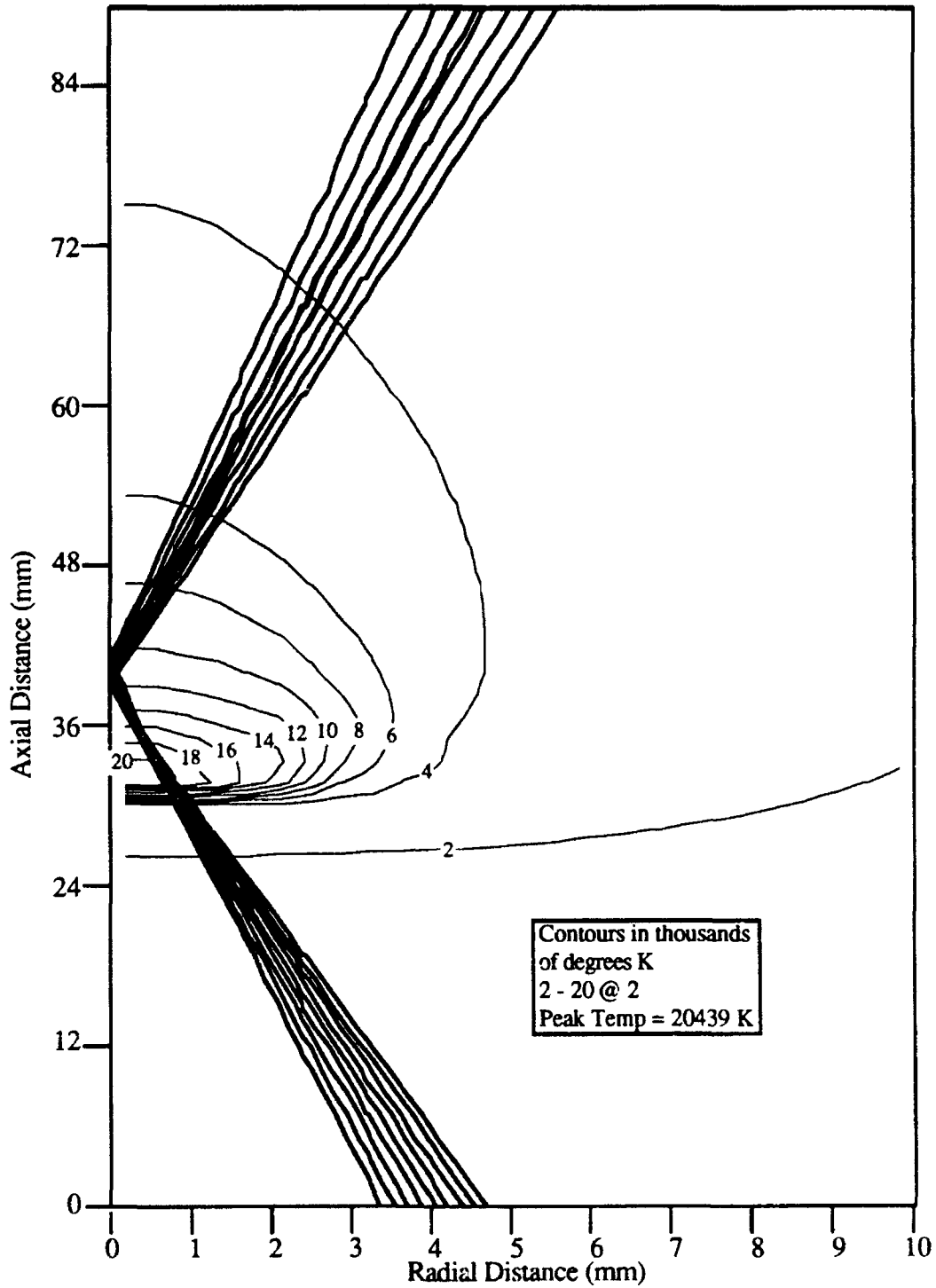
Figure 5.13   Electron temperature contours of the core region of case f4, which is a 7kW, 3.5 atm, f-4, 2192.9 gmoles/m²s hydrogen LSP.
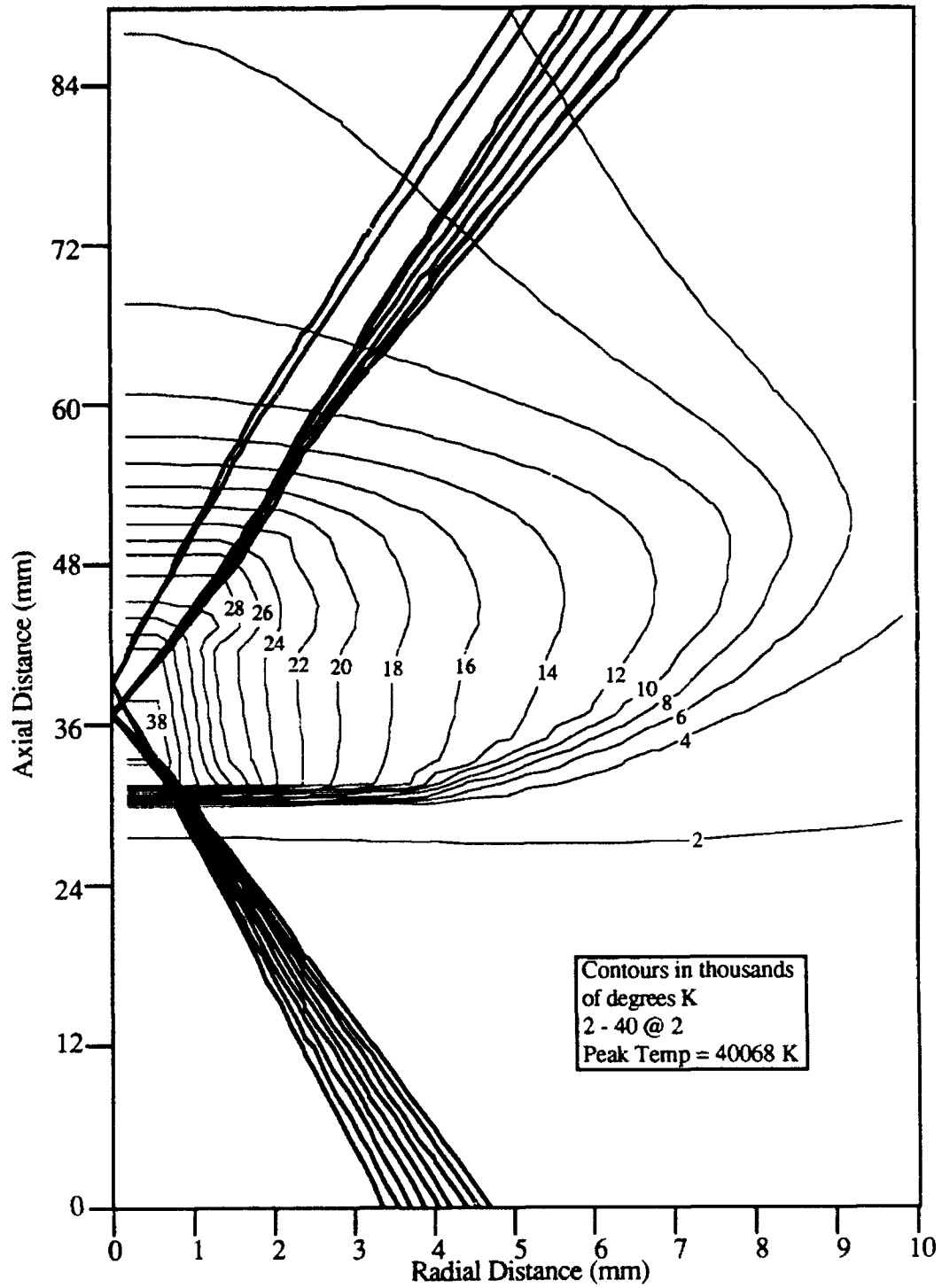
Figure 5.14 Electron temperature contours of the core region of case tf45, which is a 70kW, 3.5 atm, f-4, 2192.9 gmoles/m²s hydrogen LSP.
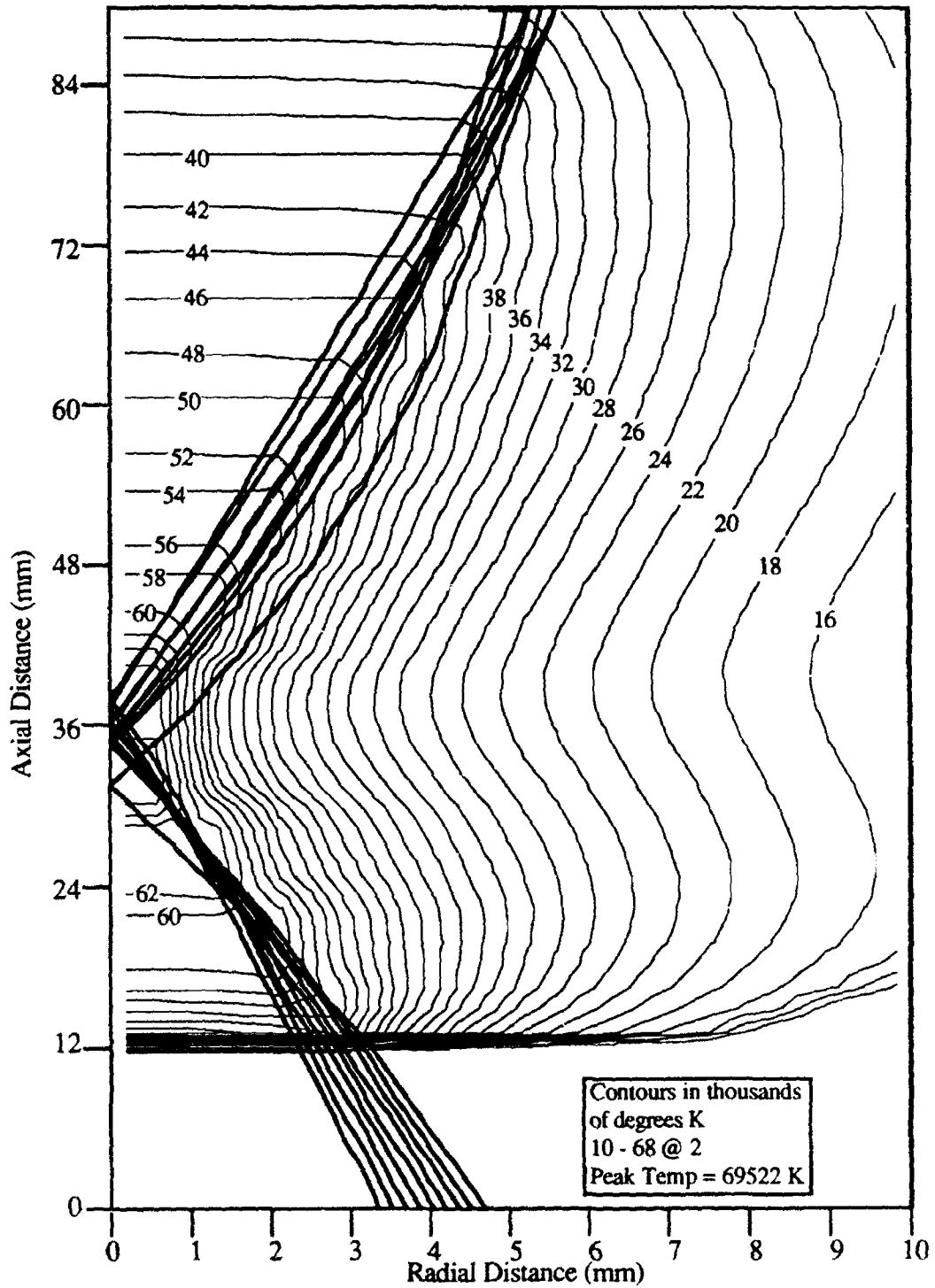
Figure 5.15 Electron temperature contours of the core region of case f5, which is a 700kW, 3.5 atm, f-4, 2192.9 gmoles/m²s hydrogen LSP.
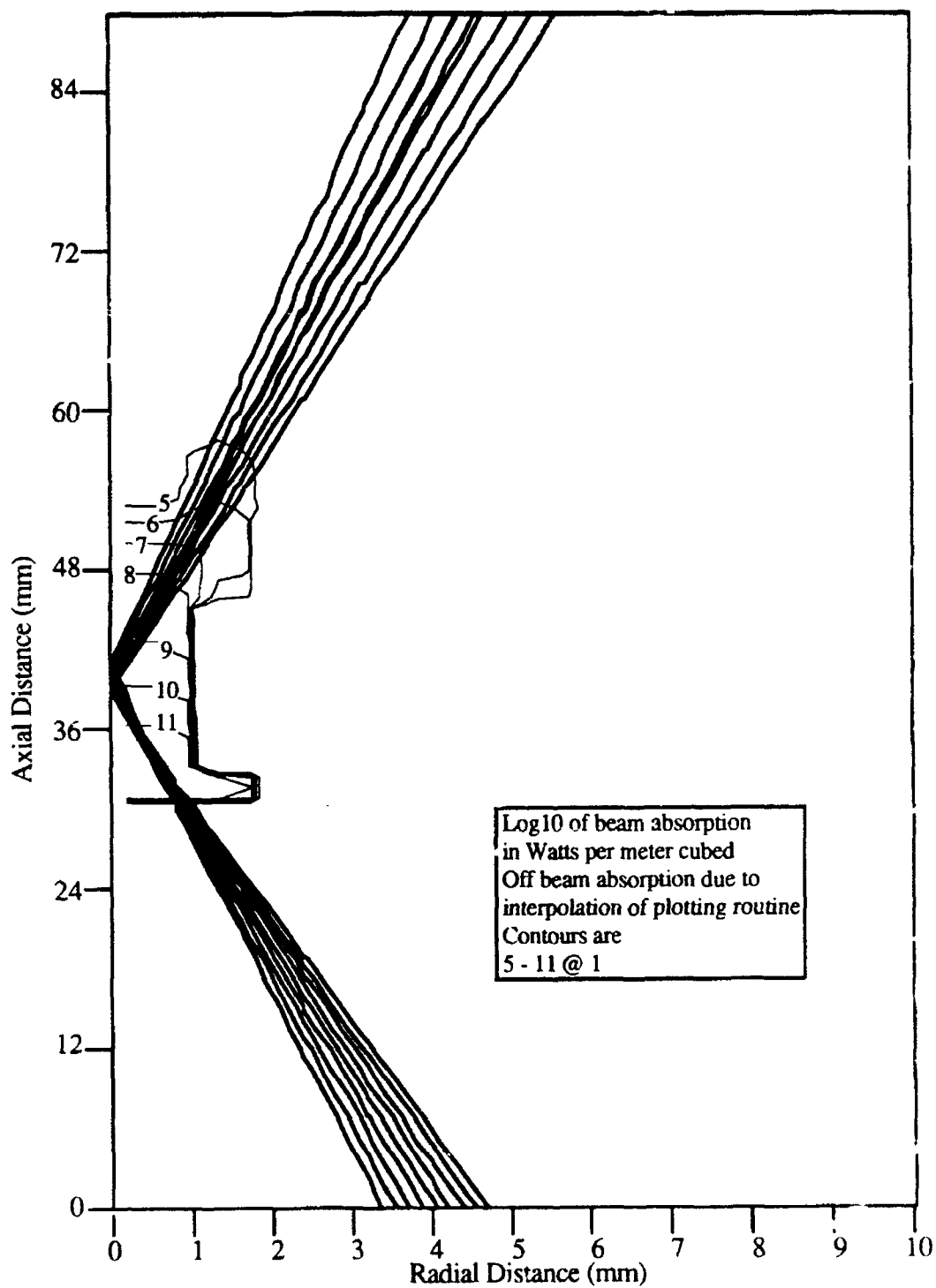
Figure 5.16 Contours of the base 10 log of beam absorption for case f4, which is a 7kW, 3.5 atm, f-4, 2192.9 gmoles/m²s case.
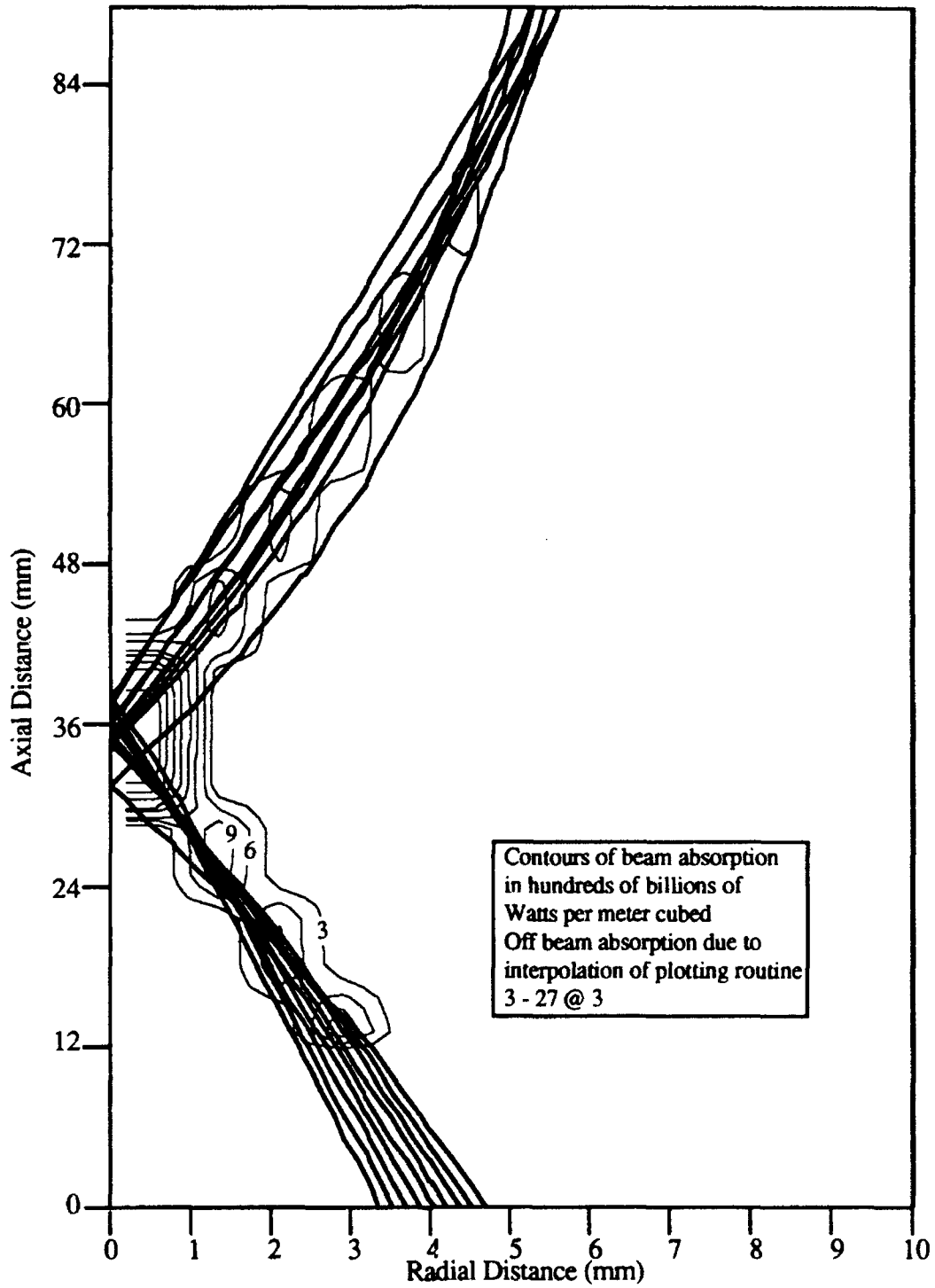
Figure 5.17   Contours of the beam absorption for case f5, which is a 700kW, 3.5 atm, f-4, 2192.9 gmoles/m²s case.

It should be noted that in an effort to include as much of the radiating volume in the domain as possible, case f5 was done on domain H, which has a total length of 406.4 mm. Clearly, as indicated from the plot in Figure 5.12, part of the tail region of the LSP is outside of the computational domain. However for comparison purposes, the plot is more than adequate.

5.5.3 Effect of Pressure Variation

Model results for global absorption and thermal efficiency for a series of 2192.9 moles/m²s, 70 kW, f-4 hydrogen LSPs can be seen in the plot of Figure 5.18. Predicted global absorption follows the experimentally observed trend of increasing with increased pressure, appearing to asymptote to 100%. For a fixed mole flux, thermal efficiency decreases with increased gas pressure due to a larger fraction of the incident power lost as radiation. It is clear from the heavy species temperature contour plots appearing in Figures 5.19 - 5.21 that an increase in gas pressure results in a decrease in both LSP length and width, and therefore volume.
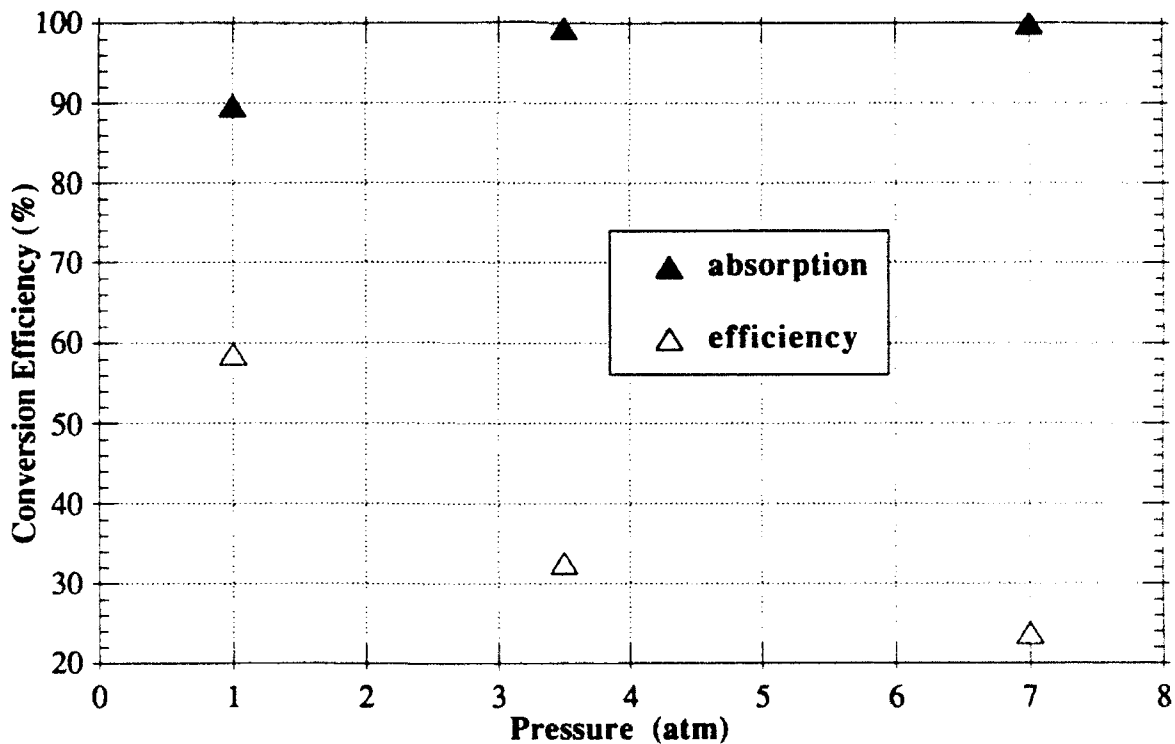
Figure 5.18   Model predictions for global absorption and thermal efficiency for a series of 70 kW, f-4, 2192.9 gmoles/m²s hydrogen LSPs initiated from a point spark versus pressure.

Note that the 5000 K temperature contour in Figure 5.19 for the 1 atm (f6) case crosses the axis near 270 mm from the inlet and extends to approximately 14 mm radially from the axis. However, the 5000 K temperature contour in Figure 5.20 for the 3.5 atm (tf45) case crosses the axis at approximately 135 mm and extends radially from the axis to approximately 10 mm. The corresponding contour in Figure 5.21 for the 7 atm (tf32) case has even smaller dimensions. In addition to a decrease in size, a peak temperature increase with increased pressure was observed. Peak heavy species temperature was 29084 K at 1 atm (case f6), 39993 K at 3.5 atm (case tf45), and 44823 K at 7 atm (case tf32).

Despite the decrease in LSP size with increased pressure, radiation loss was observed to increase, due to the increased number density of emitters (electrons). Radiation loss can be seen in the plots of Figures 5.22 and 5.23 for a 1 atm (f6) case and a 3.5 atm (tf45) case respectively. Comparing the plots of Figures 5.22 and 5.23, the radiating volume of the 1 atm case is much larger than for the 3.5 atm case, however, the 3.5 atm case radiates more in the region of the plasma core, and since the plot contours are on a log scale, the difference is an order of magnitude.

5.5.4 Effect of Beam F-Number

Model results for global absorption and thermal efficiency for cases at 2192.9 moles/m^{2}s, 7 kW, 3.5 atm and three f-numbers can be seen in the plot of Figure 5.24. Predicted global absorption is essentially constant versus f-number. Experimentally it was observed that global absorption slightly decreased when f-number was increased from f-4.1 to f-7.1, as was evident from the data in Figure 2.6.

Based on the data in Figure 5.24, thermal efficiency increases between f-2 and f-4 but decreases between f-4 and f-8. This is due at least in part to the location and magnitude of the peak temperature, which is directly effected by the beam geometry. Electron temperature contours of the core regions of the three cases plotted in Figure 5.24 can be seen in the plots of Figures 5.25 - 5.27. Note that the location of the peak temperature in each case is just upstream of the beam focus in the direct path of the beam, and that peak temperature is a maximum for the f-4 case.
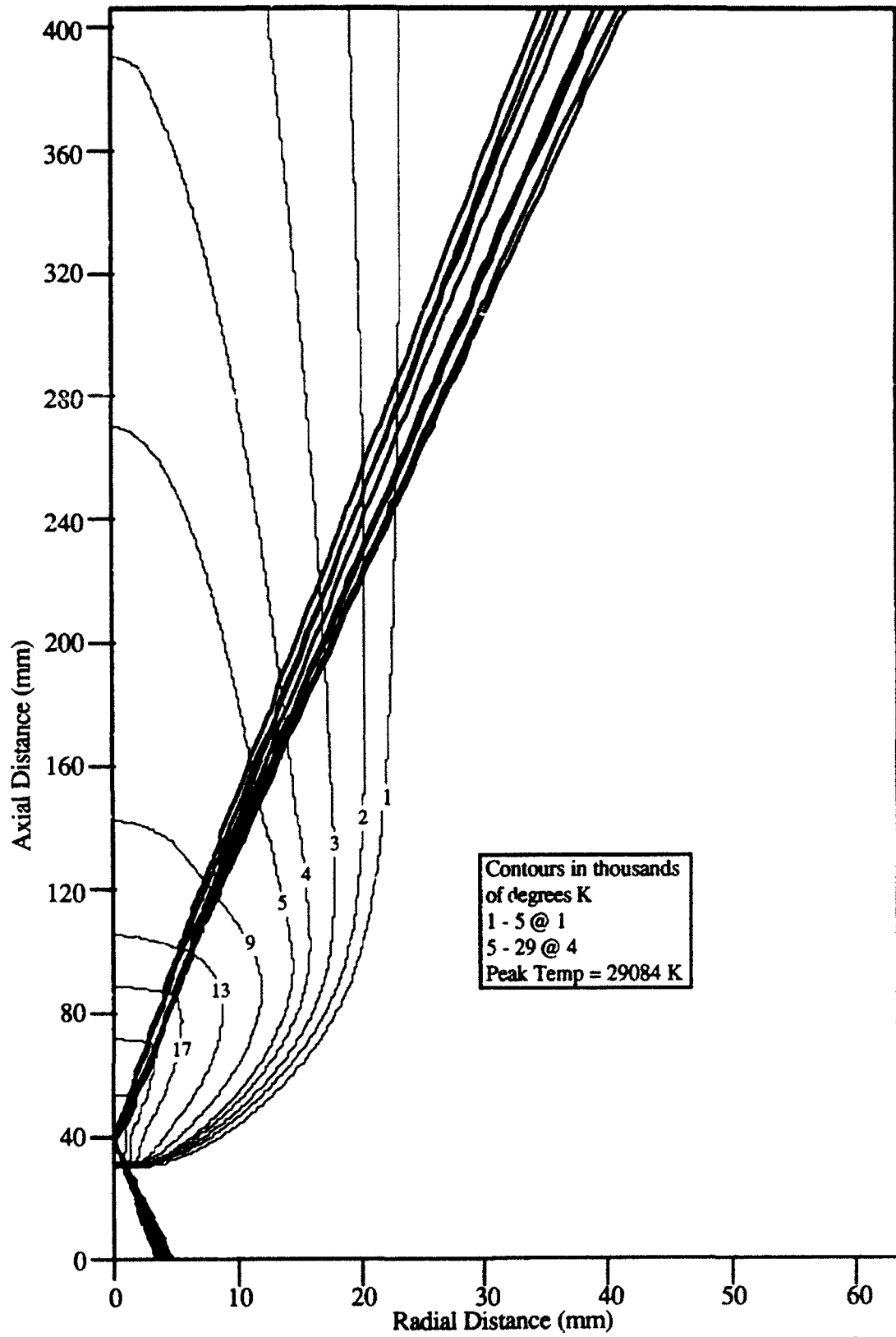
Figure 5.19 Heavy species temperature contours for case f6 which is a 1 atm, f-4, 70kW, 2192.9 moles/m²s hydrogen LSP.
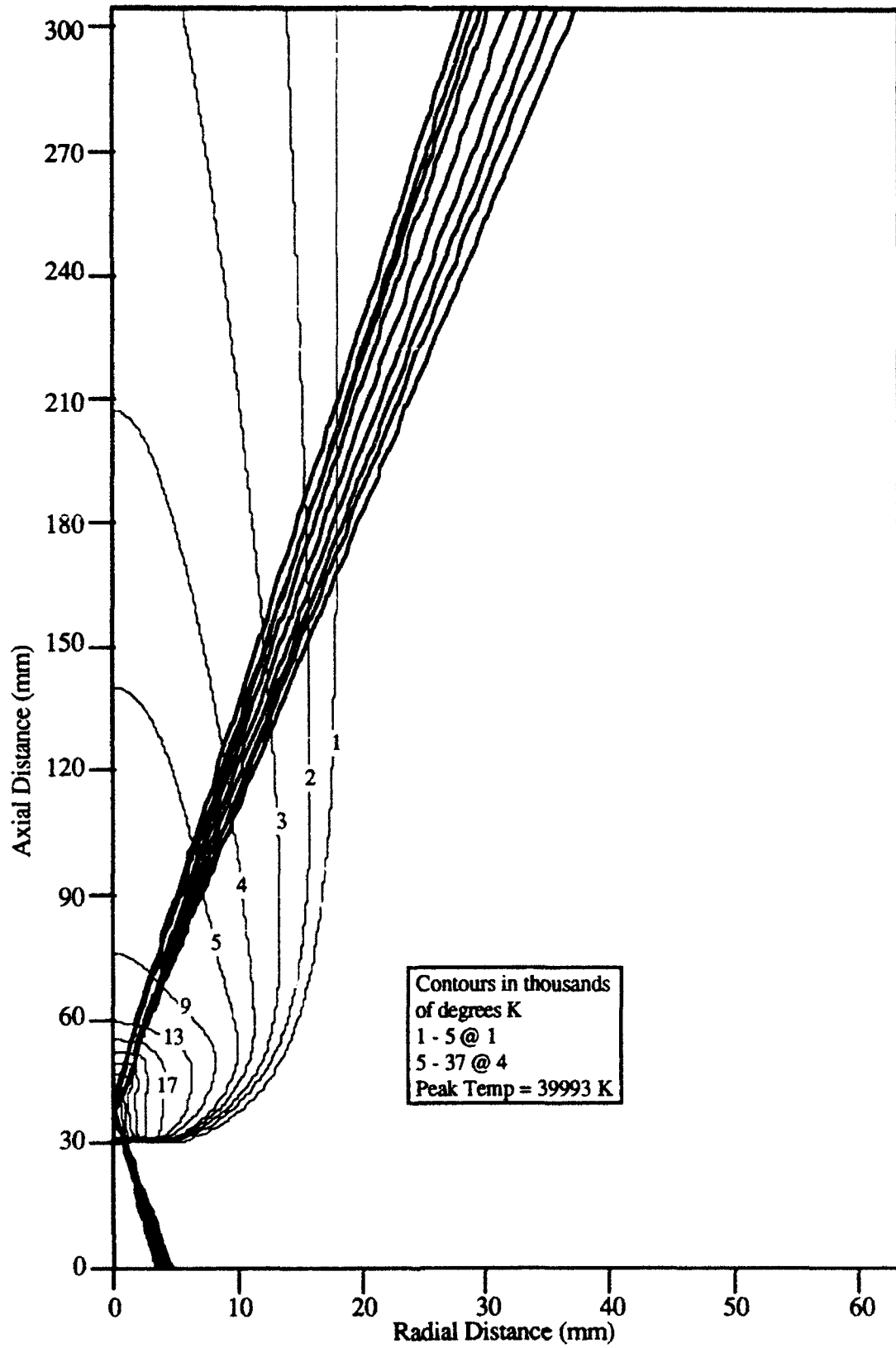
Figure 5.20   Heavy species temperature contours for case tf45 which is a 3.5 atm, f-4, 70kW, 2192.9 moles/m²s hydrogen LSP.
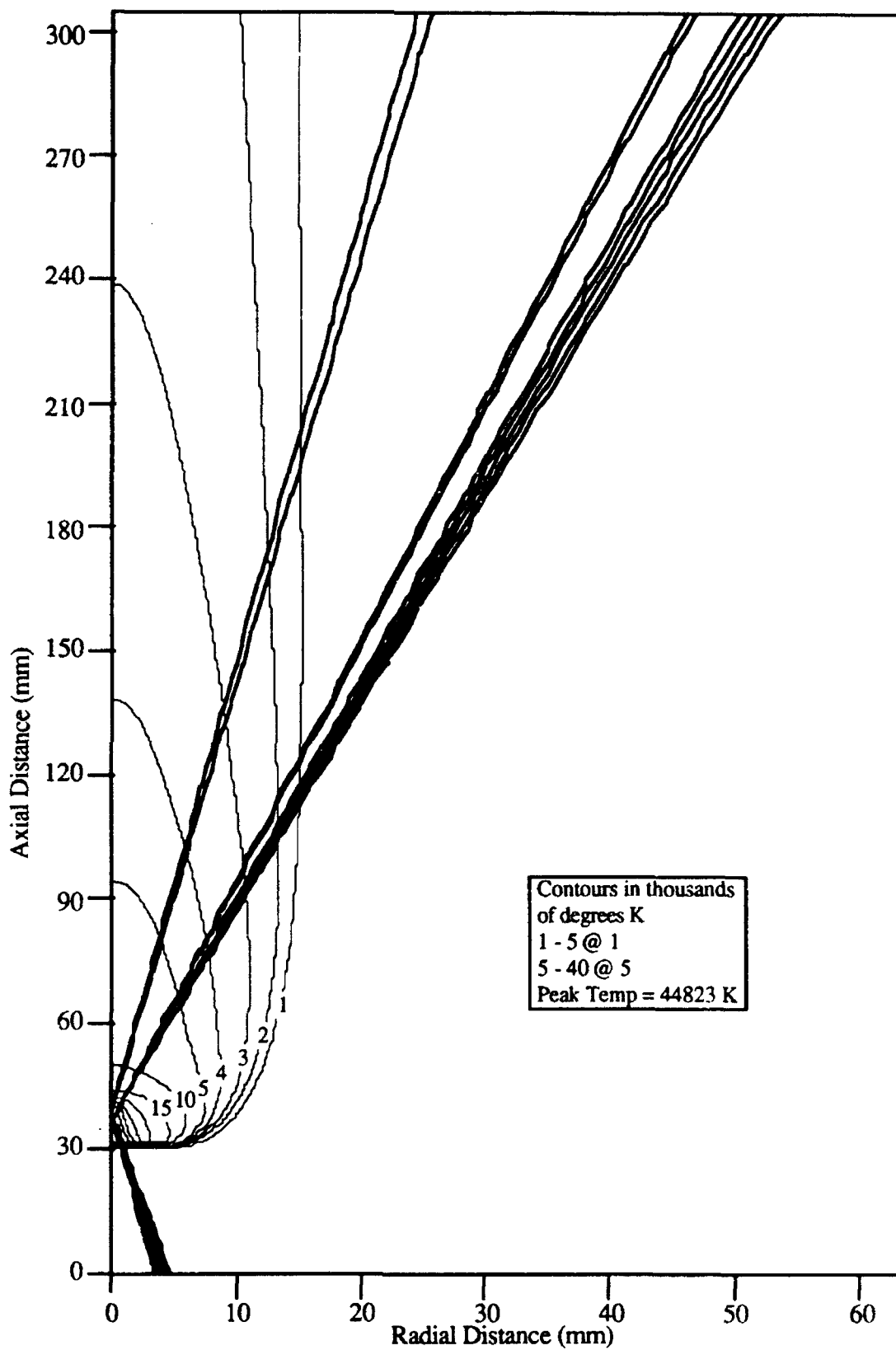
Figure 5.21   Heavy species temperature contours for case tf32 which is a 7 atm, f-4, 70kW, 2192.9 moles/m²s hydrogen LSP.
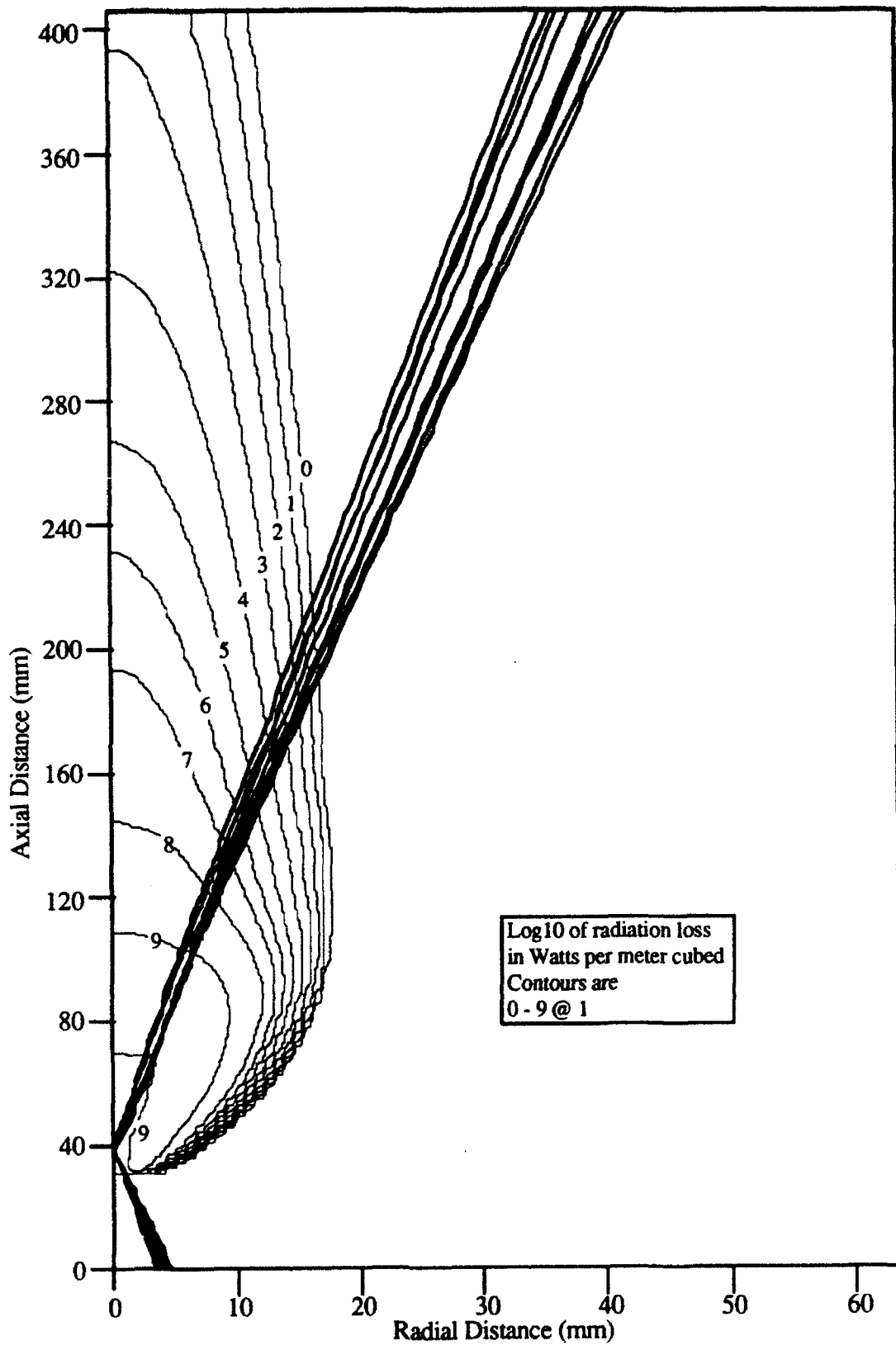
Figure 5.22   Contours of the base 10 log of radiation loss for case f6 which is a 1 atm, f-4, 70kW, 2192.9 moles/m²s hydrogen LSP.
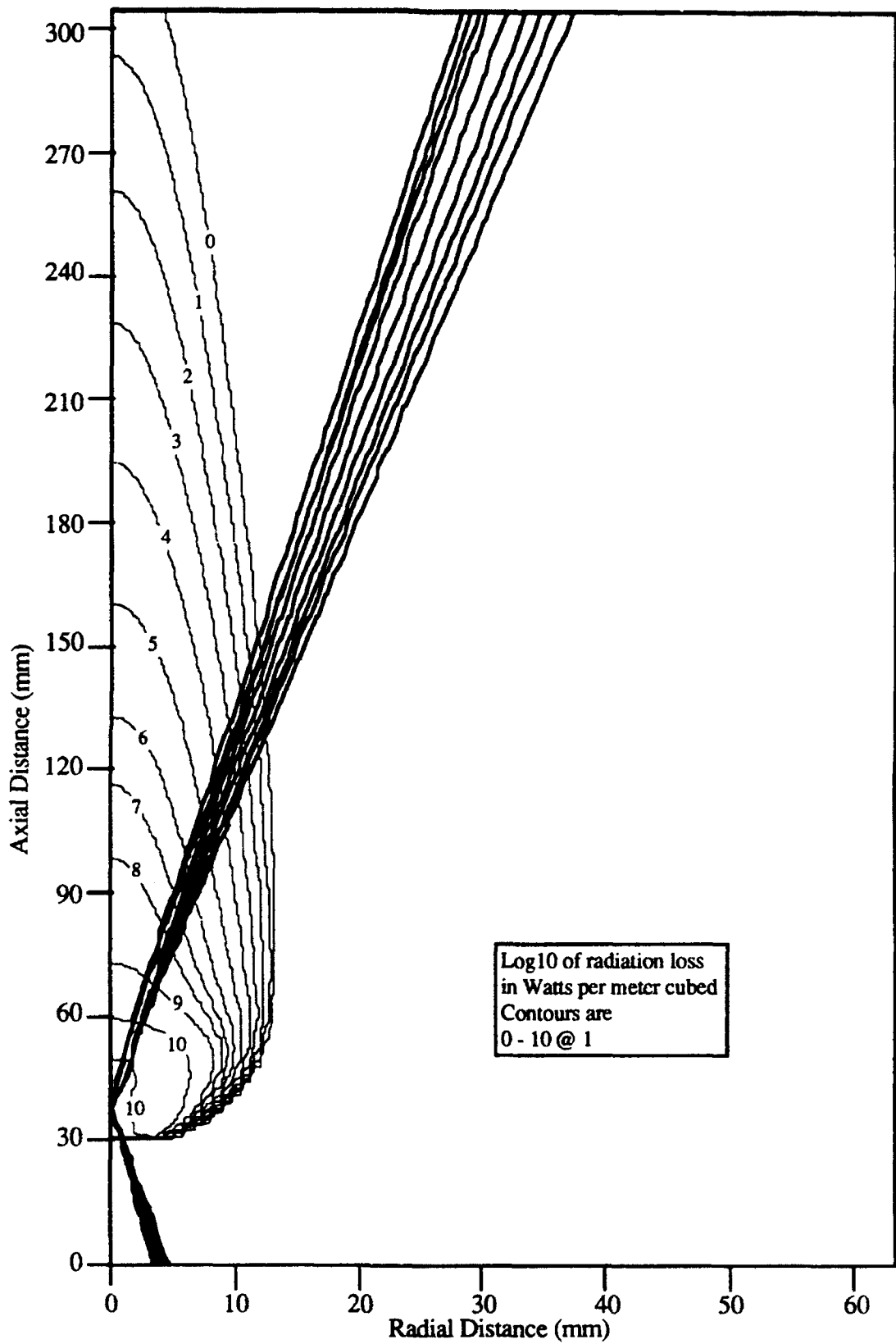
Figure 5.23 Contours of the base 10 log of radiation loss for case tf45 which is a 3.5 atm, f-4, 70kW, 2192.9 moles/m²s hydrogen LSP.
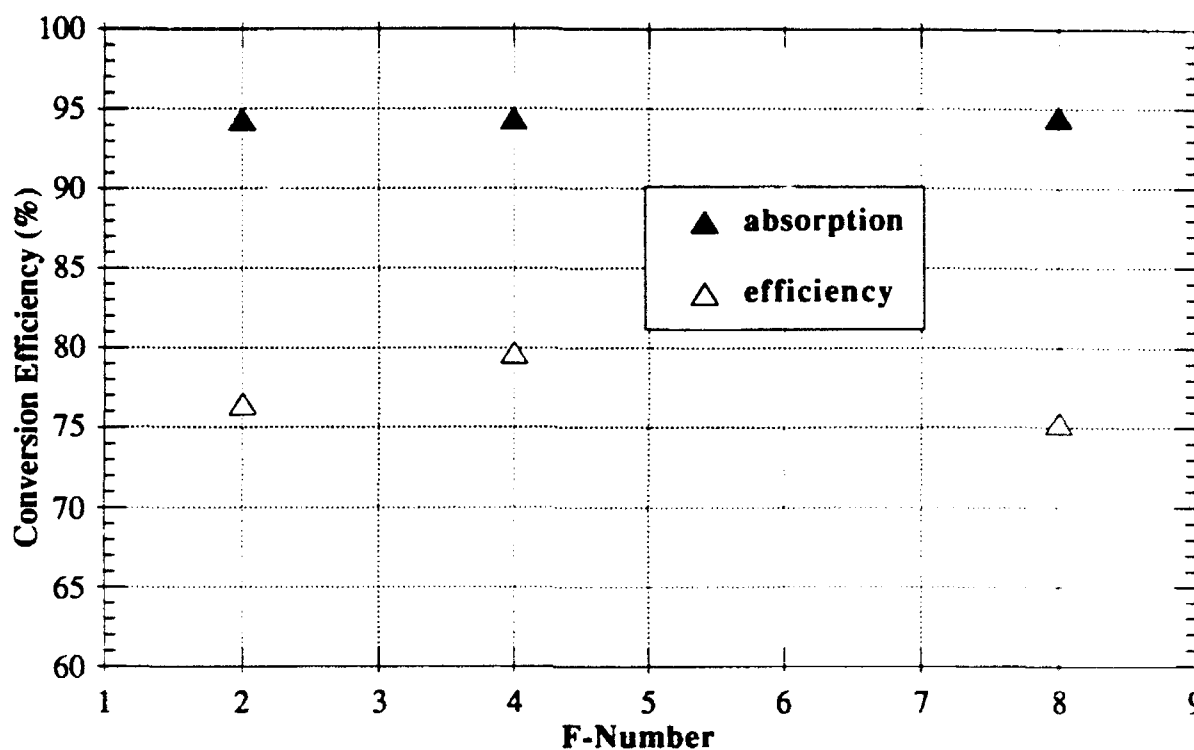
Figure 5.24   Model predictions for global absorption and thermal efficiency for 3.5 atm, 70kW, 2192.9 moles/m²s hydrogen LSPs versus beam f-number.

The f-2 case had a peak electron temperature of 21498 K (heavy species peak temperature = 21490 K) off the axis of symmetry at location x=31.33, r=1.19 mm. The f-4 case had a peak electron temperature of 20439 K (heavy species peak temperature = 20434 K) on the axis of symmetry at location x=31.33, r=0 mm. Finally, the f-8 case had a peak electron temperature of 24158 K (heavy species peak temperature ≈ 24150 K) also on the axis of symmetry at location x=31.33, r=0 mm.

The off axis peak temperature of the f-2 case was a result of beam geometry alone since there was no significant refraction effects in any of the three f-number comparison cases. At higher gas pressures, the plasma front would be expected to be further upstream with the peak temperature location following the beam upstream and away from the axis. This behavior had been observed previously for experimental high pressure argon plasmas which appeared to have "legs" which followed the beam upstream. Although the beam was assumed to be axisymmetric in the model, the laboratory laser was known to have hot spots which destroyed the symmetry. It is therefore

possible that the experimental observance of the "legs" corresponds to the off axis peak temperature displayed by case f9, but for a nonsymmetric beam.
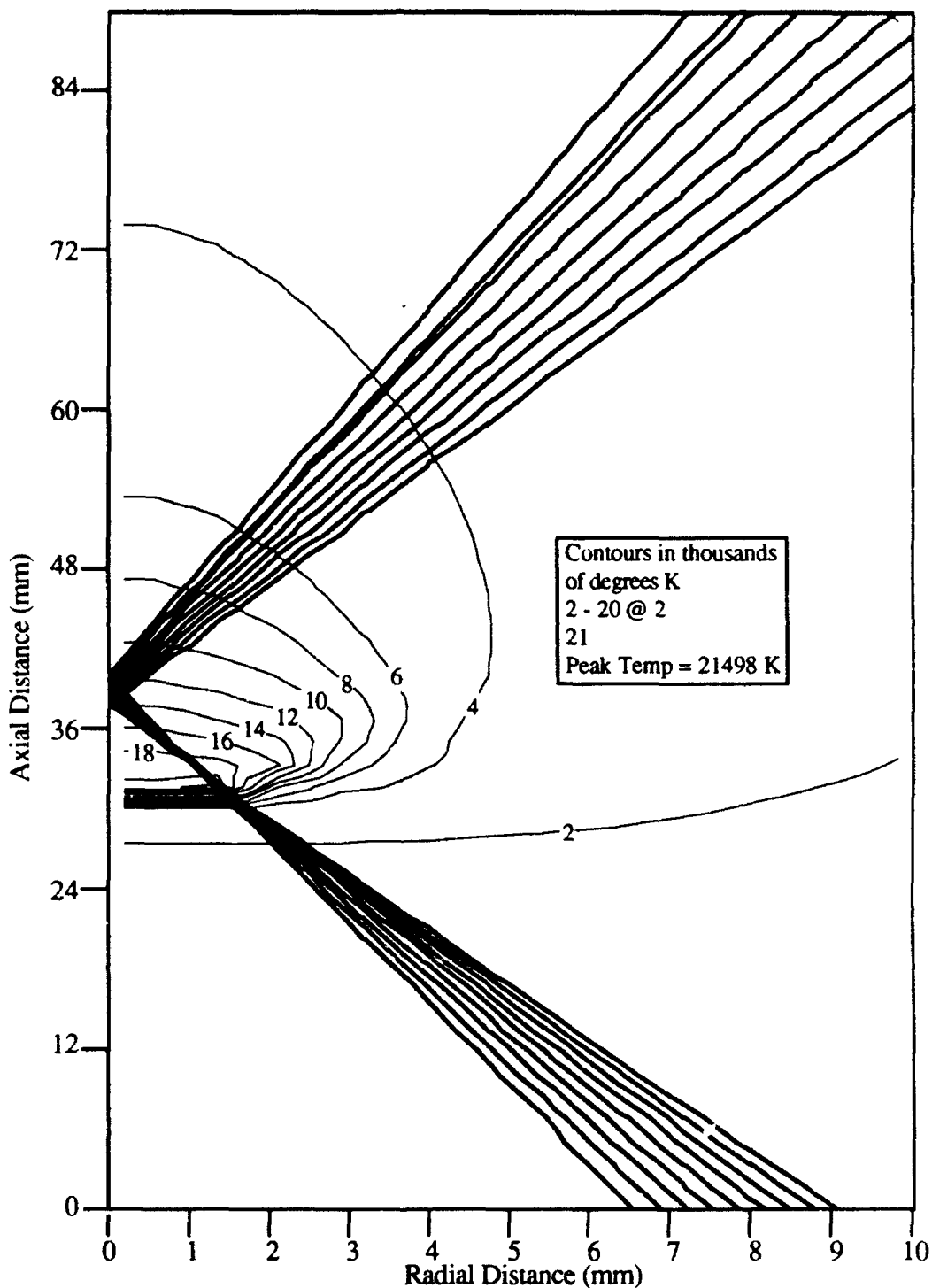
Figure 5.25   Electron temperature contours and beam ray trace for the core region of case f9, which is a 7kW, 2192.9 moles/m²s, 3.5 atm, f-2 hydrogen LSP.
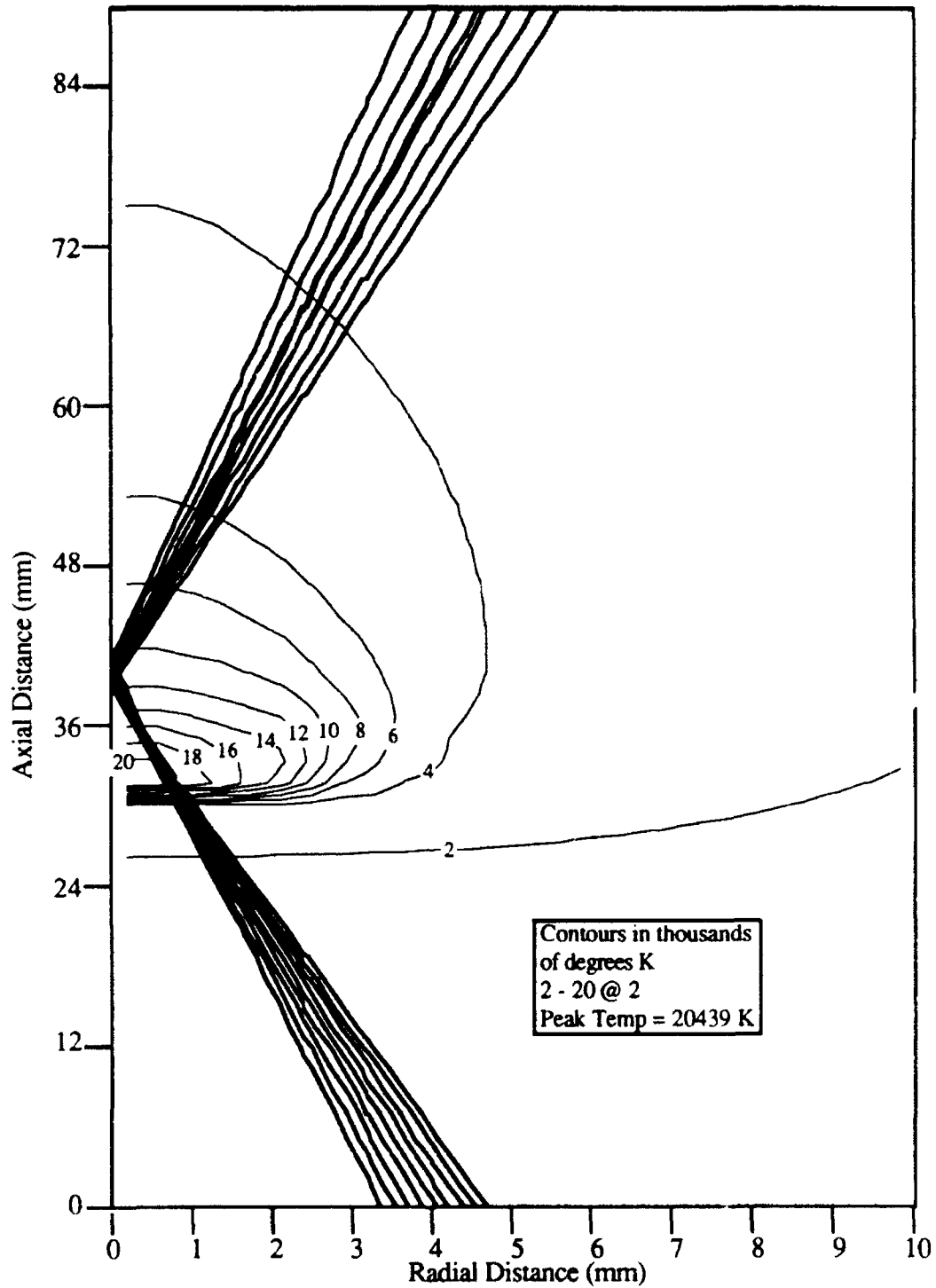
Figure 5.26 Electron temperature contours and beam ray trace for the core region of case f4, which is a 7kW, 2192.9 moles/m²s, 3.5 atm, f-4 hydrogen LSP.
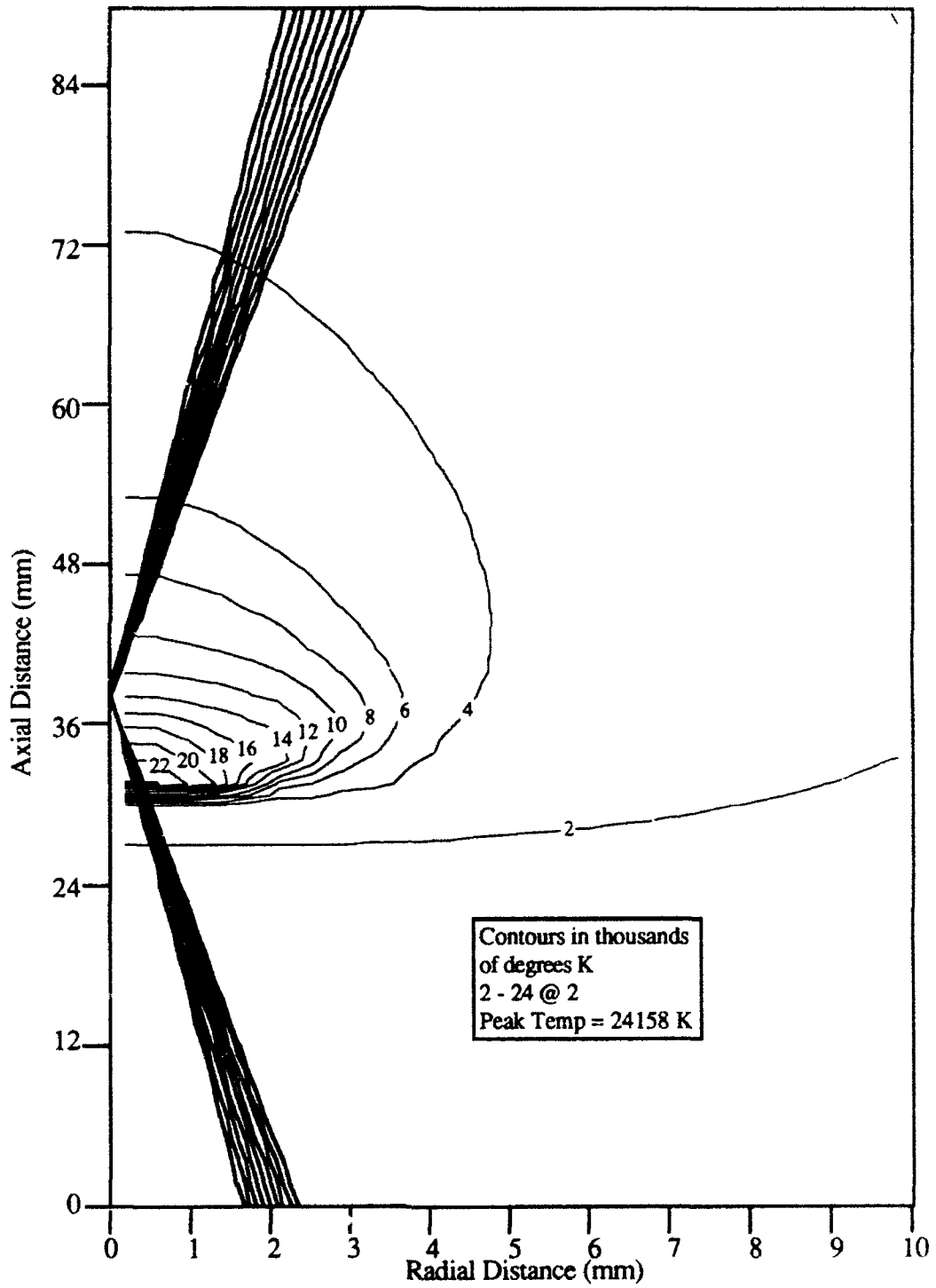
Figure 5.27   Electron temperature contours and beam ray trace for the core region of case f7, which is a 7kW, 2192.9 moles/m²s, 3.5 atm, f-8 hydrogen LSP.

Although global absorption is essentially equivalent for the three f-number comparison cases, the location of maximum beam absorption is different for the f-2 case than for the f-4 and f-8 cases due to the off axis temperature peak. As indicated by the plot in Figure 5.28, beam absorption reaches a maximum off axis and then decreases following the beam before increasing again on the axis. The off axis region corresponds to the region of maximum beam intensity, and the region just downstream of the beam focus on the axis of symmetry corresponds to the region of maximum absorption coefficient. Due to the severe angle with which the rays approach the axis of symmetry for the f-2 case, the beam had enough remaining power for a second absorption peak to become apparent. As indicated by the plots in Figures 5.29 and 5.30, the f-4 and f-8 cases each had a single peak beam absorption region just upbeam of the beam focus.

5.6 Kinetic Nonequilibrium

The existence of kinetic nonequilibrium was thought to be a likely result of the model, especially at the test cases involving high power and low pressure. However, in regions of the plasma core, kinetic nonequilibrium was practically nonexistent. Except for the cases at 700 kW, the differences between electron temperature and heavy species temperature at the plasma core were negligible. The peak electron temperature was 69522 K compared with a peak heavy species temperature of 67980 K for case f5, which was a 700 kW, 2192.9 moles/m^{2}s, 3.5 atm, f-4 case. In fact for all the cases run, the electron and heavy species temperature contours for all temperatures greater than approximately 3000 K were almost completely identical. Below approximately 3000 K however, there is a significant difference between electron temperature and heavy species gas temperature.

This difference in electron and heavy species temperatures can be vividly seen by comparing the contour plots in Figures 5.31 and 5.32 which are for electron and heavy species temperature contours respectively for a 70 kW, 7 atm, 2192.9 moles/m^{2}s, f-4 case (tf32). The ratio of electron temperature to gas temperature for case tf32 has been plotted in Figure 5.33. Note that in the region just upstream of the LSP and wrapping partly around the LSP front, the temperature ratio greatly exceeds unity. In addition, in the tail region of the LSP, as the electrons cool, the

THIS
PAGE
IS
MISSING
IN
ORIGINAL
DOCUMENT
98/99
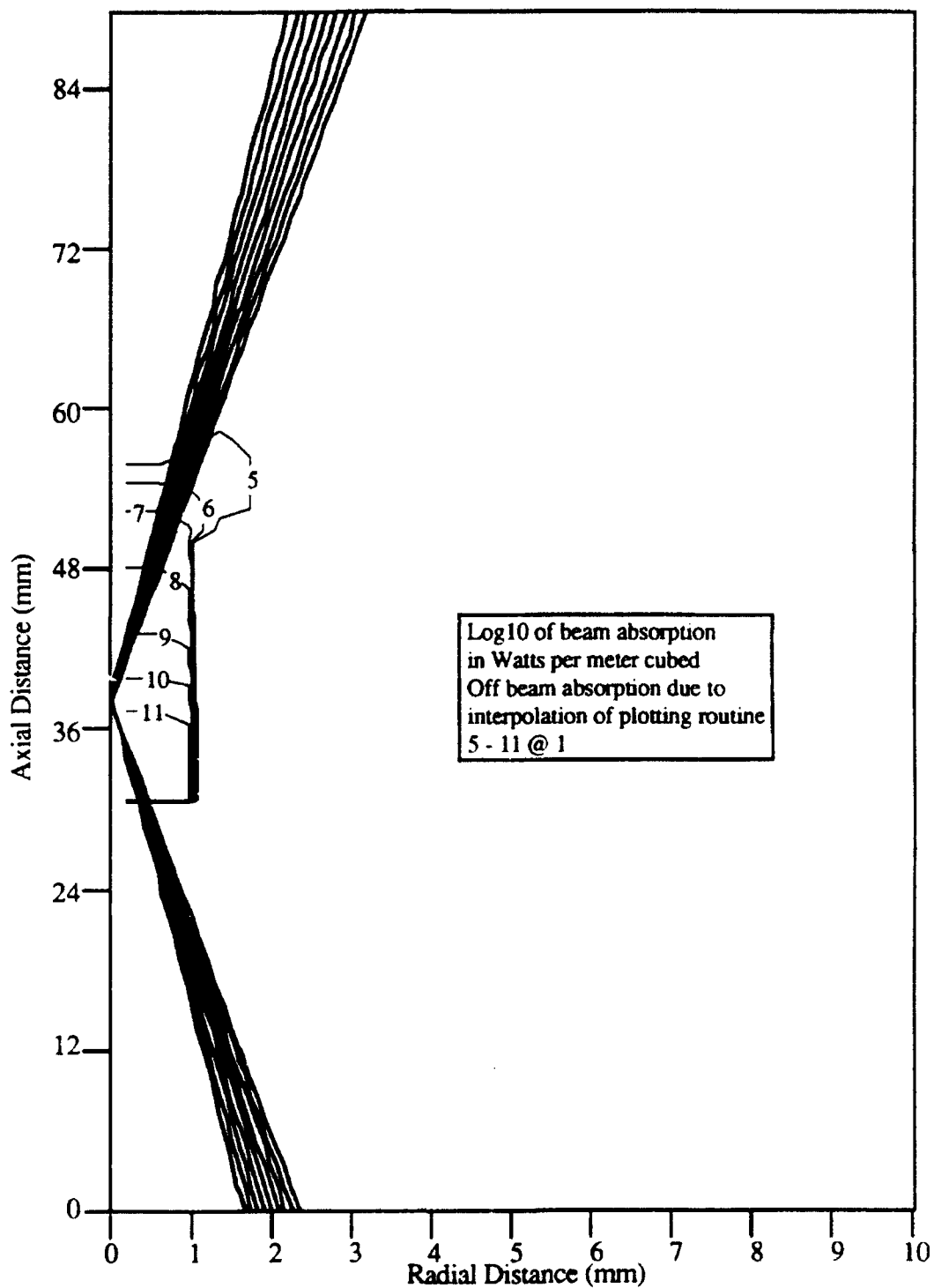
Figure 5.30   Contours of the base 10 log of beam absorption for case f7, which is a 7kW, 2192.9 moles/m²s, 3.5 atm, f-8 hydrogen LSP.
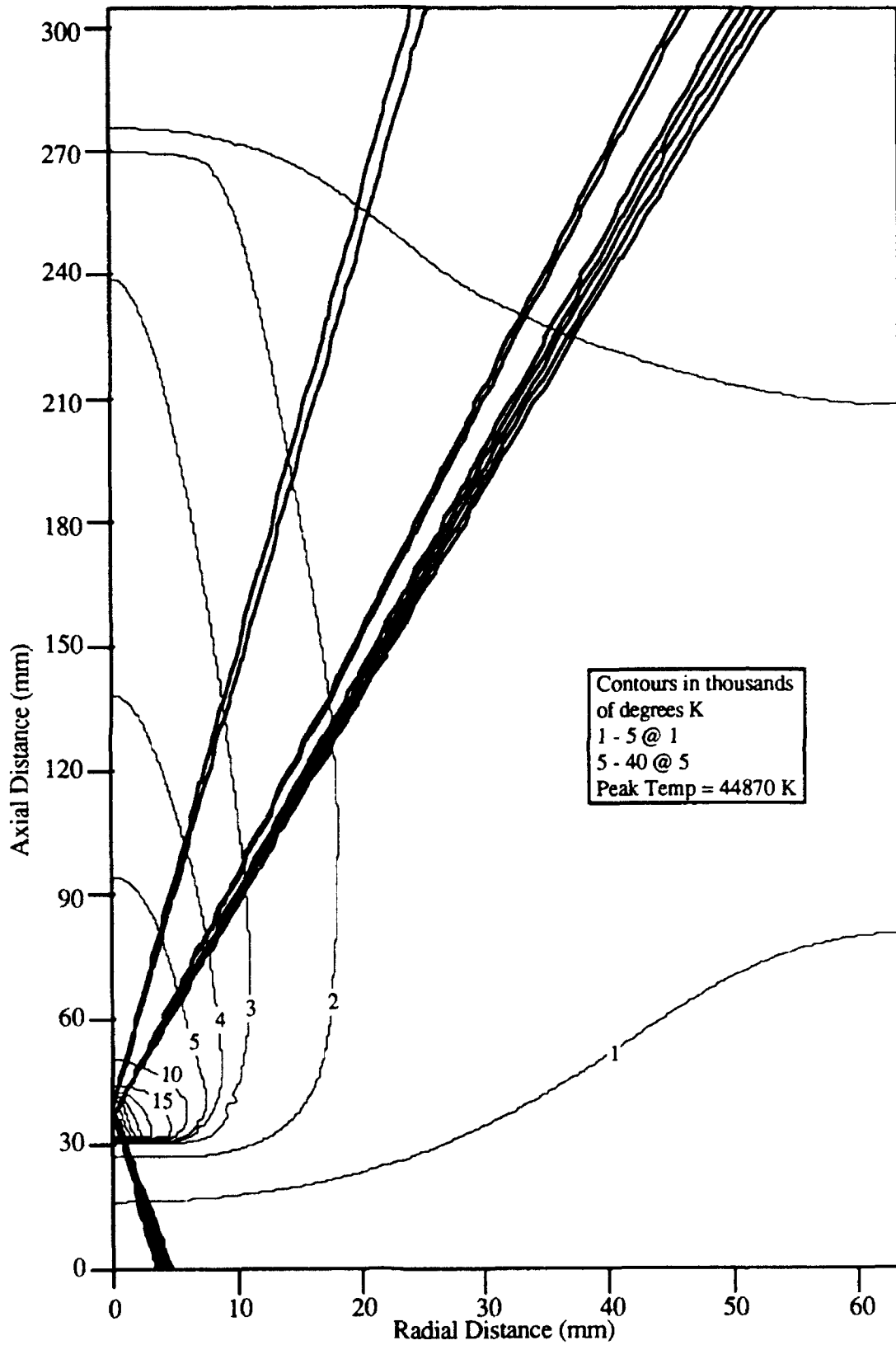
Figure 5.31   Electron temperature contours and beam raytrace for case tf32, which is a 70kW, 2192.9 moles/m²s, 7 atm, f-4 hydrogen LSP.
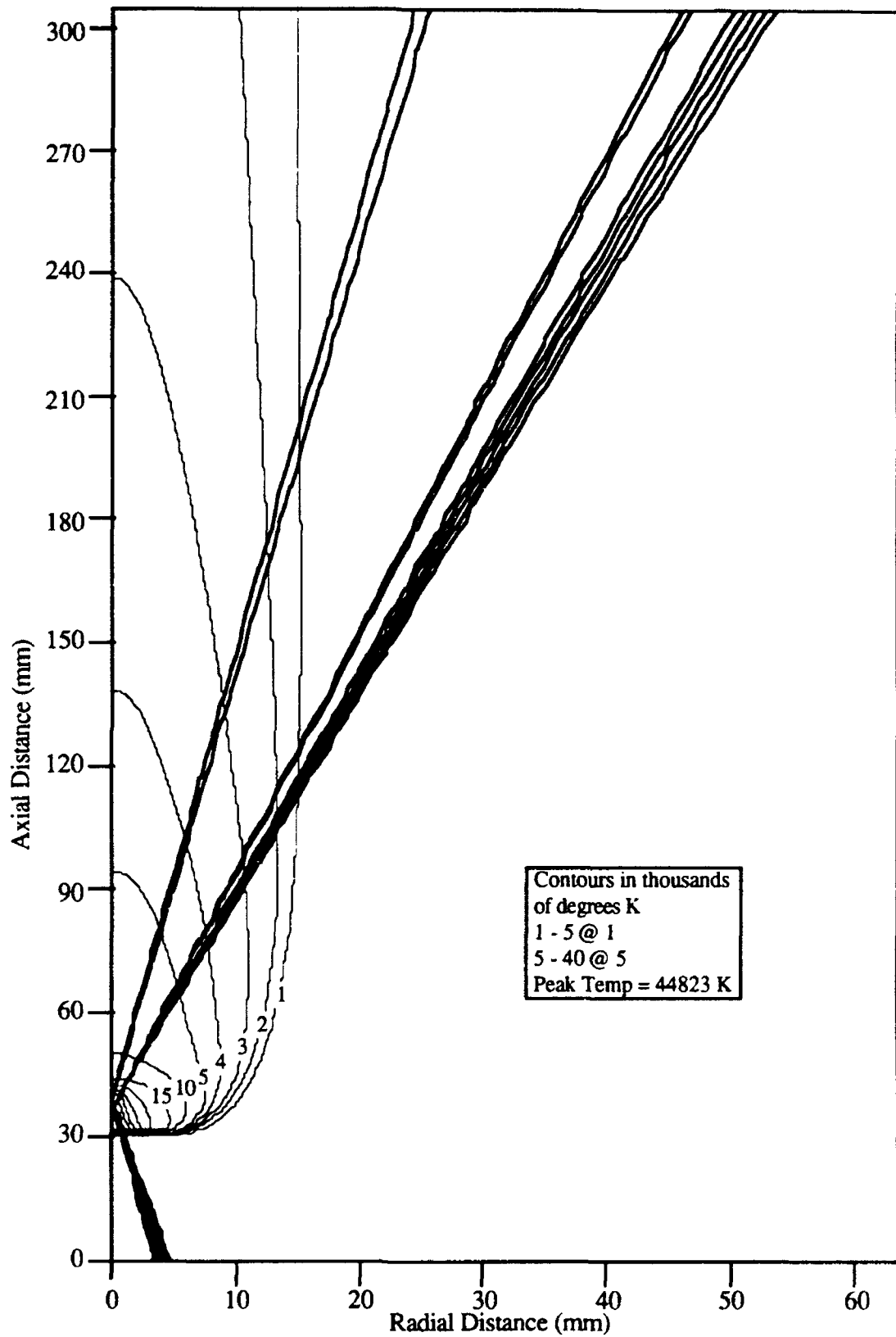
Figure 5.32   Heavy species temperature contours and beam raytrace for case tf32, which is a 70kW, 2192.9 moles/m^{2}s, 7 atm, f-4 hydrogen LSP.
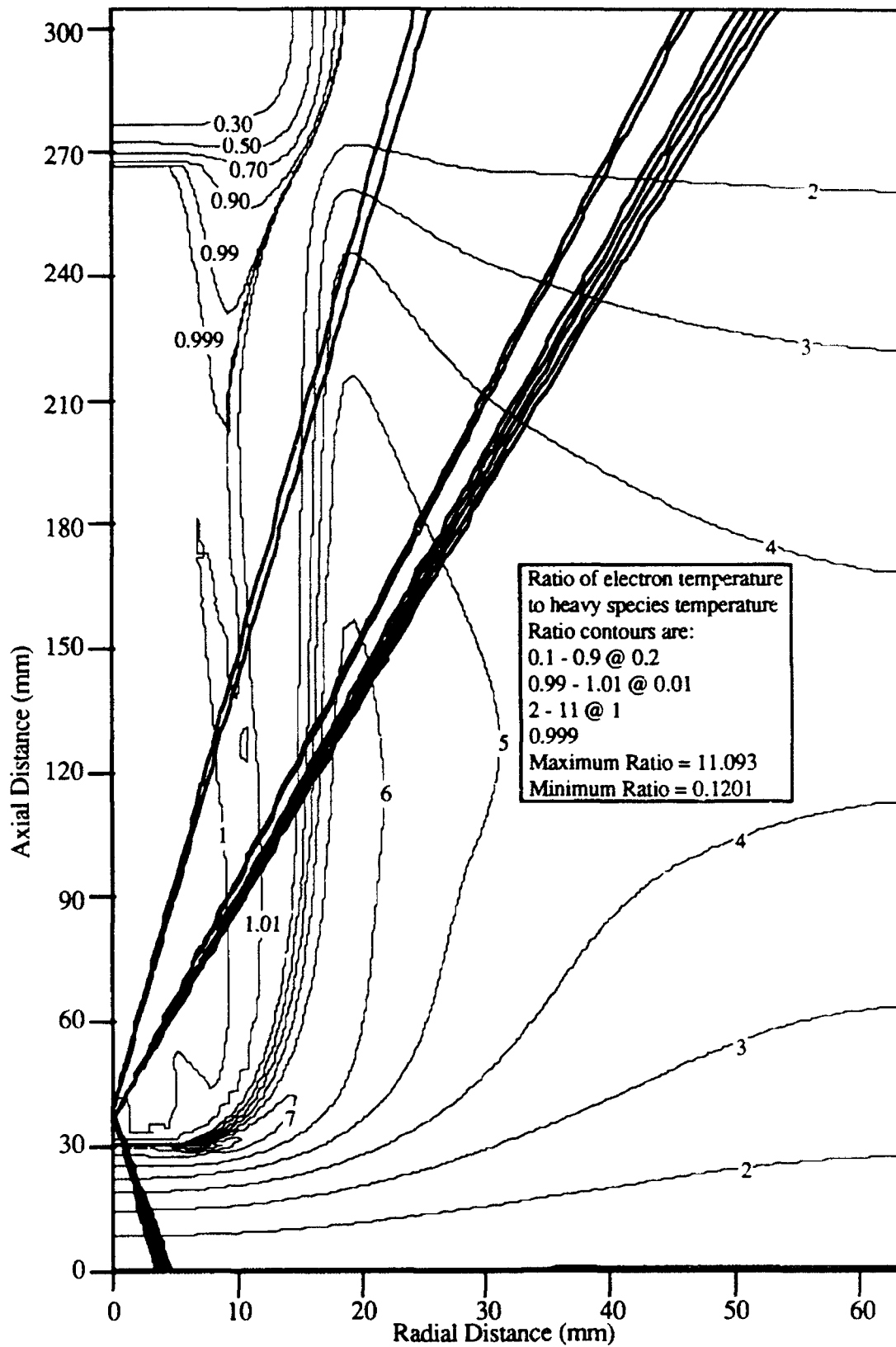
Figure 5.33   Contours of the ratio of electron temperature to heavy species temperature for case tf32, which is a 70kW, 2192.9 moles/m²s, 7 atm, f-4 hydrogen LSP.

Contours of the ratio of electron temperature to heavy species temperature for a 7 kW, 3.5 atm, 2192.9 moles/m^{2}s, f-4 case (f4) can be seen in the plot of Figure 5.34. The 3000 K electron temperature contour has been included in the plot as reference. Note that once again, there is a high degree of kinetic nonequilibrium just upstream and radially outward from the LSP front. Also note that in the LSP tail, beyond the 3000 K contour, the electron temperature drops below the heavy species temperature. However, for almost all of the region above 3000 K electron temperature, except for a small area at approximately x=32 mm, r=7mm, the value of the temperature ratio is very close to unity.

Even contours of the temperature ratio for case f5 (700 kW) are close to unity everywhere inside of the 3000 K electron temperature contour, except at the peak temperature location and in a small region near x=15 mm, r=10 mm. Contours of the ratio of electron temperature to heavy species temperature for case f5, as well as the 3000K electron temperature contour can be seen in the plot of Figure 5.35. Notice the 1.01 contour near the axis just downstream of the beam focus (actually the maximum core ratio is 1.023 for the ratio of peak temperatures). Again, kinetic nonequilibrium is evident for the same region just upstream and radially outward from the plasma front. However, kinetic nonequilibrium is not evident in the tail of this case, because the temperatures are still sufficiently high. It is very interesting to note that the region of maximum kinetic nonequilibrium appearing just upstream and radially outward from the plasma front spatially corresponds exactly to the experimentally determined region of maximum kinetic nonequilibrium identified by Zerkle (1992) for 7 kW argon LSPs.

The qualitative reason for the lack of significant kinetic nonequilibrium for temperatures above approximately 3000 K is that the number density of electrons for the cases tested was sufficient to maintain equilibrium through elastic collisions. Below approximately 3000 K, the electron number density has decreased past the point where elastic collisional transfer is sufficient to maintain equilibrium. Therefore in these regions, the electron temperature became uncoupled from the heavy species temperature.
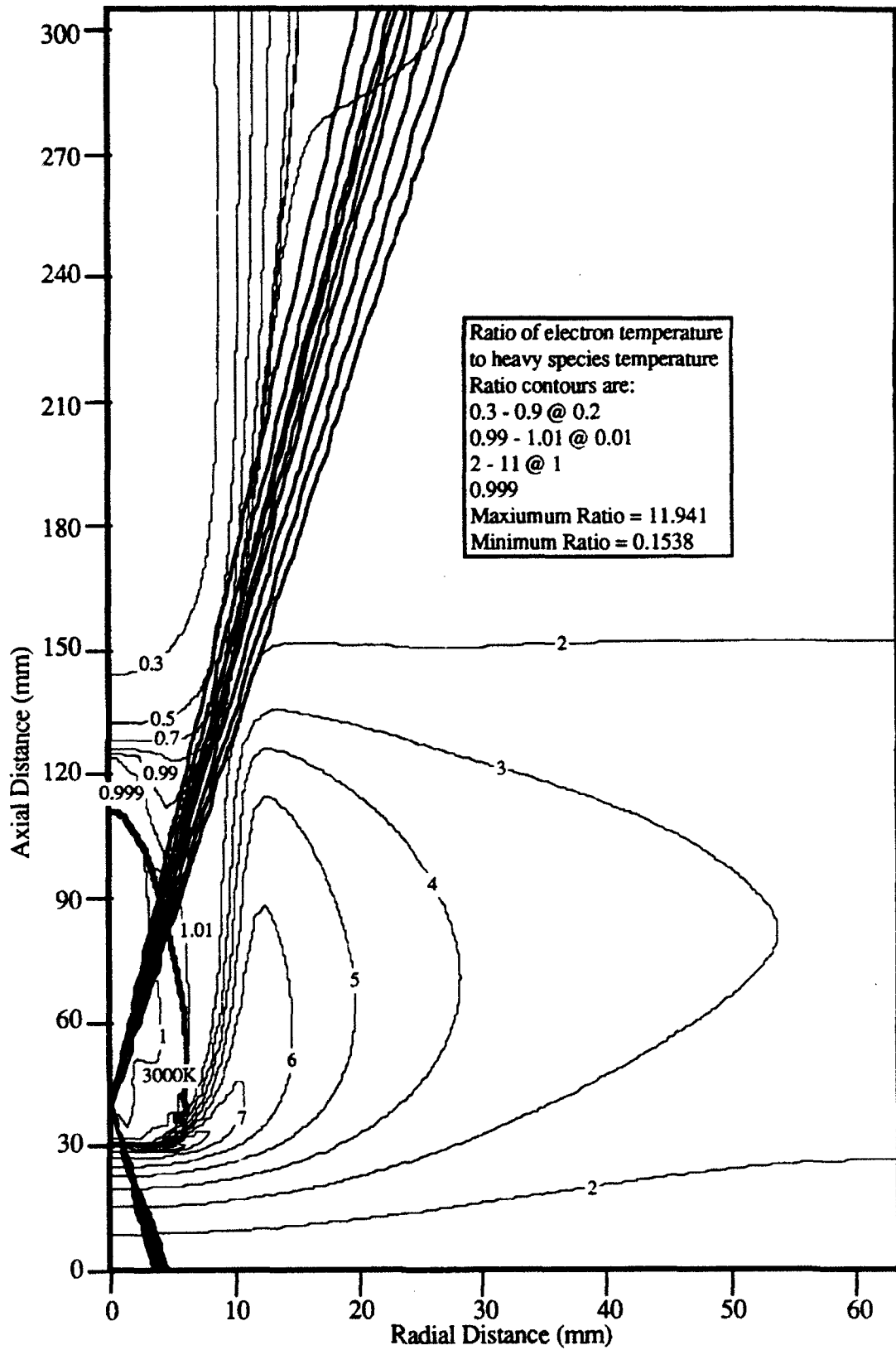
Figure 5.34   Contours of the ratio of electron temperature to heavy species temperature for case f4, which is a 7kW, 2192.9 moles/m²s, 3.5 atm, f-4 hydrogen LSP.
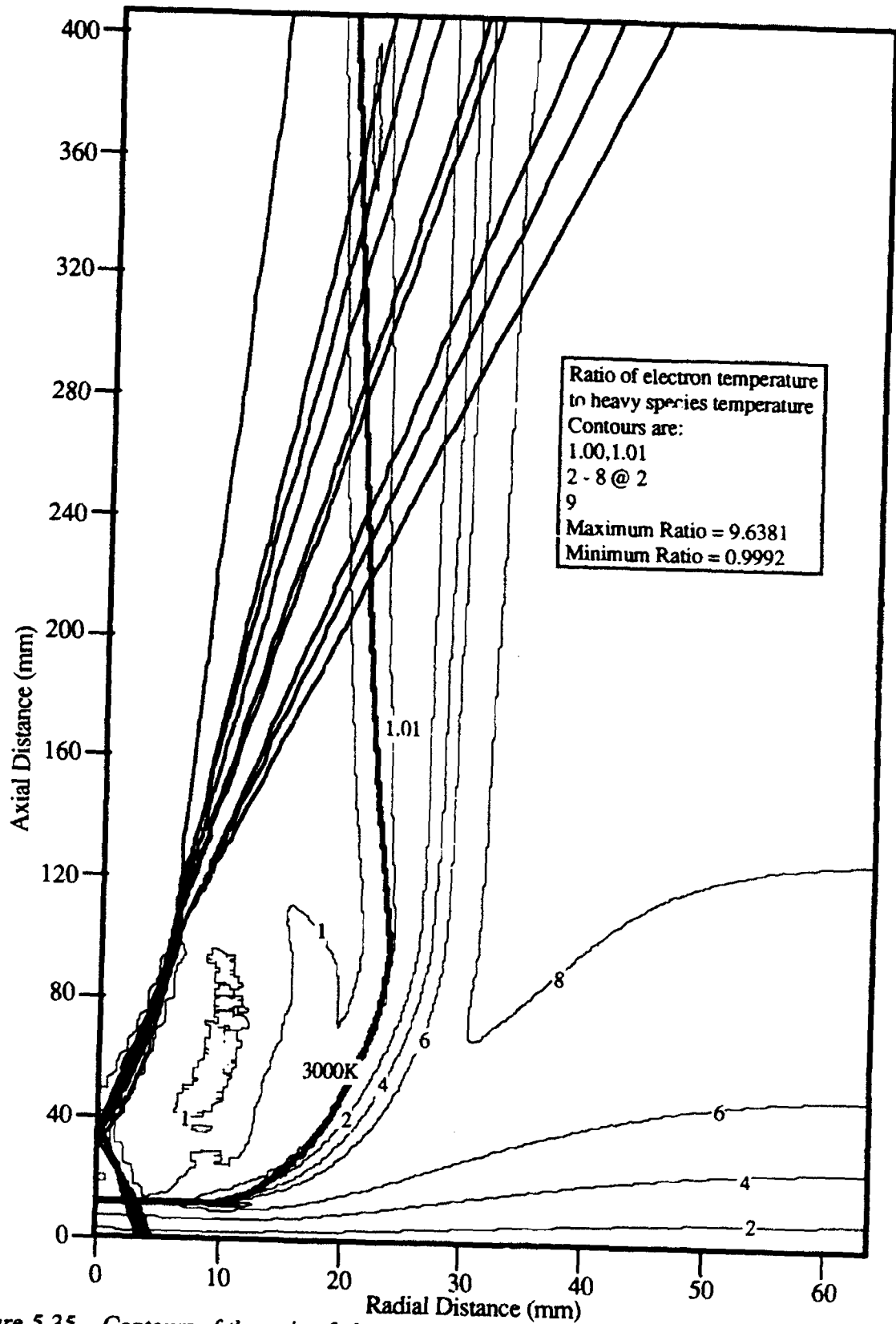
Figure 5.35   Contours of the ratio of electron temperature to heavy species temperature for case f5, which is a 700kW, 2192.9 moles/m²s, 3.5 atm, f-4 hydrogen LSP.

In the region slightly upstream and radially outward from the plasma front, the uncoupled electron energy equation resembles a conduction equation, because the convective flux of electrons is small. Since the electrons are uncoupled from the heavy species and there is essentially no convection of cold electrons from upstream, the electrons conduct heat outward toward the wall, which is assumed to be adiabatic, giving rise to kinetic nonequilibrium.

Once the electrons become uncoupled from the heavy species in the tail of the LSP, conduction to the region further downstream drives the electrons to cool to whatever the temperature happens to be at the exit plane, where the boundary condition is one of no axial derivatives.

There is one final item of note in the discussion of kinetic nonequilibrium. Careful evaluation of the ratio contours in Figures 5.33, 5.34, and 5.35 reveals that the contour representing kinetic equilibrium (ratio = 1) does not form a closed path with the axis of symmetry in any of the plots. This is because in the regions downstream of the LSP core, where the electrons are no longer absorbing the beam, the temperature ratio is just less than unity. The reason for this behavior is the simplified model assumption that only the electrons radiate. Therefore, the electrons in the core regions not in the path of the beam have an extra loss term, which causes the electron temperature to be very slightly lower.

An excellent example of this behavior can be seen in the plot of temperature ratio contours for case f5 appearing in Figure 5.35. Referring to the island of roughly drawn contours approximately 10 mm from the axis, in the core, it can easily be determined that values within the island contour are less than unity. It is not surprising then to note that the position of the island corresponds exactly to the region of maximum radiation loss which can be seen in the plot of radiation loss contours for case f5 in plotted Figure 5.12.

5.7 LSP Velocity Fields

The velocity fields of model LSPs exhibit similar qualitative features, regardless of the case conditions. The flowfields around the model LSPs are disturbed strongly in the vicinity of the plasma, near the core. The axial velocity upstream of the LSP typically slows to a few meters per second or less, and then is greatly accelerated upon reaching the plasma front. There is some radial

acceleration of the flow away from the axis but the dominant effect is axial acceleration downstream accompanied by a dramatic decrease in gas density due to the extreme core temperatures. The extent of the acceleration and the size of the accelerated region depend upon the temperature and spatial extent of the plasma core.

As indicated by the velocity vector plot for case f4 (7 kW, 2192.9 moles/m^{2}s, f-4, 3.5 atm) in Figure 5.36, much of the flow domain outside of the core region is essentially unaffected by the presence of the LSP. The vector plot indicates a tremendous acceleration axially accompanied by a diversion of the flow around the LSP. The diversion of flow around the LSP may be seen more clearly in the plot of mass flow contours of Figure 5.37. Note that the mass flow contours beyond 30 mm radius are essentially straight, indicating no diversion of the flow. In order to quantify the axial flow acceleration, radial cross sections of axial velocity for three axial locations have been plotted for case f4 in Figure 5.38. The axial velocity at the domain inlet is uniform based upon the mass flow rate. Note that the axial velocity at x=37.25 mm has a sharp peak at the axis of symmetry which becomes much less pronounced at the exit plane due to the effects of viscosity and the increased density of the cooler downstream gas.

A larger or hotter LSP core would be expected to have a greater effect on the LSP flowfield. As indicated by the radial cross sections of axial velocity for three axial locations plotted for case f5 in Figure 5.39, the magnitude of the axial acceleration by the LSP core was much greater for case f5 than for case f4. Note that the velocity peak on the axis of symmetry is much less pronounced at the exit plane than in the LSP core. The spatial extent of the flowfield acceleration is vividly demonstrated by the velocity vector plot for case f5 (700 kW, 2192.9 moles/m^{2}s, f-4, 3.5 atm) in Figure 5.40. Note that the larger region of acceleration for case f5 corresponds to the larger LSP core region as compared to case f4. In addition, the diversion of mass around the LSP can clearly be seen in the plot of mass flow contours for case f5 in Figure 5.41. This type of flow diversion in which the LSP acts as a semi-porous bluff body to the mass flow was also noted by Eguiguren (1989) in his LTE argon LSP model.
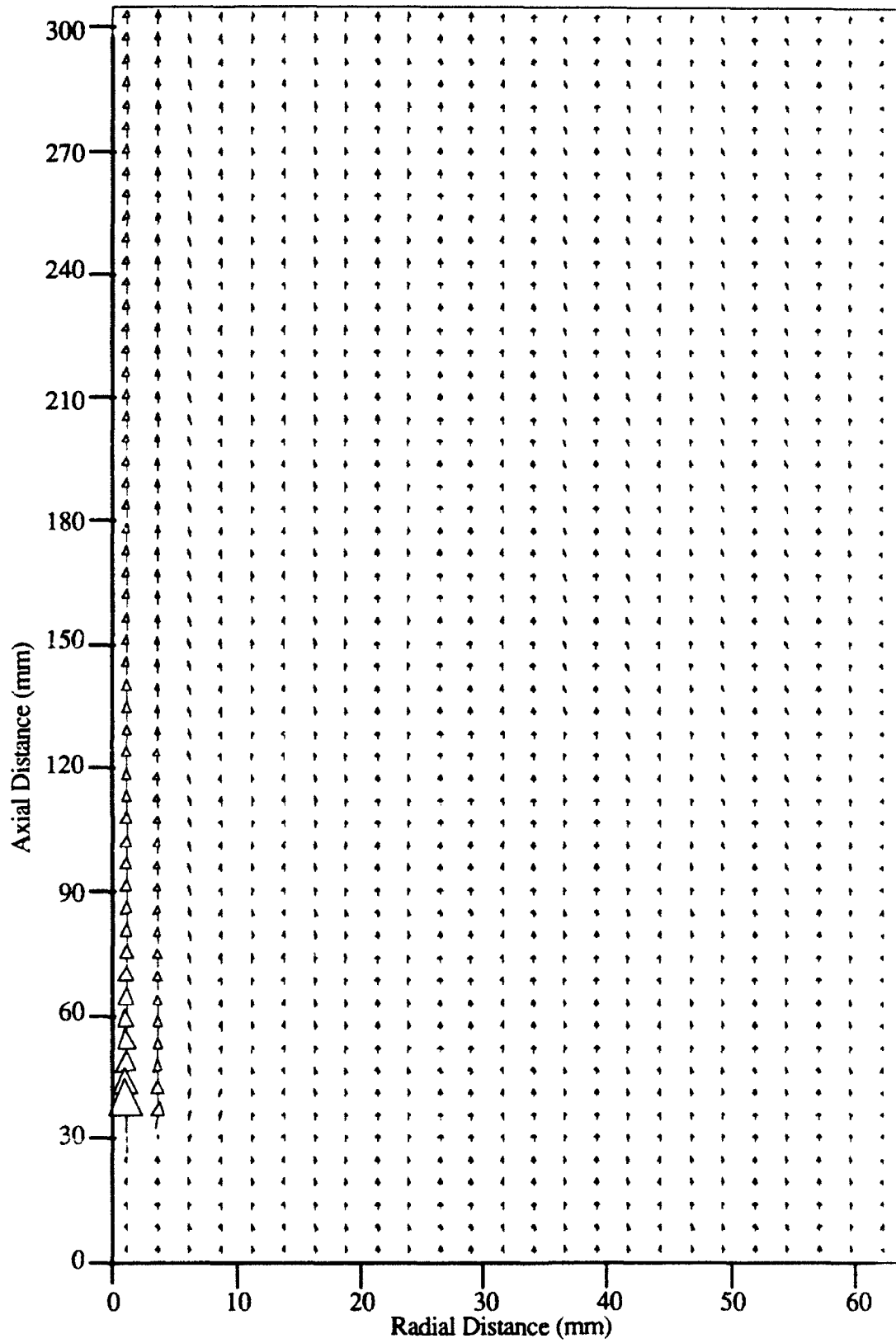
Figure 5.36   Vector plot of the velocity field of case f4.
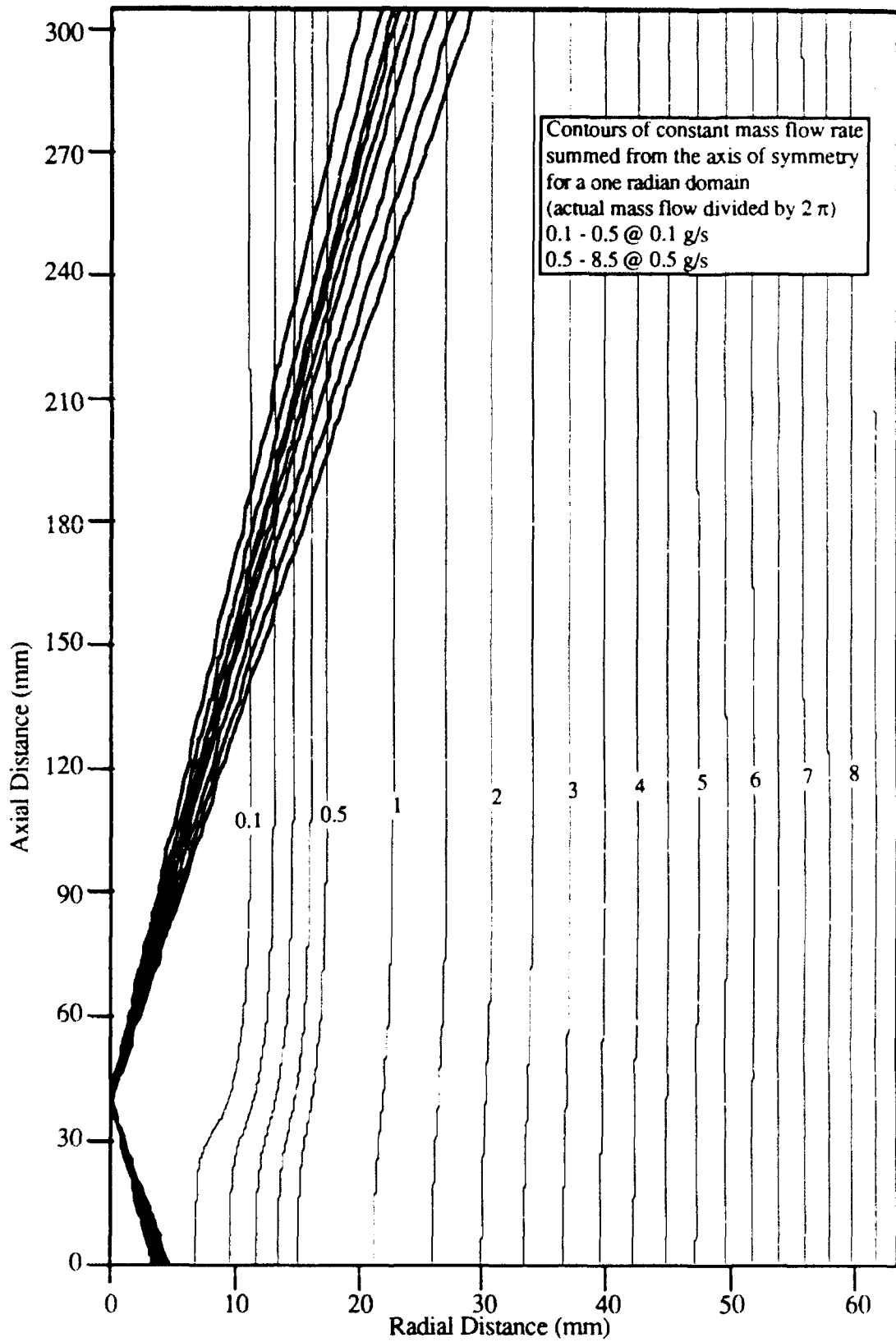
Figure 5.37   Contours of constant mass flow rate for case f4.
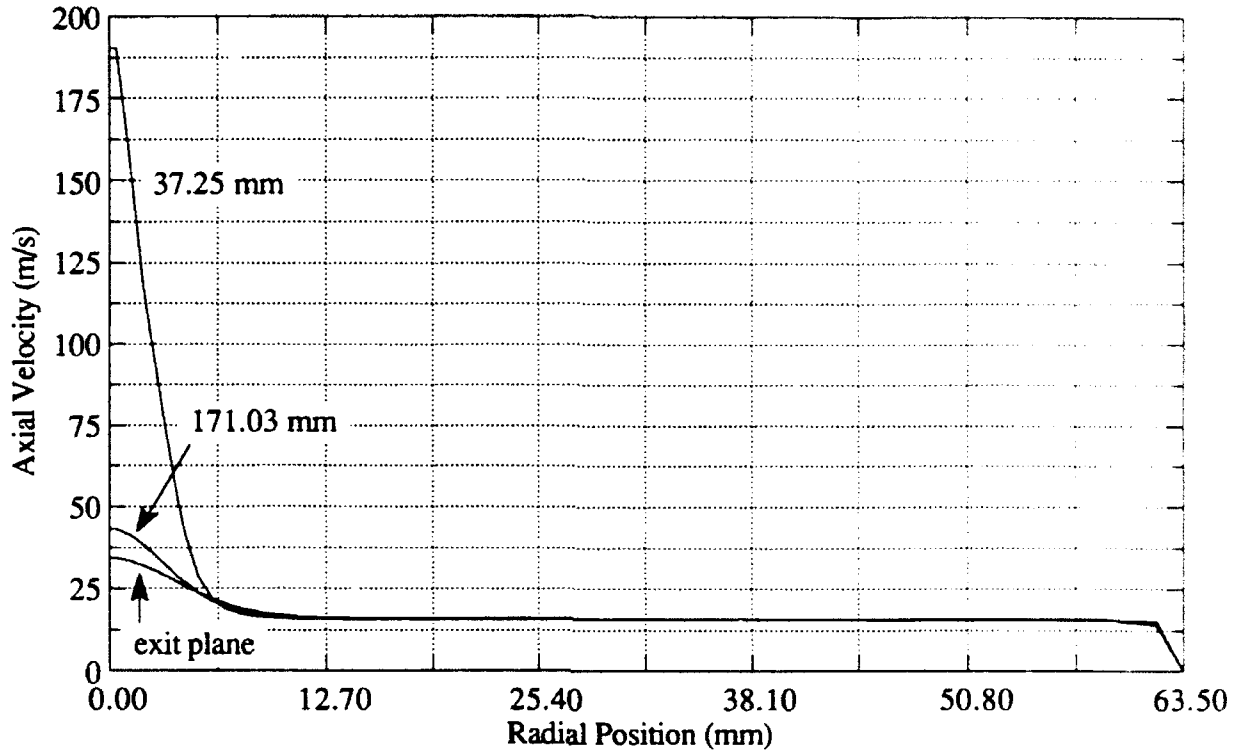
Figure 5.38   Radial cross sections of axial velocity for three axial locations of case f4.
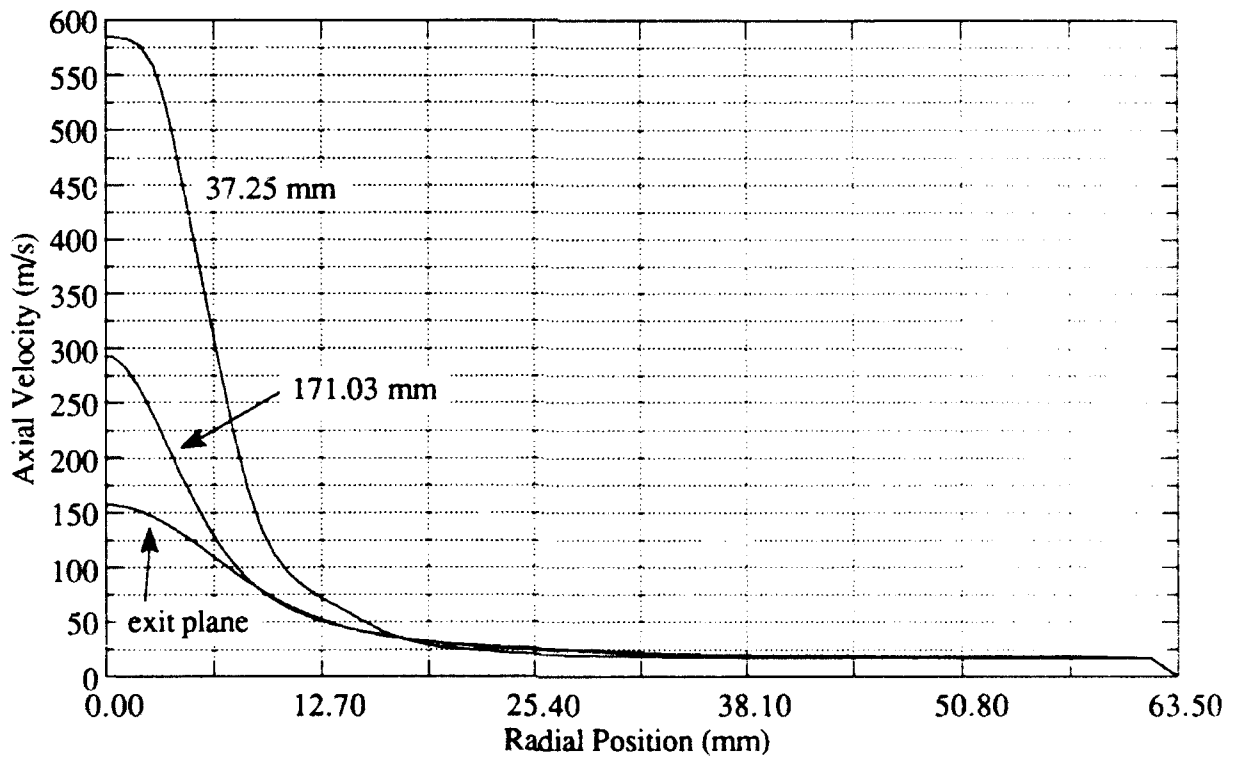
Figure 5.39   Radial cross sections of axial velocity for three axial locations of case f5.
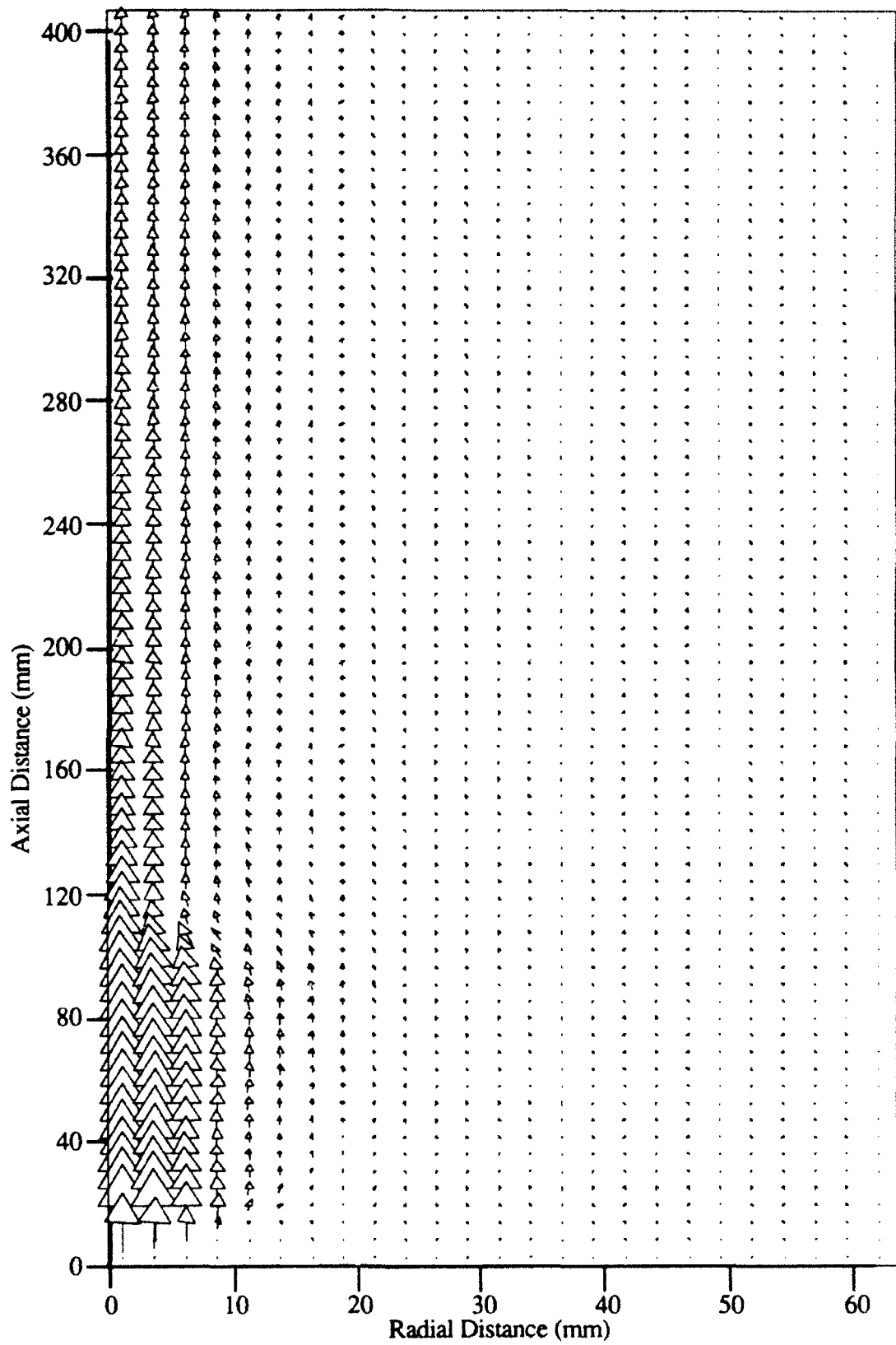
Figure 5.40   Vector plot of the velocity field of case f5.
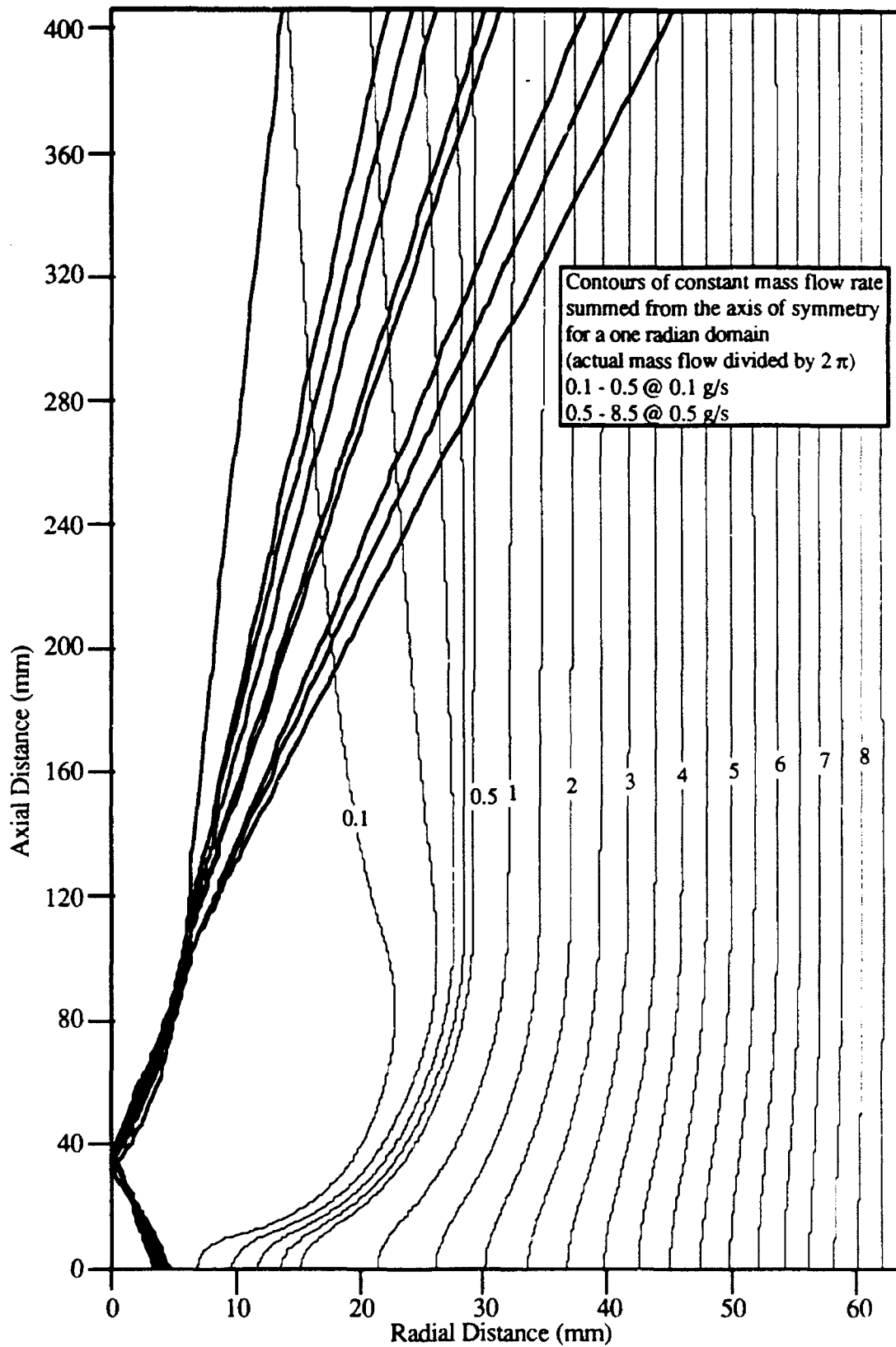
Figure 5.41 Contours of constant mass flow rate for case f5.

5.8 Model Conclusions

Based upon the model results, the conclusions may be summarized in four sections:

1) Model solutions are dependent upon initial conditions. Although not experimentally observed, this result should not be surprising, because finding multiple stable coexisting solutions is a generic situation in the system under investigation. For a set of equations representing such a strongly nonlinear process as in the simplified model, *multiple solutions are the norm, and not the exception.*

Lorenz (1963) showed that a model of convective flow could be cast as a system of three time dependent ordinary differential equations which had three steady state solutions. However, the solutions were unstable, meaning that any small perturbation would produce an unstable result. The unstable results were represented by the trajectory of the solution point following non-repeating paths in the solution phase space. These non-repeating trajectories were the result of the choice of initial conditions different from one of the three steady state solutions. Although the simplified LSP model solutions were demonstrated to be stable to small perturbations, it is not difficult to see that the dependence upon initial conditions was similar to that observed by Lorenz.

2) Model predictions for global absorption and thermal efficiency, despite being multivalued, followed experimental trends against variations in the control parameters well. In fact, the model data at 3.5 and 7 kW compared favorably with experimental data for similar conditions. Variations of model LSP size and shape versus variations of the control parameters also agreed well with experimental observations (photographic and visual).

The model prediction of blowout mole flux was high compared to the experimentally determined blowout mole flux at 3.5 kW, f-4.1, 3.5 atm. However, this may have been due to the idealized nature of the model with respect to beam symmetry and flow perturbations when compared with the actual experimental conditions as was previously described.

3) Refraction of the beam by the electrons in the plasma had a significant effect on plasma performance. The focusing effect on the incident beam resulted in so called ring foci off the axis of symmetry for some cases. The multiple solutions were the result of qualitatively different beam

focusing geometries which were caused by different amounts of beam refraction. The extent of the beam refraction was dependent upon the initial location of the LSP, which was dependent upon the initial conditions selected.

4) Kinetic nonequilibrium was not significant in the region of the plasma core, or in fact anywhere in which the electron and heavy species temperatures were coupled through elastic collisions. Therefore it may be confidently stated that the model LSPs tested in this work were collisionally dominated. In relatively cool outlying regions (below approximately 3000 K), there was significant kinetic nonequilibrium due to decoupling between the electrons and heavy species temperatures. However because the electron number density was so low in these regions, kinetic nonequilibrium had no effect on LSP performance as it would be expected to have if it existed significantly in the plasma core.

6. Recommendations

The simplified kinetic nonequilibrium model functions well despite its many assumptions, and has produced an abundance of data as described in Chapter 5. However, there are several improvements which could be made to the current model as well as recommendations for future testing which are described below.

1) A possibility for further testing of the model would be to more closely examine the nature of the multiple solutions. One method to test the multiple solutions could be to formulate the model to include an unsteady term. Different initial conditions could then be used to follow the development of the fields to the final steady state solutions. This would give better insight to the nature of the multiple solutions than the current model which only produces steady state solutions without a time evolution.

2) Several major improvements can be made to the simplified model to increase its accuracy and flexibility of use. First and foremost, the method by which the computational grid is computed can be greatly improved. Although the current use of non-uniform computational grids was sufficient to get a solution in most cases, it is awkward and definitely somewhat primitive. In order to allow far more flexibility in the selection of domains, a grid transformation should be made a standard part of the initialization sequence of subroutines. This grid transformation would allow any physical geometry to be applied to the problem as desired, with all the computations done on the transformed computational grid. The grid transformation should also have the built in capability of placing more nodes in the region of the plasma front and arbitrarily extending the exit plane downstream as far as necessary in the physical plane. This procedure is well known in the computational fluid dynamics field and should present no particular difficulty in implementation.

If the simplified model is to be used for test cases involving a nozzle, the current version of the SIMPLE methodology must be extended to a version which is applicable to compressible flow. An extension of SIMPLE called PISO (Pressure Implicit Split Operator) has been applied to the Navier-Stokes equations by Rhie (1986), and applied to the solution of an LTE LSP thruster model by Jeng and Keefer (1987a). Together with the grid transformation, the compressible version of

the simplified code could be used to model various nozzle geometries and evaluate laser thruster designs.

The computation of transport coefficients should be executed using the methodology explained in Appendix E, and as programmed in the generalized version of subroutine TRANSPORT. This would require that references be found for all the collision integrals appearing in Table E.3, and that the data for these collision integrals then be curve fit versus temperature for easy implementation into the code. As an initial step, the subroutine TRANSPORT could be altered to include only the major species, and then be used with the simplified model in its present form. This would eliminate the heuristic approximation for electron thermal conductivity as given in Chapter 4. It would also eliminate the curve fits of heavy species thermal conductivity and viscosity which have upper gas temperature limits of 60000 K, thereby making the model more flexible to operating parameters. Finally, using the methodology explained in Appendix E would allow the computation of both the multicomponent and thermal diffusion coefficients which are necessary for the inclusion of diffusion in the simplified model.

A final possible improvement of the simplified nonequilibrium model would be to include diffusive energy transfer without actually including diffusion terms in the energy equations. In this method, the diffusive energy transfer associated with the computed diffusion fluxes can be used to compute a correction to the local conductivity coefficient. The corrected conductivity coefficient would be computed based on the total net energy transfer and temperature gradient across the interface in question.

3) Although it has been demonstrated to work well, the simplified kinetic nonequilibrium model is a step backwards in complexity from the generalized non-LTE model. Restoration of the model to its original form would necessitate once again using the species conservation equations and no longer assuming chemical equilibrium. Additionally, the inelastic energy transfer terms in the energy equations would also need to be computed, as would the diffusive number and energy fluxes. In this reconstruction, it would be wise to start with a simple set of C-R reactions,

possibly involving only the major species. The reactions from Janev, et al. (1987) may have to be reevaluated before being applied.

4) A possible application of either the simplified kinetic nonequilibrium model or the restored fully generalized model would be to a model of an arcjet. With the methods described in point 2 above for grid generation and application to compressible flow, and with the addition of the appropriate electromagnetic equations, a functional kinetic nonequilibrium arcjet model could be formulated.

Appendix A. Hydrogen Safety System

Prior to conducting experiments using hydrogen, a failsafe hydrogen handling and safety system had to be designed and constructed. This system had to be capable of delivering hydrogen to the test stand while controlling the chamber pressure. Due to the explosive nature of hydrogen-air mixtures, special precautions were taken to insure that any leaks in the system would immediately cause a system shutdown. A diagram of the hydrogen handling and safety system can be seen in Figure A.1.
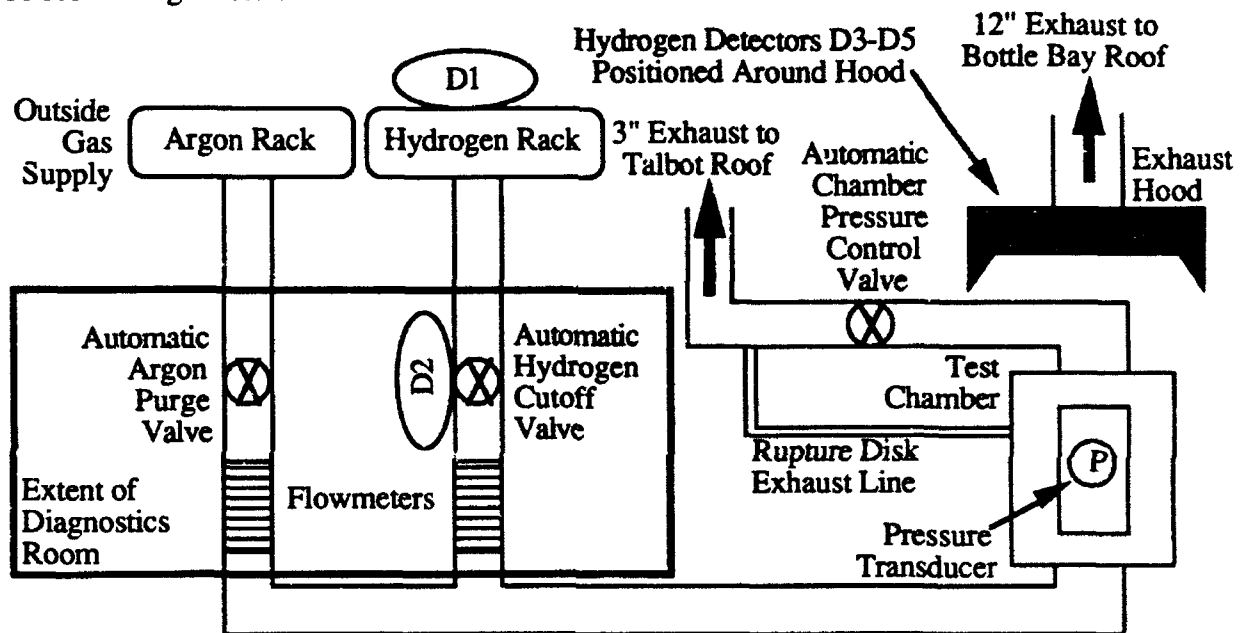
Figure A.1   Diagram of the hydrogen handling and safety system

When argon was used exclusively in the past, the chamber exhaust of hot argon was simply allowed to escape into the room. This posed no danger since argon is neither toxic nor explosive. Two additions to the laser laboratory had to be made to accommodate the hydrogen exhaust gas. The first of these was a 3" stainless steel exhaust pipe which ran outside the building to just above the Talbot Lab room 5A bottle bay roof, which was about 12' off the ground. At that point, to save cost, the stainless steel pipe ended and was mated to a painted PVC tube which was then run up the side of Talbot laboratory to above the roof line where the hydrogen was finally exhausted. The top of the tube had a butterfly attachment which would remain closed in the absence of flow to keep rain and other debris from entering the pipe. At the bottom of the long vertical exhaust pipe

was a drain to clean out the pipe since water was bound to get in. The second addition was a large (8' by 6'6") hood which was built on trolleys so that it could be positioned over the chamber during experiments and then rolled out of the way when the chamber was lifted for modification or repair. The hood was attached to a 12" circular duct which ran out of the building to the bottle bay roof where it was attached to a suction fan. Since the manifold between the chamber and the exhaust pipe was made of myriads of pieces of pipe screwed together and sealed with teflon tape, there were bound to be leaks. These leaks were practically impossible to completely eliminate, although they appeared to be minor when checked with Snoop leak detector (a commercial mix of soapy water which bubbles in the presence of a leak). The purpose of the hood positioned directly above the chamber was to capture any hydrogen which might either leak out or flow out due to catastrophic chamber damage such as a broken window or blown seal.

In addition to the exhaust system, a new experiment control system was designed. The center of this system was a control box designed by Justin Koch, and into which all the system trip inputs were connected. Five Macurco GD-1 hydrogen detectors positioned strategically above possible leak points were the first type of system trip. The detectors were sensitive to hydrogen at 1% of the lower explosive limit and could be tested with an ordinary butane lighter (since they were also sensitive to butane). Essentially each detector was no more than a switch which closed when hydrogen was detected and which opened when the hydrogen dispersed.

The first detector was mounted outside the laboratory in the bottle bay high on a wall near the hydrogen supply bottles. A sheltered hole had been cut in the ceiling just above the bottles to allow leaking hydrogen to escape the bottle bay. In addition a new rack had been built to hold up to six cylinders of hydrogen. This new bottle rack was necessary because hydrogen supply bottles have left handed threads for safety purposes and were therefore incompatible with the existing bottle rack which was used for argon supply bottles.

The second detector was mounted directly above the flowmeter in the diagnostics room within the laboratory. The other three detectors were mounted on the laboratory ceiling around the perimeter of the hood in the experiment position.

The second type of system trip was chamber over pressurization. Chamber pressure was controlled by an Eclipse Model 560 Digital Setpoint Controller with a pressure alarm setpoint. A Valtek Mark 1 valve was installed between the chamber exhaust manifold and the exhaust pipe. This valve was wired to the 560 as was the output of the chamber pressure transducer. When used in automatic mode, the 560 did a fair job of holding the chamber pressure near the desired setpoint if the mole flux was high enough, although in many cases there were unsatisfactory oscillations. Therefore for nearly all the cases, the standard procedure was to use the 560 on manual mode. The pressure control also seemed to function better when argon was used, possibly because there were less leaks with argon than hydrogen. Unfortunately, either due to the manifold leaks or an inability of the Mark 1 valve to close completely, there was a regime of low mass flow rates for which chamber pressure could not be held at the desired setpoint. Even with the pressure controller at maximum output (meaning the Mark 1 valve was as closed as possible) a minimum mass flow was required to hold the chamber pressure at a desired level. The minimum required mass flows (and mole fluxes based on the 48 mm id quartz tube) for three chamber pressures are listed in Table A.1.

Table A.1 Minimum Required Flow Rates to Hold Chamber Pressure

Chamber Pressure	Minimum Mass Flow (g/s)	Corresponding Mole Flux (gmoles/m^{2}s)
22.1	1.89	518.1
23.1	1.97	540.0
24.1	2.04	559.2

This inability to operate in low mole flux and high pressure regimes put a lower mole flux limit on which experiments could be performed. However the limit to possible operating conditions was not considered to be a problem since the optimal mole flux for a given set of operating conditions was expected to occur close to the blowout mole flux which is on the high end of the mole flux range.

The third type of system trip was a manual emergency shutdown. If the experimenter wished to trip the system for any reason, there was a large red system kill button on the front of the control

console. The fourth type of system trip was a laser kill trip. The laboratory had been wired such that opening any door while the laser was operating would immediately switch off the laser.

Regardless of the type of system trip, several actions occurred to safely shut down the system. The laser was shut down and the hydrogen supply valve (just upstream of the flowmeter) was closed via an automatic valve. The back pressure valve was automatically switched to the low pressure setpoint (1 atm) and an argon purge valve was automatically opened to flush the chamber with argon. Meanwhile a very annoying high pitched horn on the front of the control console sounded. This horn could be turned off for a short period of time to save the experimenter's ears and sanity, but it would come back on if the system has not been reset before the time was up. Nothing could be turned back on until the system reset button was pressed. This feature was required due to the nature of the hydrogen detectors which would keep the system shut down only as long as stray hydrogen was detected.

To allow the experimenter to quickly determine what caused the system trip, the front of the control console was constructed with indicator lights showing the status of the detectors as well as the pressure alarm and the overall system condition.

In addition to the active control system just described, there were some passive failsafe features. A burst plate rated 65 psig at 250 degrees Fahrenheit was installed on the absorption chamber. This burst plate would cover the unlikely case that the setpoint controller alarm did not function for whatever reason, therefore saving the chamber optics from a potentially dangerous chamber explosion. A copper tube connected the downstream side of the burst plate to the stainless steel exhaust pipe downstream of the back pressure control valve. In the event of a power failure (as has happened in Talbot Laboratory in the past), the system would shut down. All the automatic valves were set up such that the power off condition was the same as during a system trip. Also, if the supply of nitrogen that was used to actuate the valves ran low, the effect was the same as the power off situation.

In order to minimize the possibility of human error, a standard operating procedure was created. This procedure was posted in the diagnostics room and has been listed below.

Procedures for Operation of UIUC Laser Plasma Facility Using Hydrogen

Procedures for System Setup

_____(1) Turn on hood fan. (Yellow light will come on.)
_____(2) Visually check detector power (green lights should always be on).
_____(3) Check/Change 560 pressure setpoints and high pressure alarm setpoint.
_____(4) Open hydrogen and argon supply bottles, and check N_2 supply pressure.
_____(5) Turn on calorimeter power.
_____(6) Turn on calorimeter water - set to 5 liters per minute.
_____(7) Install chamber optics - turn on optics cooling water.
_____(8) Switch on solenoid #3 in control room.
_____(9) Make sure mirror water is on.
_____(10) Make sure lens translation system is operational at proper ΔZ
_____(11) Check target insertion/alignment.
_____(12) Setup Mac/Fluke 2240A combination for data collection.
_____(13) Turn off (unplug) electrostatic air cleaners.
_____(14) Turn on Valtek control pressure (green handled valve-should be ~90 psig)

Run Procedures (MIXTURES)

_____(1) Switch on argon purge/initiation flow (set at a preset value).
_____(2) Ignite in argon (fire laser).
_____(3) Add desired amount of hydrogen to the flow.
_____(4) Pressurize chamber (switch from low to high pressure).
_____(5) Lower plasma into tube if desired.
_____(6) Collect data.
_____(7) Shut off laser.
_____(8) Depressurize chamber (switch back from high pressure to low).
_____(9) Turn off hydrogen flow.
_____(10) Allow system to purge with argon for 15 seconds.
_____(11) Switch off argon purge.
_____(12) Raise lens to initiation position (if it was lowered).
_____(13) Turn off Valtek control pressure.

Run Procedures (PURE HYDROGEN)

_____(1) Switch on argon purge/initiation flow (set at a preset value) for 15 seconds.
_____(2) Add desired amount of hydrogen to the flow.
_____(3) Switch off argon purge.
_____(4) Pressurize chamber (switch from low to high pressure).
_____(5) Ignite in hydrogen (fire laser).
_____(6) Lower plasma into tube if desired.
_____(7) Collect data.
_____(8) Shut off laser.
_____(9) Depressurize chamber (switch back from high pressure to low).
_____(10) Switch on argon purge.
_____(11) Turn off hydrogen flow.
_____(12) Allow system to purge with argon for 15 seconds.
_____(13) Raise lens to initiation position (if it was lowered).
_____(14) Turn off Valtek control pressure.

Between Runs Procedures

_____(1) Check detectors visually for power on.
_____(2) Reset 560 setpoints if necessary.

_____(3) Check chamber optics.
_____(4) Check lens position.
_____(5) Reset Mac for new data (Rename new data file).
_____(6) When ready to run, turn on Valtek supply pressure.

Emergency Procedures
_____(1) Determine cause of system shutdown by referring to control panel indicator lights.
_____(2) Take appropriate action to rectify the emergency.
_____(3) After the emergency has passed or been dealt with, reset the system.

Appendix B. Experimental Data Error Analysis

Measurements of global absorption and thermal efficiency have little meaning without some estimate of the associated errors. Thermocouple temperatures and the measured transmitted power were recorded each second during each experimental run. As part of the data reduction process, all data was averaged over eight scans to reduce random fluctuations and improve the associated error. The total estimated error of any computed quantity is a function of the estimated errors of each measured component within the computation. For instance, suppose the computed quantity can be expressed as:

$$F = F(a_1, a_2, a_3, ..., a_n) \tag{B.1}$$

where the a's represent measured quantities that make up the computation. If the uncertainty of each measured quantity is represented by Wa_i, then the uncertainty in the computed quantity is given by the formula (Holman, 1984, p50):

$$WF = \sqrt{\sum_i \left(\frac{\partial F}{\partial a_i} Wa_i\right)^2} \tag{B.2}$$

The total error of both the global absorption and the thermal efficiency may now be computed as follows. The expression for global absorption was given in Chapter 2 as:

$$\alpha = 1.0 - \frac{P_{measured}}{P_{input}} \tag{B.3}$$

where P_{input} represents the input laser power based on the laser calibration, and $P_{measured}$ represents the measured transmitted power based upon the calorimeter calibration. Application of equation (B.2) to equation (B.3) results in:

$$W\alpha = \sqrt{\left(\left(\frac{P_{measured}}{P_{input}^2}\right)(WP_{input})\right)^2 + \left(-\left(\frac{1}{P_{input}}\right)(WP_{measured})\right)^2} \tag{B.4}$$

where WP_{input} represents the uncertainty inherent in the laser input power, and $WP_{measured}$ represents the uncertainty inherent in the measured transmitted power. These uncertainties may be written as an estimated error times some nominal value.

The laser calibration has been shown to have an error of no more than ± 3% (Mertogul, 1989). The error in the measured transmitted power includes the laser power calibration (±3.0%) and the calorimeter water flow (±4.0%) (Mertogul, 1989). Other errors include the effect of heated gas

entering the calorimeter cone, plasma irradiation incident upon the calorimeter cone, and laser scattering by the plasma. Heated gas entering the cone had been estimated to contribute no more than ±3% error to the measured transmitted power using argon as the propellant (Zerkle, 1988). Due to the nature of this error, it was not truly random but would tend to bias the data toward lower global absorption values. This estimated ±3% error was based upon the results of argon experiments, and the exhaust temperatures of those experiments were generally higher than for hydrogen experiments. Although it may be somewhat conservative, this error estimate was retained for hydrogen results.

The error due to laser scattering and plasma irradiation of the copper cone were previously considered to be negligible (Mertogul, 1989). Scattering was considered negligible because the plasma composition necessary to reflect 10.6 micron laser radiation was not expected to be present in any of our experimental plasmas (Mertogul, Zerkle, and Krier, 1992). Plasma irradiation, like heated gas error would tend to bias the computed global absorption to be low. It is difficult to quantify the error associated with plasma irradiation, however it has been assumed to be negligible.

Assuming that these errors are equally weighted (not a bad assumption), the error associated with each transmitted power measurement is the sum of the squares of these errors which is 5.8%. However, eight such measurements (one per second) were averaged to produce a data value. The relation representing this average is simply:

$$P_{measured} = \left(\frac{P1 + P2 + P3 + ...+ P8}{8} \right) \tag{B.5}$$

Assuming each individual power measurement may be represented by $P_{nominal}$, the application of equation (B.2) to (B.5) to compute $WP_{measured}$ yields:

$$WP_{measured} = \left(\sqrt{\frac{1}{8}} \right)(0.058)(P_{nominal}) \tag{B.6}$$

Therefore WP_{input} is equal to (0.03)(Nominal Input Power), and $WP_{measured}$ is equal to (0.021)(Nominal Measured Transmitted Power). When the nominal input power is 7.00 kW, and the nominal measured transmitted power is approximately 2 kW, these uncertainties inserted into equation (B.4) yield:

$$W\alpha = \sqrt{\left(\left(\frac{2.0}{7.0^2}\right)(0.03*7.0)\right)^2 + \left(-\left(\frac{1}{7.0}\right)(0.021*2.0)\right)^2} \tag{B.7}$$

which yields a global absorption uncertainty of 0.010. Since the nominal values for input and measured transmitted power yield a nominal global absorption of 0.714, the computed global absorption uncertainty represents an absolute error of $\pm 1.40\%$. It should be noted that as the value of the measured transmitted power becomes smaller, the global absorption absolute error also gets smaller. Based upon equation (B.4), a nominal measured transmitted power of 3.0 kW ($\alpha = 0.571$) yields an absolute global absorption error of 2.80%, and a transmitted power of 1.0 kW ($\alpha = 0.857$) yields an error of 0.58%. Since a large fraction of the experimental results yielded global absorption near or greater than 0.8 (which yields an absolute error of 0.92%), the absolute error in global absorption has been reported to be $\pm 1\%$ (Mertogul, Zerkle, and Krier, 1992, and Mertogul, et al., 1990). The absolute error associated with all pure hydrogen global absorption data in this work appears with the values for global absorption listed in Appendix C. Based on these listed values, a representative error for global absorption is $\pm 2\%$ absolute.

The expression for thermal efficiency was given in Chapter 2 as:

$$\eta = \frac{\dot{m}\, C_p\, \Delta T}{P_{input}} \tag{B.8}$$

where $\dot{m}$ represents the mass flow rate, C_p represents the gas specific heat at constant pressure (a value of 14490 J/kg K was used), ΔT represents the stagnation temperature increase ($T_{exhaust} - T_{inlet}$), and P_{input} represents the laser input power. Application of equation (B.2) to equation (B.8) yields:

$$W\eta = \sqrt{\left(\frac{\partial \eta}{\partial \dot{m}}(W\dot{m})\right)^2 + \left(\frac{\partial \eta}{\partial T_e}(WT_e)\right)^2 + \left(\frac{\partial \eta}{\partial T_i}(WT_i)\right)^2 + \left(\frac{\partial \eta}{\partial P_i}(WP_i)\right)^2} \tag{B.9a}$$

where:

$$\frac{\partial \eta}{\partial \dot{m}} = \frac{C_p(T_e - T_i)}{P_{input}} \tag{B.9b}$$

$$\frac{\partial \eta}{T_e} = \frac{\dot{m}C_p}{P_{input}} \tag{B.9c}$$

$$\frac{\partial \eta}{\partial T_i} = \frac{-\dot{m}C_p}{P_{input}} \tag{B.9d}$$

$$\frac{\partial \eta}{\partial P_i} = \frac{-\dot{m}C_p(T_e - T_i)}{P_{input}^2} \tag{B.9e}$$

and once again, the variables represent their nominal values and variables preceded by a W represent their uncertainty in units of the variable. These uncertainties may be expressed as an estimated percent error times the nominal value of the variable.

Errors associated with the thermal efficiency are due to the mass flow rate (±3%), the laser power (±3%), and the thermocouples (±1% for each). In order to compute the uncertainty of the exhaust stagnation temperature, $WT_{exhaust}$, it must be recalled that there are four exhaust thermocouples, and that the average of 8 measurements was used. Therefore the exhaust temperature may be expressed as:

$$T_{exhaust} = \frac{T_{e11}+T_{e12}+T_{e13}+T_{e14}+T_{e21}+T_{e22}+T_{e23}+T_{e24}+...+T_{e81}+T_{e82}+T_{e83}+T_{e84}}{32} \qquad (B.10)$$

Assuming each individual temperature measurement may be represented by T_e (some nominal value), the application of equation (B.2) to equation (B.10) to compute $WT_{exhaust}$ yields:

$$WT_{exhaust} = \left(\sqrt{\frac{1}{32}}\right)(0.01)(T_e) \qquad (B.11)$$

Since there was only a single inlet thermocouple, the same analysis applied to WT_{inlet} yields:

$$WT_{inlet} = \left(\sqrt{\frac{1}{8}}\right)(0.01)(T_i) \qquad (B.12)$$

Therefore, $WT_{exhaust}$ is equal to (0.0018)(nominal measured exhaust gas temperature), and WT_{inlet} is equal to (0.0035)(nominal measured inlet gas temperature). The absolute error in the computation of thermal efficiency may now be computed based upon the nominal values of the variables. The absolute error associated with all pure hydrogen thermal efficiency data in this work appears with the values for thermal efficiency listed in Appendix C. Based on these listed values, a representative error is ±6% absolute.

The error analysis for experiments involving mixtures of argon and hydrogen is slightly more complicated than that for pure mixtures. The complication enters in the extra uncertainty in the constant pressure specific heat for the mixture, C_{pmix}, and the revised uncertainty in the mass flow rate, $\dot{m}$. Since the computation of global absorption does not involve C_p or $\dot{m}$, the error analysis for global absorption of a mixture does not differ from that of a pure gas, and is given by equations

(B.4) through (B.6). However, the computation of thermal efficiency for a mixture is computed from the expression:

$$\eta = \frac{\dot{m}\, C_{pmix}\, \Delta T}{P_{input}} \qquad (B.13)$$

where
$$C_{pmix} = (C_{pH_2})(Y_{H_2}) + (C_{pAr})(Y_{Ar}) \qquad (B.14)$$

in which
$$Y_{H_2} = \frac{\dot{m}_{H_2}}{\dot{m}_{H_2} + \dot{m}_{Ar}} \qquad (B.15)$$

and
$$Y_{Ar} = \frac{\dot{m}_{Ar}}{\dot{m}_{H_2} + \dot{m}_{Ar}} \qquad (B.16)$$

In addition, the mass flow rate is now the sum of the argon and hydrogen mass flow rates as given in equation (B.17).

$$\dot{m} = \dot{m}_{H_2} + \dot{m}_{Ar} \qquad (B.17)$$

With the inclusion of equations (B.14) through (B.17), equation (B.2) (the general uncertainty formula) applied to equation (B.13) yields:

$$W\eta = \sqrt{\left(\frac{\partial\eta}{\partial\dot{m}}(W\dot{m})\right)^2 + \left(\frac{\partial\eta}{\partial T_e}(WT_e)\right)^2 + \left(\frac{\partial\eta}{\partial T_i}(WT_i)\right)^2 + \left(\frac{\partial\eta}{\partial P_i}(WP_i)\right)^2 + \left(\frac{\partial\eta}{\partial C_{pmix}}(WC_{pmix})\right)^2} \qquad (B.18)$$

where equations (B.9b) through (B.9e) are still valid, and:

$$W\dot{m} = \sqrt{(W\dot{m}_{Ar})^2 + \left(W\dot{m}_{H_2}\right)^2} \qquad (B.19)$$

$$\frac{\partial\eta}{\partial C_{pmix}} = \frac{\dot{m}(T_e - T_i)}{P_{input}} \qquad (B.20)$$

Application of equation (B.2) to equation (B.14) yields an expression for WC_{pmix}:

$$WC_{pmix} = \sqrt{(C_{pH_2})^2(WY_{H_2})^2 + (C_{pAr})^2(WY_{Ar})^2} \qquad (B.21)$$

and further application of equation (B.2) to equations (B.15) and (B.16) yields:

$$WY_{H_2} = \sqrt{\left(\frac{\dot{m}_{Ar}}{(\dot{m}_{Ar} + \dot{m}_{H_2})^2}\right)^2 (W\dot{m}_{H_2})^2 + \left(\frac{-\dot{m}_{H_2}}{(\dot{m}_{Ar} + \dot{m}_{H_2})^2}\right)^2 (W\dot{m}_{Ar})^2} \qquad (B.22)$$

and,
$$WY_{Ar} = \sqrt{\left(\frac{\dot{m}_{H_2}}{(\dot{m}_{Ar} + \dot{m}_{H_2})^2}\right)^2 (W\dot{m}_{Ar})^2 + \left(\frac{-\dot{m}_{Ar}}{(\dot{m}_{Ar} + \dot{m}_{H_2})^2}\right)^2 (W\dot{m}_{H_2})^2} \qquad (B.23)$$

Finally, substitution of equations (B.22) and (B.23) (which are actually identical) into equation (B.21), followed by substitution of equations (B.19) through (B.21) into equation (B.18) yields a

final expression for the uncertainty of the gas mixture thermal efficiency computation. Substitution of nominal values for all the variables and the assumption that the estimated error of the hydrogen and argon mass flows are both ±3% yields the uncertainties and absolute errors listed with the reduced data in Appendix C.

Appendix C. Reduced Data Listing

The error analysis of Appendix B was applied to all the data acquired, including both the preliminary argon-hydrogen mixture experiments as well as the pure hydrogen experiments. The results are presented in the following tables. All the experimental results listed in Table C.1 are for f-4.1 focusing geometry. All results listed in Table C.2 are f-4.1 focusing geometry except for runs: 052317, 052318, and 060104 through 060112 inclusive which are f-7.1 focusing geometry.

Table C.1 Argon-Hydrogen Mixture Reduced Data

A	B	C	D	E	F	G	H	I	J	K
012202	0.70	11.03	6.48	36.76	7.00	70.43±1.08	1.54	43.18±2.50	5.80	55.7
012502	0.77	9.54	5.70	36.73	7.00	70.10±1.09	1.56	43.24±2.54	5.88	61.5
012503	0.84	8.03	4.90	36.71	7.00	69.48±1.12	1.61	45.38±2.70	5.94	67.5
012504	0.91	6.44	4.06	36.08	7.00	70.04±1.10	1.57	47.05±2.82	5.99	73.7
012505	0.98	5.33	3.49	35.93	7.00	69.98±1.10	1.57	49.01±2.94	6.01	78.5
012506	1.05	3.99	2.79	33.98	7.00	71.27±1.05	1.48	51.54±3.08	5.98	83.9
020101	1.17	26.11	15.08	36.57	7.00	83.98±0.59	0.70	53.29±3.05	5.73	47.0
020102	1.24	25.21	14.62	36.95	7.00	83.80±0.59	0.71	56.07±3.23	5.76	49.4
020103	1.39	21.92	12.88	36.77	7.00	83.03±0.62	0.75	58.04±3.39	5.84	55.7
020104	1.53	19.17	11.44	37.19	7.00	82.06±0.66	0.80	62.08±3.67	5.91	61.3
020106	1.75	14.99	9.25	36.64	7.00	81.85±0.66	0.81	61.29±3.68	6.01	69.8
020107	1.96	10.73	7.01	36.60	7.00	83.38±0.61	0.73	61.96±3.75	6.05	78.4
020108	2.25	5.33	4.19	36.68	7.00	83.01±0.62	0.75	63.76±3.78	5.94	89.3
020109	2.40	2.57	2.75	37.11	7.00	82.03±0.66	0.80	66.62±3.77	5.67	94.9

Legend for Table C.1

A = Experimental Run Reference Number   G = Global Absorption ± Relative Error
B = Hydrogen Mass Flow Rate (g/s)   H = Global Absorption Absolute Error (±)
C = Argon Mass Flow Rate (g/s)   I = Thermal Efficiency ± Relative Error
D = Total Mass Flux (kg/m^{2}s)   J = Thermal Efficiency Absolute Error (±)
E = Chamber Pressure (psia)   K = % Hydrogen By Volume
F = Input Laser Power (kW)

Table C.2 Pure Hydrogen Reduced Data

A	B	C	D	E	F	G	H	I	J
020110	2.55	699.00	8.25	30.14	7.00	73.23±0.98	1.34	68.45±2.98	4.36
020701	2.57	704.48	9.61	26.08	7.00	63.26±1.35	2.13	56.03±2.47	4.41
021404	2.18	597.58	8.04	26.44	7.00	66.27±1.24	1.86	59.48±2.59	4.35
021402	3.02	827.84	11.21	26.28	7.00	64.43±1.30	2.02	61.19±2.71	4.43
021403	3.34	915.55	12.33	26.43	7.00	63.74±1.33	2.08	61.17±2.73	4.47
021405	4.37	1197.89	13.52	31.53	7.00	72.41±1.01	1.40	69.20±3.14	4.54
021406	4.54	1244.49	14.17	31.27	7.00	72.52±1.01	1.39	65.66±3.01	4.59
021407	2.78	762.05	8.70	31.16	7.00	77.04±0.84	1.09	65.58±2.88	4.39
021401	3.02	827.84	9.30	31.68	7.00	75.38±0.90	1.20	68.27±3.00	4.40
030101	3.39	929.26	8.91	37.11	7.00	83.66±0.60	0.72	64.03±2.85	4.46
030102	3.75	1027.94	10.03	36.46	7.00	81.90±0.66	0.81	67.41±3.02	4.48
030103	3.91	1071.80	10.42	36.60	7.00	80.78±0.70	0.87	72.33±3.23	4.46
032101	3.07	841.54	9.59	31.24	6.42	72.98±0.99	1.36	53.31±2.42	4.53
032102	3.26	893.62	10.07	31.57	6.42	74.10±0.95	1.28	53.73±2.45	4.56
032103	3.45	945.71	10.71	31.42	6.42	73.83±0.96	1.30	53.54±2.46	4.60

A	B	C	D	E	F	G	H	I	J
032201	3.63	995.05	11.24	31.50	6.42	72.64±1.00	1.38	54.88±2.53	4.62
032202	3.81	1044.39	12.08	30.77	6.42	72.11±1.02	1.42	57.82±2.67	4.62
032203	3.98	1090.99	12.23	31.75	6.42	71.15±1.06	1.48	57.63±2.68	4.65
032204	4.19	1148.55	12.91	31.66	6.42	71.41±1.05	1.47	56.84±2.67	4.70
032206	4.37	1197.89	11.51	37.05	6.42	79.50±0.75	0.94	60.98±2.85	4.68
032207	4.55	1247.24	12.06	36.80	6.42	79.08±0.77	0.97	61.94±2.91	4.70
032208	4.93	1351.40	12.79	37.62	6.42	78.12±0.80	1.03	63.28±3.00	4.75
032209	5.32	1458.31	14.21	36.53	6.42	78.00±0.81	1.03	63.63±3.06	4.82
032210	5.70	1562.47	15.08	36.88	6.42	77.42±0.83	1.07	64.34±3.14	4.88
032211	6.07	1663.89	16.06	36.87	6.42	79.36±0.76	0.95	62.10±3.11	5.00
032212	5.66	1551.51	12.52	44.12	6.42	85.14±0.54	0.64	66.89±3.23	4.83
052101	5.17	1417.19	9.87	51.08	7.00	87.92±0.44	0.50	69.61±3.23	4.64
052102	5.50	1507.65	10.68	50.24	7.00	88.91±0.41	0.46	67.95±3.20	4.70
052103	5.82	1595.37	10.70	53.06	7.00	89.22±0.39	0.44	71.11±3.35	4.71
052104	6.10	1672.12	11.61	51.28	7.00	89.29±0.39	0.44	73.57±3.48	4.73
052105	6.42	1759.84	12.31	50.87	7.00	89.40±0.39	0.43	73.30±3.50	4.78
052106	6.74	1847.55	12.56	52.36	7.00	89.54±0.38	0.43	76.24±3.65	4.79
052107	7.06	1935.27	13.58	50.72	7.00	89.03±0.40	0.45	78.53±3.77	4.80
052108	7.38	2022.99	13.58	53.04	7.00	89.77±0.37	0.42	77.97±3.79	4.86
052109	7.70	2110.71	14.26	52.68	7.00	88.67±0.41	0.47	78.50±3.84	4.90
052201	8.02	2198.42	14.98	52.25	7.00	89.64±0.38	0.42	74.24±3.73	5.02
052202	8.34	2286.14	15.64	52.01	7.00	89.33±0.39	0.44	78.44±3.92	5.00
05223a	7.98	2187.46	15.28	50.94	7.00	89.04±0.40	0.45	74.28±3.72	5.01
05223b	8.27	2266.95	15.52	52.00	7.00	88.33±0.43	0.48	77.44±3.88	5.00
05224a	8.27	2266.95	15.74	51.27	7.00	88.80±0.41	0.46	72.71±3.70	5.09
05224b	8.59	2354.67	15.97	52.49	7.00	88.95±0.40	0.45	78.85±3.97	5.03
052205	5.73	1570.69	12.76	43.80	7.00	85.99±0.51	0.60	69.58±3.28	4.72
052206	6.05	1658.41	13.21	44.68	7.00	85.65±0.53	0.61	69.21±3.30	4.77
052207	6.42	1759.84	13.88	45.12	7.00	85.66±0.53	0.61	71.17±3.42	4.81
052208	5.45	1493.94	11.89	44.71	7.00	86.71±0.49	0.56	70.87±3.31	4.66
052210	3.88	1063.58	8.63	43.88	7.00	87.34±0.46	0.53	64.55±2.91	4.51
052211	4.51	1236.27	10.00	43.98	7.00	87.76±0.45	0.51	67.67±3.09	4.57
052212	5.17	1417.19	11.05	45.65	7.00	88.16±0.43	0.49	69.08±3.21	4.64
052213	6.79	1861.26	14.91	44.42	7.00	85.64±0.53	0.61	77.75±3.71	4.77
052214	7.11	1948.98	15.47	44.83	7.00	85.58±0.53	0.62	78.81±3.79	4.81
052215	3.55	973.12	9.45	36.65	7.00	82.25±0.65	0.79	67.20±2.99	4.46
052216	4.17	1143.07	11.17	36.41	7.00	80.23±0.72	0.90	65.80±2.99	4.54
052301	4.49	1230.79	11.69	37.48	7.00	81.87±0.66	0.81	64.49±2.96	4.59
052302	3.87	1060.84	10.29	36.69	7.00	81.91±0.66	0.81	64.43±2.91	4.51
052303	3.85	1055.35	10.21	36.80	7.00	82.27±0.65	0.79	63.66±2.87	4.51
052305	3.85	1055.35	10.31	36.43	7.00	81.47±0.68	0.83	62.77±2.84	4.52
052304	7.38	2022.99	16.25	44.31	7.00	85.11±0.55	0.64	74.25±3.65	4.91
052306	7.95	2179.24	14.88	52.13	7.00	87.92±0.44	0.50	76.17±3.79	4.97
052307	7.70	2110.71	14.89	50.46	7.00	88.30±0.43	0.49	76.90±3.78	4.92
052308	8.14	2231.32	15.22	52.17	7.00	89.09±0.40	0.45	79.94±3.95	4.94
052310	3.22	882.66	9.92	31.68	7.00	74.05±0.95	1.28	70.01±3.09	4.41
052311	3.53	967.64	11.04	31.20	7.00	72.88±0.99	1.36	66.86±2.98	4.46
052312	3.87	1060.84	12.11	31.18	7.00	72.87±0.99	1.36	66.71±3.00	4.50
052313	4.17	1143.07	13.19	30.84	7.00	71.56±1.04	1.46	66.74±3.02	4.53
052314	4.49	1230.79	14.23	30.78	7.00	71.44±1.05	1.46	66.73±3.05	4.57
052315	4.81	1318.51	14.81	31.68	7.00	73.11±0.98	1.35	67.19±3.10	4.61
052316	2.57	704.48	9.44	26.57	7.00	65.21±1.27	1.95	53.16±2.35	4.42

A	B	C	D	E	F	G	H	I	J
052317	3.69	1011.49	11.89	30.27	7.00	72.37±1.01	1.40	65.60±2.94	4.48
052318	3.22	882.66	10.60	29.65	7.00	71.70±1.04	1.45	65.16±2.89	4.43
053101	5.41	1482.98	10.27	51.41	5.00	86.32±0.50	0.58	71.83±3.58	4.99
053102	5.41	1482.98	10.14	52.03	3.50	80.30±0.72	0.90	73.13±4.09	5.59
05313a	6.00	1644.71	11.18	52.38	5.00	86.34±0.50	0.58	73.91±3.76	5.09
05313b	6.00	1644.71	11.15	52.48	3.50	80.08±0.73	0.91	77.59±4.42	5.70
053104	3.18	871.69	9.74	31.86	5.00	67.83±1.18	1.74	55.94±2.62	4.69
053106	2.54	696.26	8.00	30.98	5.00	65.19±1.27	1.96	51.49±2.36	4.59
053107	8.20	2247.77	15.25	52.46	5.00	84.78±0.56	0.66	77.45±4.33	5.60
053108	3.47	951.19	10.63	31.85	5.00	66.19±1.24	1.87	56.94±2.71	4.75
06011a	6.63	1817.40	12.35	52.39	5.00	86.18±0.51	0.59	73.63±3.88	5.26
06011b	6.63	1817.40	12.30	52.60	3.50	79.89±0.74	0.92	75.91±4.58	6.03
06012a	7.38	2022.99	13.81	52.12	5.00	85.93±0.52	0.60	80.01±4.25	5.31
060104	6.68	1831.11	12.59	51.76	7.00	84.20±0.58	0.69	65.86±3.25	4.94
060105	7.95	2179.24	14.92	51.99	7.00	85.90±0.52	0.60	67.78±3.49	5.14
060108	7.26	1990.09	13.58	52.17	7.00	84.61±0.56	0.67	67.89±3.40	5.01
060106	6.63	1817.40	14.14	45.76	7.00	83.99±0.59	0.70	67.78±3.32	4.89
060107	5.05	1384.29	11.13	44.28	7.00	82.85±0.63	0.76	61.47±2.90	4.72
060109	5.71	1565.21	12.49	44.59	7.00	82.24±0.65	0.79	67.24±3.19	4.75
060110	3.80	1041.65	9.99	37.11	7.00	78.61±0.78	1.00	60.17±2.73	4.54
060111	4.42	1211.60	11.66	36.98	7.00	78.43±0.79	1.01	60.97±2.82	4.62
060112	4.44	1217.08	11.66	37.15	7.00	78.31±0.79	1.01	62.64±2.89	4.61
06111a	6.65	1822.88	10.82	59.95	7.00	88.01±0.44	0.50	76.26±3.64	4.77
06112a	7.23	1981.87	11.74	60.09	7.00	88.85±0.41	0.46	75.58±3.68	4.87
06111b	6.65	1822.88	10.95	59.26	5.75	86.71±0.49	0.56	76.96±3.84	4.98
06112b	7.23	1981.87	11.84	59.58	5.75	87.89±0.44	0.50	75.39±3.87	5.13
06113a	7.79	2135.38	12.85	59.13	5.75	88.78±0.41	0.46	77.98±4.06	5.20
06111c	6.65	1822.88	10.92	59.41	4.50	84.83±0.56	0.65	80.21±4.26	5.31
06112c	7.23	1981.87	11.77	59.93	4.50	85.32±0.54	0.63	79.08±4.35	5.50
06111d	6.65	1822.88	10.97	59.15	3.25	79.61±0.75	0.94	77.40±4.81	6.21
06112d	7.23	1981.87	11.85	59.53	3.25	80.14±0.73	0.91	77.78±5.04	6.48

Legend for Table C.2

A = Experimental Run Reference Number   F = Input Laser Power (kW)
B = Hydrogen Mass Flow Rate (g/s)   G = Global Absorption ± Relative Error
C = Mole Flux (gmoles/m^2s)   H = Global Absorption Absolute Error (±)
D = Incident Gas Velocity (m/s)   I = Thermal Efficiency ± Relative Error
E = Chamber Pressure (psia)   J = Thermal Efficiency Absolute Error (±)

Appendix D. Derivation of Conservation Equations

The conservation equations for the problem of an axisymmetric two temperature hydrogen laser sustained plasma of a variable number of species will now be considered. The set of equations used are listed along with the variable in question in Table D.1.

Table D.1 Summary of Conservation Equations

Conservation Equation	Equation Number	Variable to be solved
bulk continuity	D.6	local pressure variation
axial momentum	D.27	axial velocity
radial momentum	D.30	radial velocity
species continuity	D.37b	species mole fractions
electron energy	D.48	electron temperature
heavy species energy	D.59	heavy species temperature
equation of state	D.60b	total number density

The derivation of the conservation equations is presented below. In each case, except for the state equation, the vector form of the equation will be the starting point. The physical domain being considered is axisymmetric, with x representing the axial (or vertical) coordinate and r representing the radial coordinate. The cylindrical coordinate system is summarized by Table D.2.

Table D.2 Cylindrical Coordinate System

Coordinate	Velocity Component	Scale Factor
$x_1 = r$	$U_1 = v$	$h_1 = 1$
$x_2 = \theta$	$U_2 = U_\theta$	$h_2 = r$
$x_3 = x$	$U_3 = u$	$h_3 = 1$

The first equation to be considered is the bulk continuity equation. In vector form, the bulk continuity equation is:

$$\frac{\partial \rho}{\partial t} + \nabla \cdot \left(\rho \overline{V} \right) = 0 \tag{D.1}$$

in which the first term represents the time rate of change of density and the second term represents the divergence of the mass flux. With reference to Table D.2, the velocity vector can be written as:

$$\overline{V} = u\,\overline{x} + U_\theta \overline{\theta} + v\,\overline{r} \tag{D.2}$$

The expansion of the second term of equation (D.1) in arbitrary coordinates is (Anderson, Tannehill, and Pletcher, p. 195):

$$\nabla \cdot \left(\rho \overline{V} \right) = \frac{1}{h_1 h_2 h_3} \left(\frac{\partial}{\partial x_1}(h_2 h_3 \rho U_1) + \frac{\partial}{\partial x_2}(h_1 h_3 \rho U_2) + \frac{\partial}{\partial x_3}(h_1 h_2 \rho U_3) \right) \tag{D.3}$$

which, in cylindrical coordinates becomes:

$$\nabla \cdot \left(\rho \overline{V} \right) = \frac{1}{r} \left(\frac{\partial}{\partial r}(r\rho v) + \frac{\partial}{\partial \theta}(\rho U_\theta) + \frac{\partial}{\partial x}(r\rho u) \right) \qquad (D.4)$$

and which simplifies with the axisymmetric assumption ($U_\theta = 0$, and $\frac{\partial}{\partial \theta} = 0$) to become:

$$\nabla \cdot \left(\rho \overline{V} \right) = \frac{\partial}{\partial x}(\rho u) + \frac{1}{r} \frac{\partial}{\partial r}(r\rho v) \qquad (D.5)$$

so that with the steady state assumption ($\frac{\partial}{\partial t} = 0$), the BULK CONTINUITY EQUATION is:

$$\frac{\partial}{\partial x}(\rho u) + \frac{1}{r} \frac{\partial}{\partial r}(r\rho v) = 0 \qquad (D.6)$$

The momentum equations are derived from the Navier-Stokes equations which in vector form are (Anderson, Tannehill, and Pletcher, p. 195):

$$\frac{\partial}{\partial t}\left(\rho \overline{V} \right) + \nabla \cdot \left(\rho \overline{V} \overline{V} \right) = \rho \overline{F} + \nabla \cdot \Pi_{ij} \qquad (D.7)$$

in which the first term represents the time rate of change of momentum, the second term represents the divergence of momentum, the third term represents the body force (if any), and the last term represents the divergence of the stress tensor (pressure and viscous forces).

The expansion of the second term in equation (D.7) is:

$$\nabla \cdot \left(\rho \overline{V} \overline{V} \right) = \rho \overline{V} \cdot \nabla \overline{V} + \overline{V}\left(\nabla \cdot \left(\rho \overline{V} \right) \right) \qquad (D.8)$$

Upon substitution of (D.8) into (D.7), the equation becomes:

$$\frac{\partial}{\partial t}\left(\rho \overline{V} \right) + \rho \overline{V} \cdot \nabla \overline{V} + \overline{V}\left(\nabla \cdot \left(\rho \overline{V} \right) \right) = \rho \overline{F} + \nabla \cdot \Pi_{ij} \qquad (D.9)$$

In many cases, the first term in equation (D.9) is expanded at this point to yield:

$$\left(\frac{\partial \rho}{\partial t} + \nabla \cdot \left(\rho \overline{V} \right) \right)\overline{V} + \rho \frac{\partial \overline{V}}{\partial t} + \rho \overline{V} \cdot \nabla \overline{V} = \rho \overline{F} + \nabla \cdot \Pi_{ij} \qquad (D.10)$$

where the first term in equation (D.10) is identically zero by the continuity equation (D.1). If the steady state assumption is now envoked, the final vector form of the equation becomes:

$$\rho \overline{V} \cdot \nabla \overline{V} = \rho \overline{F} + \nabla \cdot \Pi_{ij} \qquad (D.11)$$

The expansion of $\overline{V} \cdot \nabla \overline{V}$ in arbitrary coordinates is (Anderson, Tannehill, and Pletcher, p. 195):

$$\overline{V} \cdot \nabla \overline{V} =$$
$$\left(\frac{U_1}{h_1} \frac{\partial U_1}{\partial x_1} + \frac{U_2}{h_2} \frac{\partial U_1}{\partial x_2} + \frac{U_3}{h_3} \frac{\partial U_1}{\partial x_3} + \frac{U_1 U_2}{h_1 h_2} \frac{\partial h_1}{\partial x_2} + \frac{U_1 U_3}{h_1 h_3} \frac{\partial h_1}{\partial x_3} - \frac{U_2 U_2}{h_1 h_2} \frac{\partial h_2}{\partial x_1} - \frac{U_3 U_3}{h_1 h_3} \frac{\partial h_3}{\partial x_1} \right) \overline{r}$$
$$+ \left(\frac{U_1}{h_1} \frac{\partial U_2}{\partial x_1} + \frac{U_2}{h_2} \frac{\partial U_2}{\partial x_2} + \frac{U_3}{h_3} \frac{\partial U_2}{\partial x_3} - \frac{U_1 U_1}{h_1 h_2} \frac{\partial h_1}{\partial x_2} + \frac{U_1 U_2}{h_1 h_2} \frac{\partial h_2}{\partial x_1} + \frac{U_2 U_3}{h_2 h_3} \frac{\partial h_2}{\partial x_3} - \frac{U_3 U_3}{h_2 h_3} \frac{\partial h_3}{\partial x_2} \right) \overline{\theta}$$

$$+ \left(\frac{U_1}{h_1} \frac{\partial U_3}{\partial x_1} + \frac{U_2}{h_2} \frac{\partial U_3}{\partial x_2} + \frac{U_3}{h_3} \frac{\partial U_3}{\partial x_3} - \frac{U_1 U_1}{h_1 h_3} \frac{\partial h_1}{\partial x_3} \right.$$
$$\left. - \frac{U_2 U_2}{h_2 h_3} \frac{\partial h_2}{\partial x_3} + \frac{U_1 U_3}{h_1 h_3} \frac{\partial h_3}{\partial x_1} + \frac{U_2 U_3}{h_2 h_3} \frac{\partial h_3}{\partial x_2} \right) \overline{x} \qquad (D.12)$$

and, upon combining equations (D.12) and (D.2), the left hand side (LHS) of equation (D.11) may be written in cylindrical coordinates as:

$$\text{LHS} = \rho \left(v \frac{\partial v}{\partial r} + \frac{U_\theta}{r} \frac{\partial v}{\partial \theta} + u \frac{\partial v}{\partial x} - \frac{U_\theta U_\theta}{r} \right) \overline{r}$$
$$+ \rho \left(v \frac{\partial U_\theta}{\partial r} + \frac{U_\theta}{r} \frac{\partial U_\theta}{\partial \theta} + u \frac{\partial U_\theta}{\partial x} + \frac{v U_\theta}{r} + \frac{u U_\theta}{r} \frac{\partial r}{\partial x} \right) \overline{\theta}$$
$$+ \rho \left(v \frac{\partial u}{\partial r} + \frac{U_\theta}{r} \frac{\partial u}{d\theta} + u \frac{\partial u}{\partial x} - \frac{U_\theta U_\theta}{r} \frac{\partial r}{\partial x} \right) \overline{x} \qquad (D.13)$$

which is further simplified because $\frac{\partial r}{\partial x} = 0$ to become:

$$\text{LHS} = \rho \left(v \frac{\partial v}{\partial r} + \frac{U_\theta}{r} \frac{\partial v}{\partial \theta} + u \frac{\partial v}{\partial x} - \frac{U_\theta U_\theta}{r} \right) \overline{r}$$
$$+ \rho \left(v \frac{\partial U_\theta}{\partial r} + \frac{U_\theta}{r} \frac{\partial U_\theta}{\partial \theta} + u \frac{\partial U_\theta}{\partial x} + \frac{v U_\theta}{r} \right) \overline{\theta}$$
$$+ \rho \left(v \frac{\partial u}{\partial r} + \frac{U_\theta}{r} \frac{\partial u}{d\theta} + u \frac{\partial u}{\partial x} \right) \overline{x} \qquad (D.14)$$

Equation (D.14) may now be further simplified through the introduction of the axisymmetric assumption, $U_\theta = 0$, and $\frac{\partial}{\partial \theta} = 0$, to yield:

$$\text{LHS} = \rho \left(v \frac{\partial v}{\partial r} + u \frac{\partial v}{\partial x} \right) \overline{r} + \rho \left(v \frac{\partial u}{\partial r} + u \frac{\partial u}{\partial x} \right) \overline{x} \qquad (D.15)$$

Now turning our attention to the right hand side (RHS) of equation (D.11),

$$\text{RHS} = \rho \overline{F} + \overline{\nabla} \cdot \Pi_{ij} \qquad (D.16)$$

recall that the first term represents the effect of body forces, and the second term is the divergence of the stress tensor, Π_{ij}. The divergence of the stress tensor in arbitrary coordinates is (Anderson, Tannehill, and Pletcher, p. 195):

$$\overline{\nabla} \cdot \Pi_{ij} =$$
$$x_1: \frac{1}{h_1 h_2 h_3} \left(\frac{\partial}{\partial x_1} \left(h_2 h_3 \Pi_{x_1 x_1} \right) + \frac{\partial}{\partial x_2} \left(h_1 h_3 \Pi_{x_1 x_2} \right) + \frac{\partial}{\partial x_3} \left(h_1 h_2 \Pi_{x_1 x_3} \right) \right)$$
$$+ \Pi_{x_1 x_2} \frac{1}{h_1 h_2} \frac{\partial h_1}{\partial x_2} + \Pi_{x_1 x_3} \frac{1}{h_1 h_3} \frac{\partial h_1}{\partial x_3} - \Pi_{x_2 x_2} \frac{1}{h_1 h_2} \frac{\partial h_2}{\partial x_1} - \Pi_{x_3 x_3} \frac{1}{h_1 h_3} \frac{\partial h_3}{\partial x_1} \qquad (D.17a)$$

$$x_2: \frac{1}{h_1h_2h_3}\left(\frac{\partial}{\partial x_1}\left(h_2h_3\Pi_{x_1x_2}\right) + \frac{\partial}{\partial x_2}\left(h_1h_3\Pi_{x_2x_2}\right) + \frac{\partial}{\partial x_3}\left(h_1h_2\Pi_{x_2x_3}\right)\right)$$

$$+ \Pi_{x_2x_3}\frac{1}{h_2h_3}\frac{\partial h_2}{\partial x_3} + \Pi_{x_1x_2}\frac{1}{h_1h_2}\frac{\partial h_2}{\partial x_1} - \Pi_{x_3x_3}\frac{1}{h_2h_3}\frac{\partial h_3}{\partial x_2} - \Pi_{x_1x_1}\frac{1}{h_1h_2}\frac{\partial h_1}{\partial x_2} \qquad \text{(D.17b)}$$

$$x_3: \frac{1}{h_1h_2h_3}\left(\frac{\partial}{\partial x_1}\left(h_2h_3\Pi_{x_1x_3}\right) + \frac{\partial}{\partial x_2}\left(h_1h_3\Pi_{x_2x_3}\right) + \frac{\partial}{\partial x_3}\left(h_1h_2\Pi_{x_3x_3}\right)\right)$$

$$+ \Pi_{x_1x_3}\frac{1}{h_1h_3}\frac{\partial h_3}{\partial x_1} + \Pi_{x_2x_3}\frac{1}{h_2h_3}\frac{\partial h_3}{\partial x_2} - \Pi_{x_1x_1}\frac{1}{h_1h_3}\frac{\partial h_1}{\partial x_3} - \Pi_{x_2x_2}\frac{1}{h_2h_3}\frac{\partial h_2}{\partial x_3} \qquad \text{(D.17c)}$$

where the components of the stress tensor are (Anderson, Tannehill, and Pletcher, p. 195):

$$\Pi_{x_1x_1} = -p + \frac{2}{3}\mu\left(2e_{x_1x_1} - e_{x_2x_2} - e_{x_3x_3}\right) \qquad \text{(D.18a)}$$

$$\Pi_{x_2x_2} = -p + \frac{2}{3}\mu\left(2e_{x_2x_2} - e_{x_1x_1} - e_{x_3x_3}\right) \qquad \text{(D.18b)}$$

$$\Pi_{x_3x_3} = -p + \frac{2}{3}\mu\left(2e_{x_3x_3} - e_{x_1x_1} - e_{x_2x_2}\right) \qquad \text{(D.18c)}$$

$$\Pi_{x_2x_3} = \Pi_{x_3x_2} = \mu e_{x_2x_3} \qquad \text{(D.18d)}$$

$$\Pi_{x_1x_3} = \Pi_{x_3x_1} = \mu e_{x_1x_3} \qquad \text{(D.18e)}$$

$$\Pi_{x_1x_2} = \Pi_{x_2x_1} = \mu e_{x_1x_2} \qquad \text{(D.18f)}$$

and the rates of strain in equations (D.18) are (Anderson, Tannehill, and Pletcher, p. 195):

$$e_{x_1x_1} = \frac{1}{h_1}\frac{\partial U_1}{\partial x_1} + \frac{U_2}{h_1h_2}\frac{\partial h_1}{\partial x_2} + \frac{U_3}{h_1h_3}\frac{\partial h_1}{\partial x_3} \qquad \text{(D.19a)}$$

$$e_{x_2x_2} = \frac{1}{h_2}\frac{\partial U_2}{\partial x_2} + \frac{U_3}{h_2h_3}\frac{\partial h_2}{\partial x_3} + \frac{U_1}{h_1h_2}\frac{\partial h_2}{\partial x_1} \qquad \text{(D.19b)}$$

$$e_{x_3x_3} = \frac{1}{h_3}\frac{\partial U_3}{\partial x_3} + \frac{U_1}{h_1h_3}\frac{\partial h_3}{\partial x_1} + \frac{U_2}{h_2h_3}\frac{\partial h_3}{\partial x_2} \qquad \text{(D.19c)}$$

$$e_{x_1x_2} = \frac{h_2}{h_1}\frac{\partial}{\partial x_1}\left(\frac{U_2}{h_2}\right) + \frac{h_1}{h_2}\frac{\partial}{\partial x_2}\left(\frac{U_1}{h_1}\right) \qquad \text{(D.19d)}$$

$$e_{x_1x_3} = \frac{h_3}{h_1}\frac{\partial}{\partial x_1}\left(\frac{U_3}{h_3}\right) + \frac{h_1}{h_3}\frac{\partial}{\partial x_3}\left(\frac{U_1}{h_1}\right) \qquad \text{(D.19e)}$$

$$e_{x_2x_3} = \frac{h_2}{h_3}\frac{\partial}{\partial x_3}\left(\frac{U_2}{h_2}\right) + \frac{h_3}{h_2}\frac{\partial}{\partial x_2}\left(\frac{U_3}{h_3}\right) \qquad \text{(D.19f)}$$

Substitution of equations (D.19) into equations (D.18), and equations (D.18) into equations (D.17) with the coordinates, velocities, and scale factors for cylindrical coordinates listed in Table D.2 will yield the answer for the divergence of the stress tensor. This will be done one step at a time, starting with the substitution of the coordinates, velocities, and scale factors for cylindrical coordinates into equations (D.19) which define the strains:

$$e_{x_1x_1} = \frac{\partial v}{\partial r} \qquad \text{(D.20a)}$$

$$e_{x_2x_2} = \frac{1}{r}\frac{\partial U_\theta}{\partial \theta} + \frac{u}{r}\frac{\partial r}{\partial x} + \frac{v}{r} \qquad\qquad (D.20b)$$

$$e_{x_3x_3} = \frac{\partial u}{\partial x} \qquad\qquad (D.20c)$$

$$e_{x_1x_2} = r\frac{\partial}{\partial r}\left(\frac{U_\theta}{r}\right) + \frac{1}{r}\frac{\partial v}{\partial \theta} \qquad\qquad (D.20d)$$

$$e_{x_1x_3} = \frac{\partial u}{\partial r} + \frac{\partial v}{\partial x} \qquad\qquad (D.20e)$$

$$e_{x_2x_3} = r\frac{\partial}{\partial x}\left(\frac{U_\theta}{r}\right) + \frac{1}{r}\frac{\partial u}{\partial \theta} \qquad\qquad (D.20f)$$

Substitution of the rates of strain (with $\frac{\partial r}{\partial x} = 0$) given by equations (D.20) into the components

of the stress tensor given by equations (D.18) yields:

$$\Pi_{x_1x_1} = -p + \frac{2}{3}\mu\left(2\frac{\partial v}{\partial r} - \frac{1}{r}\frac{\partial U_\theta}{\partial \theta} - \frac{v}{r} - \frac{\partial u}{\partial x}\right) \qquad (D.21a)$$

$$\Pi_{x_2x_2} = -p + \frac{2}{3}\mu\left(2\left(\frac{1}{r}\frac{\partial U_\theta}{\partial \theta} + \frac{v}{r}\right) - \frac{\partial v}{\partial r} - \frac{\partial u}{\partial x}\right) \qquad (D.21b)$$

$$\Pi_{x_3x_3} = -p + \frac{2}{3}\mu\left(2\frac{\partial u}{\partial x} - \frac{\partial v}{\partial r} - \frac{1}{r}\frac{\partial U_\theta}{\partial \theta} - \frac{v}{r}\right) \qquad (D.21c)$$

$$\Pi_{x_2x_3} = \Pi_{x_3x_2} = \mu\left(r\frac{\partial}{\partial x}\left(\frac{U_\theta}{r}\right) + \frac{1}{r}\frac{\partial u}{\partial \theta}\right) \qquad (D.21d)$$

$$\Pi_{x_1x_3} = \Pi_{x_3x_1} = \mu\left(\frac{\partial u}{\partial r} + \frac{\partial v}{\partial x}\right) \qquad (D.21e)$$

$$\Pi_{x_1x_2} = \Pi_{x_2x_1} = \mu\left(r\frac{\partial}{\partial r}\left(\frac{U_\theta}{r}\right) + \frac{1}{r}\frac{\partial v}{\partial \theta}\right) \qquad (D.21f)$$

Finally, equations (D.21) may be substituted into equations (D.17) which yields:

$$\nabla\cdot\Pi_{ij} =$$

x:
$$\frac{1}{r}\frac{\partial}{\partial r}\left(r\mu\left(\frac{\partial u}{\partial r} + \frac{\partial v}{\partial x}\right)\right) + \frac{1}{r}\frac{\partial}{\partial \theta}\left(\mu\left(r\frac{\partial}{\partial x}\left(\frac{U_\theta}{r}\right) + \frac{1}{r}\frac{\partial u}{\partial \theta}\right)\right)$$
$$+ \frac{1}{r}\frac{\partial}{\partial x}\left(r\left(-p + \frac{2}{3}\mu\left(2\frac{\partial u}{\partial x} - \frac{\partial v}{\partial r} - \frac{1}{r}\frac{\partial U_\theta}{\partial \theta} - \frac{v}{r}\right)\right)\right) \qquad (D.22a)$$

θ:
$$\frac{1}{r}\frac{\partial}{\partial r}\left(r\mu\left(r\frac{\partial}{\partial r}\left(\frac{U_\theta}{r}\right) + \frac{1}{r}\frac{\partial v}{\partial \theta}\right)\right) + \frac{1}{r}\frac{\partial}{\partial \theta}\left(-p + \frac{2}{3}\mu\left(2\left(\frac{1}{r}\frac{\partial U_\theta}{\partial \theta} + \frac{v}{r}\right) - \frac{\partial v}{\partial r} - \frac{\partial u}{\partial x}\right)\right)$$
$$+ \frac{1}{r}\frac{\partial}{\partial x}\left(r\mu\left(r\frac{\partial}{\partial x}\left(\frac{U_\theta}{r}\right) + \frac{1}{r}\frac{\partial u}{\partial \theta}\right)\right) + \frac{\mu}{r}\left(r\frac{\partial}{\partial r}\left(\frac{U_\theta}{r}\right) + \frac{1}{r}\frac{\partial v}{\partial \theta}\right) \qquad (D.22b)$$

r:
$$\frac{1}{r}\frac{\partial}{\partial r}\left(-pr + \frac{2}{3}\mu r\left(2\frac{\partial v}{\partial r} - \frac{1}{r}\frac{\partial U_\theta}{\partial \theta} - \frac{v}{r} - \frac{\partial u}{\partial x}\right)\right) + \frac{1}{r}\frac{\partial}{\partial \theta}\left(\mu\left(r\frac{\partial}{\partial r}\left(\frac{U_\theta}{r}\right) + \frac{1}{r}\frac{\partial v}{\partial \theta}\right)\right)$$

$$+ \frac{1}{r}\frac{\partial}{\partial x}\left(r\mu\left(\frac{\partial u}{\partial r} + \frac{\partial v}{\partial x}\right)\right) - \frac{1}{r}\left(-p + \frac{2}{3}\mu\ \left(2\left(\frac{1}{r}\frac{\partial U_\theta}{\partial \theta} + \frac{v}{r}\right) - \frac{\partial v}{\partial r} - \frac{\partial u}{\partial x}\right)\right) \quad \text{(D.22c)}$$

At this point, introduction of the axisymmetric assumption, $U_\theta = 0$, and $\frac{\partial}{\partial \theta} = 0$, allows equations (D.22) to be simplified to become:

$$\text{x component of } \nabla\cdot\Pi_{ij} = \frac{1}{r}\frac{\partial}{\partial r}\left(r\mu\left(\frac{\partial u}{\partial r} + \frac{\partial v}{\partial x}\right)\right) + \frac{1}{r}\frac{\partial}{\partial x}\left(r\ \left(-p + \frac{2}{3}\mu\ \left(2\frac{\partial u}{\partial x} - \frac{\partial v}{\partial r} - \frac{v}{r}\right)\right)\right) \quad \text{(D.23a)}$$

r component of $\nabla\cdot\Pi_{ij} =$

$$\frac{1}{r}\frac{\partial}{\partial r}\left(-pr + \frac{2}{3}r\mu\left(2\frac{\partial v}{\partial r} - \frac{v}{r} - \frac{\partial u}{\partial x}\right)\right) + \frac{1}{r}\frac{\partial}{\partial x}\left(r\mu\left(\frac{\partial u}{\partial r} + \frac{\partial v}{\partial x}\right)\right) - \frac{1}{r}\left(-p + \frac{2}{3}\mu\left(2\frac{v}{r} - \frac{\partial v}{\partial r} - \frac{\partial u}{\partial x}\right)\right) \quad \text{(D.23b)}$$

Following algebraic manipulation, equations (D.23) may be simplified to become:

$$\text{x component of } \nabla\cdot\Pi_{ij} = \frac{1}{r}\frac{\partial}{\partial r}\left(\mu r\frac{\partial u}{\partial r}\right) + \frac{1}{r}\frac{\partial}{\partial r}\left(\mu r\frac{\partial v}{\partial x}\right) - \frac{\partial p}{\partial x} + \frac{2}{3}\frac{\partial}{\partial x}\left(2\mu\frac{\partial u}{\partial x} - \mu\frac{\partial v}{\partial r} - \mu\frac{v}{r}\right) \quad \text{(D.24a)}$$

$$\text{r component of } \nabla\cdot\Pi_{ij} = -\frac{\partial p}{\partial r} + \frac{1}{r}\frac{\partial}{\partial r}\left(\frac{4}{3}\mu r\frac{\partial v}{\partial r}\right) - \frac{1}{r}\frac{\partial}{\partial r}\left(\frac{2}{3}\mu v\right) - \frac{1}{r}\frac{\partial}{\partial r}\left(\frac{2}{3}\mu r\frac{\partial u}{\partial x}\right)$$

$$+ \frac{1}{r}\frac{\partial}{\partial x}\left(\mu r\frac{\partial u}{\partial r}\right) + \frac{1}{r}\frac{\partial}{\partial x}\left(\mu r\frac{\partial v}{\partial x}\right) - \frac{4}{3}\frac{\mu v}{r^2} + \frac{2\mu}{3r}\frac{\partial v}{\partial r} + \frac{2\mu}{3r}\frac{\partial u}{\partial x} \quad \text{(D.24b)}$$

Gravity is the only body force, acting in the negative x direction, so the first term in equation (D.16) becomes $-\rho g\ \overline{x}$. After more simplifications and rearrangement of terms, equation (D.24a) may be combined with the body force in equation (D.16), and the LHS as given by equation (D.15) to yield:

$$\rho\left(u\frac{\partial u}{\partial x} + v\frac{\partial u}{\partial r}\right) =$$

$$\frac{4}{3}\frac{\partial}{\partial x}\left(\mu\frac{\partial u}{\partial x}\right) + \frac{1}{r}\frac{\partial}{\partial r}\left(\mu r\frac{\partial u}{\partial r}\right) - \frac{2}{3}\frac{\partial}{\partial x}\left(\mu\frac{\partial v}{\partial r}\right) - \frac{2}{3r}\frac{\partial}{\partial x}(\mu v) + \frac{1}{r}\frac{\partial}{\partial r}\left(\mu r\frac{\partial v}{\partial x}\right) - \frac{\partial p}{\partial x} - \rho g \quad \text{(D.25)}$$

If the continuity equation (D.6) multiplied by the axial velocity, u, is now added to the LHS of equation (D.25) the result is:

$$u\left(\frac{\partial}{\partial x}(\rho u) + \frac{1}{r}\frac{\partial}{\partial r}(r\rho v)\right) + \rho u\frac{\partial u}{\partial x} + \rho v\frac{\partial u}{\partial r} =$$

$$\frac{4}{3}\frac{\partial}{\partial x}\left(\mu\frac{\partial u}{\partial x}\right) + \frac{1}{r}\frac{\partial}{\partial r}\left(\mu r\frac{\partial u}{\partial r}\right) - \frac{2}{3}\frac{\partial}{\partial x}\left(\mu\frac{\partial v}{\partial r}\right) - \frac{2}{3r}\frac{\partial}{\partial x}(\mu v) + \frac{1}{r}\frac{\partial}{\partial r}\left(\mu r\frac{\partial v}{\partial x}\right) - \frac{\partial p}{\partial x} - \rho g \quad \text{(D.26)}$$

which can be simplified by applying the product derivative rule backwards to the LHS to yield the

AXIAL MOMENTUM EQUATION:

$$\frac{\partial}{\partial x}(\rho uu) + \frac{1}{r}\frac{\partial}{\partial r}(r\rho uv) =$$

$$\frac{4}{3}\frac{\partial}{\partial x}\left(\mu\frac{\partial u}{\partial x}\right)+\frac{1}{r}\frac{\partial}{\partial r}\left(\mu r\frac{\partial u}{\partial r}\right)-\frac{2}{3}\frac{\partial}{\partial x}\left(\mu\frac{\partial v}{\partial r}\right)-\frac{2}{3r}\frac{\partial}{\partial x}(\mu v)+\frac{1}{r}\frac{\partial}{\partial r}\left(\mu r\frac{\partial v}{\partial x}\right)-\frac{\partial p}{\partial x}-\rho g \quad (D.27)$$

After more simplifications and rearrangement of terms, equation (D.24b) may be combined with the LHS as given by equation (D.15) to yield:

$$\rho\left(u\frac{\partial v}{\partial x}+v\frac{\partial v}{\partial r}\right)=-\frac{\partial p}{\partial r}+\frac{1}{r}\frac{\partial}{\partial r}\left(\frac{4}{3}\mu r\frac{\partial v}{\partial r}\right)-\frac{1}{r}\frac{\partial}{\partial r}\left(\frac{2}{3}\mu v\right)-\frac{1}{r}\frac{\partial}{\partial r}\left(\frac{2}{3}\mu r\frac{\partial u}{\partial x}\right)$$
$$+\frac{\partial}{\partial x}\left(\mu\frac{\partial u}{\partial r}\right)+\frac{\partial}{\partial x}\left(\mu\frac{\partial v}{\partial x}\right)-\frac{4}{3}\frac{\mu v}{r^2}+\frac{2\mu}{3r}\frac{\partial v}{\partial r}+\frac{2\mu}{3r}\frac{\partial u}{\partial x} \quad (D.28)$$

If the continuity equation (D.6) is multiplied by the radial velocity, v, and added to the LHS of equation (D.28), and the derivative in the third term on the RHS is expanded by applying the product derivative rule, equation (D.28) becomes:

$$v\left(\frac{\partial}{\partial x}(\rho u)+\frac{1}{r}\frac{\partial}{\partial r}(r\rho v)\right)+\rho u\frac{\partial v}{\partial x}+\rho v\frac{\partial v}{\partial r}=-\frac{\partial p}{\partial r}+\frac{4}{3r}\frac{\partial}{\partial r}\left(\mu r\frac{\partial v}{\partial r}\right)-\frac{2v}{3r}\frac{\partial\mu}{\partial r}-\frac{2}{3r}\frac{\partial}{\partial r}\left(\mu r\frac{\partial u}{\partial x}\right)$$
$$+\frac{\partial}{\partial x}\left(\mu\frac{\partial u}{\partial r}\right)+\frac{\partial}{\partial x}\left(\mu\frac{\partial v}{\partial x}\right)-\frac{4}{3}\frac{\mu v}{r^2}+\frac{2\mu}{3r}\frac{\partial u}{\partial x} \quad (D.29)$$

and if the product derivative rule is applied backwards to the LHS, and the terms on the RHS are rearranged, the result is the RADIAL MOMENTUM EQUATION:

$$\frac{\partial}{\partial x}(\rho uv)+\frac{1}{r}\frac{\partial}{\partial r}(r\rho vv)=\frac{\partial}{\partial x}\left(\mu\frac{\partial v}{\partial x}\right)+\frac{4}{3r}\frac{\partial}{\partial r}\left(\mu r\frac{\partial v}{\partial r}\right)+\frac{\partial}{\partial x}\left(\mu\frac{\partial u}{\partial r}\right)$$
$$-\frac{2}{3r}\frac{\partial}{\partial r}\left(\mu r\frac{\partial u}{\partial x}\right)+\frac{2\mu}{3r}\frac{\partial u}{\partial x}-\frac{\partial p}{\partial r}-\frac{4}{3}\frac{\mu v}{r^2}-\frac{2v}{3r}\frac{\partial\mu}{\partial r} \quad (D.30)$$

The species continuity equation may be written in vector form as (Mitchner and Kruger, 1973, p.186):

$$\frac{\partial n_s}{\partial t}+\nabla\cdot\left(n_s\overline{V}_s\right)=\left(\dot{n}_s\right)_{CR} \quad (D.31)$$

where the first term represents the time rate of change of the number density of species s, and the second term represents the divergence of the species s number density flux. The term on the right hand side represents the rate of production of species s, as computed through the collisional-radiative (CR) model which is described in Appendix F. The velocity of species s, $\overline{V}_s$, may be written as the sum of two parts, the bulk (mass averaged) velocity, $\overline{V}$, and the species diffusion velocity, $\overline{v}_s$:

$$\overline{V}_s=\overline{V}+\overline{v}_s \quad (D.32)$$

Writing equation (D.31) with the definition of velocity as given in equation (D.32) yields:

$$\frac{\partial n_s}{\partial t} + \nabla \cdot \left(n_s \overline{V}\right) + \nabla \cdot \left(n_s \overline{v_s}\right) = \left(\dot{n}_s\right)_{CR} \tag{D.33}$$

The problem formulation includes an equation identical to equation (D.33) for each species, s. If each of these species equations is multiplied by the mass of the species, m_s, and the equations are added, the result would be:

$$\sum_s \frac{\partial (m_s n_s)}{\partial t} + \sum_s \left(\nabla \cdot \left(m_s n_s \overline{V}\right)\right) + \sum_s \left(\nabla \cdot \left(m_s n_s \overline{v_s}\right)\right) = \sum_s \left(m_s \dot{n}_s\right)_{CR} \tag{D.34}$$

where it has been assumed that the mass of a particle is invariant in time and space. Since the sum of derivatives is the derivative of the sum, equation (D.34) is equivalent to:

$$\frac{\partial}{\partial t}\left(\sum_s m_s n_s\right) + \nabla \cdot \left(\sum_s m_s n_s \overline{V}\right) + \nabla \cdot \left(\sum_s m_s n_s \overline{v_s}\right) = \sum_s \left(m_s \dot{n}_s\right)_{CR} \tag{D.35}$$

The first two terms in equation (D.35) are exactly equivalent to the two terms in the continuity equation (D.6), since the sum of the species number densities multiplied by the species masses is simply the bulk density, ρ. The third term is the sum of the diffusive mass fluxes, which is equal to zero. The last term represents the total amount of mass created or destroyed, and is also equal to zero. Therefore, the species continuity equations may be added to yield the bulk continuity equation.

Introducing the steady state assumption eliminates the first term in equation (D.33), and the second and third terms in equation (D.33) may be expanded into cylindrical coordinates by application of equation (D.4). The resulting equation is:

$$\frac{1}{r}\left(\frac{\partial}{\partial r}(v n_s r) + \frac{\partial}{\partial \theta}(U_\theta n_s) + \frac{\partial}{\partial x}(u n_s r)\right) + \frac{1}{r}\left(\frac{\partial}{\partial r}(v_s n_s r) + \frac{\partial}{\partial \theta}(U_{\theta s} n_s) + \frac{\partial}{\partial x}(u_s n_s r)\right) = \left(\dot{n}_s\right)_{CR} \tag{D.36}$$

which simplifies with the axisymmetric assumption ($U_\theta = 0$, and $\frac{\partial}{\partial \theta} = 0$) and some rearrangement of terms to yield:

$$\frac{\partial}{\partial x}(n_s u) + \frac{1}{r}\frac{\partial}{\partial r}(v n_s r) = -\frac{\partial}{\partial x}(n_s u_s) - \frac{1}{r}\frac{\partial}{\partial r}(v_s n_s r) + \left(\dot{n}_s\right)_{CR} \tag{D.37a}$$

If the expression for species diffusion velocity given by equation (E.9) is substituted into equation (D.37a), and the number densities are rewritten as the mole fraction multiplied by the total number density, the result is the SPECIES CONTINUITY EQUATION for species s:

$$\frac{\partial}{\partial x}(n_{tot}X_s u) + \frac{1}{r}\frac{\partial}{\partial r}(v n_{tot}X_s r) = \frac{\partial}{\partial x}\left(D_{eff u}\frac{\partial X_s}{\partial x}\right) + \frac{1}{r}\frac{\partial}{\partial r}\left(r D_{eff v}\frac{\partial X_s}{\partial r}\right) + \frac{\partial}{\partial x}\left(\frac{1}{m_s}D_i^T\frac{\partial}{\partial x}(\ln T_i)\right)$$
$$+ \frac{1}{r}\frac{\partial}{\partial r}\left(\frac{r}{m_s}D_i^T\frac{\partial}{\partial r}(\ln T_i)\right) + (\dot{n}_s)_{CR} \qquad (D.37b)$$

where the D_{eff} are the effective diffusion coefficients discussed in Appendix G, and D_i^T is the thermal diffusion coefficient for species i as discussed in Appendix E.

The variable in question for which an electron energy equation is required is the electron temperature, T_e. Assuming that the electrons have a Maxwellian velocity distribution, the average thermal energy per unit mass may be written as:

$$\frac{\text{average thermal energy}}{\text{unit mass}} = \frac{3k_b T_e}{2m_e} \qquad (D.38)$$

where k_b is Boltzmann's constant, and m_e is the mass of an electron. Multiplying the average thermal energy per unit mass by the electron mass density, $m_e n_e$, would then yield the average thermal energy per unit volume:

$$\frac{\text{average thermal energy}}{\text{unit volume}} = (m_e n_e)\left(\frac{3k_b T_e}{2m_e}\right) = \frac{3}{2}n_e k_b T_e \qquad (D.39)$$

The equation which governs the electron temperature, through the average thermal energy per unit volume, may be written in the absence of sources as (Mitchner and Kruger, 1973, p.183):

$$\frac{\partial}{\partial t}\left(\frac{3}{2}n_e k_b T_e\right) + \nabla \cdot \left(\frac{3}{2}n_e k_b T_e \overline{V}\right) = -\nabla \cdot \overline{Q} + \Pi_{ij} : \overline{\nabla}\overline{V} \qquad (D.40)$$

where $\overline{V}$ represents the electron bulk velocity, $\overline{Q}$ represents the heat flux vector, Π_{ij} represents the stress tensor, and the colon represents a double product between two tensors. In terms of physical quantities, the first term represents the time rate of change of internal energy per unit volume, the second term represents the divergence of the convective energy flux, the third term represents the divergence of the conductive and diffusive heat fluxes, and the last term represents flow work and viscous dissipation.

Further terms are necessary to include the effects of energy addition, radiation, and collisional transfer. The rate of energy absorbed from the incident laser beam is accounted for by the term BABS which is described in Appendix H. The rate of energy lost through elastic collisions with the heavy species is accounted for by the term ELST. The rate of energy exchanged through

inelastic collisions with the heavy species is accounted for by the term INSTE. The rate of optically thin bremsstrahlung continuum radiation lost is accounted for by the term RADLS. Finally, the rate of non-optically thin continuum radiation energy transfer is accounted for by the term CONRAD. ELST, INSTE, RADLS, and CONRAD are described in Appendix F. Therefore, assuming steady state conditions, equation (D.40) including the source terms is:

$$\nabla \cdot \left(\frac{3}{2} n_e k_b T_e \overline{V}\right) = - \nabla \cdot \overline{Q} + \Pi_{ij} : \nabla V + BABS - ELST + INSTE - RADLS + CONRAD \quad (D.41)$$

The term involving the stress tensor in equation (D.41) may be split into a part involving pressure (flow work) and a part involving viscosity (rate of energy dissipation through viscous stresses). If the assumption is made that electron viscous dissipation is negligible, then the remaining term (the flow work) may be written as:

$$\text{flow work} = - p_e \nabla \cdot \overline{V} \quad (D.42)$$

Application of equation (D.4) to expand the first three terms in equation (D.41) in cylindrical coordinates yields:

$$\frac{1}{r}\left(\frac{\partial}{\partial r}\left(r\left(\frac{3}{2}n_e k_b T_e\right)v\right) + \frac{\partial}{\partial \theta}\left(\left(\frac{3}{2}n_e k_b T_e\right)U_\theta\right) + \frac{\partial}{\partial x}\left(r\left(\frac{3}{2}n_e k_b T_e\right)u\right)\right) =$$

$$-\frac{1}{r}\left(\frac{\partial}{\partial r}(r\,Q_r) + \frac{\partial}{\partial \theta}(Q_\theta) + \frac{\partial}{\partial x}(r\,Q_x)\right) - p_e \frac{1}{r}\left(\frac{\partial}{\partial r}(rv) + \frac{\partial}{\partial \theta}(U_\theta) + \frac{\partial}{\partial x}(ru)\right)$$

$$+ BABS - ELST + INSTE - RADLS + CONRAD \quad (D.43)$$

Introduction of the axisymmetric assumption, $(U_\theta = 0, \text{ and } \frac{\partial}{\partial \theta} = 0)$ to equation (D.43) along with some manipulation yields:

$$\frac{1}{r}\frac{\partial}{\partial r}\left(r\left(\frac{3}{2}n_e k_b T_e\right)v\right) + \frac{\partial}{\partial x}\left(\left(\frac{3}{2}n_e k_b T_e\right)u\right) = -\frac{1}{r}\frac{\partial}{\partial r}(r\,Q_r) - \frac{\partial Q_x}{\partial x} - p_e \frac{1}{r}\frac{\partial}{\partial r}(rv) - p_e \frac{\partial u}{\partial x}$$

$$+ BABS - ELST + INSTE - RADLS + CONRAD \quad (D.44)$$

where the heat fluxes may be written as:

$$Q_x = - \lambda_e \frac{\partial T_e}{\partial x} + \frac{3}{2} k_b T_e (\text{unflx}) \quad (D.45a)$$

$$Q_r = - \lambda_e \frac{\partial T_e}{\partial r} + \frac{3}{2} k_b T_e (\text{vnflx}) \quad (D.45b)$$

in which λ_e represents the electron thermal conductivity, unflx is the axial diffusive flux of electrons, and vnflx is the radial diffusive flux of electrons. The electron pressure to a very good approximation may be written as:

$$p_e = n_e k_b T_e \tag{D.46}$$

Substitution of equations (D.45) and (D.46) into equation (D.44) yields:

$$\frac{1}{r}\frac{\partial}{\partial r}\left(r\left(\frac{3}{2}n_e k_b T_e\right)v\right) + \frac{\partial}{\partial x}\left(\left(\frac{3}{2}n_e k_b T_e\right)u\right) = -\frac{1}{r}\frac{\partial}{\partial r}\left(-r\lambda_e\frac{\partial T_e}{\partial r}\right) - \frac{\partial}{\partial x}\left(-\lambda_e\frac{\partial T_e}{\partial x}\right)$$

$$-\frac{1}{r}\frac{\partial}{\partial r}\left(r\frac{3}{2}k_b T_e(vnflx)\right) - \frac{\partial}{\partial x}\left(\frac{3}{2}k_b T_e(unflx)\right) - n_e k_b T_e \frac{1}{r}\frac{\partial}{\partial r}(rv) - n_e k_b T_e\frac{\partial u}{\partial x}$$

$$+ \text{ BABS - ELST + INSTE - RADLS + CONRAD} \tag{D.47}$$

Note that the diffusive heat flux terms in equation (D.47) may be grouped with the convective terms on the left hand side or may be left on the right hand side and treated as source terms in the discretization. Rearrangement of terms in equation (D.47), including placing the diffusive heat flux terms on the left hand side, yields the ELECTRON ENERGY EQUATION:

$$\frac{\partial}{\partial x}\left(\left(\frac{3}{2}k_b\left(unflx+n_e u\right)\right)T_e\right) + \frac{1}{r}\frac{\partial}{\partial r}\left(\left(\frac{3}{2}rk_b\left(vnflx+n_e v\right)\right)T_e\right) = \frac{\partial}{\partial x}\left(\lambda_e\frac{\partial T_e}{\partial x}\right) + \frac{1}{r}\frac{\partial}{\partial r}\left(r\lambda_e\frac{\partial T_e}{\partial r}\right)$$

$$-\left(n_e k_b\frac{\partial u}{\partial x}\right)T_e - \left(\frac{n_e k_b}{r}\frac{\partial}{\partial r}(rv)\right)T_e + \text{ BABS - ELST + INSTE - RADLS + CONRAD} \tag{D.48}$$

The variable in question for which a heavy species energy equation is required is the gas temperature, T_g. Assuming that all the heavy species have a Maxwellian velocity distribution governed by the same kinetic temperature, the average thermal energy per unit volume may be written as:

$$\frac{\text{average thermal energy}}{\text{unit volume}} = \frac{3}{2}n_h k_b T_g \tag{D.49}$$

where n_h is the total heavy species number density given by:

$$n_h = \sum_s n_s, \ s \neq 1 \tag{D.50}$$

The equation which governs the heavy species temperature (gas temperature), through the average thermal energy per unit volume, may be written in the absence of sources as:

$$\frac{\partial}{\partial t}\left(\frac{3}{2}n_h k_b T_g\right) + \nabla\bullet\left(\frac{3}{2}n_h k_b T_g\overline{V}\right) = -\nabla\bullet\overline{Q} + \Pi_{ij}:\nabla V \tag{D.51}$$

where $\overline{V}$ represents the heavy species bulk velocity, $\overline{Q}$ represents the heat flux vector, Π_{ij} represents the stress tensor, and the colon represents a double product between two tensors. In terms of physical quantities, the first term represents the time rate of change of thermal energy per unit volume, the second term represents the divergence of the convective energy flux, the third term represents the divergence of the conductive and diffusive heat fluxes, and the last term represents flow work and viscous dissipation.

As with the electron energy equation (D.48), additional terms are required to complete the formulation. The rate of energy exchange due to elastic collisions with the electrons is accounted for by the term ELST, which is identical to the term ELST in the eletron energy equation (D.48). The rate of energy exchange due to inelastic collisions is accounted for by the term INSTH which is described in Appendix F. Therefore with the steady state assumption, and including the source terms, equation (D.51) may be written as:

$$\nabla \cdot \left(\frac{3}{2} n_h k_b T_g \overline{V} \right) = - \nabla \cdot \overline{Q} + \Pi_{ij} : \nabla V + ELST + INSTH \qquad (D.52)$$

Once again, the term involving the stress tensor will be split into a non-viscous (flow work) part and a viscous (dissipation by viscous stresses) part. As with the electron energy equation (D.48), the viscous dissipation will be neglected, leaving only the flow work which may be written:

$$\text{flow work} = - p_h \nabla \cdot \overline{V} \qquad (D.53)$$

Application of equation (D.4) to expand the first three terms in equation (D.52) in cylindrical coordinates yields:

$$\frac{1}{r} \left(\frac{\partial}{\partial r} \left(r \left(\frac{3}{2} n_h k_b T_g \right) v \right) + \frac{\partial}{\partial \theta} \left(\left(\frac{3}{2} n_h k_b T_g \right) U_\theta \right) + \frac{\partial}{\partial x} \left(r \left(\frac{3}{2} n_h k_b T_g \right) u \right) \right) =$$
$$- \frac{1}{r} \left(\frac{\partial}{\partial r} (r\, Q_r) + \frac{\partial}{\partial \theta} (Q_\theta) + \frac{\partial}{\partial x} (r\, Q_x) \right)$$
$$- p_h \frac{1}{r} \left(\frac{\partial}{\partial r} (rv) + \frac{\partial}{\partial \theta} (U_\theta) + \frac{\partial}{\partial x} (ru) \right) + ELST + INSTH \qquad (D.54)$$

Introduction of the axisymmetric assumption, ($U_\theta = 0$, and $\dfrac{\partial}{\partial \theta} = 0$) to equation (D.54) along with some manipulation yields:

$$\frac{1}{r} \frac{\partial}{\partial r} \left(r \left(\frac{3}{2} n_h k_b T_g \right) v \right) + \frac{\partial}{\partial x} \left(\left(\frac{3}{2} n_h k_b T_g \right) u \right) = - \frac{1}{r} \frac{\partial}{\partial r} (r\, Q_r) - \frac{\partial Q_x}{\partial x} - p_h \frac{1}{r} \frac{\partial}{\partial r} (rv) - p_h \frac{\partial u}{\partial x}$$

$$+ \text{ELST} + \text{INSTH} \qquad \text{(D.55)}$$

where the heat fluxes may be written as:

$$Q_x = -\lambda_h \frac{\partial T_g}{\partial x} + \frac{3}{2} k_b T_g (\text{hunflx}) \qquad \text{(D.56a)}$$

$$Q_r = -\lambda_h \frac{\partial T_g}{\partial r} + \frac{3}{2} k_b T_g (\text{hvnflx}) \qquad \text{(D.56b)}$$

in which λ_h represents the heavy species thermal conductivity, hunflx is the total heavy species axial diffusive number flux, and hvnflx is the total heavy species radial diffusive number flux. The heavy species pressure to a very good approximation may be written as:

$$P_h = n_h k_b T_g \qquad \text{(D.57)}$$

Substitution of equations (D.56), and (D.57) into equation (D.55) yields:

$$\frac{1}{r}\frac{\partial}{\partial r}\left(r\left(\frac{3}{2}n_h k_b T_g\right)v\right) + \frac{\partial}{\partial x}\left(\left(\frac{3}{2}n_h k_b T_g\right)u\right) = -\frac{1}{r}\frac{\partial}{\partial r}\left(-r\lambda_h \frac{\partial T_g}{\partial r}\right) - \frac{\partial}{\partial x}\left(-\lambda_h \frac{\partial T_g}{\partial x}\right)$$

$$-\frac{1}{r}\frac{\partial}{\partial r}\left(r\frac{3}{2}k_b T_g(\text{hvnflx})\right) - \frac{\partial}{\partial x}\left(\frac{3}{2}k_b T_g(\text{hunflx})\right) - n_h k_b T_g \frac{1}{r}\frac{\partial}{\partial r}(rv) - n_h k_b T_g \frac{\partial u}{\partial x}$$

$$+ \text{ELST} + \text{INSTH} \qquad \text{(D.58)}$$

Rearrangement of terms in equation (D.58) yields the HEAVY SPECIES ENERGY EQUATION:

$$\frac{\partial}{\partial x}\left(\left(\frac{3}{2}k_b\left(\text{hunflx}+n_h u\right)\right)T_g\right) + \frac{1}{r}\frac{\partial}{\partial r}\left(\left(\frac{3}{2}k_b r\left(\text{hvnflx}+n_h v\right)\right)T_g\right) = \frac{\partial}{\partial x}\left(\lambda_h \frac{\partial T_g}{\partial x}\right) + \frac{1}{r}\frac{\partial}{\partial r}\left(r\lambda_h \frac{\partial T_g}{\partial r}\right)$$

$$-\left(n_h k_b \frac{\partial u}{\partial x}\right)T_g - \left(\frac{n_h k_b}{r}\frac{\partial}{\partial r}(rv)\right)T_g + \text{ELST} + \text{INSTH} \qquad \text{(D.59)}$$

The final equation to be discussed in this appendix is not a conservation equation, but an equation of state. This equation is usually written as (Cho, 1988):

$$P = \left(n_e k_b T_e + n_h k_b T_g\right)\left(1 - P_c^{DH}\right) \qquad \text{(D.60a)}$$

An alternate formulation of equation (D.60) would be to replace the number densities with mole fractions multiplied by the total number density which yields the MULTITEMPERATURE PLASMA EQUATION OF STATE:

$$P = n_{tot}\left(X_e k_b T_e + X_h k_b T_g\right)\left(1 - P_c^{DH}\right) \qquad \text{(D.60b)}$$

Regardless of whether equation (D.60a) or (D.60b) is used, P is the system pressure, and P_c^{DH} is the Debye-Hückel pressure correction which is (Cho, 1988):

$$P_c^{DH} = \left(24\pi(n_e + n_h)\left(\frac{4\pi e^2 k_c}{k_b}\left(\frac{n_e}{T_e} + \frac{(n_{H^+}) + (n_{H^-}) + (n_{H_2^+}) + (n_{H_3^+})}{T_g}\right)\right)^{-1.5}\right)^{-1} \quad (D.61)$$

where e is the charge of an electron in Coulombs, k_c is the Coulomb constant, and k_b is Boltzmann's constant. Equation (D.60a) can be manipulated into a form which involves the bulk density as follows. Recall that the mass of a particle may be written as the species molecular weight divided by Avogadro's number:

$$m_s = \frac{MW_s}{n_A} \quad (D.62)$$

so that equation (D.60a) may be written as:

$$P = \left(n_e k_b T_e\left(\frac{m_e n_A}{MW_e}\right) + n_h k_b T_g\left(\frac{m_h n_A}{MW_h}\right)\right)(1 - P_c^{DH}) \quad (D.63)$$

where m_h is the average mass per heavy particle which may be written as:

$$m_h = \frac{\sum_s m_s n_s}{n_h}, \; s \neq 1 \quad (D.64)$$

and MW_h is the molecular weight for the mixture of heavy particles given by:

$$MW_h = \frac{\sum_s MW_s n_s}{n_h}, \; s \neq 1 \quad (D.65)$$

Equation (D.63) may then be written as:

$$P = \left(n_e m_e\left(\frac{k_b n_A}{MW_e}\right)T_e + \rho_h\left(\frac{k_b n_A}{MW_h}\right)T_g\right)(1 - P_c^{DH}) \quad (D.66)$$

where the heavy species mass density has been included. Now since the electron and heavy species mass densities must sum to the bulk density, equtaion (D.66) may be written as:

$$P = \left(n_e m_e\left(\left(\frac{k_b n_A}{MW_e}\right)T_e - \left(\frac{k_b n_A}{MW_h}\right)T_g\right) + \rho\left(\frac{k_b n_A}{MW_h}\right)T_g\right)(1 - P_c^{DH}) \quad (D.67)$$

which may be rearranged to yield a variation of the multitemperature plasma equation of stste involving the bulk density:

$$\rho = \frac{\frac{P}{(1 - P_c^{DH})} - n_e m_e k_b n_A\left(\left(\frac{T_e}{MW_e}\right) + \left(\frac{T_g}{MW_h}\right)\right)}{\left(\frac{k_b n_A}{MW_h}\right)T_g} \quad (D.68)$$

The conservation equations have been presented. It is hoped that enough detail has been included to allow the reader to follow without getting confused. Several terms were only briefly

mentioned, which include diffusion fluxes, and source terms. A detailed explanation of all source terms except BABS can be found in Appendix F on the collisional-radiative model. The explanation of the computation of BABS can be found in Appendix H on the ray trace. The computation of the transport coefficients can be found in Appendix E on transport coefficients. Finally, the theory behind the computation of the diffusion velocities is explained in Appendix E, and the actual computation of all diffusion fluxes is explained in Appendix G.

As part of the code validation procedure, the three flowfield subroutines were tested without the scalar subroutines. In order to test the accuracy of the discretization as mentioned in Appendix I, results of the continuity and momentum equations using a formulation with variable density and viscosity were compared results of a constant density and viscosity formulation. The constant density cylindrical momentum equations are well known (Kuo, 1986, p.189) and are simply a degenerate case of the variable property momentum equations. Although the constant property equations can be derived from the vector equations as was done above for the variable property equations, the complete axisymmetric momentum equations (D.27), and (D.30), will be reduced to the constant property equations.

The constant density continuity equation may be written by simply removing the density from the derivatives of equation (D.6) as:

$$\frac{\partial u}{\partial x} + \frac{1}{r}\frac{\partial}{\partial r}(rv) = 0 \tag{D.69}$$

If the axial momentum equation (D.27) is rewritten as:

$$\frac{\partial}{\partial x}(\rho uu) + \frac{1}{r}\frac{\partial}{\partial r}(r\rho uv) = \mu\frac{\partial}{\partial x}\left(\frac{\partial u}{\partial x}\right) + \frac{\mu}{r}\frac{\partial}{\partial r}\left(r\frac{\partial u}{\partial r}\right) - \frac{\partial p}{\partial x} - \rho g$$

$$- \frac{2\mu}{3}\frac{\partial}{\partial x}\left(\frac{\partial v}{\partial r}\right) - \frac{2\mu}{3r}\frac{\partial v}{\partial x} + \frac{\mu}{3}\frac{\partial}{\partial x}\left(\frac{\partial u}{\partial x}\right) + \frac{\mu}{r}\frac{\partial}{\partial r}\left(r\frac{\partial v}{\partial x}\right) \tag{D.70}$$

it can then be shown that the last four terms on the right hand side are identically zero. Substituting equation (D.69) into the first of the four terms yields:

$$\text{LAST FOUR TERMS} = -\frac{2\mu}{3}\frac{\partial}{\partial x}\left(-\frac{v}{r} - \frac{\partial u}{\partial x}\right) - \frac{2\mu}{3r}\frac{\partial v}{\partial x} + \frac{\mu}{3}\frac{\partial}{\partial x}\left(\frac{\partial u}{\partial x}\right) + \frac{\mu}{r}\frac{\partial}{\partial r}\left(r\frac{\partial v}{\partial x}\right) \tag{D.71}$$

which simplifies to:

$$\text{LAST FOUR TERMS} = \mu\frac{\partial}{\partial x}\left(\frac{\partial u}{\partial x}\right) + \frac{\mu}{r}\frac{\partial}{\partial r}\left(r\frac{\partial v}{\partial x}\right) \qquad (D.72)$$

Switching the order of differentiation in the second term of equation (D.72) then yields:

$$\text{LAST FOUR TERMS} = \mu\frac{\partial}{\partial x}\left(\frac{\partial u}{\partial x} + \frac{1}{r}\frac{\partial}{\partial r}(rv)\right) = 0 \qquad (D.73)$$

since the bracketed terms are simply the constant density continuity equation (D.69). The end result is the constant property axial momentum equation, which is:

$$\frac{\partial}{\partial x}(\rho uu) + \frac{1}{r}\frac{\partial}{\partial r}(r\rho uv) = \mu\frac{\partial}{\partial x}\left(\frac{\partial u}{\partial x}\right) + \frac{\mu}{r}\frac{\partial}{\partial r}\left(r\frac{\partial u}{\partial r}\right) - \frac{\partial p}{\partial x} - \rho g \qquad (D.74)$$

Similarly, if the radial momentum equation (D.30) is rewritten as:

$$\frac{\partial}{\partial x}(\rho uv) + \frac{1}{r}\frac{\partial}{\partial r}(r\rho vv) = \mu\frac{\partial}{\partial x}\left(\frac{\partial v}{\partial x}\right) + \mu\left(\frac{1}{r}\frac{\partial}{\partial r}\left(r\frac{\partial v}{\partial r}\right) - \frac{v}{r^2}\right) - \frac{\partial p}{\partial r}$$
$$+ \mu\frac{\partial}{\partial x}\left(\frac{\partial u}{\partial r}\right) - \frac{2\mu}{3r}\frac{\partial}{\partial r}\left(r\frac{\partial u}{\partial x}\right) + \frac{2\mu}{3r}\frac{\partial u}{\partial x} + \frac{\mu}{3}\left(\frac{1}{r}\frac{\partial}{\partial r}\left(r\frac{\partial v}{\partial r}\right) - \frac{v}{r^2}\right) \qquad (D.75)$$

it can be shown that the bracketed quantity appearing in the second and last terms on the right hand side may be written as:

$$\left(\frac{1}{r}\frac{\partial}{\partial r}\left(r\frac{\partial v}{\partial r}\right) - \frac{v}{r^2}\right) = \frac{\partial}{\partial r}\left(\frac{\partial v}{\partial r}\right) + \frac{1}{r}\frac{\partial v}{\partial r} - \frac{v}{r^2} \qquad (D.76)$$

$$\left(\frac{1}{r}\frac{\partial}{\partial r}\left(r\frac{\partial v}{\partial r}\right) - \frac{v}{r^2}\right) = \frac{\partial}{\partial r}\left(\frac{\partial v}{\partial r}\right) + \frac{\partial}{\partial r}\left(\frac{v}{r}\right) \qquad (D.77)$$

$$\left(\frac{1}{r}\frac{\partial}{\partial r}\left(r\frac{\partial v}{\partial r}\right) - \frac{v}{r^2}\right) = \frac{\partial}{\partial r}\left(\frac{1}{r}\frac{\partial}{\partial r}(rv)\right) \qquad (D.78)$$

and upon substitution of equation (D.78) into the last term of equation (D.75) yields:

$$\frac{\partial}{\partial x}(\rho uv) + \frac{1}{r}\frac{\partial}{\partial r}(r\rho vv) = \mu\frac{\partial}{\partial x}\left(\frac{\partial v}{\partial x}\right) + \mu\left(\frac{1}{r}\frac{\partial}{\partial r}\left(r\frac{\partial v}{\partial r}\right) - \frac{v}{r^2}\right) - \frac{\partial p}{\partial r}$$
$$+ \mu\frac{\partial}{\partial x}\left(\frac{\partial u}{\partial r}\right) - \frac{2\mu}{3r}\frac{\partial}{\partial r}\left(r\frac{\partial u}{\partial x}\right) + \frac{2\mu}{3r}\frac{\partial u}{\partial x} + \frac{\mu}{3}\frac{\partial}{\partial r}\left(\frac{1}{r}\frac{\partial}{\partial r}(rv)\right) \qquad (D.79)$$

where, again, it can be shown that the last four terms on the right hand side are identically zero. Substitution of equation (D.69) into the last of the four terms yields:

$$\text{LAST FOUR TERMS} = \mu\frac{\partial}{\partial x}\left(\frac{\partial u}{\partial r}\right) - \frac{2\mu}{3r}\frac{\partial}{\partial r}\left(r\frac{\partial u}{\partial x}\right) + \frac{2\mu}{3r}\frac{\partial u}{\partial x} - \frac{\mu}{3}\frac{\partial}{\partial r}\left(\frac{\partial u}{\partial x}\right) \qquad (D.80)$$

and upon expansion of the derivative in the second term, equation (D.80) becomes:

$$\text{LAST FOUR TERMS} = \mu\frac{\partial}{\partial x}\left(\frac{\partial u}{\partial r}\right) - \mu\frac{\partial}{\partial r}\left(\frac{\partial u}{\partial x}\right) \qquad (D.81)$$

Switching the order of differentiation in the second term of equation (D.81) then yields:

$$\text{LAST FOUR TERMS} = \mu\frac{\partial}{\partial x}\left(\frac{\partial u}{\partial r}\right) - \mu\frac{\partial}{\partial x}\left(\frac{\partial u}{\partial r}\right) = 0 \tag{D.82}$$

so that the end result is the constant property radial momentum equation:

$$\frac{\partial}{\partial x}(\rho uv) + \frac{1}{r}\frac{\partial}{\partial r}(r\rho vv) = \mu\frac{\partial}{\partial x}\left(\frac{\partial v}{\partial x}\right) + \mu\left(\frac{1}{r}\ \frac{\partial}{\partial r}\left(r\ \frac{\partial v}{\partial r}\right) - \frac{v}{r^2}\right) - \frac{\partial p}{\partial r} \tag{D.83}$$

Appendix E. Computation of Transport Coefficients

The transport coefficients required for the solution of the conservation equations presented in Chapter 3 are listed in Table 3.1. In general the transport coefficients will be functions of the number densities of the species in question, their masses, and their temperatures. The complexity of the functional relation is a function of both the level of approximation and the number of components considered (for a mixture). The source of these relations is the well documented Chapman-Enskog approach which is a technique whereby an infinite series solution is sought for the distribution function of the Boltzmann equation as described by Chapman and Cowling (1990), Hirschfelder, Curtiss and Bird (1954), Kruger and Mitchner (1967), Chmieleski and Ferziger (1967), Devoto and Li (1968), Williams and DeWitt (1969), Miller and Sandler (1973), Devoto (1967a, 1967b and 1973), Mason (1954), and Vasil'evskii, Sokolova, and Tirskii (1984). This theory depends on the four assumptions that only binary collisions between molecules are important, the binary collisions are elastic, the intermolecular force field is spherically symmetric, and molecular collisions are adequately described by classical mechanics (Mason, 1954). Although the theory is strictly applicable only to conditions where these four assumptions hold, it has shown success in predictions of polyatomic gas transport coefficients (Mason, 1954).

The level of approximation of the distribution function refers to the number of terms retained in the infinite Sonine polynomial solution expansion (Hirschfelder, Curtiss and Bird, 1954). Values for the transport coefficients are considered to be exact when the addition of further terms in the expansion no longer changes their value, or in other words when the expansion has converged. Therefore comparisons of lower approximations to exact values are merely comparisons to the converged values. For a mixture of neutral (unionized) gases the first nonzero approximations for the transport coefficients are generally considered to be adequate (Vasil'evskii, Sokolova, and Tirskii, 1984, and Devoto 1966). In particular, the first approximation for viscosity and electrical conductivity, and the second approximation for thermal conductivity, thermal diffusion and multicomponent diffusion are the levels of approximation required (Devoto, 1966).

However when there is a high degree of ionization, the lowest approximations do not converge as quickly and higher approximations are required (Miller and Sandler, 1973, Vasil'evskii, Sokolova, and Tirskii, 1984, and Devoto, 1966). Devoto has shown that in general one higher level of approximation is required for the case of an ionized gas (Devoto, 1966 and 1967a). For fully ionized hydrogen the first approximation of the viscosity, and the second approximation to the other coefficients, except for translational thermal conductivity are within 15% of the converged higher approximations (Grier, 1966). The calculated values for the third approximation of the translational thermal conductivity were approximately twice those of the second approximation and approximately equal to the fourth approximation (Grier, 1966). Devoto (1973) has calculated the thermal conductivity and viscosity of argon at 1 atm using the lowest approximations for each (2nd for thermal conductivity and 1st for viscosity) and has found errors of 12% and 8% respectively at and near full ionization. However in the same paper, Devoto states, "that the probable accuracy does not warrant the additional effort of using the second approximation."

The reason for this statement is that the expressions used for the calculation of the transport coefficients have the form of a ratio of determinants times a function of temperature, number density, and species mass. The ratio of determinants are of order NX+1 in the numerator and NX in the denominator where N is the level of approximation and X is the number of species in the mixture (Vasil'evskii, Sokolova, and Tirskii, 1984, Devoto, 1966, and Hirschfelder, Curtiss, and Bird, 1954). Each element within the determinants are in turn functions of species densities, masses, and velocity averaged collision integrals for the particular interaction in effect (Vasil'evskii, Sokolova, and Tirskii, 1984, Devoto, 1966, and Hirschfelder, Curtiss, and Bird, 1954). The exact expressions for the transport coefficients will be presented in the next section. All of this means that in order to calculate the viscosity of an ionized gas mixture of electrons and six heavy components to the second approximation requires the calculation a 15 by 15 determinant divided by a 14 by 14 determinant. Similarly, the third approximation of the heavy species thermal conductivity (neglecting electrons) requires the ratio of a 19 by 19 determinant and an 18 by 18 determinant. When implemented into an overall non-LTE code, this coefficient evaluation

procedure must then be evaluated for each grid location, and within every iteration (or perhaps every fifth or so iteration) of the conservation equations. In addition, every higher level of approximation requires higher levels of the velocity averaged collision integrals (Devoto, 1966). These integrals may not have been tabulated for the level of approximation required, thus necessitating approximation of their values, and thereby introducing error (Devoto, 1967a). I· should be noted that computing speed and memory have come a long way since DeVoto's 1973 paper and computations of this magnitude, although not trivial, need no longer be avoided or considered too complex.

With the above discussion in mind, the exact formulations for the transport coefficients are presented followed by a discussion of possible alternatives designed to decrease computational complexity without a severe loss of accuracy. Finally conclusions will be presented on the best approach to the calculation of the coefficients.

E.1 Complete Expressions for the Transport Coefficients

In this section the complete expressions for the second approximation of the viscosity, the third approximation of the heavy species thermal conductivity, the third approximation of the electron thermal conductivity, the third approximation of the multicomponent species diffusion coefficient, and the third approximation to the thermal diffusion coefficient will be given.

According to the Chapman-Enskog theory of the calculation of the transport coefficients, the viscosity as well as the thermal conductivity are independent of the gas pressure for an undissociated and unionized gas (Chapman and Cowling, 1990, and Vanderslice et al., 1962). However as gas temperature is increased, and dissociation and ionization occur, these properties will depend on pressure because the composition of species present will depend upon pressure (Vanderslice et al., 1962). Therefore thermal conductivity and viscosity are functions of temperature and species involved (number densities and masses as well as interaction potentials).

The expressions will be given in the form of ratios of determinants. The determinant elements are functions of interaction potentials and species masses. The elements will be given in a shorthand system where an array of values are represented by a single symbol:

$$
q_{ij}^{mp} =
\begin{matrix}
q_{11}^{mp} & q_{12}^{mp} & \cdots & q_{1v}^{mp} \\
q_{21}^{mp} & q_{22}^{mp} & \cdots & q_{2v}^{mp} \\
\cdots & \cdots & \cdots & \cdots \\
q_{v1}^{mp} & q_{v2}^{mp} & \cdots & q_{vv}^{mp}
\end{matrix}
\tag{E.1}
$$

where v is the number of species in the mixture, and the superscripts are numbers ranging from zero to the level of approximation minus one (Devoto, 1966).

E.1.1 Viscosity

In the calculation of the mixture viscosity, the contribution of electrons is sometimes assumed to be negligible due to their small mass (Mitchner and Kruger, 1973). Devoto (1967b) has noted that the neglect of electron-heavy collisions causes a deviation of only 0.9% at 20000K, 1 atm argon in the 2nd approximation when compared with the complete expression including electron-heavy collisions. Devoto also notes that in the case of a fully ionized hydrogen plasma (protons and electrons), that the neglect of electron-heavy collisions causes a 6.1% higher value for the viscosity (Devoto, 1967b and 1968).

The second approximation of the viscosity of a multicomponent mixture of v species is given by Devoto (1966):

$$
[\mu]_2 = -\frac{5\sqrt{2\pi k_b T}}{2 \, |q|}
\begin{vmatrix}
q_{ij}^{00} & q_{ij}^{01} & n_i\sqrt{m_i} \\
q_{ij}^{10} & q_{ij}^{11} & 0 \\
n_j & 0 & 0
\end{vmatrix}
\tag{E.2}
$$

where each element q_{ij}^{00}, represents an array of elements as defined above with $m=p=0$ and with i and j going from 1 to v. The $|q|$ appearing in the denominator represents the determinant of the numerator with the last row and column deleted. Therefore it is clear that a 7 component mixture would yield an expression with a 15 by 15 determinant divided by a 14 by 14 determinant.

The expressions for the q elements are also given by Devoto (1966). The first shorthand array symbol is :

$$q_{ij}^{00} = 8n_i \left(\frac{m_i}{m_j}\right) \sum_s \frac{n_s \sqrt{m_s}}{(m_i + m_s)^{3/2}} \left[\frac{10}{3} \bar{Q}^{(1,1)}(\delta_{ij} - \delta_{js})m_j + 2m_s \bar{Q}^{(2,2)}(\delta_{ij} + \delta_{js})\right] \quad (E.3)$$

where the $\bar{Q}^{(a,b)}$ are velocity averaged collision integrals for the particular interaction between species i and s with understood subscripts of i and s.

The other three array q elements are also functions of number density, species masses, and various collision integrals similar to the expression above (Devoto, 1966). As an exception to my self enforced rule of completeness, these expressions will not be listed here but can be seen in Devoto (1966). It is important to note which collision integrals are involved in the construction of the viscosity determinant elements. These are $\bar{Q}^{(1,1)}$, $\bar{Q}^{(2,2)}$, $\bar{Q}^{(1,2)}$, $\bar{Q}^{(2,3)}$, $\bar{Q}^{(1,3)}$, $\bar{Q}^{(3,3)}$, $\bar{Q}^{(2,4)}$. It should be understood that these integrals as listed are required for every interaction between all species i and j. Fortunately this represents relatively few types of interaction since most are simply shielded coulomb interactions between charged species. More will be said regarding these collision integrals in a later section.

E.1.2 Heavy Species Thermal Conductivity

The thermal conductivity may have contributions due to several effects which include frozen conductivity, thermal diffusion, and reactive thermal conductivity due to chemical reactions (Devoto, 1966, Grier, 1966, Butler and Brokaw, 1957, and Muckenfuss and Curtiss, 1958). The frozen thermal conductivity can be subdivided further into a translational portion and an internal portion which represents internal modes of energy (rotation, vibration, electronic excitation) (Vanderslice, et al., 1962).

In the case of an unionized gas the contribution of thermal diffusion to the thermal conductivity has been found to be less than 2% (Devoto, 1966, and Muckenfuss and Curtiss, 1958). However there is a non-negligible contribution to the gas thermal conductivity when ionization is present due to thermal diffusion of the electrons (Devoto, 1966, and Grier, 1966). This contribution however is to the gas thermal conductivity *including the electrons*. For a hydrogen plasma at conditions between 10^{-5} and 100 atmospheres pressure, and 5000 K and 40000 K temperature, the

contribution of thermal diffusion to the thermal conductivity is always less than 6% of the total thermal conductivity (Grier, 1966).

In the context of the current work, the heavy species conductivity is to be calculated separately from that of the electrons. Therefore the approach here will be to calculate the thermal diffusion components of thermal conductivity for both electrons and heavy species separately from the thermal conductivity coefficients. The calculation of the thermal diffusion coefficient is presented in a later section.

The contribution of internal modes of energy can be significant in the case of polyatomic molecules with internal degrees of freedom. The model has no provision for the various rotational and vibrational states of molecular hydrogen or of the minor molecular hydrogen ions. However the population of excited neutral states are included. Therefore the internal conductivity associated with electronic excitation is included in the model but rotational and vibrational modes are neglected. The collisional-radiative model is the tool for keeping track of translational energy lost or gained due to electronic transitions within neutrals.

The final contribution to the heavy species thermal conductivity is the reactive thermal conductivity. The reactions of interest in the hydrogen plasma are dissociation, ionization and recombination of species. The reactive conductivity is a consequence of the possibility that atoms resulting from molecular dissociation, or an ion and an electron resulting from ionization in a hot region may then diffuse to a cooler region and recombine, thereby releasing the energy of dissociation or ionization carried from the hot region. The reactive thermal conductivity may be comparable to or even greater than the translational thermal conductivity for hydrogen at 1 atm in the temperature range from 12000 to 18000 K (Devoto, 1968). In the scheme of the overall model reactive thermal conductivity is accounted for by the collisional-radiative model, which produces source terms for species production and also the corresponding energy sources or sinks.

Therefore, to summarize the approach to the heavy thermal conductivity, the contribution of internal energy due to electronic excitation is included through the C-R model, as is the reactive thermal conductivity. The contribution of thermal diffusion is handled through calculation of

species thermal diffusion coefficients and corresponding thermal diffusion mass fluxes. Finally, rotational and vibrational internal energy modes are neglected. The calculation of the third approximation of the translational heavy thermal conductivity coefficient is then given by the expression (Devoto, 1966):

$$
[\lambda_h]_3 = - \frac{75 k_b \sqrt{2\pi k_b T}}{8 \ |d|} \begin{vmatrix} d_{ij}^{00} & d_{ij}^{01} & d_{ij}^{02} & 0 \\ d_{ij}^{10} & d_{ij}^{11} & d_{ij}^{12} & n_i \\ d_{ij}^{20} & d_{ij}^{21} & d_{ij}^{22} & 0 \\ 0 & \dfrac{n_j}{\sqrt{m_j}} & 0 & 0 \end{vmatrix} \tag{E.4}
$$

where each d_{ij}^{00} element represents a two dimensional array with dimensions equal to the number of species being considered and the $|d|$ appearing in the denominator represents the determinant of the numerator with the last row and column deleted. Therefore for a mixture of six heavy species equation (E.4) represents a 19 by 19 determinant divided by an 18 by 18 determinant.

Again the d array elements are given in Devoto ('966). An example of such an element is:

$$
d_{ij}^{00} = 8 \sum_s \frac{n_s \sqrt{m_i}}{(m_i + m_s)^{1/2}} \bar{Q}^{(1,1)} \left[n_i \sqrt{\frac{m_s}{m_j}} (\delta_{ij} - \delta_{js}) - n_j \frac{\sqrt{m_s m_j}}{m_i} (1 - \delta_{is}) \right] \tag{E.5}
$$

where again the $\bar{Q}^{(a,b)}$ are velocity averaged collision integrals for the particular interaction between species i and s with understood subscripts of i and s. The expressions for the other array elements are in Devoto (1966) and need not be reproduced here. However, as for the case of viscosity the collision integrals that appear in the expressions should be noted. These integrals are $\bar{Q}^{(1,1)}$, $\bar{Q}^{(1,2)}$, $\bar{Q}^{(1,3)}$, $\bar{Q}^{(1,4)}$, $\bar{Q}^{(1,5)}$, $\bar{Q}^{(2,2)}$, $\bar{Q}^{(2,3)}$, $\bar{Q}^{(2,4)}$, and $\bar{Q}^{(3,3)}$. Again it should be understood that these integrals as listed are required for every interaction between all species i and j.

E.1.3 Electron Thermal Conductivity

The coefficient of thermal conductivity for electrons only can be calculated from a simplified expression which was derived with the assumption that in an electron heavy particle collision only the momentum of the electron is appreciably altered (Devoto, 1967b). The expression for the third approximation of the electron thermal conductivity is (Devoto, 1967b):

$$[\lambda_e]_3 = \frac{75n_e^2 k_b}{8}\sqrt{\frac{2\pi k_b T_e}{m_e}}\frac{b^{22}}{b^{11}b^{22} - b^{12}b^{12}} \tag{E.6}$$

where the b elements are functions of electron mass, all the species number densities and collision integrals. These integrals are $\bar{Q}^{(1,1)}$, $\bar{Q}^{(1,2)}$, $\bar{Q}^{(1,3)}$, $\bar{Q}^{(1,4)}$, $\bar{Q}^{(1,5)}$, $\bar{Q}^{(2,2)}$, $\bar{Q}^{(2,3)}$, and $\bar{Q}^{(2,4)}$. In this case only the collisions between electrons and the other species are involved (Devoto, 1967b).

E.1.4 Species Diffusion Coefficients

In the framework of the Chapman-Enskog Theory with which all the transport coefficients are to be computed, there are two types of diffusion coefficient to be considered. The diffusion velocity of a species, i, within a mixture of gases can therefore be divided into two parts, each with its corresponding diffusion coefficient (Chapman and Cowling, 1990, and Hirschfelder, Curtiss, and Bird, 1954). The diffusion coefficient usually associated with species gradients will be referred to herein as the multicomponent diffusion coefficient. The other diffusion coefficient is the thermal diffusion coefficient which was briefly mentioned above.

The complete expression for the calculation of the diffusion velocity of species i as given by Hirschfelder, Curtiss, and Bird, (1954, p. 479), and Devoto (1966) is:

$$\mathbf{V}_i = \left(\frac{n^2}{n_i\rho}\right)\sum_j m_j D_{ij} \mathbf{d}_j - \frac{1}{n_i m_i}D_i^T \frac{\partial}{\partial r}(\ln T) \tag{E.7}$$

where n is number density, ρ is mass density, m is species mass, T is kinetic temperature, D_{ij} is the multicomponent diffusion coefficient, and D_i^T is the thermal diffusion coefficient. The vector quantities are denoted with boldface type. The quantity represented by $\mathbf{d}_j$ is also given by Devoto (1966) as:

$$\mathbf{d}_j = \frac{\partial}{\partial r}\left(\frac{n_j}{n}\right) + \left(\frac{n_j}{n} - \frac{n_j m_j}{\rho}\right)\frac{\partial}{\partial r}(\ln P) - \left(\frac{n_j m_j}{P\rho}\right)\left(\frac{\rho}{m_j}\mathbf{X}_j - \sum_i n_i\mathbf{X}_i\right) \tag{E.8}$$

where P represents gas pressure, and $\mathbf{X}_j$ is the external force on species j. The quantity represented by $\mathbf{d}_j$ in equation (E.8) has three components, each of which drive the diffusion of species. The first term is the familiar species gradient term which tends to reduce the inhomogeneity of a nonuniform gas (Chapman and Cowling, 1990, p.141). The second term indicates the effect in a gas with nonuniform pressure in which the heavier species diffuse towards

the region of greater pressure (Chapman and Cowling, 1990, p.141). Finally, the third term represents the effect of unequal external forces acting on the different species (Chapman and Cowling, 1990, p.141). In the case of uniform pressure and no external forces acting on the gas, the last two terms in equation (E.8) disappear and the species gradient is all that remains. For the problem at hand, there are no external fields and the pressure is close to uniform (The SIMPLE algorithm is based upon a reference pressure with a small pressure variation) so the third term is identically zero while the second term is small compared to the first and is therefore neglected. Therefore combining equations (E.7) and (E.8) with only the species gradient term remaining results in:

$$V_i = \left(\frac{n^2}{n_i \rho}\right) \sum_j m_j \, D_{ij} \frac{\partial}{\partial r}\left(\frac{n_j}{n}\right) - \frac{1}{n_i m_i} D_i^T \frac{\partial}{\partial r}(\ln T_i) \qquad (E.9)$$

The second contribution to the total diffusion velocity is that due to thermal diffusion. This phenomenon was unknown theoretically and unobserved experimentally before the work of Chapman and Enskog (Hirschfelder, Curtiss, and Bird, 1954, p. 479). In gas mixtures of neutral species, the diffusion due to thermal gradients is usually ignored (Devoto, 1966). However in the case of a highly ionized gas at least the third approximation of the thermal diffusion coefficient must be used for accuracy (Devoto, 1966).

From the structure of equation (E.9), it is easily seen that the diffusion velocity of species i depends upon the local temperature gradient and the species gradients of all the other species. This at first may seem strange but it makes good sense if it is remembered that the sum of all the species diffusion mass fluxes must be zero, or (Hirschfelder, Curtiss, and Bird, 1954, p. 516):

$$\sum_i n_i m_i \, V_i = 0 \qquad (E.10)$$

Therefore with equation (E.10) in mind, it can be shown that the diffusion mass flux of species i as given by equation (E.9) is the negative of the collective mass flux of all the other species due to multicomponent diffusion plus a contribution due to thermal diffusion. The expressions for the third approximations of the multicomponent and thermal diffusion coefficients will now be presented. The third approximation of the multicomponent diffusion coefficient is (Devoto, 1966):

$$[D_{ij}]_3 = \frac{3\rho n_i}{2nm_j|\xi|}\sqrt{\frac{2\pi k_b T}{m_i}}\begin{vmatrix} \xi_{hk}^{00} & \xi_{hk}^{01} & \xi_{hk}^{02} & (\delta_{hj} - \delta_{hi}) \\ \xi_{hk}^{10} & \xi_{hk}^{11} & \xi_{hk}^{12} & 0 \\ \xi_{hk}^{20} & \xi_{hk}^{21} & \xi_{hk}^{22} & 0 \\ \delta_{ki} & 0 & 0 & 0 \end{vmatrix}$$

(E.11)

Similarly the third approximation of the thermal diffusion coefficient is (Devoto, 1966):

$$[D_i^T]_3 = \frac{15n_i\sqrt{2\pi m_i k_b T}}{4\ |\xi|}\begin{vmatrix} \xi_{hk}^{00} & \xi_{hk}^{01} & \xi_{hk}^{02} & 0 \\ \xi_{hk}^{10} & \xi_{hk}^{11} & \xi_{hk}^{12} & n_h \\ \xi_{hk}^{20} & \xi_{hk}^{21} & \xi_{hk}^{22} & 0 \\ \delta_{ki} & 0 & 0 & 0 \end{vmatrix}$$

(E.12)

In both equations (E.11), and (E.12), the ξ_{hk}^{00} are representative of an array of elements as given in equation (E.1), and the δ_{ki} is the Kronecker delta. As with the case of thermal conductivity and viscosity, each of the ξ elements is a function of temperature, number densities, species masses, and collision integrals. The expressions for the ξ elements appearing in equations (E.11) and (E.12) are identical with the expressions for the d elements of the thermal conductivity given in equation (E.5) from Devoto (1966). Therefore the same set of collision integrals are required for the calculation of the diffusion coefficients as were required for the heavy species thermal conductivity. However in this case the electrons must also be included in the collision integrals. These integrals are $\bar{Q}^{(1,1)}$, $\bar{Q}^{(1,2)}$, $\bar{Q}^{(1,3)}$, $\bar{Q}^{(1,4)}$, $\bar{Q}^{(1,5)}$, $\bar{Q}^{(2,2)}$, $\bar{Q}^{(2,3)}$, $\bar{Q}^{(2,4)}$, and $\bar{Q}^{(3,3)}$.

E.1.5 Electrical Conductivity

Although it will not be used directly in this work, the calculation of electrical conductivity may also be of interest in the analysis of plasmas, especially in the case of arc discharges. The expression for electrical conductivity is a function of temperature, species density, species masses, multicomponent diffusion coefficients, and species charges (Devoto, 1966). Simplified expressions which neglect the contribution of ions (anything other than electrons) to the current are given by Devoto (1966 and 1967b). Therefore the calculation of the electrical conductivity is not

any more difficult than the other transport coefficients and will not be considered further in this work.

E.2 Collision Integrals

Essential to any calculation of transport coefficients are values of the previously mentioned velocity averaged collision integrals. The general expression for the collision integral is given by Hirschfelder, Curtiss, and Bird (1954, p. 484) as:

$$Q_{ij}^{(p,s)} = \sqrt{\frac{2\pi k_b T}{\mu_{ij}}} \int_0^\infty \int_0^\infty \left(e^{-\gamma_{ij}^2}\right) \gamma_{ij}^{2s+3} \left(1 - \cos^p\chi\right) b \, db \, d\gamma_{ij} \qquad (E.13)$$

where μ_{ij} is the reduced mass of colliding molecules i and j, γ_{ij} is the reduced relative speed of the colliding molecules, χ is the angle of deflection of the molecules in the center of gravity coordinate system, b is the impact parameter, and the superscripts of Q are related to be the values of the exponents in the integrand. The χ are in turn functions of the interaction potential between the colliding molecules (see Hirschfelder, Curtiss, and Bird, 1954, p. 525). The exact theory behind the calculation of these integrals is not of particular interest to the problem at hand. Rather the question is the determination of which integrals are necessary for the calculation of the above discussed transport coefficients. In each of the above sections, the types of collision integrals necessary for the particular transport coefficient were listed. In this section a complete accounting of the assumed interaction potentials between species and the references for the corresponding collision integrals is presented.

Assuming that all the neutral excited levels represent the same species, there are a total of seven species to be considered in the problem at hand. Including the interaction between both like and unlike species this results in 28 possible types of interaction. Fortunately because several of the species are singly charged ions, and will be treated as having the same potential, there are only 9 different interactions. The most concise way to summarize these interactions will be to present them in Table E.1, with references listed in Table E.2.

Table E.1 Summary of Assumed Interaction Potentials Between Species

Interaction Potential	e⁻	H⁺	H₂	H⁻	H₂⁺	H₃⁺	H
e⁻	RSC	ASC	EMP1	RSC	ASC	RSC	EMP2
H⁺		RSC	IPA	ASC	RSC	RSC	CTR
H₂			HYB1	IPA	IPA	IPA	RE
H⁻				RSC	ASC	ASC	CTR
H₂⁺					RSC	RSC	CTR
H₃⁺						RSC	CTR
H							HYB2

Legend for Table E.1 (References Listed in Table E.2)
RSC - Repulsive Screened Coulomb [1,2,3,4]
ASC - Attractive Screened Coulomb [1,2,3]
EMP1 - Curve fit of integrated empirical cross-sections [5,6,7,8]
EMP2 - Curve fit of integrated empirical cross sections [5,6]
IPA - Inverse Power Attractive Potential [5,9]
CTR - Charge Transfer [2,10]
HYB1 - Multiple interaction potentials depending upon temperature [11,12]
HYB2 - Multiple interaction potentials weighted by statistical weights of states [2,11]
RE - Repulsive Exponential Potential [11]

Table E.2 List of References for Tables E.1 and E.3

[1] Devoto (1973).
[2] Grier (1966).
[3] Mason, Munn, and Smith (1967).
[4] Smith, Mason, and Munn (1965).
[5] Aubreton and Fauchais (1983).
[6] Itikawa (1974).
[7] Itikawa (1978).
[8] Gupta and Khare (1978).
[9] Kihara, Taylor, and Hirschfelder (1960).
[10] Devoto (1968).
[11] Vanderslice, et al. (1962).
[12] Grier (1962).
[13] Monchick (1959).
[14] Mason (1954).
[15] Hirschfelder, Curtiss, and Bird (1954).
[16] Brokaw (1961).

The acronyms used in the table are written out in the legend and some are explained more completely in the following. The repulsive and attractive screened potentials (RSC and ASC) are to be used whenever the interaction involves two charged species. The Debye length for these shielded (or screened) potentials are calculated under the assumption that the shielding is by electrons only (Devoto, 1973). The expression for the Debye length is then only a function of electron temperature and number density (Devoto, 1973):

$$\lambda_D = \sqrt{\frac{k_b T_e}{4\pi e^2 n_e k_c}}$$
(E.14)

Using this Debye length, a nondimensional temperature is generated which is also a function of the heavy species temperature (Devoto, 1973, and Mason, Munn, and Smith, 1967):

$$T^* = \frac{k_b T_g \lambda_D}{e^2 k_c}$$
(E.15)

The values of the collision integrals are then calculated based on this nondimensional temperature.

Curve fits of integrated experimental and theoretical data from Itikawa (1974 and 1978), and Gupta and Khare (1978) were calculated by Aubreton and Fauchais (1983) for the interactions above with the acronyms EMP1 and EMP2. The cases of a neutral molecule interacting with an ion will be treated with the inverse power attractive potential (IPA) (Aubreton and Fauchais, 1983, and Kihara, Taylor, and Hirschfelder, 1960). The multiple interaction potentials (HYB1 and HYB2) refer to cases where more than one interaction potential may be in effect depending upon the energy states of the colliding molecules. In the calculation of the collision integrals for the molecule-molecule collision, the Modified Buckingham potential was used at low temperatures with the exponential repulsive potential used at high temperatures (Vanderslice, et al., 1962, and Grier, 1962). The collision integrals for the atom-atom collision have been calculated using two different sets of potentials. In the first formulation, the total collision integral was a statistically weighted average of an exponential attractive potential and an exponential repulsive potential (Grier, 1966). The second formulation used a statistically weighted average of one of two inverse

power attractive potentials (depending on the temperature) and an exponential repulsive potential (Vanderslice, et al., 1962).

The details of the interaction potentials and the computation of the collision integrals from the potentials are really not relevant to this work. All that really matters from a practical point of view is that the correct values for collision integrals be used for each interaction. The above discussion briefly described these interactions. Now the practical matter of which collision integrals are necessary for use in transport coefficient calculations will be discussed. First the collision integrals necessary for the levels of approximation described above will be listed.

Based on the discussion above and the expressions taken from Devoto (1966), the set of collision integrals necessary to calculate the above listed set of transport coefficients (including the second approximation of the mixture viscosity, and the third approximations to the heavy and electron thermal conductivity, multicomponent diffusion coefficient and thermal diffusion coefficient) includes $\bar{Q}^{(1,1)}$, $\bar{Q}^{(1,2)}$, $\bar{Q}^{(1,3)}$, $\bar{Q}^{(1,4)}$, $\bar{Q}^{(1,5)}$, $\bar{Q}^{(2,2)}$, $\bar{Q}^{(2,3)}$, $\bar{Q}^{(2,4)}$, and $\bar{Q}^{(3,3)}$. The exact sources for each of these integrals has not been completely sorted out. References as listed in Table E.2 for the collision integrals are tabulated in Table E.3 versus the interaction potentials.

Table E.3 Summary of References for Collision Integrals

Reference for Potential	$\bar{Q}^{(1,1)}$	$\bar{Q}^{(1,2)}$	$\bar{Q}^{(1,3)}$	$\bar{Q}^{(1,4)}$	$\bar{Q}^{(1,5)}$	$\bar{Q}^{(2,2)}$	$\bar{Q}^{(2,3)}$	$\bar{Q}^{(2,4)}$	$\bar{Q}^{(3,3)}$
RSC	3,4	3,4	3,4	1	1	3,4	3,4	1	3,4
ASC	3	3	3	1	1	3	3	1	3
EMP1	5	5	5	5	5				
EMP2	2,10, 5	2,5	2,5	5	5	2	2	2	
CTR	2,5	2	2			2,5			
RE	11,5, 13	11,13	11,13	13	13	11,5	13	13	13
IPA	5					5			
HYB1	5	15,13, 14	15,13, 14	15,13, 14	15,13, 14	5	15,13, 14	15,13, 14	15,13, 14
HYB2	5	13,16	13,16			2,5			

E.3 Possible Simplifications

Because of the great complexity of the calculation of the transport coefficients, it would be foolish not to try and simplify the calculation procedure. However as will be shown, none of the simplified schemes are accurate enough to justify their use simply to speed up computation.

Obviously a way to reduce the complexity of the calculations for the transport coefficients is simply to use lower approximations. However it has already been stated that the levels of approximation presented above are the minimum required to adequately predict coefficients at high degrees of ionization. In fact as has been mentioned above for completely ionized hydrogen, the third approximation to the thermal conductivity was found to be approximately *twice* the value of the second approximation (Grier, 1966).

The second alternative to the higher approximations involves what are commonly referred to as mixture rules (Brokaw, 1958, Mason and Saxena, 1958, Gambill, 1958, and Wilke, 1950). These are usually derived empirically by proposing an analytical relation with some variable constants and then adjusting the constants to fit experimental data. These mixture rules are usually applied when the the transport coefficients of each species of a mixture are known (most likely from experimental data) and the mixture coefficient is desired. These mixture rules may also be used if the pure species coefficients are calculated from theory. In cases of neutral gas mixtures these rules often perform very well in the prediction of the mixture coefficients. However, when ionized gas mixtures are considered, unacceptable errors may result (up to 30% error in argon) (Devoto, 1967a). If high level approximations are used to calculate the pure species coefficients, it makes little sense to then use a mixing rule instead of using the high level approximation for the mixture. Therefore the only practical use of the mixing rules would be when the pure component coefficients are computed with the first nonzero approximations and these have already been shown to be inadequate.

Another way of possibly simplifying the calculations would be to simply neglect the minor species (H^-, H_2^+, and H_3^+) in the above expressions. This simplification may not introduce much error to the mixture viscosity or the heavy species thermal conductivity if the minor species mole

fractions were negligible. However by eliminating these species from consideration, a region in which their mole fractions are not negligible would result in large errors in the calculation of the transport coefficients. In addition none of the species may be neglected for the accurate calculation of the multicomponent and thermal diffusion coefficients.

E.4 Conclusions on Transport Coefficients

The rigorous method for the calculation of the transport coefficients has been presented. The physical ideas behind the calculations and how the calculations are used in the generalized non-LTE model have been briefly described. It is clear that no simplifications will be acceptable and that the complete expressions as presented are necessary. Therefore if all the exact collision integrals as required were found in the literature (those already identified were presented in Table E.2 above), the complete expressions could be implemented. In fact, for the generalized model, the complete expressions for all the coefficients have been programmed in subroutine TRANSPORT and can be run with dummy values for the collision integrals to produce dummy results for the transport coefficients.

Assuming that sources for all the required collision integrals are available, the procedure for the calculation of the transport coefficients involves:

1. The necessary collision integrals are to be evaluated using the heavy temperature for collisions involving only heavy species (Debye shielding is to be calculated with the electron temperature) and the electron temperature for collisions involving electrons and any species.

2. The transport coefficients are to be calculated to the levels of approximation described above with the following additional fine points. Electrons are included in the calculation of viscosity to avoid errors at high levels of ionization using equation (E.2) (Devoto, 1967b and 1968). The value for the temperature appearing in this equation is the heavy species temperature. Only heavy species are included in the heavy thermal conductivity, and of course the heavy species temperature is used in equation (E.4). The electron thermal conductivity is calculated with equation (E.6) which involves electron temperature and only collisions between electrons and the other species. The diffusion coefficients are computed using equations (E.11) and (E.12) with electron

temperature used for cases of electron diffusion, and heavy species temperature used for cases of heavy species diffusion.

3. The species diffusion velocities and diffusive heat fluxes are calculated in subroutine DIFFVEL which is called in every iteration since the species and temperature gradients may continuously be changing. In particular, the total (ordinary and thermal) electron and heavy species diffusive fluxes are computed using equation (E.9) for use in the electron and heavy energy equations. Due to the nature of the diffusion terms in the species continuity equations, it is necessary to compute an effective ordinary diffusion coefficient, D_{eff}, which is described further in Appendix G. The term for ordinary diffusion is accompanied by terms that account for thermal diffusion of the particular species. Since these thermal diffusion terms do not involve the species number density, they are treated as source terms in the species continuity equations.

4. The contributions of internal and reactive thermal conductivity are handled through the use of the collisional-radiative model and its resulting species and energy source terms. A description of the C-R model follows in Appendix F.

Appendix F. Collisional - Radiative Model

The species populations in a non-LTE plasma may or may not be determined in the same way as for an LTE plasma as was briefly described in Chapter 1. There, as an example, the law of mass action was applied to a hydrogen atom ionization reaction to derive what is commonly called the Saha equation. Potapov (1966) originally derived the most general form of the law of mass action, allowing for kinetic nonequilibrium. If the kinetic and excitation temperatures are known or assumed in advance, then electron and ion number densities may be computed using Potapov's relation. An improved version of of Potapov's law of mass action applicable to electron excitational nonequilibrium (different electron and Boltzmann temperatures) was part of the Generalized Multithermal Equilibrium (GMThE) model used by Cho (1988) to compute species densities. The GMThE model was applied by Sedghinasab and Eddy (1991) to compute argon thermodynamic properties for the case of kinetic, and electron excitational nonequilibrium. The GMThE model was extended to include chemical nonequilibrium (non-zero chemical affinity) by Eddy and Cho (1991), applied to an experimental analysis by Eddy, Grandy and Detering (1991), and as part of a theoretical species density computation by Chen and Eddy (1991). In all of these cases, some aspect of the system such as the kinetic temperatures, or the chemical affinity was known or assumed. A variation of these methods was used to compute species densities for the simplified model as described in Appendix J.

Even if the kinetic temperatures and the chemical affinity are known, determination of species populations in a non-LTE LSP may not be possible through the use of a Boltzmann distribution, because in general there may not be a well defined Boltzmann temperature. In additi , in a stationary steady state LSP, diffusion of species is important and should not be ignored. In the non-LTE case the collisional and radiative processes and their competing rates of reaction should be examined in detail, which Siegel and Howell (1981, p. 447) refer to as, "...a most formidable undertaking." Nevertheless, a collisional-radiative (C-R) model such as those given by Bates, Kingston, and McWhirter (1962a and 1962b), Cho and Eddy (1989), Gomes (1983), Drawin (1969a and 1969b), Venugopalan (1971a, pp. 126-221), Kunc (1984 and 1987), Braun and Kunc

(1987), Kunc and Soon (1989), Kroesen, et al. (1990), and Vlcek (1989) must be used to determine the production rate of species (including photons) and the rates of elastic and inelastic energy transfer between species which are used as source terms in the conservation equations.

The following description of the collisional-radiative model will be given in four sections. The first section examines the reactions included, the corresponding rate coefficients, and the rates of inelastic energy transfer associated with each reaction. The second section describes the radiation discretization and the structure of the bands and lines. The third section examines the formulation of the inelastic and elastic energy transfer source terms for the energy equations. The fourth section explains the method of accounting for non-local radiation.

F.1 C-R Model Reaction Rates

The model operates by the inclusion of a rate term for every important process occuring within the plasma. A C-R model is intrinsically limited in accuracy by the accuracy of the rate coefficients, the number of excited neutral levels used and the possible exclusion of important non-local radiative effects. Obviously the most important factor in such a model is the inclusion of a rate term for every important reaction. The rate terms are products of reactant number densities and a rate coefficient that is an analytical function of reactant energy (and frequency if photons are involved). There are twenty seven separate types of reaction (with some of these types representing multiple reactions) included in the model which are listed in Table F.1 and discussed individually in what follows. The reactions included do not represent all possible reactions that may occur in a hydrogen plasma but rather have been chosen based on the magnitude of the reaction coefficients.

Keeping with the aforementioned policy of completeness, each of the rate coefficients listed in Table F.1 will now be described in order. All expressions will be in MKS units (except where noted) for consistency and because MKS units are the naturally superior choice for all engineering applications.

Table F.1 Summary of reactions included in the C-R model

Reaction Description	Reaction	Rate Coefficient
1) Electron Collisional Ionization	$H(m) + e \Rightarrow H^+ + e + e$	S_{ic} [1]
2) Three Body Recombination	$H^+ + e + e \Rightarrow H(m) + e$	β_{ci} [1]
3) Photoionization	$H(m) + h\nu \Rightarrow H^+ + e$	σ_{ic} [1]
4) Radiative Recombination	$H^+ + e \Rightarrow H(m) + h\nu$	α_{ci} [1]
5) Excitation by Electron Collision	$H(m) + e \Rightarrow H(j) + e$ (j>m)	C_{mj} [1]
6) Deexcitation by Electron Collision	$H(j) + e \Rightarrow H(m) + e$ (j>m)	R_{jm} [1]
7) Spontaneous Emission	$H(j) \Rightarrow H(m) + h\nu$ (j>m)	A_{jm} [2]
8) Line Absorption	$H(m) + h\nu \Rightarrow H(j)$ (j>m)	B_{mj}
9) Stimulated Emission	$H(j) + h\nu \Rightarrow H(m) + 2h\nu$ (j>m)	B_{jm}
10) Electron Molecular Dissociation (A)	$e + H_2 \Rightarrow e + 2H(1)$	Rcoef(10) [3]
11) Electron Molecular Dissociation (B)	$e + H_2 \Rightarrow e + H(1) + H(2)$	Rcoef(11) [3]
12) Electron Molecular Ionization	$e + H_2 \Rightarrow 2e + H_2^+$	Rcoef(12) [3]
13) Electron Molecular Dissociative Ionization	$e + H_2 \Rightarrow 2e + H(1) + H^+$	Rcoef(13) [3]
14) Electron Diatomic Ion Dissociative Ionization	$e + H_2^+ \Rightarrow 2e + 2H^+$	Rcoef(14) [3]
15) Electron Diatomic Ion Dissociation (A)	$e + H_2^+ \Rightarrow e + H(1) + H^+$	Rcoef(15) [3]
16) Electron Diatomic Ion Dissociation (B)	$e + H_2^+ \Rightarrow e + H(2) + H^+$	Rcoef(16) [3]
17) Electron Diatomic Ion Dissociative Recombination	$e + H_2^+ \Rightarrow H(1) + H(n)$, n≥2	Rcoef(17) [3]
18) Electron Triatomic Ion Dissociative Recombination	A Branch: $e + H_3^+ \Rightarrow 3H(1)$ B Branch: $e + H_3^+ \Rightarrow H_2 + H(2)$	Rcoef(18) [3]
19) Electron Triatomic Ion Dissociation	$e + H_3^+ \Rightarrow e + 2H(1) + H^+$	Rcoef(19) [3]
20) Electron Molecular Dissociative Attachment	$e + H_2 \Rightarrow H(1) + H^-$	Rcoef(20) [3]
21) Diatomic Ion Molecular Dissociation	$H_2^+ + H_2 \Rightarrow H_3^+ + H(1)$	Rate(21) [3]
22) Electron Negative Ion Detachment	$e + H^- \Rightarrow 2e + H(1)$	Rcoef(22) [3]
23) Electron Negative Ion Ionization	$e + H^- \Rightarrow 3e + H^+$	Rcoef(23) [3]
24) Proton Negative Ion Neutralization (A)	$H^+ + H^- \Rightarrow H(1) + H(2)$	Rcoef(24) [3]
25) Proton Negative Ion Neutralization (B)	$H^+ + H^- \Rightarrow H(1) + H(3)$	Rcoef(25) [3]
26) Molecular Dissociation	$H_2 + H_2 \Rightarrow H_2 + 2H(1)$	molcoef [4]
27) Molecular Recombination	$H_2 + 2H(1) \Rightarrow 2H_2$	recom [4]

Legend for References Cited Above

[1] Kunc and Soon (1989).
[2] Wiese, Smith and Glennon (1966).
[3] Janev, et al. (1987).
[4] Oppenheim, et al. (1975).

F.1.1 Reaction One

Reaction number one is electron collisional ionization $\left(H(m) + e \Rightarrow H^+ + e + e\right)$ from any bound level, m. The source for rate number one was Kunc and Soon (1989) and the coefficient is given by:

$$S_{ic}(m) = \frac{\left(9.56 \times 10^{-12}\right)\left(\frac{k_b T_e}{jev}\right)^{-1.5}\exp(-\beta)}{\left(\beta^{2.33} + 4.38\beta^{1.72} + 1.32\beta\right)} \quad \left(\frac{m^3}{s}\right) \tag{F.1}$$

in which β is given by:

$$\beta = \frac{Ui(m)}{\left(\frac{k_b T_e}{jev}\right)} \tag{F.2}$$

and where $Ui(m)$ is the energy in eV required to ionize bound level m based on the value of the lowered ionization potential, m going from 1 to the uppermost bound level. Obviously, at each gridpoint there would be an $S_{ic}(m)$ coefficient for every bound level, m.

Since the energy required to ionize an atom in level m is $Ui(m)$, every time this reaction occurs the ionizing electron loses thermal energy in the amount equal to $Ui(m)$. Meanwhile, the heavy species experiences no change in thermal energy. Therefore the associated net thermal energy transfer for electrons and heavy species for reaction one can be written as:

$$\Delta E_{e1} = -Ui(m) \tag{F.2a}$$

$$\Delta E_{heavy1} = 0 \tag{F.2b}$$

F.1.2 Reaction Two

Reaction number two is three body recombination $\left(H^+ + e + e \Rightarrow H(m) + e\right)$ to any bound level, m. The source for rate number two was also Kunc and Soon (1989) and the coefficient is given by:

$$\beta_{ci}(m) = \left(\frac{g(m)}{g_e g_{H^+}}\right)\left(\frac{h^2}{2\pi m_e k_b T_e}\right)^{1.5}\exp(\beta)S_{ic}(m) \quad \left(\frac{m^6}{s}\right) \tag{F.3}$$

where the β in the exponent is given by equation (F.2) and the $g(m)$, g_e and g_{H^+} are degeneracies for atoms in level m, electrons, and protons, respectively.

In the recombination reaction above, every time a proton and an electron recombine the remaining electron recoils with an additional amount of thermal energy equal to Ui(m) plus whatever thermal energy the first electron may have had. Therefore the associated net thermal energy transfer for electrons and heavy species for reaction two can be written as:

$$\Delta E_{e2} = +Ui(m) \tag{F.3a}$$

$$\Delta E_{heavy2} = 0 \tag{F.3b}$$

F.1.3 Reaction Three

Reaction number three is photoionization $\left(H(m) + h\nu \Rightarrow H^+ + e\right)$. The rate coefficient for this reaction was computed by multiplying the cross section for photoionization (again from Kunc and Soon, 1989) by the speed of the impinging particles which are photons of energy $h\nu$. Due to the method in which radiation was discretized into bands and lines, the cross section for photoionization is a two dimensional array at each grid point. The index nband refers to the band or line involved in the reaction. The structure of the radiation discretization will be explained below. For now it is sufficient to note that if the average band energy (abe) of the photoionizing photons is not sufficient to ionize bound level m, then the cross section for the reaction is set to zero. If, however, the photoionizing photons are energetic enough to ionize level m, the expression for the photoionization cross-section (units of meters squared) is given by:

$$\sigma_{ic}(nband,m) = \left(\pi a_0^2\right)\left(\frac{64\alpha}{3^{1.5}}\right)\left(\frac{Ry}{h\nu}\right)^{1.5}\left(\frac{gf(m)}{m^5}\right) \ \left(m^2\right) \tag{F.4}$$

where a_0 is the first Bohr radius in meters, α is the fine structure constant, Ry is the Rydberg constant (in eV), and gf(m) is the dimensionless Gaunt factor (quantum correction) which is given by Kunc and Soon (1989) as:

$$gf(m) = 1 + (0.1728)\left(m^{-2/3}\right)\left(\psi+1\right)^{-2/3}\left(\psi-1\right) - (0.0496)\left(m^{-4/3}\right)\left(\psi+1\right)^{-4/3}\left(\psi^2+\left(\frac{4\psi}{3}\right)+1\right) \tag{F.5}$$

where $$\psi = m^2\varepsilon(nband,m) \tag{F.6}$$

and $\varepsilon(nband,m)$ is the energy of the ionized electron in eV.

Based on the definition of $\varepsilon(nband,m)$, it is apparent that whenever photoionization occurs, the ionized electron has a thermal energy equal to the difference between the energy of the ionizing

radiation and the ionization energy for level m, Ui(m). Therefore the associated net thermal energy transfer for electrons and heavy species for reaction three can be written as:

$$\Delta E_{e3} = \varepsilon(\text{nband},m) = E_{h\nu} - Ui(m) \tag{F.6a}$$

$$\Delta E_{heavy3} = 0 \tag{F.6b}$$

F.1.4 Reaction Four

The fourth rate coefficient is that of radiative recombination $\left(H^+ + e \Rightarrow H(m) + h\nu\right)$. Once again the source for this coefficient is Kunc and Soon (1989), although the original source quoted by Kunc and Soon is Johnson (1972). There is mention by Johnson (1972) of a slightly different formulation for the radiative recombination rate coefficient. In this approach, it is assumed that all bound levels with principal quantum number greater than a given number are in Saha equilibrium, and are treated as part of the continuum. However Kunc and Soon (1989) do not make this assumption and their expression for the rate coefficient for radiative recombination to bound atomic level m is given by:

$$\alpha_{ci}(m) = \left(5.197 \times 10^{-20}\right)\left(\beta^{3/2}\right)\exp(\beta)\left(\sum_{k=0}^{2} G_k(m)E_{k+1}(\beta)\right) \left(\frac{m^3}{s}\right) \tag{F.7}$$

where β is once again given by equation (F.2), the $G_k(m)$ are Gaunt factors which are functions of m, and the $E_{k+1}(\beta)$ are exponential integrals from p. 231 of Abramowitz and Stegun (1965).

The energy of the photons produced by reaction number four is equal to the sum of the thermal energy of the recombining electron and the ionization energy of level m, Ui(m). As will be explained below, the photon energy will determine to which band (or line) production term it is added. Therefore the associated net thermal energy transfer for electrons and heavy species for reaction four can be written as:

$$\Delta E_{e4} = -\frac{3}{2}\frac{k_b T_e}{jev} \tag{F.7a}$$

$$\Delta E_{heavy4} = 0 \tag{F.7b}$$

F.1.5 Reaction Five

Rate coefficient five is excitation by electronic collision $\left(H(m) + e \Rightarrow H(j) + e \ (j>m)\right)$. This reaction represents all reactions in which a hydrogen atom in bound principal quantum state m

is excited to bound principal quantum state j through electron collision. Therefore the rate coefficient is actually a two dimensional array of m and j, $m \neq j$. The expression for this rate coefficient is given by Kunc and Soon (1989) as:

$$C_{mj}(m,j) = \left(\frac{(1.6 \times 10^{-13}) \sqrt{\frac{k_b T_e}{jev}}}{\frac{k_b T_e}{jev} + \Gamma_{mj}}\right) \left\{(X_{mj}) \ln\left(\frac{0.3 k_b T_e}{(jev)(Ry)} + \Delta_{mj}\right) + Y_{mj}\right\} \exp(-\xi) \quad \left(\frac{m^3}{s}\right) \quad (F.8)$$

where ξ, X_{mj}, Y_{mj}, Δ_{mj}, and Γ_{mj} are given by the expressions:

$$\xi = \frac{\Delta E_{mj}}{\left(\frac{k_b T_e}{jev}\right)} \quad (F.9)$$

$$X_{mj} = \left(\frac{2Ry}{\Delta E_{mj}}\right) f_{mj} \quad (F.10)$$

$$Y_{mj} = \left(\frac{4Ry^2}{j^3}\right)\left(\frac{1}{\Delta E_{mj}^2} + \frac{4 Ui(m)}{3 \Delta E_{mj}^3} + b_m \frac{Ui(m)^2}{\Delta E_{mj}^4}\right) \quad (F.11)$$

$$\Delta_{mj} \approx \frac{(Ry) \ln\left(1 + m^3\left(\frac{k_b T_e}{jev \, Ry}\right)\right)\left(3 + 11\frac{(j-m)^2}{m^2}\right)}{6 + 1.6(j)(j-m) + 0.3(j-m)^{-2} + 0.8(j^{3/2})\left((j-m)^{-1/2}\right)((j-m)-0.6)} \quad (F.12)$$

$$\Gamma_{mj} = \frac{0.06 \, (j-m)^2}{mj^2} \exp\left(\frac{-Y_{mj}}{X_{mj}}\right) \quad (F.13)$$

in which f_{mj} are oscillator strengths from Wiese, Smith and Glennon (1966), ΔE_{mj} is the energy difference in eV between bound levels m and j, and the b_m in Y_{mj} are given by the expression:

$$b_m = \frac{(1.4) \ln(m)}{m} - \frac{0.7}{m} - \frac{0.51}{m^2} + \frac{1.16}{m^3} - \frac{0.55}{m^4} \quad (F.14)$$

Once again reaction five has zero heavy thermal energy transfer associated with it. However excitation energy gained by the atom in reaction five is supplied by a loss of thermal energy of the electron. Therefore the associated net thermal energy transfer for electrons and heavy species for reaction five can be written as:

$$\Delta E_{e5} = -\Delta E_{mj} \quad (F.14a)$$

$$\Delta E_{heavy5} = 0 \quad (F.14b)$$

F.1.6 Reaction Six

The rate coefficient for the sixth reaction, $\left(H(j) + e \Rightarrow H(m) + e \; (j>m)\right)$, deexcitation by electronic collision, is given by Kunc and Soon (1989) as:

$$R_{jm}(j,m) = \frac{C_{mj}(m,j)}{exp(-\xi)} \frac{g(m)}{g(j)}$$

(F.15)

where $g(m)$ and $g(j)$ are the degeneracies of bound levels m and j respectively.

As with reaction five, the energy of deexcitation of the atom in reaction six is carried away by the electron. Therefore the associated net thermal energy transfer for electrons and heavy species for reaction six can be written as:

$$\Delta E_{e6} = + \Delta E_{mj}$$

(F.15a)

$$\Delta E_{heavy6} = 0$$

(F.15b)

It can be noted that all the first six rate coefficients were taken from Kunc and Soon (1989) and therefore all have the same validity conditions. The first six rates are valid for stationary hydrogen plasma with $11000K \leq T_e \leq 15000K$ and $10^{16} \leq n_{tot} \leq 10^{24}$ m^{-3}.

F.1.7 Reaction Seven

The seventh reaction is spontaneous emission $\left(H(j) \Rightarrow H(m) + h\nu \quad (j>m)\right)$. As the name implies, this reaction occurs spontaneously, independent of the plasma conditions. The spontaneous emission rate coefficients (also known as the spontaneous Einstein coefficient), A_{jm}, have units of inverse seconds and have been taken from the compilation of Wiese, Smith and Glennon (1966). The structure of the lines included in the C-R model (and the corresponding A_{jm}) are discussed below in the section on radiation discretization.

F.1.8 Reaction Eight

Reaction number eight is line (induced) absorption $\left(H(m) + h\nu \Rightarrow H(j) \quad (j>m)\right)$. The induced absorption coefficient, B_{mj}, may easily be computed from the spontaneous emission coefficient through the relation (Venugopalan, 1971a, p. 104):

$$B_{mj} = \frac{g(j)}{g(m)} \frac{c^3}{8\pi h\nu_{jm}^3} A_{jm}$$

(F.16)

in which the ν_{jm} is the nominal frequency of the line transition between levels m and j. The induced absorption coefficient is also known as the Eintein induced absorption coefficient.

F.1.9 Reaction Nine

Einstein's third coefficient, the stimulated emission coefficient, B_{jm} is reaction coefficient number nine. The reason coefficients seven through nine carry Einstein's name is because he was responsible for postulating their existence in the context of a radiating system in thermal equilibrium (Einstein, 1916). The stimulated emission coefficient may easily be computed from the induced absorption coefficient using the simple relation given by Venugopalan (1971a, p. 104):

$$B_{jm} = \frac{g(m)}{g(j)} B_{mj} \tag{F.17}$$

Since reactions seven through nine involve only the production or destruction of photons and the associated internal energy changes of excited atoms, the net thermal energy transfer for electrons and heavy species are both zero for all three reactions.

Reactions one through nine along with a consistently discretized radiation structure would be sufficient to model the reactions of hydrogen plasma if only atoms, electrons and protons were involved. However, due to the fact that molecules and the minor species are also included in the full analysis, 18 additional reactions had to be included. It was essential that each species had at least one production and one destruction reaction.

F.1.10 Additional Reactions

The source for reaction coefficients ten through twenty five was Janev, et al. (1987). The reaction coefficient for each of these reactions, which appear in Table F.1, was computed through an eighth order polynomial/logarithmic curve fit provided by Janev, et al. (1987). Each curve fit has the form:

$$\text{rate coefficient} = \sum_{n=0}^{8} bj1(R,n)(\ln T)^n \tag{F.18}$$

for the electron-heavy particle collision reactions, and:

$$\text{rate coefficient} = \sum_{nn=0}^{8} \sum_{n=0}^{8} bj2(R,nn,n)(\ln E)^{nn}(\ln T)^n \tag{F.19}$$

for the heavy-heavy collision reactions. E represents the kinetic energy of the impinging particles (for heavy-heavy reactions) in eV and T represents a variation of kinetic temperature of the

electrons in the electron-heavy reactions in eV. It should be noted that T does not represent true kinetic temperature as it is defined by Janev et al., but rather it actually represents $1.5k_bT$. The R appearing in the curve fit coefficients refers to the reaction number.

Due to the nature of the curve fits, the coefficients required will not be listed here but may be found in arrays bj1 and bj2 which are initialized in the generalized model version of subroutine BLOCK DATA. Each curve fit was stated to be valid between some lower temperature value and some upper temperature value. All the reactions cited (10-25) except for reaction 21 have curve fits valid up to 20000 eV (as defined by Janev, et al., and which converts to 1.547×10^8 K). Reaction number 21 is valid up to 50 eV Janev temperature. Although it doesn't appear likely. if the local temperature exceeds the upper curve fit validity limit, then the coefficients are computed using the upper limiting temperature. The lower validity limits on temperature for all the Janev reactions are listed in Table F.2. If the local electron temperature is less than the lower validity limit for a particular electron-heavy reaction, then the rate coefficient is either set to zero or the low end limiting value for that reaction depending on the slope of the coefficient versus temperature. The low limit coefficient values are also listed in Table F.2. In the case of the three heavy-heavy collision reactions included (21, 22, and 25), if the local heavy temperature is lower than the low limit, then the low limit is used in the curve fit. The rjh term appearing in Table F.2 is a weighting factor used to determine the distribution of excited atomic states resulting from reaction 17.

The species produced in reaction 18 depend upon which branch is being considered. The two branches are weighted as a function of electron temperature such that, if $T_e \leq 1.0$ eV (Janev temperature), then the A Branch is weighted by $\left(\frac{2.5}{3.5}\right)$ and the B Branch is weighted by $\left(\frac{1.0}{3.5}\right)$ However if $T_e > 1.0$ eV (Janev temperature), then the A Branch is weighted by $\left(\frac{1.0}{3.5}\right)$ and the B Branch is weighted by $\left(\frac{2.5}{3.5}\right)$

Finally, because the reaction coefficient for reaction 20 is only strictly applicable to molecules that are in at least the fifth excited ($v \geq 4$) vibrational state, a further validity limit was imposed. If the heavy temperature is not at least equal to 0.1eV Janev temperature (773K), then the rate

coefficient for reaction 20 is set to zero. This heavy temperature condition appears in Table F.2 in parenthesis next to the electron temperature validity limit and rate coefficient for reaction 20.

The net thermal energy transfer associated with reactions 10 through 25 are summarized in Table F.2. It should be noted that in most cases the net electron thermal energy transfer does not balance the net heavy species thermal energy transfer due to changes in internal energy of heavy species, or energy lost to or gained from dissociation or ionization. In cases where there is no value given for thermal energy transfer by Janev, et al. (1987), such as for reaction 25, the net thermal energy transfer terms have been computed based on the energy level structure of the species involved.

Table F.2 Validity Limits, Coefficient Values and Energy Transfer

Reaction Number	Low Temp Limit (K)	Low Limit Rate Coefficient	ΔE_e (eV)	ΔE_{heavy} (eV)
10	9745	0	-10.5	+6.024
11	19413	0	-15.3	+0.628
12	15469	0	-15.427	0
13	30783	0	-18.5	+0.5
14	24441	0	-15.5	+0.8
15	1547	0	-10.5	+8.6
16	15469	0	-17.5	+3.0
17	773	2.23×10^{-13} (m^3/s)	$-\frac{3}{2}\frac{k_b T_e}{jev}$	$+\left(\frac{3k_b T_e}{2jev} + \frac{R\,y}{n^2}\right)rjh(n)$
18 (both branches)	773	1.05×10^{-13} (m^3/s)	$-\frac{3}{2}\frac{k_b T_e}{jev}$	$+\frac{3}{2}\frac{k_b T_e}{jev}$
19	9745	0	-14.0	+13.0
20	773 (773)	1.58×10^{-14} (m^3/s) (0)		
		$T_e \leq 5762$:	$-\frac{3}{2}\frac{k_b T_e}{jev}$	$+\frac{3}{2}\frac{k_b T_e}{jev}$
		$T_e > 5762$	-0.745	+0.745
21	773	Low Limit Used in Curve Fit	0	1.17
22	975	0	-0.754	0
23	19413	0	-14.35	0
24	773	Low Limit Used in Curve Fit	0	2.645
25	773	Low Limit Used in Curve Fit	0	0.757

F.1.11 Molecular Hydrogen Reactions

The final two reactions, 26 and 27, are the molecular dissociation $\left(H_2 + H_2 \Rightarrow H_2 + 2H(1)\right)$ and recombination $\left(H_2 + 2H(1) \Rightarrow 2H_2\right)$ reactions. The source for the molecular dissociation rate coefficient is Oppenheim, et al. (1975), and the expression for the coefficient is:

$$\text{molcoef} = \left(8.643 \times 10^{-15}\right)\left(T_g^{0.07}\right)\exp\left(\frac{-52249.4}{T_g}\right)\left(\frac{m^3}{s}\right) \qquad (F.20)$$

The net thermal energy lost by the heavy species in dissociation induced through collisions with other heavy species is the dissociation energy of the hydrogen molecule, -4.476 eV.

The rate coefficient for molecular recombination is given by Oppenheim, et al. (1975) as a constant:

$$recom = 2.757 \times 10^{-45} \left(\frac{m^6}{s}\right) \qquad (F.21)$$

The net thermal energy gained by the heavy species from the recombination of reaction 27 is simply the dissociation energy, +4.476 eV.

F.2 Discretized Radiation Structure

Radiation in the LSP will consist of contributions from line emission, free-bound emission, and free-free emission. In many cases the wavelength structure of the radiation is conveniently ignored by assuming that the radiation is either optically thick or optically thin (Glumb and Krier, 1986, Jeng and Keefer, 1987b, and Eguiguren, 1989). In this approach, the energy associated with the optically thin part of the radiation is assumed to pass through the plasma to the surroundings, and is therefore represented by a sink (energy loss) term in the energy equation. Conversely, the optically thick radiation energy is modeled as conductive energy transfer and is included in the energy equation by enhancing the local thermal conductivity coefficient. The enhancement is referred to as the radiative conductivity coefficient which was modeled by Kemp and Root (1979) for radiation of photon energy greater than 13 eV. It was assumed that this radiation was near equilibrium with the plasma species, which would mean the species had an unlikely kinetic temperature of 100548K. Unfortunately, as mentioned by Jeng and Keefer (1987b), the radiative conductivity coefficient depends upon plasma size and geometry, as well as the assumed radiation structure of the plasma. In a nonequilibrium plasma, all of the assumptions and dependencies cited above raise questions as to the validity and accuracy of the radiative thermal conductivity approach.

An alternative to the optically thin or thick treatment is to employ what are called radiative escape factors which are a quantitative measure of the optical thickness of radiation of a given frequency. These escape factors are determined through the calculation of the absorption coefficient for a given

transition which includes the effects of geometry and the line broadening mechanism (Cho and Eddy, 1989, Gomes, 1983, Drawin, 1969a, Kunc and Soon, 1989, and Weisheit, et al., 1976). Although escape factors may give a measure of the degree of optical thickness of a local plasma region, they do not appear to be useful in tracking photon populations or the effects of non-local radiation. In addition, the actual computation of radiation factors (Kunc and Soon, 1989) is an involved computational process which needlessly adds more complexity to an already complex model.

The approach taken for the generalized model was a discretization of the plasma radiation into a structure that had a basis in reality. Accordingly, the radiation was split into 13 discrete lines contained within 22 discrete bands. A diagram of the band structure can be seen in Figure F.1.

Bands 3 through 22 are allowed to participate in photoionization reactions. Band 1 is considered to be optically thick and is therefore not included in any radiation transfer computations. Band 2 accounts for continuum radiation only, and band 22 is assumed to be optically thin. Each of the 13 lines has an assumed linewidth of $\pm 1\%$ of nominal line energy based upon the estimated line broadening of 50 Å for the 4861.32 Å H Balmer β line (which is line number 8). A detailed listing of energies for all lines and bands can be seen in Tables F.3 and F.4.

An accounting of radiation energy may now be explained based upon the discretized radiation structure. Each band and line is assumed to have a photon population exactly analogous to a particle number density. The array which stores the band and line populations, n_{phot}, goes from 1 to 34 to accomodate bands 1 to 21 and lines 1 to 13 in order. Therefore, line number three has a photon population stored in location $n_{phot}(24)$. In addition, each band has an average band energy which may vary (lines are of fixed energy). Continuum Bremsstrahlung from electrons is computed band by band at the average band energy, yielding a photon production rate for each band as well as an electron radiative emission term. Photons produced from radiative recombination are added to the appropriate photon band production term based upon the energy of the photon. Average band energies are recomputed to include the latest new photons using a small time step chosen to correspond with the minimum computational cell dimension. Photon

populations are then computed across the computational domain using the photon production terms and assuming the radiation to be a gradient driven diffusion process occurring at the speed of light. Average band energies are then recomputed to account for diffusion based on average band energies of surrounding cells. If it happens that photons produced from radiative recombination have an energy within the linewidth of a line, then the photons thus produced are added to the source term for that line population. Photon tracking is discussed in section F.4.
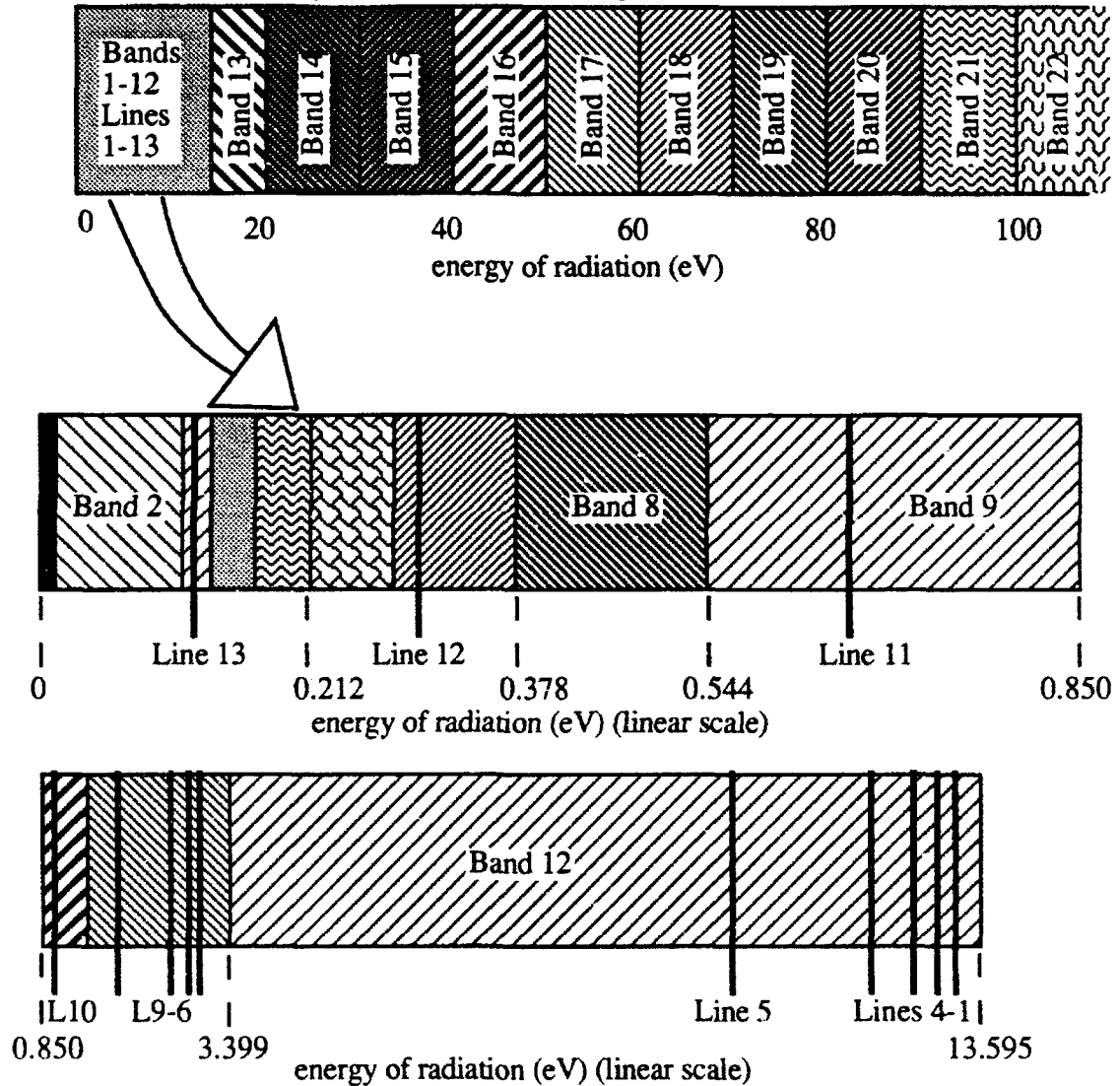
Figure F.1   Diagram of discretized radiation structure

Bands may be depopulated through photoionization of neutrals (reaction 3), or continuum absorption by electrons (described in the next section). Line photons of sufficient energy may also participate in photoionization and be thereby lost. Photons produced with energy greater than

100 eV are considered to be optically thin and are summed into one of two loss terms depending on whether the photons were the result of radiative recombination or electron continuum emission.

Table F.3 Discretized Line Structure

Line (transition)	Energy (eV) (±1%)	A_{ij} (x10^{-6})	Series Designation	Within Band
1 (6-1)	13.221	1.644	Lyman ε	12
2 (5-1)	13.055	4.125	Lyman δ	12
3 (4-1)	12.749	12.78	Lyman γ	12
4 (3-1)	12.088	55.75	Lyman β	12
5 (2-1)	10.199	469.9	Lyman α	12
6 (6-2)	3.023	0.9732	Balmer δ	11
7 (5-2)	2.856	2.530	Balmer γ	11
8 (4-2)	2.550	8.419	Balmer β	11
9 (3-2)	1.88921	44.10	Balmer α	11
10 (5-3)	0.96726	2.201	Paschen β	10
11 (4-3)	0.66122	8.986	Paschen α	9
12 (5-4)	0.30605	2.699	Brackett α	7
13 (6-5)	0.16625	1.025	Pfund α	3

Table F.4 Discretized Band Structure

Band	Energy Range (eV)	Comment
1	0 - 0.01	optically thick continuum
2	0.01 - 0.112	not included in photoionization
3	0.112 - 0.136	surrounds Line 13
4	0.136 - 0.168	
5	0.168 - 0.212	
6	0.212 - 0.277	
7	0.277 - 0.378	surrounds Line 12
8	0.378 - 0.544	
9	0.544 - 0.850	surrounds Line 11
10	0.850 - 1.511	surrounds Line 10
11	1.511 - 3.399	surrounds Lines 6-9
12	3.399 - 13.595	surrounds Lines 1-5
13	13.595 - 20.0	
14	20.0 - 30.0	
15	30.0 - 40.0	
16	40.0 - 50.0	
17	50.0 - 60.0	
18	60.0 - 70.0	
19	70.0 - 80.0	
20	80.0 - 90.0	
21	90.0 - 100.0	
22	> 100.0	optically thin

The upper limit of 100 eV, above which radiation is considered optically thin, was selected based upon an analysis of continuum emission and absorption for a wide range of temperatures.

Similarly, the lower limit of 0.01 eV, below which radiation is consudered optically thick, was selected by a similar analysis.

F.3 Formulation of Source Terms

The conservation equations require a number of source terms which are formulated in this section. The most basic source is the species source. Each species has a net rate of production or destruction based upon a combination of the reactions listed in section F.1, and which will be described here in detail. Each species has been arbitrarily assigned a species reference number for ease of species number density manipulation using an array. The species reference numbers are listed in Table F.5.

Table F.5 Species Reference Numbers

Species	Reference Number
electron	1
proton	2
H_2	3
H^-	4
H_2^+	5
H_3^+	6
$H(n)$	$n+6$

F.3.1 Species Source Terms

F.3.1.1 Electron Source Term

The source term for electrons comprises terms from reactions 1-4, 12-14, 17, 18, 20, 22, and 23, and has the form:

$$\frac{d}{dt}(n_s(1)) = \sum_m S_{ic}(m)n_s(1)n_s(m+6) - \sum_m \beta_{ci}(m)n_s(1)n_s(1)n_s(2)$$

$$+ \sum_{nband}\sum_m \sigma_{ic}(nband,m)(c)n_s(m+6)n_{phot}(nband) - \sum_m \alpha_{ci}(m)n_s(1)n_s(2)$$

$$+ Rcoef(12)n_s(1)n_s(3) + Rcoef(13)n_s(1)n_s(3) + Rcoef(14)n_s(1)n_s(5)$$

$$- Rcoef(17)n_s(1)n_s(5) - Rcoef(18)n_s(1)n_s(6) - Rcoef(20)n_s(1)n_s(3)$$

$$+ Rcoef(22)n_s(1)n_s(4) + (2.0)Rcoef(23)n_s(1)n_s(4) \qquad (F.22)$$

in which the n_S are the number densities of the species involved, and the rate coefficients are as described in section F.1.

F.3.1.2 Proton Source Term

The source term for protons comprises terms from reactions 1-4, 13-16, 19, and 23-25, and has the form:

$$\frac{d}{dt}(n_s(2)) = \sum_m S_{ic}(m)n_s(1)n_s(m+6) - \sum_m \beta_{ci}(m)n_s(1)n_s(1)n_s(2)$$

$$+ \sum_{nband}\sum_m \sigma_{ic}(nband,m)(c)n_s(m+6)n_{phot}(nband) - \sum_m \alpha_{ci}(m)n_s(1)n_s(2)$$

$$+ Rcoef(13)n_s(1)n_s(3) + (2.0)Rcoef(14)n_s(1)n_s(5) + Rcoef(15)n_s(1)n_s(5)$$

$$+ Rcoef(16)n_s(1)n_s(5) + Rcoef(19)n_s(1)n_s(6) + Rcoef(23)n_s(1)n_s(4)$$

$$- Rcoef(24)n_s(2)n_s(4) - Rcoef(25)n_s(2)n_s(4) \qquad (F.23)$$

F.3.1.3 H_2 Source Term

The source term for H_2 comprises terms from reactions 10-13, 18 (Branch B), 20, 21, 26, and 27, and has the form:

$$\frac{d}{dt}(n_s(3)) = - Rcoef(10)n_s(1)n_s(3) - Rcoef(11)n_s(1)n_s(3) - Rcoef(12)n_s(1)n_s(3)$$

$$- Rcoef(13)n_s(1)n_s(3) + Rcoef(18B)n_s(1)n_s(5) - Rcoef(20)n_s(1)n_s(3)$$

$$- Rcoef(21)n_s(3)n_s(5) - Rcoef(26)n_s(3)n_s(3) + Rcoef(27)n_s(3)n_s(7)n_s(7) \qquad (F.24)$$

F.3.1.4 H^- Source Term

The source term for H^- comprises terms from reactions 20, and 22-25, and has the form:

$$\frac{d}{dt}(n_s(4)) = Rcoef(20)n_s(1)n_s(3) - Rcoef(22)n_s(1)n_s(4)$$

$$- Rcoef(23)n_s(1)n_s(4) - Rcoef(24)n_s(2)n_s(4) - Rcoef(25)n_s(2)n_s(4) \qquad (F.25)$$

F.3.1.5 H_2^+ Source Term

The source term for H_2^+ comprises terms from reactions 12, 14-17, and 21, and has the form:

$$\frac{d}{dt}(n_s(5)) = Rcoef(12)n_s(1)n_s(3) - Rcoef(14)n_s(1)n_s(5) - Rcoef(15)n_s(1)n_s(5)$$

$$- Rcoef(16)n_s(1)n_s(5) - Rcoef(17)n_s(1)n_s(5) - Rcoef(21)n_s(3)n_s(5) \qquad (F.26)$$

F.3.1.6 H_3^+ Source Term

The source term for H_3^+ comprises terms from reactions 18, 19, and 21, and has the form:

$$\frac{d}{dt}(n_s(6)) = - Rcoef(18)n_s(1)n_s(6) - Rcoef(19)n_s(1)n_s(6) + Rcoef(21)n_s(3)n_s(5) \qquad (F.27)$$

F.3.1.7 H(1) Source Term

The source term for the ground state hydrogen atom, H(1), comprises terms from reactions 1-11, 13, 15, 17, 18 (Branch A), 19-22, and 24-27, and has the form:

$$\frac{d}{dt}(n_s(7)) = - S_{ic}(1)n_s(1)n_s(7) + \beta_{ci}(1)n_s(1)n_s(1)n_s(2) - \sum_{nband}\sigma_{ic}(nband,1)(c)n_s(7)n_{phot}(nband)$$

$$+ \alpha_{ci}(1)n_s(1)n_s(2) + \sum_{j>1}(R_{jm}(j,1)n_s(1)n_s(j+6) - C_{mj}(1,j)n_s(1)n_s(7))$$

$$+ \sum_{line=1}^{5}(A_{jm}(line)n_s(13-line) - B_{mj}(line)n_s(7)n_{phot}(line+21) + B_{jm}(line)n_s(13-line)n_{phot}(line+21))$$

$$+ (2.0)Rcoef(10)n_s(1)n_s(3) + Rcoef(11)n_s(1)n_s(3) + Rcoef(13)n_s(1)n_s(3) + Rcoef(15)n_s(1)n_s(5)$$

$$+ Rcoef(17)n_s(1)n_s(5) + (3.0)Rcoef(18A)n_s(1)n_s(6) + (2.0)Rcoef(19)n_s(1)n_s(6)$$

$$+ Rcoef(20)n_s(1)n_s(3) + Rcoef(21)n_s(3)n_s(5) + Rcoef(22)n_s(1)n_s(4) + Rcoef(24)n_s(2)n_s(4)$$

$$+ Rcoef(25)n_s(2)n_s(4) + (2.0)(molcoef)n_s(3)n_s(3) - (2.0)(recom)n_s(3)n_s(7)n_s(7) \qquad (F.28)$$

where the Einstein coefficients with line number subscripts refer to the line transitions as listed in Table F.4.

F.3.1.8 First Excited Level, H(2), Source Term

The source term for the first excited level of the hydrogen atom, H(2), comprises terms from reactions 1-9, 11, 16, 17, 18 (Branch B), and 24, and has the form:

$$\frac{d}{dt}(n_s(8)) = - S_{ic}(2)n_s(1)n_s(8) + \beta_{ci}(2)n_s(1)n_s(1)n_s(2) - \sum_{nband}\sigma_{ic}(nband,2)(c)n_s(8)n_{phot}(nband)$$

$$+ \alpha_{ci}(2)n_s(1)n_s(2) - \sum_{j>2}(C_{mj}(2,j)n_s(1)n_s(8)) + C_{mj}(1,2)n_s(1)n_s(7)$$

$$+ \sum_{j>2}(R_{jm}(j,2)n_s(1)n_s(j+6)) - R_{jm}(2,1)n_s(1)n_s(8)$$

$$+ \sum_{line=6}^{9}(A_{jm}(line)n_s(18-line) - B_{mj}(line)n_s(8)n_{phot}(line+21) + B_{jm}(line)n_s(18-line)n_{phot}(line+21))$$

$$- A_{jm}(5)n_s(8) + B_{mj}(5)n_s(7)n_{phot}(26) - B_{jm}(5)n_s(8)n_{phot}(26) + Rcoef(11)n_s(1)n_s(3)$$

$$+ Rcoef(16)n_s(1)n_s(5) + Rcoef(17)n_s(1)n_s(5)rjh(2)$$

$$+ Rcoef(18B)n_s(1)n_s(6) + Rcoef(24)n_s(2)n_s(4) \qquad (F.29)$$

F.3.1.9 Second Excited Level, H(3), Source Term

The source term for the second excited level of the hydrogen atom, H(3), comprises terms from reactions 1-9, 17, and 25, and has the form:

$$\frac{d}{dt}(n_s(9)) = - S_{ic}(3)n_s(1)n_s(9) + \beta_{ci}(3)n_s(1)n_s(1)n_s(2) - \sum_{nband}\sigma_{ic}(nband,3)(c)n_s(9)n_{phot}(nband)$$

$$+ \alpha_{ci}(3)n_s(1)n_s(2) - \sum_{j>3}\left(C_{mj}(3,j)n_s(1)n_s(9)\right) + \sum_{m<3}\left(C_{mj}(m,3)n_s(1)n_s(m+6)\right)$$

$$+ \sum_{j>3}\left(R_{jm}(j,3)n_s(1)n_s(j+6)\right) - \sum_{m<3}\left(R_{jm}(3,m)n_s(1)n_s(9)\right)$$

$$+ \sum_{line=10}^{11}\left(A_{jm}(line)n_s(21\text{-}line)\text{-}B_{mj}(line)n_s(9)n_{phot}(line+21)+B_{jm}(line)n_s(21\text{-}line)n_{phot}(line+21)\right)$$

$$- A_{jm}(4)n_s(9) - A_{jm}(9)n_s(9) + B_{mj}(4)n_s(7)n_{phot}(25) + B_{mj}(9)n_s(8)n_{phot}(30)$$

$$- B_{jm}(4)n_s(9)n_{phot}(25) - B_{jm}(9)n_s(9)n_{phot}(30)$$

$$+ Rcoef(17)n_s(1)n_s(5)rjh(3) + Rcoef(25)n_s(2)n_s(4) \qquad (F.30)$$

F.3.1.10 Third Excited Level, H(4), Source Term

The source term for the third excited level of the hydrogen atom, H(4), comprises terms from reactions 1-9, and 17, and has the form:

$$\frac{d}{dt}(n_s(10)) = - S_{ic}(4)n_s(1)n_s(10) + \beta_{ci}(4)n_s(1)n_s(1)n_s(2) - \sum_{nband}\sigma_{ic}(nband,4)(c)n_s(10)n_{phot}(nband)$$

$$+ \alpha_{ci}(4)n_s(1)n_s(2) - \sum_{j>4}\left(C_{mj}(4,j)n_s(1)n_s(10)\right) + \sum_{m<4}\left(C_{mj}(m,4)n_s(1)n_s(m+6)\right)$$

$$+ \sum_{j>4}\left(R_{jm}(j,4)n_s(1)n_s(j+6)\right) - \sum_{m<4}\left(R_{jm}(4,m)n_s(1)n_s(10)\right)$$

$$+ A_{jm}(12)n_s(11) - A_{jm}(3)n_s(10) - A_{jm}(8)n_s(10) - A_{jm}(11)n_s(10)$$

$$+ B_{mj}(3)n_s(7)n_{phot}(24) + B_{mj}(8)n_s(8)n_{phot}(29) + B_{mj}(11)n_s(9)n_{phot}(32) - B_{mj}(12)n_s(10)n_{phot}(33)$$

$$+ B_{jm}(12)n_s(11)n_{phot}(33) - B_{jm}(3)n_s(10)n_{phot}(24) - B_{jm}(8)n_s(10)n_{phot}(29)$$

$$- B_{jm}(11)n_s(10)n_{phot}(32) + Rcoef(17)n_s(1)n_s(5)rjh(4) \qquad (F.31)$$

F.3.1.11 Fourth Excited Level, H(5), Source Term

The source term for the fourth excited level of the hydrogen atom, H(5), comprises terms from reactions 1-9, and 17, and has the form:

$$\frac{d}{dt}(n_s(11)) = - S_{ic}(5)n_s(1)n_s(11) + \beta_{ci}(5)n_s(1)n_s(1)n_s(2) - \sum_{nband}\sigma_{ic}(nband,5)(c)n_s(11)n_{phot}(nband)$$

$$+ \alpha_{ci}(5)n_s(1)n_s(2) - \sum_{j>5}\left(C_{mj}(5,j)n_s(1)n_s(11)\right) + \sum_{m<5}\left(C_{mj}(m,5)n_s(1)n_s(m+6)\right)$$

$$+ \sum_{j>5}\left(R_{jm}(j,5)n_s(1)n_s(j+6)\right) - \sum_{m<5}\left(R_{jm}(5,m)n_s(1)n_s(11)\right)$$

$$+ A_{jm}(13)n_s(12) - A_{jm}(2)n_s(11) - A_{jm}(7)n_s(11) - A_{jm}(10)n_s(11) - A_{jm}(12)n_s(11)$$

$$+ B_{mj}(2)n_s(7)n_{phot}(23) + B_{mj}(7)n_s(8)n_{phot}(28) + B_{mj}(10)n_s(9)n_{phot}(31)$$

$$+ B_{mj}(12)n_s(10)n_{phot}(33) - B_{mj}(13)n_s(11)n_{phot}(34) - B_{jm}(2)n_s(11)n_{phot}(23)$$

$$- B_{jm}(7)n_s(11)n_{phot}(28) - B_{im}(10)n_s(11)n_{phot}(31) - B_{jm}(12)n_s(11)n_{phot}(33)$$

$$+ B_{jm}(13)n_s(12)n_{phot}(34) + Rcoef(17)n_s(1)n_s(5)rjh(5) \qquad (F.32)$$

F.3.1.12 Fifth Excited Level, H(6), Source Term

The source term for the fifth excited level of the hydrogen atom, H(6), comprises terms from reactions 1-9, and 17, and has the form:

$$\frac{d}{dt}(n_s(12)) = - S_{ic}(6)n_s(1)n_s(12) + \beta_{ci}(6)n_s(1)n_s(1)n_s(2) - \sum_{nband}\sigma_{ic}(nband,6)(c)n_s(12)n_{phot}(nband)$$

$$+ \alpha_{ci}(6)n_s(1)n_s(2) - \sum_{j>6}\left(C_{mj}(6,j)n_s(1)n_s(12)\right) + \sum_{m<6}\left(C_{mj}(m,6)n_s(1)n_s(m+6)\right)$$

$$+ \sum_{j>6}\left(R_{jm}(j,6)n_s(1)n_s(j+6)\right) - \sum_{m<6}\left(R_{jm}(6,m)n_s(1)n_s(12)\right)$$

$$- A_{jm}(1)n_s(12) - A_{jm}(6)n_s(12) - A_{jm}(13)n_s(12)$$

$$+ B_{mj}(1)n_s(7)n_{phot}(22) + B_{mj}(6)n_s(8)n_{phot}(27) + B_{mj}(13)n_s(11)n_{phot}(34)$$

$$- B_{jm}(1)n_s(12)n_{phot}(22) - B_{jm}(6)n_s(12)n_{phot}(27) - B_{jm}(13)n_s(12)n_{phot}(34)$$

$$+ Rcoef(17)n_s(1)n_s(5)rjh(6) \qquad (F.33)$$

F.3.1.13 Sixth Excited Level, H(7), Source Term

The source term for the sixth excited level of the hydrogen atom, H(7), comprises terms from reactions 1-6, and 17, and has the form:

$$\frac{d}{dt}(n_s(13)) = - S_{ic}(7)n_s(1)n_s(13) + \beta_{ci}(7)n_s(1)n_s(1)n_s(2) - \sum_{nband}\sigma_{ic}(nband,7)(c)n_s(13)n_{phot}(nband)$$

$$+ \alpha_{ci}(7)n_s(1)n_s(2) - \sum_{j>7}\left(C_{mj}(7,j)n_s(1)n_s(13)\right) + \sum_{m<7}\left(C_{mj}(m,7)n_s(1)n_s(m+6)\right)$$

$$+ \sum_{j>7}\left(R_{jm}(j,7)n_s(1)n_s(j+6)\right) - \sum_{m<7}\left(R_{jm}(7,m)n_s(1)n_s(13)\right)$$

$$+ Rcoef(17)n_s(1)n_s(5)rjh(7) \qquad (F.34)$$

F.3.1.13 Seventh Excited Level, H(8), Source Term

The source term for the seventh excited level of the hydrogen atom, H(8), comprises terms from reactions 1-6, and 17, and has the form:

$$\frac{d}{dt}(n_s(14)) = - S_{ic}(8)n_s(1)n_s(14) + \beta_{ci}(8)n_s(1)n_s(1)n_s(2) - \sum_{nband}\sigma_{ic}(nband,8)(c)n_s(14)n_{phot}(nband)$$

$$+ \alpha_{ci}(8)n_s(1)n_s(2) - \sum_{j>8}(C_{mj}(8,j)n_s(1)n_s(14)) + \sum_{m<8}(C_{mj}(m,8)n_s(1)n_s(m+6))$$

$$+ \sum_{j>8}(R_{jm}(j,8)n_s(1)n_s(j+6)) - \sum_{m<8}(R_{jm}(8,m)n_s(1)n_s(14))$$

$$+ Rcoef(17)n_s(1)n_s(5)rjh(8) \qquad (F.35)$$

F.3.1.13 Higher Excited Levels, H(m>8), Source Terms

Assuming that the highest bound level included in the analysis is greater than 8, then source terms for these species are comprised of terms from reactions 1-6. If k is the bound level, then for k>8 the species source terms have the form:

$$\frac{d}{dt}(n_s(k+6)) = - S_{ic}(k)n_s(1)n_s(k+6) + \beta_{ci}(k)n_s(1)n_s(1)n_s(2)$$

$$- \sum_{nband}\sigma_{ic}(nband,k)(c)n_s(k+6)n_{phot}(nband) + \alpha_{ci}(k)n_s(1)n_s(2)$$

$$- \sum_{j>k}(C_{mj}(k,j)n_s(1)n_s(k+6)) + \sum_{m<k}(C_{mj}(m,k)n_s(1)n_s(m+6))$$

$$+ \sum_{j>k}(R_{jm}(j,k)n_s(1)n_s(j+6)) - \sum_{m<k}(R_{jm}(k,m)n_s(1)n_s(k+6)) \qquad (F.36)$$

The rate equations (F.22) to (F.36) comprise the set of species production rate source terms to be supplied to the species conservation equations. In addition to these rates, there are also a number of photon production rates. Photon production and destruction has been divided into three components, that due to photoionization and radiative recombination, that due to line transitions, and that due to continuum.

F.3.1.14 Photon Source Terms

In accounting for photon production due to photoionization and radiative recombination, photoionization is dealt with first. A double loop is employed over the bands and the bound atomic levels. The outer loop consists of the bands which are stepped through from 3 to 34. For each band, the inner loop steps through all the bound atomic levels. The rate of photons lost due to

photoionization for each atomic level is equivalent to the rate of atoms lost from that atomic level due to photoionization as given in the expressions for species sources above. The rate of photons lost for each atomic level and band is given by:

$$\text{sigrate(nband,m)} = \sigma_{ic}(\text{nband,m})(c)n_s(m+6)n_{phot}(\text{nband}) \tag{F.37}$$

The expression given in equation (F.37) is summed over all bound atomic levels, m, which yields a photon rate of loss term for each band, which is labeled photsp(nband).

Photon production due to radiative recombination is handled in a different fashion. A single loop is used to step through the bound atomic levels. The radiative recombination rate for each level has already been computed above in the species source terms as:

$$\text{alphrate(m)} = \alpha_{ci}(\text{nband,m})n_s(1)n_s(2) \tag{F.38}$$

Therefore the rate of photons produced due to radiative recombination to level m is known. However the energy of the produced photons depends upon the local electron temperature and the level being recombined. For each level, the line or band with which the rate of photon production is to be associated is determined based upon the photon energy. Once again, the bands are stepped through in order until the energy of the produced photon falls within the band (or line) limits. If the photon has energy greater than 100 eV it is lumped into a loss term.

Photon production and destruction due to line transitions are easily accounted for because the lines are self contained. The production term for a given line photon is given by:

$$\text{photsc(line+21)} = \text{spon(line)} + \text{stim(line)} - \text{ind(line)} \tag{F.39}$$

where the three terms on the right hand side represent contributions to photon production due to spontaneous emission, stimulated emission and induced absorption. These terms have been written generically this way because their exact forms depend upon the particular line involved which is not relevant to the immediate discussion.

The final contribution to the production rate of photons is that due to continuum emission and absorption. The continuum emission is assumed to be made up of a contribution due to electron-ion Bremsstrahlung and and a contribution due to electron-atom Bremsstrahlung. The free-bound contribution to the continuum emission has been neglected, since that is already included in the

radiative recombination reaction. The expressions for electron-ion and electron-atom continuum emission (Eddy, et al., 1991) include a free-free Gaunt factor for each type of emission. However, a source could not be found (including those listed by Eddy) which distinguished between e-i and e-a free-free Gaunt factors. Accordingly, the free-free Gaunt factors taken from Figures 4 and 5 of Karzas and Latter (1961) were curve fit versus the ratio of photon energy to electron thermal energy for several electron temperatures. Values for the Gaunt factors were then computed from interpolations between the curve fits as required. Expressions for the curve fits are:

$$\text{for } T_e = 1578, \qquad G_{ff} = 1.26696(U_{kl})^{-0.10105} \qquad \text{(F.40)}$$

$$\text{for } T_e = 15778, \qquad G_{ff} = 1.37590(U_{kl})^{-0.11468} \qquad \text{(F.41)}$$

$$\text{for } T_e = 52594, \qquad G_{ff} = 1.38936(U_{kl})^{-0.12703} \qquad \text{(F.42)}$$

$$\text{for } T_e = 157783, \qquad G_{ff} = 1.30883(U_{kl})^{-0.14845} \qquad \text{(F.43)}$$

where U_{kl} is given by:

$$U_{kl} = \frac{h\nu}{\left(\dfrac{k_b T_e}{jev}\right)} \qquad \text{(F.44)}$$

Using the values for free-free Gaunt factors computed with equations (F.40) to (F.43), the expression for electron-ion Bremsstrahlung emission is given by (Eddy, et al., 1991) as:

$$\varepsilon_{\nu,ei} = C_c\, Z^2\, G_{ff} \left(\frac{n_e n_i}{\sqrt{T_e}}\right) \exp\left(\frac{\Delta E_s - h\nu}{\dfrac{k_b T_e}{jev}}\right) \exp\left(\frac{-\Delta E_\infty}{\dfrac{k_b T_{xB}}{jev}}\right) \quad \left(\frac{W}{m^3 HzSr}\right) \qquad \text{(F.45)}$$

where T_{xB} is the excitation temperature of the upper excited levels, Z is the ionic charge, ΔE_∞ is the magnitude of the lowering of the ionization potential in eV, C_c is termed the continuum constant, having a value of 5.44×10^{-52} $Wm^3sK^{1/2}$, and ΔE_s is the advance of the series limit given by Cho (1988), p.53 to be:

$$\Delta E_s = 4\, Z^{0.8}\left(a_0^3 n_e\right)^{4/15} Ry \qquad \text{(eV)} \qquad \text{(F.46)}$$

The expression for electron - atom Bremsstrahlung emission is nearly identical to the electron - ion case and is given by Eddy, et al. (1991) to be:

$$\varepsilon_{v,ea} = C_c\, Z^2\, G_{ff} \left(\frac{n_e n_a}{\sqrt{T_e}}\right) \exp\left(\frac{\Delta E_s - hv}{\frac{k_b T_e}{jev}}\right) \exp\left(\frac{-\Delta E_\infty}{\frac{k_b T_{xB}}{jev}}\right) \quad \left(\frac{W}{m^3 Hz Sr}\right) \qquad (F.47)$$

Since the ionic charge, Z, for hydrogen is one, the total Bremsstrahlung emission per unit volume per frequency can be then written as a sum of the atomic and ionic components to be:

$$\varepsilon_{v,total} = 4\pi\, C_c\, G_{ff} \left(\frac{n_e(n_a + n_i)}{\sqrt{T_e}}\right) \exp\left(\frac{\Delta E_s - hv}{\frac{k_b T_e}{jev}}\right) \exp\left(\frac{-\Delta E_\infty}{\frac{k_b T_{xB}}{jev}}\right) \quad \left(\frac{W}{m^3 Hz}\right) \qquad (F.48)$$

This continuum has been split into two parts, the optically thin part above 100 eV and the interacting part below 100 eV. Below 100 eV, equation (F.48) is evaluated at the average band energies of each band. The photon production rate due to this emission is then computed by dividing by the average energy per photon, namely the average band energy. Between 100 and 1000 eV, the expression is evaluated every 50 eV starting at 125 eV, and the result is summed into an optically thin loss term, RADLS.

In addition, to the continuum emission rate for each band below 100 eV, the continuum absorption rate is also computed. Just as for emission, continuum absorption is assumed to consist of a contribution due to e-i Bremsstrahlung and e-a Bremsstrahlung absorption. The absorption coefficients necessary for this computation are identical to those used for beam absorption described in Appendix H, except for the form of the Gaunt factors which become a function of the absorbed photon frequency. The absorption coefficients are fully described in Appendix H and will therefore not be duplicated here. The local rate of photon absorption for each band may then be computed by multiplying the sum of the absorption coefficients by the speed of light by the local photon population for the band in question. The net thermal energy transfer by the electrons due to continuum radiation is summed into the term, CONRAD, which may be negative or positive.

F.3.2 Energy Transfer Source Terms

As a result of all the individual reactions described above, there are five energy transfer source terms which are computed and supplied to the energy equations, and another term useful in tracking radiation energy.

As described in Chapter 1, collisions may be classified as either inelastic or elastic depending upon whether or not the kinetic energy of the colliding particles is conserved. The inelastic collisions which are included in the model have been described above as the 27 types of chemical reaction. There are also elastic collisions included in the model between both like species and unlike species. Elastic collisions between like species are not included explicitly, but are included implicitly through the assumption of Maxwellian velocity distributions for the electrons and the heavy species. Elastic collisions between electrons and heavy species are included explicitly as the elastic collisional transfer term below.

F.3.2.1 Electron Inelastic Transfer

The net electron inelastic transfer term has been labeled as INSTE in the electron energy equation (3.1). This term is the sum of all the individual inelastic thermal energy transfer terms multiplied by the rates of reaction for all the reactions involving electron inelastic thermal energy transfer. Therefore, INSTE involves reactions 1-6, 10-20, 22, and 23, and in units of $eVm^{-3}s^{-1}$ has the form:

$$INSTE = \sum_m \left(-U_i(m)S_{ic}(m)n_s(1)n_s(m+6)\right) + \sum_m \left(U_i(m)\beta_{ci}(m)n_s(1)n_s(1)n_s(2)\right)$$

$$+ \sum_{nband}\sum_m \left(\epsilon(nband,m)\sigma_{ic}(nband,m)(c)n_s(m+6)n_{phot}(nband)\right) + \sum_m \left(-\frac{3k_bT_e}{2jev}\alpha_{ci}(m)n_s(1)n_s(2)\right)$$

$$+ \sum_m\sum_{j>m}\left(-\Delta E_{mj}C_{mj}(m,j)n_s(1)n_s(m+6)\right) + \sum_m\sum_{j<m}\left(\Delta E_{mj}R_{jm}(j,m)n_s(1)n_s(j+6)\right)$$

$$- (10.5)Rcoef(10)n_s(1)n_s(3) - (15.3)Rcoef(11)n_s(1)n_s(3) - (15.427)Rcoef(12)n_s(1)n_s(3)$$

$$- (18.5)Rcoef(13)n_s(1)n_s(3) - (15.5)Rcoef(14)n_s(1)n_s(5) - (10.5)Rcoef(15)n_s(1)n_s(5)$$

$$- (17.5)Rcoef(16)n_s(1)n_s(5) - \left(\frac{3k_bT_e}{2jev}\right)Rcoef(17)n_s(1)n_s(5) - \left(\frac{3k_bT_e}{2jev}\right)Rcoef(18)n_s(1)n_s(6)$$

$$- (14.0)Rcoef(19)n_s(1)n_s(6) - \Delta E_e(20)Rcoef(20)n_s(1)n_s(3)$$

$$- (0.754)Rcoef(22)n_s(1)n_s(4) - (14.35)Rcoef(23)n_s(1)n_s(4) \qquad \left(\frac{eV}{m^3s}\right) \qquad (F.49)$$

in which $\Delta E_e(20)$ depends upon electron temperature as can be seen in Table F.2.

F.3.2.2 Heavy Species Inelastic Transfer

The net heavy species inelastic transfer term has been labeled as INSTH in the heavy species energy equation (3.2). This term is the sum of all the individual inelastic thermal energy transfer terms multiplied by the rates of reaction for all the reactions involving heavy species inelastic thermal energy transfer. Therefore, INSTH involves reactions 10, 11, 13-21, and 24-27, and in units of $eVm^{-3}s^{-1}$ has the form:

$$INSTH = (6.024)Rcoef(10)n_s(1)n_s(3) + (0.628)Rcoef(11)n_s(1)n_s(3)$$

$$+ (0.5)Rcoef(13)n_s(1)n_s(3) + (0.8)Rcoef(14)n_s(1)n_s(5) + (8.6)Rcoef(15)n_s(1)n_s(5)$$

$$+ (3.0)Rcoef(16)n_s(1)n_s(5) + \sum_{n=2}^{nupper} \left(\frac{3k_bT_e}{2jev} + \frac{R\,y}{n^2}\right)jh(n)Rcoef(17)n_s(1)n_s(5)$$

$$+ \left(\frac{3k_bT_e}{2jev}\right)Rcoef(18)n_s(1)n_s(6) + (13.0)Rcoef(19)n_s(1)n_s(6) + \Delta E_{heavy}(20)Rcoef(20)n_s(1)n_s(3)$$

$$+ (1.17)Rcoef(21)n_s(3)n_s(5) + (2.645)Rcoef(24)n_s(2)n_s(4) + (0.757)Rcoef(25)n_s(2)n_s(4)$$

$$- (4.476)(molcoef)n_s(3)n_s(3) + (4.476)(recom)n_s(3)n_s(3)n_s(7) \qquad \left(\frac{eV}{m^3s}\right) \qquad (F.50)$$

F.3.2.3 Elastic Collisional Transfer

The expression for elastic energy transfer between electrons and heavy particles is well known (Miller and Martinez-Sanchez, 1990, Chen and Pfender, 1981, Kruger, 1970, and Kruger and Mitchner, 1967) as:

$$ELST = 3k_b(T_e-T_g)n_em_e \sum_{heavies} \left(\frac{\bar{v}_{es}}{m_s}\right) \qquad (F.51)$$

where m_e is the electron mass, m_s is the heavy particle mass, the summation is over all heavy species, and $\bar{v}_{es}$ is the average collision frequency between electrons and each heavy species given by:

$$\bar{v}_{es} = \bar{C}_e n_s Q_{es} \qquad (F.52)$$

in which Q_{es} is the collision cross section between electrons and species s, n_s is the number density of species s, and $\bar{C}_e$ is the mean thermal speed of the electrons given by:

$$\bar{C}_e = \sqrt{\frac{8k_bT_e}{\pi m_e}} \qquad (F.53)$$

The collision cross sections required for the elastic transfer computation may be divided into three categories which are Coulomb collisions, electron-atom collisions and electron-H_2 collisions. The cross section for Coulomb collisions from Jaffrin (1965) may be written:

$$Q_{ei} = \frac{\pi e^4 k_c^2 (\ln \Lambda_e)}{2(k_b T_e)^2}$$ (F.54)

in which k_c is the Coulomb constant (necessary for proper conversion to MKS units), and Λ_e is the Spitzer logarithm given by:

$$\Lambda_e = \frac{1.5 \sqrt{\frac{k_b^3 T_e^3}{\pi n_e}}}{e^3 k_c^{1.5}}$$ (F.55)

The collision cross sections for electron-atom and electron-H_2 collisions were taken from the tabulations of Itikawa (1974 and 1978).

F.3.2.4 Continuum Radiative Transfer

The term for the net thermal energy transfer by the electrons due to continuum radiation was labeled CONRAD above. This term represents a sum over all bands of the difference between the rates of energy absorbed and energy emitted by the electrons. Explicitly, in units of Watts/m^3, this may be written as:

$$CONRAD = \sum_{nband=2}^{21} c(k_{ei}+k_{en})n_{phot}(nband)abe(nband)(jev)$$

$$- \sum_{nband=2}^{21} 4\pi C_c G_{ff}(nband)\left(\frac{n_e(n_a+n_i)}{\sqrt{T_e}}\right)\exp\left(\frac{\Delta E_s - abe(nband)}{\frac{k_b T_e}{jev}}\right)\exp\left(\frac{-\Delta E_\infty}{\frac{k_b T_{xB}}{jev}}\right)bw(nband)$$ (F.56)

in which k_{ei} and k_{en} are Bremsstrahlung absorption coefficients, n_{phot} is the photon number density, abe is the average band energy, and bw is the bandwidth in Hz.

F.3.2.5 Optically Thin Radiation Loss

The term for thermal energy lost by the electrons in the form of optically thin radiation was labeled above as RADLS. This term is computed as the sum of equation (F.48) evaluated at the band centers of energy bands 50 eV wide between 100 and 1000 eV, starting at 125 eV. Explicitly, in units of Watts/m^3, this may be written:

$$RADLS = \sum_{hv=100}^{1000} 4\pi \, C_c \left(1.209 \times 10^{16}\right) G_{ff} \left(\frac{n_e(n_a+n_i)}{\sqrt{T_e}}\right) \exp\left(\frac{\Delta E_s - hv}{\frac{k_b T_e}{jev}}\right) \exp\left(\frac{-\Delta E_\infty}{\frac{k_b T_{xB}}{jev}}\right) \quad (F.57)$$

where the factor of 1.209×10^{16} is the equivalent bandwidth in Hz corresponding to 50 eV.

Since this sum is always positive, RADLS has a negative sign preceding it in equation (3.1). Note that since CONRAD may be negative or positive, it is preceded by a positive sign in equation (3.1).

F.3.2.6 High Energy Radiative Recombination

The rate of photons produced due to radiative recombination with energies greater than 100 eV are summed in the term DOTHEN. Since these photons have energies which exceed that of any band, they are simply lumped together. Although the term DOTHEN does not appear in any conservation equation it was thought that it would be useful to keep track of the production of high energy photons. The term probably does not have any practical use, however, since it would require electrons with kinetic temperature of approximately 1002240K to produce photons of energy 100eV (through radiative recombination to the ground state of the hydrogen atom), and such a high electron temperature is extremely unlikely.

F.4 Non-Local Radiation Transfer

The tracking of radiation across the computational domain is perhaps the most difficult aspect of the generalized model. However, a method has been developed which fits in well with the ideas of photon number densities and local photon source terms.

At each computational cell, the production or destruction rate of photons for every band is computed as described above, accounting for continuum and line radiation, including production due to radiative recombination. Physically, photons produced in a local volume will diffuse outward at the speed of light, equally in all directions. The photon travel may be considered a diffusion process because the photons will be scattered, or may be absorbed due to the reactions which comprise the source terms. Absorption of photons which have diffused across the computational domain from a distant cell would contribute to what has been labeled non-local

radiative effects. With the assumption that radiative transfer can be treated as a diffusive process, a photon continuity equation for each photon band may be written as:

$$\nabla \cdot \left(n_{phot} \overline{c} \right) = \left(\dot{n}_{phot} \right)_{CR} \tag{F.58}$$

in which $n_{phot} \overline{c}$ represents a flux of photons due to diffusion between cells. Since light travels isotropically at a constant speed, the vector representation of $\overline{c}$ has no real significance. Equation (F.58) may be written in cylindrical coordinates as:

$$\frac{\partial}{\partial x}(n_{phot}c) + \frac{1}{r}\frac{\partial}{\partial r}(m_{phot}c) = \left(\dot{n}_{phot} \right)_{CR} \tag{F.59}$$

Finally, to allow for proper discretization in the realm of the SIMPLE algorithm, the first two terms in equation (F.59) are rewritten in terms of gradients of number densities and effective diffusion coefficients to yield:

$$\frac{\partial}{\partial x}(D_{effx}\frac{\partial n_{phot}}{\partial x}) + \frac{1}{r}\frac{\partial}{\partial r}(rD_{effr}\frac{\partial n_{phot}}{\partial r}) + \left(\dot{n}_{phot} \right)_{CR} = 0 \tag{F.60}$$

in which the effective photon diffusion coefficients are simply defined as:

$$D_{effx} = \frac{-n_{phot}c}{\left(\frac{\partial n_{phot}}{\partial x} \right)} \tag{F.61}$$

$$D_{effr} = \frac{-n_{phot}c}{\left(\frac{\partial n_{phot}}{\partial r} \right)} \tag{F.62}$$

The average band energy, abe, of photons is determined by both local and diffusive processes. In each cell, the local rate of production of photons may change the local average band energy. The average band energy may be computed locally for each computational cell as:

$$abe_{local} = \frac{n_{phot}abe_{old} + \left(\dot{n}_{phot} \right)_{CR}abe_{new}time_{abe}}{n_{phot} + \left(\dot{n}_{phot} \right)_{CR}time_{abe}} \tag{F.63}$$

where the new subscript on the right hand side refers to the average band energy of the newly produced photons, and $time_{abe}$ represents a small time step computed based on the time it would take light to traverse the minimum computational cell dimension.

Then, after solution of equation (F.60) to yield updated photon number densities, the local average band energy may be changed again due to diffusion from surrounding cells. Therefore, abe would be recomputed a second time as:

$$abe(i,j) = \frac{abe_{old}(i,j)n_{photold}(i,j) + \Delta n_{phot}(i,j)(\text{average of neighbor cell abes})}{n_{phot}(i,j)} \qquad (F.64)$$

Although it is admittedly unorthodox, the use of photon continuity equations does not appear to present any computational problems. It should be stated that tests of the generalized model which included the photon continuity equations failed to produce meaningful results. However, it is believed that this was not due to the photon continuity equations, but rather due to errors in other portions of the overall algorithm.

Appendix G. Computation of Diffusion Fluxes

This appendix explains the computation of the diffusion fluxes of all species as well as the effective diffusion coefficients required by the species conservation equations. The multicomponent and thermal diffusion coefficients are computed for all scalar cells by subroutine TRANSPORT and as explained in Appendix E.

Under the assumption of ambipolar diffusion, which accounts for the induced electric field caused by charge separation, both the multicomponent and thermal diffusion coefficients are corrected by additive factors (Devoto, 1966). The corrected multicomponent diffusion coefficient is given by:

$$D_{ij,c} = D_{ij} + \frac{\alpha_i}{\beta} \sum_{s=1}^{6} Z_s D_{sj} \tag{G.1}$$

and the corrected thermal diffusion coefficient is given by:

$$D_{i,c}^T = D_i^T + \frac{m_i \alpha_i}{\beta} \sum_{s=1}^{6} \frac{Z_s D_s^T}{m_s} \tag{G.2}$$

in which Z represents the species charge, the summations are over the charged species (1 to 6), and the α_i and β terms are given by:

$$\alpha_i = \sum_{j=1}^{6} n_j m_j Z_j D_{ij} \tag{G.3}$$

$$\beta = - \sum_{i=1}^{6} \sum_{j=1}^{6} Z_i Z_j n_j m_j D_{ij} \tag{G.4}$$

The first step in the computation of the diffusion fluxes is to compute the corrected multicomponent and thermal diffusion coefficients at the scalar cell interfaces based on the harmonic rule as was stressed in Appendix I. Having values for mole fractions at each scalar node, the total number flux of any species may be computed at each interface through the use of equation (E.9). The computation is done in two parts, the first being the species gradient term in equation (E.9), and the second being the thermal diffusion term in equation (E.9).

In the first part of the computation, the number flux of each species is computed at the scalar cell interfaces accounting for gradient diffusion. However, the discretization of the species continuity equations using the SIMPLE algorithm as described in Appendix I requires a diffusion type term

with the gradient of the variable in question, in this case, the species mole fraction. Therefore, instead of supplying the ordinary number fluxes directly to the species conservation equations (3.7), the effective ordinary diffusion coefficient, D_{eff} is computed at each interface in both the axial and radial directions as:

$$D_{effu} = -\frac{(n_s u_s)}{\left(\frac{\partial X_s}{\partial x}\right)} \qquad (G.5)$$

$$D_{effv} = -\frac{(n_s v_s)}{\left(\frac{\partial X_s}{\partial r}\right)} \qquad (G.6)$$

where the gradient is easily computed and the species ordinary diffusive number flux (the numerator) has already been computed using the first term of equation (E.9).

Following the computation of the effective diffusion coefficients, the total diffusive number fluxes for each species are computed by adding the contribution of thermal diffusion given by the second term of equation (E.9) to the mole fraction gradient diffusion flux. The total electron number fluxes in the axial and radial directions, unflx, and vnflx, are used in the electron energy equation (3.1). Finally, the total number fluxes for all the heavy species are summed in the axial and radial directions to yield the terms hunflx and hvnflx which are used in the heavy species energy equation (3.2).

Appendix H. Laser Beam Ray Trace

In order to model the deposition of power from the laser beam into the computational domain through heating of the electrons, the beam path and intensity throughout its path must be known. The beam has therefore been discretized by splitting the annulus axially into several smaller pieces, as determined at program run time as an input parameter. Initially, the beam is assumed to be annular with a 50 mm inner diameter and a 75 mm outer diameter to match the beam size as measured in the laboratory. Additionally, the intensity distribution across the annulus is assumed to be Gaussian, with the total power input specified by the user at run time.

The ray trace is split into two regions. The first region lies outside of the computational domain before the beam has yet reached the inlet. In this region the discretized rays are passed through a lens having user specified parameters (radius of curvature, index of refraction, and external thickness) selected to match one of the two lenses used in the laboratory. This external ray trace is performed in subroutine RAYINIT. The radial position, intensity, and direction of each ray at the inlet of the computational domain is computed as follows.

The incident annular beam is first split into a number of individual rays (annuli), each with a finite area. Based on the total power to be input, the intensity of each ray is computed with a Gaussian distribution centered on the center of the annulus. At this point, each ray has an assigned intensity and area, and therefore an assigned power. A ray power distribution can be seen in Table H.1 for which the incident beam of 7000 Watts has been split into 25 discrete rays. Each ray is next traced through a focusing lens up to the computational domain boundary.

The geometry of the external lens ray trace can be seen in the diagram of Figure H.1. Following the ray in from the left hand side, the angle θ_1 is first computed using trigonometry:

$$\theta_1 = \sin^{-1}\left(\frac{r}{Rc}\right) \qquad (H.1)$$

where Rc is the lens radius of curvature. The refracted angle within the lens, θ_2 is computed from θ_1 using the indices of refraction n_1 and n_2 and Snell's Law:

$$\theta_2 = \sin^{-1}\left(\frac{n_1 \sin\theta_1}{n_2}\right) \qquad (H.2)$$

Table H.1 Discretization of Annular Beam Before Optics

ray	r-pos. (m)	ray pow (W)	tot pow (W)	area (m^2)	intensity (W/m^2)
1	0.02525	19.642	19.642	0.00007933	247610.3739
2	0.02575	27.585	47.227	0.00008090	340991.1207
3	0.02625	38.725	85.952	0.00008247	469588.3397
4	0.02675	54.346	140.298	0.00008404	646683.1404
5	0.02725	76.240	216.538	0.00008561	890565.3074
6	0.02775	106.919	323.456	0.00008718	1226422.2108
7	0.02825	149.893	473.350	0.00008875	1688940.0772
8	0.02875	210.076	683.425	0.00009032	2325886.2727
9	0.02925	294.333	977.758	0.00009189	3203042.5628
10	0.02975	412.262	1390.021	0.00009346	4410998.8436
11	0.03025	577.280	1967.300	0.00009503	6074508.9759
12	0.03075	808.128	2775.429	0.00009660	8365374.9655
13	0.03125	1130.992	3906.421	0.00009817	11520190.1240
14	0.03175	834.409	4740.830	0.00009975	8365374.9655
15	0.03225	615.447	5356.277	0.00010132	6074508.9759
16	0.03275	453.835	5810.112	0.00010289	4410998.8436
17	0.03325	334.583	6144.696	0.00010446	3203042.5628
18	0.03375	246.611	6391.306	0.00010603	2325886.2727
19	0.03425	181.729	6573.036	0.00010760	1688940.0772
20	0.03475	133.889	6706.924	0.00010917	1226422.2108
21	0.03525	98.622	6805.547	0.00011074	890565.3074
22	0.03575	72.630	6878.177	0.00011231	646683.1404
23	0.03625	53.478	6931.655	0.00011388	469588.3397
24	0.03675	39.369	6971.024	0.00011545	340991.1207
25	0.03725	28.976	7000.000	0.00011702	247610.3739
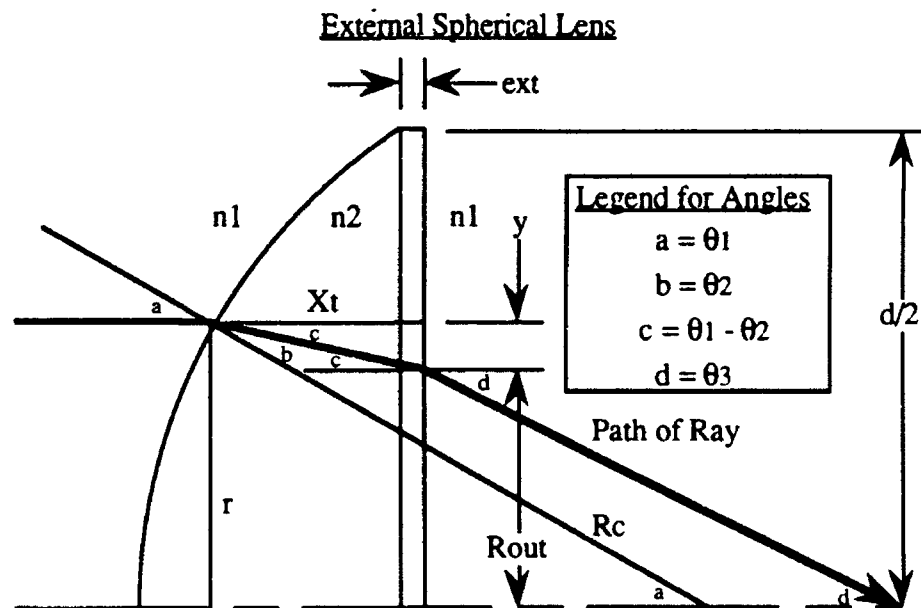
Figure H.1   Geometry of external ray trace

Based on the value of θ_2, the value of angle c in the diagram of Figure H.1 is easily computed as the difference between θ_1 and θ_2. The horizontal distance, Xt is easily computed through multiple application of Pythagoras' theorem:

$$Xt = \sqrt{\left(Rc^2 - r^2\right)} - \sqrt{\left(Rc^2 - \left(\frac{d}{2}\right)^2\right)} + ext \tag{H.3}$$

where ext is the lens extra thickness as can be seen in the diagram of Figure H.1. The radial position where the ray exits the lens may be computed from the other known quantities as:

$$Rout = r - (Xt)\tan\left(\theta_1 - \theta_2\right) \tag{H.4}$$

The ray lens exit angle may next be computed as:

$$\theta_3 = \sin^{-1}\left(\frac{n_2\sin\left(\theta_1 - \theta_2\right)}{n_1}\right) \tag{H.5}$$

Finally, the ray is followed from the lens exit to the computational domain inlet which is a specified distance from the lens. After tracing each of the discretized rays through the lens and up to the domain, the position, angle, and intensity of each ray are known. For a lens to domain distance of 0.22 meters, the radial position, propagation angle and intensity of each ray at the domain inlet is listed in Table H.2 for the same set of rays listed in Table H.1. The internal domain ray trace may now begin. It should be noted that diffraction of the beam through the lens has been neglected because diffraction is a wave phenomenon and rays have been considered.

The second region of the ray trace is within the computational domain and is performed within subroutine RAYS. This region is recomputed at every iteration because both beam path and attenuation are functions of the local species number densities and temperatures. The rays are traced through the domain one at a time, starting at the domain inlet and ending when the ray has exited the domain.

There are 8 cases involved with tracing a ray through the computational domain. Since each computation cell is a rectangle, it must be determined at which face the ray enters the cell and at which face the ray exits the cell, and whether the ray is going toward or away from the axis of symmetry. The 8 cases of ray propagation are summarized in Table H.3.

Once the case of propagation has been determined, the ray path length through the cell must be computed. This is done by first determining the angle at which the ray propagates through the cell

Table H.2 Discretization of Annular Beam After Optics

Radius of curvature is   0.426770000000000
n2=   2.40500000000000   n1=   1.00000000000000

ray	Rdomain (m)	θ_3 (rad)	Intensity (W/m²)
1	0.007	0.083	247610.3739
2	0.007	0.085	340991.1207
3	0.007	0.087	469588.3397
4	0.007	0.088	646683.1404
5	0.007	0.090	890565.3074
6	0.007	0.092	1226422.2108
7	0.007	0.093	1688940.0772
8	0.008	0.095	2325886.2727
9	0.008	0.097	3203042.5628
10	0.008	0.098	4410998.8436
11	0.008	0.100	6074508.9759
12	0.008	0.102	8365374.9655
13	0.008	0.103	11520190.1240
14	0.008	0.105	8365374.9655
15	0.008	0.107	6074508.9759
16	0.009	0.108	4410998.8436
17	0.009	0.110	3203042.5628
18	0.009	0.111	2325886.2727
19	0.009	0.113	1688940.0772
20	0.009	0.115	1226422.2108
21	0.009	0.116	890565.3074
22	0.009	0.118	646683.1404
23	0.009	0.120	469588.3397
24	0.010	0.121	340991.1207
25	0.010	0.123	247610.3739

Table H.3 Summary of 8 Cases of Ray Propagation

Case	Direction	Entrance Face	Exit Face
A1	Toward	West	East
A2	Toward	West	South
B1	Toward	North	South
B2	Toward	North	East
C1	Away	West	East
C2	Away	West	North
D1	Away	South	North
D2	Away	South	East

by again applying Snell's Law to the interface between the current and previous propagation cells.

The index of refraction, n, required for this computation is given by Edwards and Fleck (1979):

$$n = \left(1 - \left(\frac{n_e \lambda_L^2 e^2 k_c}{m_e c^2 \pi}\right)\right)^{1/2} \tag{H.6}$$

where λ_L^2 is the laser wavelength, c is the speed of light in a vacuum, and k_c is the Coulomb constant. With the values for n calculated from equation (H.6) it is clear that rays traveling from regions of lesser ionization to regions of greater ionization will be bent away from the normal, or focused, whereas rays traveling from regions of greater ionization to regions of lesser ionization will be bent toward the normal, or defocused. It should be noted that Jeng and Keefer (1987a and 1987b) neglect changes in plasma refractive index.

The path length through the cell is computed through simple trigonometry depending upon the case of propagation. Attenuation of the ray is computed based upon the ray path length, s, and the computed absorption coefficient, k_{tot}, through Beer's Law:

$$I = I_0 \exp(-k_{tot}s) \tag{H.7}$$

Attenuation of ray intensity is converted to ray power lost to a given cell, which is added to a running total of power absorbed for each cell. The power absorbed by the electrons in each cell is stored for use in the electron energy equation in the array BABS(I,J). The logic determining which case of ray propagation is to be computed next can be seen in the diagram of Figure H.2.

The beam is attenuated by electrons in its path through inverse bremsstrahlung (IB) absorption. The three categories of IB absorption, which depend upon what type of third particle the electron is near when a photon is absorbed, are electron-ion (ei), electron-atom (ea) and electron-molecular (em). The absorption coefficient for each type of IB is computed and then summed to get the total absorption coefficient.

The expression used for the computation of e-i IB coefficient in m^{-1} is that given by Stallcop (1974b):

$$k_{ei} = \frac{c_3(n_e)(n_{H^+})\lambda^3\left(1 - \exp\left(\frac{-hc}{k_b\lambda T_e}\right)\right)gff(\lambda,T_e)}{\sqrt{T_e}} \tag{H.8}$$

where c_3 is given by the expression:

$$c_3 = \left(\frac{256}{3}\right)\left(\sqrt{\frac{\pi}{3}}\right)\pi^2(fsc)a_0^5\left(\frac{(Ry)(jev)}{hc}\right)^3\left(\sqrt{\frac{(Ry)(jev)}{k_b}}\right) \tag{H.9}$$

in which a_0 is the first Bohr radius, λ is the laser wavelength, fsc is the fine structure constant, and $gff(\lambda,T_e)$ is the free-free Gaunt factor which has been crudely curve fitted from the data seen in Figure 2 of Karzas and Latter (1961) for $\lambda = 10.6\mu m$, and Te < 10000K.

$$gff(T_e) = 1.07 + 6.9643 \times 10^{-5} T_e - 2.6786 \times 10^{-9} T_e^2 \tag{H.10}$$

and for $T_e > 10000K$:

$$gff(T_e) = 1.50 + 10^{-5} T_e \tag{H.11}$$
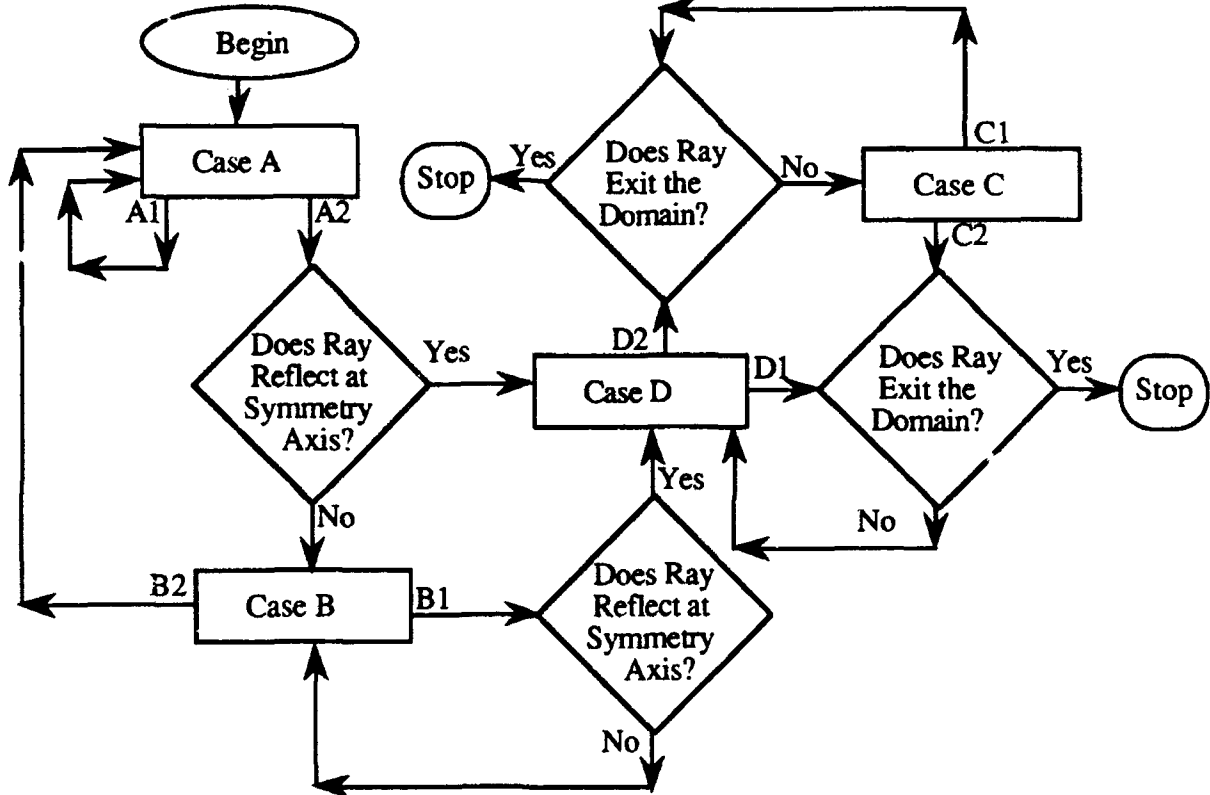
Figure H.2   Logic of computational domain internal ray trace

The expression used for the computation of e-n IB coefficient in m^{-1} is that given by Stallcop (1974a):

$$k_{en} = 2.15 \times 10^{-32} \left(\frac{(Ry)(jev)}{hc} \right)^2 \lambda^2 \left(\sqrt{\frac{(Ry)(jev)}{k_b}} \right) \exp(-c_5)(n_e)(n_H) k_b \sqrt{T_e} \tag{H.12}$$

where c_5 is given by the expression:

$$c_5 = 4.862 k_t \left(1.0 - 0.2096 k_t + 0.017 k_t^2 - 0.00968 k_t^3 \right) \tag{H.13}$$

in which k_t is given by:

$$k_t = \sqrt{\frac{k_b T_e}{(Ry)(jev)}} \tag{H.14}$$

At a laser wavelergth of 10.6μm, equation (H.12) is only valid in the temperature range 1578.5K ≤ T_e ≤ 157846K. At electron temperatures less than 1578.5K, k_{en} is set equal to 0, and at temperatures greater than 157846K, equation (H.12) is evaluated with T_e = 157846K.

The expression used for the computation of e-m IB coefficient in m^{-1} is that given by Caledonia, Wu, and Pirri (1975) from the work of Dalgarno and Lane (1966):

$$k_{em} = \frac{4.51 \times 10^{-44} (n_e)(n_{H_2})(D_{lm})}{(T_e)^{\frac{3}{2}} (1 - \exp(-a))}$$ (H.15)

in which a is given by:

$$a = \frac{hc}{k_b \lambda T_e}$$ (H.16)

and D_{lm} is given by:

$$D_{lm} = D_1 I_1 + \sqrt{b} D_2 I_2 + b D_3 I_3 + b D_3 \left(\frac{3}{a}\right) I_1 \ln(b) + b D_4 \left(\frac{3}{a}\right) I_1 + \left((b)^{\frac{3}{2}}\right) D_5 I_4$$ (H.17)

where b is given by:

$$b = \frac{hc}{(jev)\lambda}$$ (H.18)

The D terms in equation (H.17) are constants, and the I terms are integrals computed as functions of a. At a laser wavelength of 10.6μm, equation (H.15) for k_{em} is only valid for electron temperatures less than 4321.5K. For temperatures above 4321.5K, k_{em} is set equal to 0. The three absorption coefficients from equations (H.8), (H.12), and (H.15) are summed and used as the total absorption coefficient in equation (H.7).

Appendix I. SIMPLE Discretization of Conservation Equations

The techniques involved in the discretization of equations solved using the SIMPLE procedure are explained by Patankar (1980). The discretization of the conservation equations used in this work following the methods of Patankar (1980) is presented below to clarify the solution procedure. Three separate, staggered grids are used for the computation of scalar quantities, and the axial and radial components of velocity. The staggered grid system including boundaries can be seen in the diagram of Figure I.1.
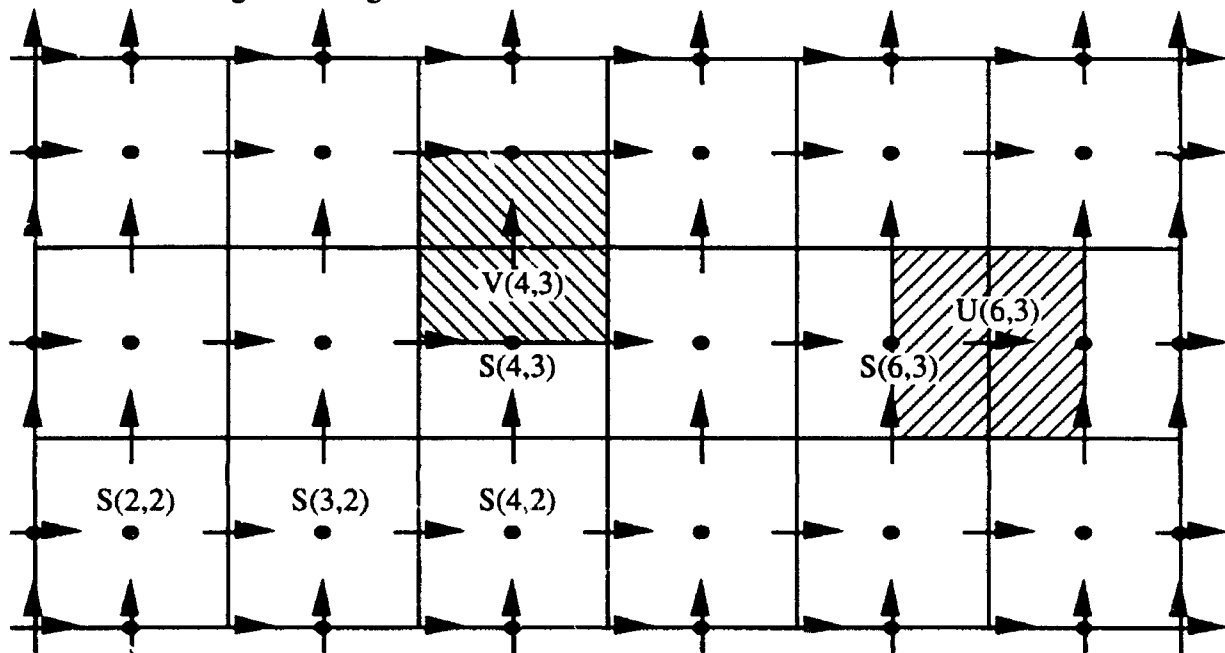
Figure I.1   Diagram of staggered computational grid

Scalar nodes are centered within scalar cells. With reference to Figure I.1, axial velocity nodes are represented by horizontal arrows and radial velocity nodes by vertical arrows. The left side of the diagram represents the inlet, the right side represents the outlet, the top represents the wall, and the bottom represents the axis of symmetry. Axial velocity nodes are centered on scalar cell east faces, with the width of the axial velocity cells extending between the scalar nodes on the east and west sides as indicated by the crosshatching in the diagram of Figure I.1. Radial velocity nodes are centered on scalar cell north faces, with the height of the radial velocity cells extending between the scalar nodes on the north and south sides, again as indicated by the crosshatching in the diagram of Figure I.1.

Boundary nodes follow this same type of arrangement, however boundary cells have no area. In other words, scalar cells, axial velocity cells, and radial velocity cells at the inlet and exit have no width. Similarly, cells at the wall and axis have no height.

The convention for the numbering of nodes follows the node positions. The number of internal scalar nodes in the axial and radial directions are represented by NI and NJ. Scalar nodes are numbered from 1 to NI+2 in the axial direction, and 1 to NJ+2 in the radial direction. This means that internal scalar cells go from 2 to NI+1 and 2 to NJ+1, axially and radially, respectively. Axial velocity nodes are numbered from 1 to NI+1 in the axial direction and 1 to NJ+2 in the radial direction. As a result of the geometry, there are NI-1 internal axial velocity nodes in the axial direction. Finally, radial velocity nodes are numbered from 1 to NI+2 in the axial direction and 1 to NJ+1 in the radial direction. Again, due to the grid layout, there are NJ-1 internal radial velocity nodes in the radial direction. It should be noted that although Figure J.1 represents a uniform grid, the same relations between nodes and cells apply to a nonuniform grid as well.

Values for variables at cell interfaces will be necessary as will be seen in the following procedure. The computation of these interface quantities presents no problem whatsoever for a uniformly sized grid. However, because it may be advantageous to allow for a nonuniform grid to place more nodes in regions of high gradients, the computation of interface values becomes slightly more involved. Weighting factors are introduced to allow for interface value computation on a nonuniform grid. The weighting factor for a particular cell on a particular interface represents the effect of that cell on the value of the quantity in question at the interface. From a practical standpoint, the weighting factors are no more than factors for linear interpolation between nodes, since it is assumed that there exists a linear variation of quantities from node to node. The cell widths and heights necessary to compute east-west and north-south weighting factors can be seen in the diagrams of Figure I.2.

With reference to the diagrams of Figure I.2, weighting factors are defined as:

$$WFE(I) \equiv \frac{SEW(I+1)}{SEW(I) + SEW(I+1)} \tag{I.1}$$

$$WFW(I) \equiv \frac{SEW(I-1)}{SEW(I-1) + SEW(I)} \tag{I.2}$$

$$WFN(J) \equiv \frac{SNS(J+1)}{SNS(J) + SNS(J+1)} \tag{I.3}$$

$$WFS(J) \equiv \frac{SNS(J-1)}{SNS(J-1) + SNS(J)} \tag{I.4}$$
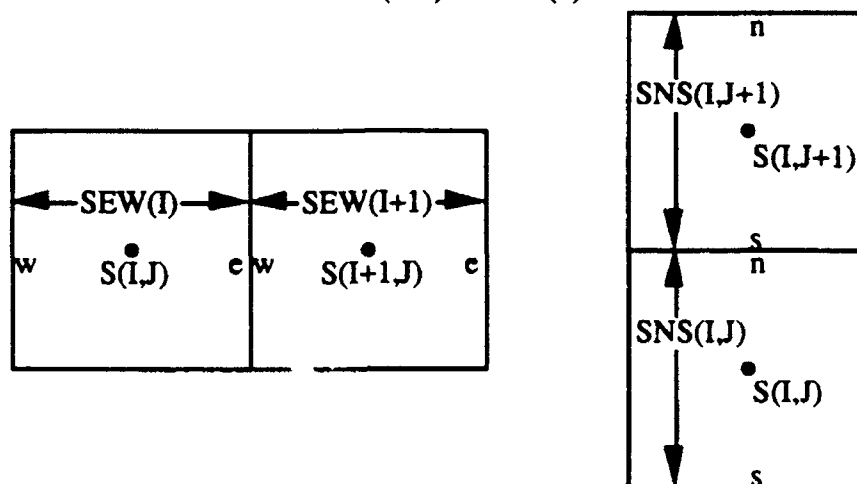
Figure I.2   Quantities necessary to compute weighting factors

It should be noted that for all internal cells of a uniform grid, the weighting factors as defined by equations (I.1) to (I.4) reduce to a value of 0.5. Boundary weighting factors also naturally yield a value of either 1.0 or 0.0 depending on which direction the weighting factor is applied.

The method used to determine the variable interface value will depend upon how the value is to be used. If the interface value is to be multiplied by a gradient across the interface, and therefore represents a type of diffusive flux, the value must be computed as a harmonic mean of the known values at the nodes on either side of the interface. This case will be referred to as the diffusive interface value. If the interface value is not to be multiplied by a gradient across the interface, then the interface value will be computed as a simple arithmetic mean. This case will be referred to as the convective interface value. The distinction between the two cases will become more clear as this discussion progresses. Through the weighting factors defined in equations (I.1) to (I.4), the value for convective interface values may be computed at all cell interfaces. The expressions used for convective axial and radial interfaces are given respectively by:

$$VALUE_{axial\ interface} = (WFE(I))(VALUE(I,J)) + (WFW(I+1))(VALUE(I+1,J)) \tag{I.5}$$

$$\text{VALUE}_{\text{radial interface}} = (\text{WFN}(J))(\text{VALUE}(I,J)) + (\text{WFS}(J+1))(\text{VALUE}(I,J+1)) \qquad (I.6)$$

The computation of diffusive interface values, such as required for viscosity, thermal conductivity, and multicomponent and thermal diffusion coefficients, is handled somewhat differently. Since what is really required at the interface is a computation of some type of flux, the coefficient used to determine the flux should reflect the geometry between the nodes across which the gradient is taken. The diffusive interface values can be correctly computed by application of the harmonic rule (Patankar, 1980, pp. 44-47). In the axial and radial directions, the diffusive interface values respectively, are:

$$\text{VALUE}_{\text{axial interface}} = \left(\frac{\text{WFW}(I+1)}{\text{VALUE}(I,J)} + \frac{\text{WFE}(I)}{\text{VALUE}(I+1,J)} \right)^{-1} \qquad (I.7)$$

$$\text{VALUE}_{\text{radial interface}} = \left(\frac{\text{WFS}(J+1)}{\text{VALUE}(I,J)} + \frac{\text{WFN}(J)}{\text{VALUE}(I,J+1)} \right)^{-1} \qquad (I.8)$$

Now that the computational grid and interface computational methods have been described, the discretization of the conservation equations may be intelligibly presented. The methodology is basically the application of an overall flux balance at each computational cell. The end result of the discretization at a gridpoint P is an equation of the form:

$$a_P \Phi_P = a_E \Phi_E + a_W \Phi_W + a_N \Phi_N + a_S \Phi_S + \text{Sources} \qquad (I.9)$$

for two dimensions in which Φ is the variable in question, and the subscripts represent the influence of the neighbor gridpoints to the east, west, north, and south directions. The term for sources may include rates of production or destruction of Φ, or any terms in the original differential equation not involving Φ.

Each of the neighbor coefficients is a function of the total flux of Φ crossing the interface between the center point and the neighbor point. The total flux J across an interface is the sum of convective and diffusive contributions, and may be written as:

$$J = C\Phi - D\frac{\partial \Phi}{\partial x} \qquad (I.10)$$

in which C is the convective coefficient and D is the diffusive coefficient. Once the proper convective and diffusive coefficients have been identified, the application of the discretization procedure may proceed in a straightforward manner as described by Patankar (1980, pp. 92-100).

Although the discretization procedure is essentially the same for all equations, the determination of the convective and diffusive coefficients may be different and requires careful attention. With reference to the diagram of an axial velocity cell in Figure I.3, the axial momentum equation is presented as an example of the discretization procedure.
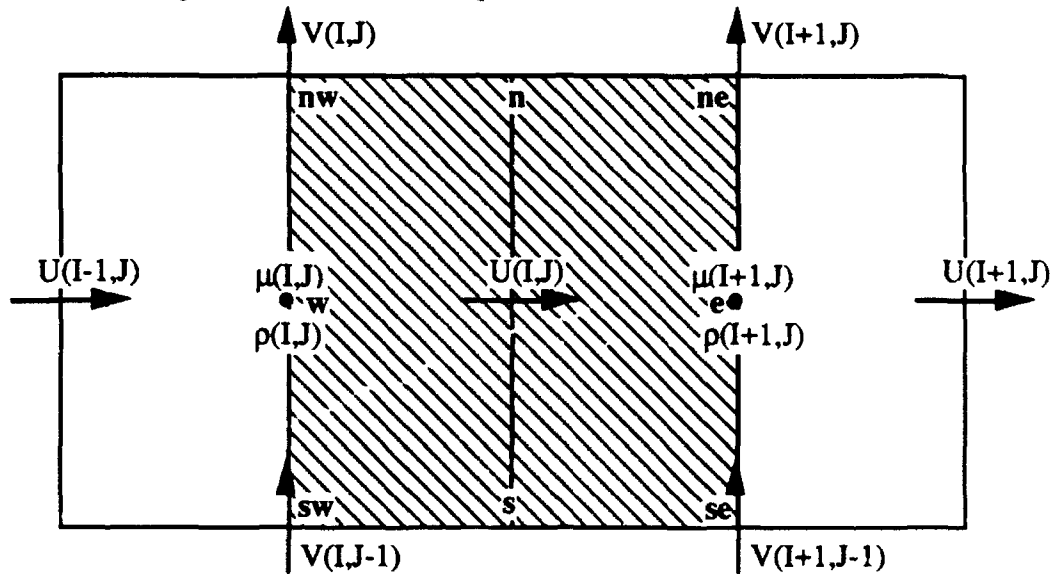
Figure I.3   Diagram of an axial velocity cell

The axial momentum equation is:

$$\frac{\partial}{\partial x}(\rho uu) + \frac{1}{r}\frac{\partial}{\partial r}(r\rho uv) = \frac{4}{3}\frac{\partial}{\partial x}\left(\mu\frac{\partial u}{\partial x}\right) + \frac{1}{r}\frac{\partial}{\partial r}\left(\mu r\frac{\partial u}{\partial r}\right)$$

$$\quad\quad\text{C1}\quad\quad\quad\text{C2}\quad\quad\quad\quad\text{D1}\quad\quad\quad\text{D2}$$

$$-\frac{2}{3}\frac{\partial}{\partial x}\left(\mu\frac{\partial v}{\partial r}\right) - \frac{2}{3r}\frac{\partial}{\partial x}(\mu v) + \frac{1}{r}\frac{\partial}{\partial r}\left(\mu r\frac{\partial v}{\partial x}\right) - \frac{\partial p}{\partial x} - \rho g \quad\quad\quad (I.11)$$

$$\quad\quad\text{S1}\quad\quad\quad\quad\text{S2}\quad\quad\quad\quad\text{S3}\quad\quad\quad\text{S4}\ \text{S5}$$

where the terms have been labeled as either convection, diffusion or source terms. With reference to Figure I.3, the subscript of a variable will refer to the interface at which the variable is to be evaluated. Since the computational domain is axisymmetric, each term is integrated over a slice of one radian width so that the integration is a double integral over r dr and over dx. Integration of the first convection term yields:

$$\int_{w}^{e}\int_{s}^{n}\left(\frac{\partial}{\partial x}(\rho uu)\right) r\ dr\ dx = \left(\frac{rv_n^2}{2} - \frac{rv_s^2}{2}\right)\left((\rho uu)_e - (\rho uu)_w\right) \quad\quad (I.12)$$

$$= AREAEW(J)\left((\rho u)_e u_e - (\rho u)_w u_w\right) \quad\quad (I.13)$$

where AREAEW(J) represents the cross sectional area of the axial cell face for all axial velocity (and scalar) nodes at radial index J. Integration of the second convection term yields:

$$\int_w^e \int_s^n \left(\frac{1}{r}\frac{\partial}{\partial r}(r\rho uv)\ r\ dr\ dx\right) = \left((r\rho uv)_n - (r\rho uv)_s\right)\left(X_e - X_w\right) \tag{I.14}$$

$$= AREANU(I,J)(\rho v)_n u_n - AREASU(I,J)(\rho v)_s u_s \tag{I.15}$$

where AREANU(I,J) represents the area of the north face, and AREASU(I,J) represents the area of the south face of the axial velocity cell at index (I,J). Integration of the first diffusion term yields:

$$\int_w^e \int_s^n \left(\frac{4}{3}\frac{\partial}{\partial x}\left(\mu\frac{\partial u}{\partial x}\right)\ r\ dr\ dx\right) = \frac{4}{3}\left(\frac{rv_n^2}{2} - \frac{rv_s^2}{2}\right)\left(\left(\mu\frac{\partial u}{\partial x}\right)_e - \left(\mu\frac{\partial u}{\partial x}\right)_w\right) \tag{I.16}$$

$$= \frac{4}{3}AREAEW(J)\left((\mu_e)\left(\frac{\partial u}{\partial x}\right)_e - (\mu_w)\left(\frac{\partial u}{\partial x}\right)_w\right) \tag{I.17}$$

and integration of the second diffusion term yields:

$$\int_w^e \int_s^n \left(\frac{1}{r}\frac{\partial}{\partial r}\left(\mu r\frac{\partial u}{\partial r}\right)\ r\ dr\ dx\right) = \left(\left(\mu r\frac{\partial u}{\partial r}\right)_n - \left(\mu r\frac{\partial u}{\partial r}\right)_s\right)\left(X_e - X_w\right) \tag{I.18}$$

$$= AREANU(I,J)(\mu_n)\left(\frac{\partial u}{\partial r}\right)_n - AREASU(I,J)(\mu_s)\left(\frac{\partial u}{\partial r}\right)_s \tag{I.19}$$

The five remaining terms have been labeled as source terms because the axial velocity does not appear in them. Integration of the first source term yields:

$$\int_w^e \int_s^n \left(-\frac{2}{3}\frac{\partial}{\partial x}\left(\mu\frac{\partial v}{\partial r}\right)\ r\ dr\ dx\right) = -\frac{2}{3}\left(\frac{rv_n^2}{2} - \frac{rv_s^2}{2}\right)\left(\left(\mu\frac{\partial v}{\partial r}\right)_e - \left(\mu\frac{\partial v}{\partial r}\right)_w\right) \tag{I.20}$$

$$= -\frac{2}{3}AREAEW(J)\left((\mu_e)\left(\frac{\partial v}{\partial r}\right)_e - (\mu_w)\left(\frac{\partial v}{\partial r}\right)_w\right) \tag{I.21}$$

and integration of the second source term yields:

$$\int_w^e \int_s^n \left(-\frac{2}{3r}\frac{\partial}{\partial x}(\mu v)\ r\ dr\ dx\right) = -\frac{2}{3}\left(rv_n - rv_s\right)\left((\mu v)_e - (\mu v)_w\right) \tag{I.22}$$

$$= -\frac{2}{3}SNS(J)\left(\mu_e v_e - \mu_w v_w\right) \tag{I.23}$$

and integration of the third source term yields:

$$\int_w^e \int_s^n \left(\frac{1}{r}\frac{\partial}{\partial r}\left(\mu r\frac{\partial v}{\partial x}\right)\ r\ dr\ dx\right) = \left(\left(\mu r\frac{\partial v}{\partial x}\right)_n - \left(\mu r\frac{\partial v}{\partial x}\right)_s\right)\left(X_e - X_w\right) \tag{I.24}$$

$$= \text{AREANU}(I,J)(\mu_n)\left(\frac{\partial v}{\partial x}\right)_n - \text{AREASU}(I,J)(\mu_s)\left(\frac{\partial v}{\partial x}\right)_s \qquad (I.25)$$

and, finally, integration of the fourth and fifth source terms yields:

$$\int_w^e \int_s^n \left(\left(-\frac{\partial p}{\partial x} - \rho g\right) r \, dr \, dx\right) = -\left(\frac{rv_n^2}{2} - \frac{rv_s^2}{2}\right)(p_e - p_w) - (\rho g)\left(\frac{rv_n^2}{2} - \frac{rv_s^2}{2}\right)(X_e - X_w) \qquad (I.26)$$

$$= - \text{AREAEW}(J)(p_e - p_w) - (\rho g)\text{AREAEW}(J)(X_e - X_w) \qquad (I.27)$$

The next stage in the discretization is to write the integrated expressions for each term including the appropriate expressions for interface values. The first convection term (I.13) may be written:

$$\text{AREAEW}(J)\left((\rho u)_e u_e - (\rho u)_w u_w\right) = C_e u_e - C_w u_w \qquad (I.28)$$

in which the convective coefficients, C_e, and C_w, are:

$$C_e = \rho(I+1,J)(0.5)(u(I,J)+u(I+1,J))\text{AREAEW}(J) \qquad (I.29)$$

$$C_w = \rho(I+1,J)(0.5)(u(I,J)+u(I+1,J))\text{AREAEW}(J) \qquad (I.30)$$

Similarly, the second convection term (I.15) may be written:

$$\text{AREANU}(I,J)(\rho v)_n u_n - \text{AREASU}(I,J)(\rho v)_s u_s = C_n u_n - C_s u_s \qquad (I.31)$$

in which the convective coefficients, C_n, and C_s, are:

$$C_n = \text{AREANU}(I,J)\text{WFE}(I)v(I,J)\left(\text{WFN}(J)\rho(I,J)+\text{WFS}(J+1)\rho(I,J+1)\right)$$

$$+ \text{AREANU}(I,J)\text{WFW}(I+1)v(I+1,J)\left(\text{WFN}(J)\rho(I+1,J)+\text{WFS}(J+1)\rho(I+1,J+1)\right) \qquad (I.32)$$

$$C_s = \text{AREASU}(I,J)\text{WFE}(I)v(I,J-1)\left(\text{WFS}(J)\rho(I,J)+\text{WFN}(J-1)\rho(I,J-1)\right)$$

$$+ \text{AREASU}(I,J)\text{WFW}(I+1)v(I+1,J-1)\left(\text{WFS}(J)\rho(I+1,J)+\text{WFN}(J-1)\rho(I+1,J-1)\right) \qquad (I.33)$$

Note that all the interface values in the convective coefficients have been computed as arithmetic means through the use of the weighting factors. The first diffusion term (I.17) may be written as:

$$\frac{4}{3}\text{AREAEW}(J)\left((\mu_e)\left(\frac{\partial u}{\partial x}\right)_e - (\mu_w)\left(\frac{\partial u}{\partial x}\right)_w\right) = D_e(u(I+1,J)-u(I,J)) - D_w(u(I,J)-u(I-1,J)) \qquad (I.34)$$

in which the diffusive coefficients, D_e, and D_w, are:

$$D_e = \frac{4}{3}\text{AREAEW}(J)\frac{\mu(I+1,J)}{\text{SEW}(I+1)} \qquad (I.35)$$

$$D_w = \frac{4}{3}\text{AREAEW}(J)\frac{\mu(I,J)}{\text{SEW}(I)} \qquad (I.36)$$

The second diffusion term (I.19) may be similarly written as:

$$\text{AREANU}(I,J)(\mu_n)\left(\frac{\partial u}{\partial r}\right)_n - \text{AREASU}(I,J)(\mu_s)\left(\frac{\partial u}{\partial r}\right)_s =$$

$$D_n(u(I,J+1)-u(I,J)) - D_s(u(I,J)-u(I,J-1)) \tag{I.37}$$

where the diffusive coefficients, D_n, and D_s, are given by:

$$D_n = \frac{AREANU(I,J)\ \mu_n}{r(J+1)-r(J)} \tag{I.38}$$

$$D_s = \frac{AREASU(I,J)\ \mu_s}{r(J)-r(J-1)} \tag{I.39}$$

and the interface viscosities, μ_n, and μ_s are computed as the harmonic means of the arithmetic mean values at the axial velocity nodes as:

$$\mu_n = \left(\frac{WFS(J+1)}{WFE(I)\mu(I,J)+WFW(I+1)\mu(I+1,J)} + \frac{WFN(J)}{WFE(I)\mu(I,J+1)+WFW(I+1)\mu(I+1,J+1)}\right)^{-1} \tag{I.40}$$

$$\mu_s = \left(\frac{WFS(J)}{WFE(I)\mu(I,J-1)+WFW(I+1)\mu(I+1,J-1)} + \frac{WFN(J-1)}{WFE(I)\mu(I,J)+WFW(I+1)\mu(I+1,J)}\right)^{-1} \tag{I.41}$$

Following the same procedure for the sources, the first source term (I.21) may be written:

$$-\frac{2}{3}AREAEW(J)\left(\left(\mu_e\right)\left(\frac{\partial v}{\partial r}\right)_e - \left(\mu_w\right)\left(\frac{\partial v}{\partial r}\right)_w\right) =$$

$$-\frac{2}{3}AREAEW(J)\left(\mu(I+1,J)\frac{v(I+1,J)-v(I+1,J-1)}{SNS(J)} - \mu(I,J)\frac{v(I,J)-v(I,J-1)}{SNS(J)}\right) \tag{I.42}$$

The second source term (I.23) may be written:

$$-\frac{2}{3}SNS(J)\left(\mu_e v_e - \mu_w v_w\right) =$$

$$-\frac{1}{3}SNS(J)\left(\mu(I+1,J)(v(I+1,J)+v(I+1,J-1)) - \mu(I,J)(v(I,J)+v(I,J-1))\right) \tag{I.43}$$

The third source term (I.25) may be written:

$$AREANU(I,J)\left(\mu_n\right)\left(\frac{\partial v}{\partial x}\right)_n - AREASU(I,J)\left(\mu_s\right)\left(\frac{\partial v}{\partial x}\right)_s =$$

$$AREANU(I,J)\left(\mu_{n1}\right)\frac{v(I+1,J)-v(I,J)}{X(I+1)-X(I)} - AREASU(I,J)\left(\mu_{s1}\right)\frac{v(I+1,J-1)-v(I,J-1)}{X(I+1)-X(I)} \tag{I.44}$$

where the interface viscosities, μ_{n1}, and μ_{s1}, are computed as the harmonic means of the arithmetic mean values at the axial velocity cell corners as:

$$\mu_{n1} = \left(\frac{WFE(I)}{WFN(J)\mu(I+1,J)+WFS(J+1)\mu(I+1,J+1)} + \frac{WFW(I+1)}{WFN(J)\mu(I,J)+WFS(J+1)\mu(I,J+1)}\right)^{-1} \tag{I.45}$$

$$\mu_{s1} = \left(\frac{WFE(I)}{WFN(J-1)\mu(I+1,J-1)+WFS(J)\mu(I+1,J)} + \frac{WFW(I+1)}{WFN(J-1)\mu(I,J-1)+WFS(J)\mu(I,J)}\right)^{-1} \tag{I.46}$$

The fourth and fifth source terms (I.27) may be written as:

$$-AREAEW(J)\left(p_e - p_w\right) - \left(\rho g\right)AREAEW(J)\left(X_e - X_w\right) =$$

$$-AREAEW(J)\left((p(I+1,J)-p(I,J)) + \left(WFE(I)\rho(I,J)+WFW(I+1)\rho(I+1,J)\right)g(X(I+1)-X(I))\right) \tag{I.47}$$

in which the pressure terms are the latest values for pressure variation as supplied by the pressure correction equation.

At this stage all that remains is to choose the appropriate scheme with which to weight the interface values of the variable in question, Φ. The Peclet number is defined at each interface, i, as:

$$P_i = \frac{C_i}{D_i} \tag{I.48}$$

Clearly the Peclet number is a ratio of the contributions of convection and diffusion to the total flux. Based upon the magnitude of the interface Peclet numbers, the neighbor coefficients are computed using the power law method as recommended by Patankar (1980, p. 100). The neighbor coefficients are then:

$$a_E = D_e MAX[0, \left(1 - 0.1|P_e|\right)^5] + MAX[-C_e, 0] \tag{I.49}$$

$$a_W = D_w MAX[0, \left(1 - 0.1|P_w|\right)^5] + MAX[C_w, 0] \tag{I.50}$$

$$a_N = D_n MAX[0, \left(1 - 0.1|P_n|\right)^5] + MAX[-C_n, 0] \tag{I.51}$$

$$a_S = D_s MAX[0, \left(1 - 0.1|P_s|\right)^5] + MAX[C_s, 0] \tag{I.52}$$

The center coefficient, a_P is then the sum of the neighbor coefficients:

$$a_P = a_E + a_W + a_N + a_S \tag{I.53}$$

The discretized equation (I.9) has been constructed. The solution subroutines for the conservation equations formulate an equation such as (I.9) for every point in the solution domain which are then solved alternately along lines of constant x or constant r by the subroutine ADI. The solution for Φ is underrelaxed from iteration to iteration using an underrelaxation factor typically around 0.5 for this work. The solution algorithm is unconditionally stable, and convergence is reached when the normalized sum of the difference between the left hand side of equation (I.9) and the right hand side of equation (I.9) for all points in the domain is less than some convergence criterion which is typically on the order of 1×10^{-4}.

The discretization of the other conservation equations requires diagrams of the radial velocity and scalar cells. A diagram of the radial velocity cell can be seen in Figure I.4. The scalar cell

geometry appears in sufficient detail in both Figures I.3 and I.4. The discretization of the other conservation equations is not presented here.
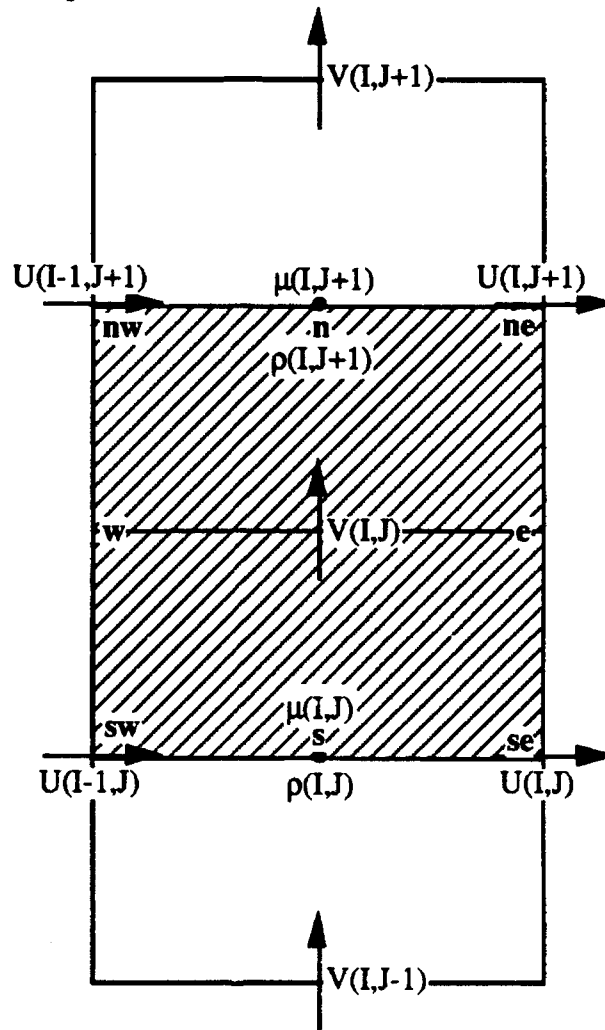
Figure I.4   Diagram of a radial velocity cell

For conditions where the flowfield is far from convergence, an additional term has been added which acts as extra underrelaxation. The term is labeled as SMP in the UMOM and VMOM subroutines and represents the absolute value of the net convective flux for the computational cell. Since SMP is added to both sides of the discretized equation, and since SMP goes to zero as mass is conserved, it has no effect on the final solution.

The boundary conditions for the conservation equations are straightforward. The axial velocity equation has inlet velocity constrained by the selected mass flow rate, zero velocity at the outer wall, zero radial derivative at the axis, and zero axial derivative at the exit. The radial velocity

equation has zero velocities at the inlet, axis and outer wall, and zero axial derivative at the exit. The energy equations have fixed inlet temperatures, zero radial derivatives at the axis and wall, and zero axial derivative at the exit.

The bulk continuity equation is transformed into the pressure correction equation as prescribed by Patankar (1980). The pressure field floats around an arbitrary level and so there are no boundary conditions required for the pressure correction equation. All values of pressure are given relative to internal scalar node (2,2). The derivation of the pressure correction equation is described well by Patankar (1980) and will not be reproduced here.

There was some question as to whether a laminar flow code would be sufficient to handle some of the desired test cases because of high the Reynolds numbers involved. The situation is complicated by the fact that the flow is not fully developed, and there is a plasma in the center of the duct which changes the fluid density and accelerates the flow. These effects were seen in the previous LTE model of Eguiguren (1989). Due to these two factors, Eguiguren stated that the usual transition Reynolds number does not apply to the LSP problem, and the laminar code was sufficient. In fact the limiting factor affecting the maximum Reynolds number that could be run in the LTE code was not a transition to turbulence but rather the plasma blowout.

In order to confirm that the discretization of the momentum equations was correct, two formulations were tested. The first formulation was the complete variable property formulation, and the second was the constant property formulation. Although the equations for each of these formulations are somewhat different, it can be easily shown as in Appendix D that the first reduces to the second when constant properties are assumed. Therefore, the discretization of the first case run with constant properties should yield the exact same solutions for the axial and radial velocities as the discretization of the second case. In fact this was shown to be true. The results were also compared with the results of Cebeci and Bradshaw (1977, pp. 117-123) and showed good agreement.

Appendix J. Simplified Number Density Computation

Assuming that the kinetic temperatures and system pressure of a hydrogen plasma are known, then the major species ($H(n)$, H^+, H_2, and e^-) number densities may be computed using the iterative method described in this appendix and performed in subroutine SPECIES. This simplified number density computation assumes that the atomic (bound electron) excitation temperature equals the electron kinetic temperature, and that all the molecular internal mode temperatures equal the gas kinetic temperature. Assuming that the bound electron excitational temperature equals the kinetic electron temperature allows the computation of all the neutral hydrogen atom excited level populations from the total neutral population. This assumption reduces the total number of species to be computed by n-1 (where n is the uppermost excited level), making the number of unknown number densities equal to four. Further assuming the plasma to be electrically neutral reduces the number of unknowns from four to three since in this case, $n_{e^-} = n_{H^+}$. Therefore three equations are required to solve for the number densities based on a given set of electron kinetic temperature, heavy kinetic temperature, and pressure. These three equations are the kinetic nonequilibrium laws of mass action for the hydrogen dissociation and ionization reactions, and the multitemperature plasma equation of state.

The generalized law of mass action for multimode thermal nonequilibrium and chemical equilibrium has been presented by Eddy and Cho (1991) as:

$$\left(\prod_j n_j^{(v_j k_b T_{jt})} \right) = \exp\left(-\left(\sum_j v_j E_{oj} \right) \right) \left(\prod_j \left(\frac{Z_{jt}}{V} \right)^{(v_j k_b T_{jt})} \right) \left(\prod_{k>1} Z_{jk}^{(v_j k_b T_{jk})} \right) \quad (J.1)$$

where the j subscripts refer to species in the reaction, the t subscript means translational, and the k subscripts represent internal energy modes (rotational, vibrational, and electronic). The v_j are the stoichiometric coefficients for the specific reaction, the Z terms are the partition functions, and the E_{oj} are the zero point energies. Application of equation J.1 to the dissociation and ionization reactions is straightforward as follows. Beginning with the symbolic equation for the dissociation reaction:

$$H_2 \Leftrightarrow 2H \quad (J.2)$$

equation J.1 takes the form:

$$\frac{\left(n_{H_2}\right)^{k_b T_g}}{\left(n_H\right)^{2k_b T_g}} =$$

$$\exp\left(-\left(E_{oH_2} - 2E_{oH}\right)\right)\frac{\left(\frac{Z_{H_2 t}}{V}\right)^{k_b T_g}}{\left(\frac{Z_{Ht}}{V}\right)^{2k_b T_g}}\left(\frac{\left(Z_{H_2 rot}\right)^{k_b T_{H_2 rot}}\left(Z_{H_2 vib}\right)^{k_b T_{H_2 vib}}\left(Z_{H_2 ex}\right)^{k_b T_{H_2 ex}}}{\left(Z_{Hex}\right)^{2k_b T_{Hex}}}\right) \quad (J.3)$$

where the appropriate energy modes have been written in as either translational, rotational, vibrational, or excitational. The translational partition function may be written as:

$$Z_t = V\left(\frac{2\pi m k_b T_t}{h^2}\right)^{\frac{3}{2}} \quad (J.4)$$

where m is the mass of the particle and h is Planck's constant. After taking the k_bth root of both sides of equation (J.3), and assuming that the mass of H_2 is twice the mass of H, substitution of equation (J.4) into equation (J.3) yields:

$$\frac{\left(n_{H_2}\right)^{T_g}}{\left(n_H\right)^{2T_g}} =$$

$$\exp\left(-\left(\frac{E_{oH_2} - 2E_{oH}}{k_b}\right)\right)\left(\frac{1}{\left(\frac{\pi m_H k_b T_g}{h^2}\right)^{\frac{3T_g}{2}}}\right)\left(\frac{\left(Z_{H_2 rot}\right)^{T_{H_2 rot}}\left(Z_{H_2 vib}\right)^{T_{H_2 vib}}\left(Z_{H_2 ex}\right)^{T_{H_2 ex}}}{\left(Z_{Hex}\right)^{2T_{Hex}}}\right) \quad (J.5)$$

Since it has been assumed that all the molecular internal mode temperatures equal the heavy kinetic temperature, the temperatures in the exponents of the numerator of the last bracketed term simplify to T_g. In addition, the atomic excitational temperature was assumed to be equal to the electron kinetic temperature, T_e. This leaves only the partition functions and the zero point energies as unknowns on the RHS of equation (J.5). The partition functions may all be computed as functions of temperature alone as done by Moder (1990). In general, the values for the zero point energies are most easily derived if the zero point is chosen as the ground state of the dissociated or ionized species. This may bring up the question as to whether the same zero point value must be used in all the equations, if more than one law of mass action equation is included. Further, it may be asked how the value of the single zero point is to be determined, and how the

value affects the partition functions. The answer is that as long as the energy of the reacting system represented by each equation is assured to be conserved, the choice of the zero point is arbitrary for each reaction and has no effect on the partition functions (Zerkle, 1992b). For the purpose of this work, the zero point chosen for the dissociation reaction is the ground state of the hydrogen atom, making $E_{oH_2} = -E_{H_2d}$ (negative of the molecular dissociation energy), and $E_{oH} = 0$.

Substituting for the internal mode temperatures and the zero point energies, taking the T_gth root, and inverting both sides of equation (J.5) yields:

$$\frac{(n_H)^2}{n_{H_2}} = \exp\left(\frac{-E_{H_2d}}{k_bT_g}\right)\left(\frac{\pi m_H k_b T_g}{h^2}\right)^{\frac{3}{2}}\left(\frac{(Z_{Hex})^{\frac{2T_e}{T_g}}}{(Z_{H_2rot})(Z_{H_2vib})(Z_{H_2ex})}\right) \qquad (J.6)$$

Next considering the symbolic equation for the ionization reaction:

$$H^+ + e^- \Leftrightarrow H \qquad (J.7)$$

equation J.1 takes the form:

$$\frac{(n_{H^+})^{k_bT_g}(n_e)^{k_bT_e}}{(n_H)^{k_bT_g}} =$$

$$\exp\left(-\left(E_{oH^+} + E_{oe} - E_{oH}\right)\right)\left(\frac{\left(\frac{Z_{H^+t}}{V}\right)^{k_bT_g}\left(\frac{Z_{et}}{V}\right)^{k_bT_e}}{\left(\frac{Z_{Ht}}{V}\right)^{k_bT_g}}\right)\left(\frac{(Z_{H^+ex})^{k_bT_{H^+ex}}(Z_{eex})^{k_bT_{eex}}}{(Z_{Hex})^{k_bT_{Hex}}}\right) \qquad (J.8)$$

The values for the excitational partition functions of protons and electrons are 1 and 2 respectively. Assuming that the free electron excitational temperature is equal to the bound electron excitational temperature, which is also equal to the electron kinetic temperature, allows all the temperatures in the exponents of the last bracket to be replaced by T_e. Choosing the zero point to be the ground state of the proton results in $E_{oH^+} = E_{oe} = 0$, and $E_{oH} = -E_i$ (the negative of the lowered ionization potential). Substituting for the electron excitational temperatures and zero point energies, assuming that the mass of a proton is approximately the mass of a hydrogen atom, and taking the (k_bT_e)th root of equation (J.8) yields:

$$n_e \left(\frac{n_{H^+}}{n_H}\right) \frac{T_g}{T_e} = \left(\frac{2\exp\left(\frac{-E_i}{k_b T_e}\right)\left(\frac{2\pi m_e k_b T_e}{h^2}\right)^{\frac{3}{2}}}{Z_{Hex}}\right) \tag{J.9}$$

Equations (J.6) and (J.9) are the laws of mass action for the hydrogen dissociation and ionization reactions under the assumptions listed above. The partition functions necessary for these equations are Z_{H_2rot}, Z_{H_2vib}, Z_{H_2ex}, and Z_{Hex}. The first three partition functions are given by Moder (1990) as:

$$Z_{H_2rot} \approx \frac{T_g}{175.24} \tag{J.10}$$

$$Z_{H_2vib} = \left(1 - e^{-\left(\frac{5983}{T_g}\right)}\right)^{-1} \tag{J.11}$$

$$Z_{H_2ex} \approx 1 \tag{J.12}$$

The atomic excitational partition function, Z_{Hex}, includes a term for every bound level of the hydrogen atom. Therefore Z_{Hex} represents an infinite series unless an uppermost bound level can be chosen to truncate the series. The uppermost bound level is chosen by computing the lowering of the ionization potential based upon the Debye-Hückel and Bethe methods. The lowering in eV based on the Debye-Hückel method, and neglecting the minor species is (Cho, 1988):

$$\Delta Ei_{DH} = \frac{e^2 k_c}{jev}\sqrt{\left(\frac{4\pi e^2 k_c}{k_b}\right)\left(\frac{n_e}{T_e} + \frac{n_{H^+}}{T_g}\right)} \tag{J.13}$$

where e is the charge on an electron in Coulombs, k_c is the Coulomb constant, and jev is the conversion from joules to eV. Cho (1988) also gives the lowering based upon the Bethe method:

$$\Delta Ei_B = \frac{a_0 Ry}{\left(\frac{3}{4\pi n_h}\right)^{\frac{1}{3}}} \tag{J.14}$$

where n_h is the total heavy species number density in m^{-3}, a_0 is the first Bohr radius in meters, and Ry is the Rydberg constant in eV. In terms of more basic constants, the Bethe lowering is given in units of eV by:

$$\Delta Ei_B = \frac{e^2 k_c m_H}{2jev(m_e + m_H)\left(\frac{3}{4\pi n_h}\right)^{\frac{1}{3}}} \tag{J.15}$$

The maximum computed lowering is then used to compute the uppermost bound level. This uppermost level is constrained to be greater than or equal to six. The final required partition function is then computed as a sum over the included levels:

$$Z_{Hex} = \sum_j \left(2j^2\right) \exp\left(\frac{-E_j}{k_b T_e}\right) \tag{J.16}$$

Once the ionization lowering has been computed, the right hand sides of equations (J.6) and (J.9) are completely determined.

The third equation necessary for the major species computation is the multitemperature plasma equation of state (Cho, 1988):

$$P = \left(n_e k_b T_e + n_h k_b T_g\right)\left(1 - P_C^{DH}\right) \tag{J.17}$$

where P is the system pressure, and P_C^{DH} is the Debye-Hückel pressure correction which, neglecting the minor species, is:

$$P_C^{DH} = \left(24\pi(n_e+n_h)\left(\frac{4\pi e^2 k_c}{k_b}\left(\frac{n_e}{T_e} + \frac{n_{H^+}}{T_g}\right)\right)^{-1.5}\right)^{-1} \tag{J.18}$$

where n_h represents the sum of the heavy species. The solution algorithm for equations (J.6), (J.9), and (J.17) is represented below in Figure J.1. Initial guesses for the number densities of n_{H_2}, n_H, and n_e are all unity. Underrelaxation is used for the state equation, as well as for the dissociation and ionization equations. There are two branches of the algorithm, one for low temperatures and the other for high temperatures. If the low temperature version of the state equation produces a negative value for n_{H_2}, then the algorithm sets $n_{H_2} = 1.0$ and switches to the other branch. After a given iteration, the state equation is used to compute the pressure based upon the latest values of number densities. If the computed pressure is within a preset error of the system pressure, the number density values are considered converged. The algorithm works for a wide range of input temperatures and pressure. The output for the major species agrees well with the output of Patch (1969), although there is some error due to neglect of the minor species, and estimated molecular hydrogen partition functions.

Begin

Loop=1

Switch Algorithm
$n_{H2}=1.0$
$n_H=1.0$

Loop=2

Compute Lowering

Compute Lowering

Compute Partition Fctns.

Compute Partition Fctns.

Compute Pressure Correction

Compute Pressure Correction

State Eqn. → n_{H2}

If $n_{H2}<0$ Yes

No

State Eqn. → n_e

If $n_e<0$ Yes

$n_{H2}=n_H=n_e=1.0$

Compute n_H from n_{H2} Equation (K.6)

No

relx = 0.9*relx

Compute n_e from n_H Equation (K.9)

Compute n_H from n_e Equation (K.9)

Compute n_{H2} from n_H Equation (K.6)

Compute Pressure Correction

Compute Pressure Correction

Compute Pressure from State Equation

Compute Pressure from State Equation

Is Pressure Converging?   No

relx = 0.9*relx

Is Pressure Converging?   Yes

Adjust Species to Converge on Pressure

relx = 0.9*relx

Adjust Species to Converge on Pressure

Is Pressure Converged Or, Have Iterations Maxed?   Yes   No

Is Pressure Converged Or, Have Iterations Maxed?   Yes   No

Reset Loop 1

If Loop   =1   =2

relx = 0.9*relx

Is Pressure Converged?   No   Yes

Update Species Arrays

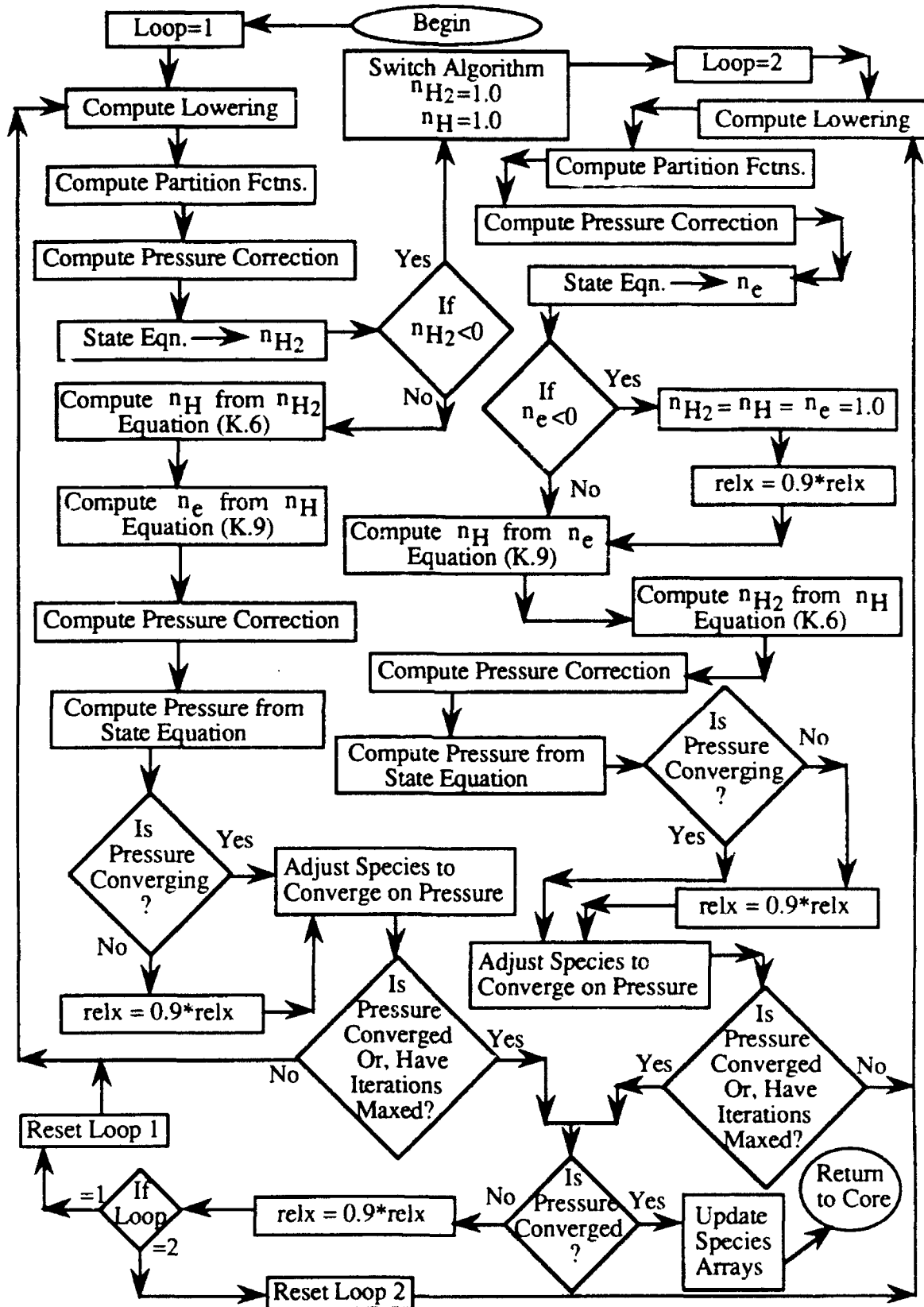Return to Core

Reset Loop 2

Figure J.1   Flowchart of major species number density computation

Bibliography

Abramowitz, M. and Stegun, I. A. (1965). Handbook of Mathematical Functions, with Formulas, Graphs, and Mathematical Tables, Dover Publications, Inc., New York, 1965.

Anderson, D.A., Tannehill, J.C., and Pletcher, R.H. (1984). Computational Fluid Mechanics and Heat Transfer, Hemisphere Publishing Corporation, New York, 1984.

Aubreton, J., and Fauchais, P. (1983). "Influence des Potentials d'Interaction sur les Proprietes de Transport des Plasmas Thermiques: Exemple d'Application le Plasma Argon Hydrogene a la Pression Atmospherique," *Revue Phys. Appl.*, Vol. 18, pp. 51-66, January 1983.

Bates, D.R., Kingston, A.E., and McWhirter, R.W.P. (1962a). "Recombination Between Electrons and Atomic Ions II. Optically Thick Plasmas," *Proc. R. Soc. (Lond.)*, Vol. A270, p. 155, 1962.

Bates, D.R., Kingston, A.E., and McWhirter, R.W.P. (1962b). "Recombination Between Electrons and Atomic Ions I. Optically Thin Plasmas," *Proc. R. Soc. (Lond.)*, Vol. A267, p. 297, 1962.

Beddini, R.A., and Owano, T.G. (1987). "Analysis of Turbulent Convective and Radiative Heat Transfer in High Temperature Rocket Chamber Flows," AIAA/ASME/SAE/ASEE 23rd Joint Propulsion Conference, July 1987.

Beddini, R.A., Owano, T.G., and Kuo, S.-L. (1987). "Analysis of Gas Dynamic Interactions with Intense Optical Beams," AIAA Paper No. 87-1455, AIAA 19th Fluid Dynamics, Plasma Dynamics and Lasers Conference, June 1987.

Black, J., Krier, H., and Glumb, R.J. (1992). "Laser Propulsion 10 kW Thruster Test Program Results," AIAA Paper No. 92-3218, AIAA 28th Joint Propulsion Conference and Exhibit, July 1992, Nashville, Tennessee.

Black, J., Krier, H., Zerkle, D., and Glumb, R.J. (1992). "Characterization of Laser-Sustained Plasma Behavior During 10 kW Laser Thruster Tests," AIAA Paper No. 92-3022, AIAA 28th Joint Propulsion Conference and Exhibit, July 1992, Nashville, Tennessee.

Braun, C. G., and Kunc, J. A. (1987). "Collisional-Radiative Coefficients from a Three-Level Atomic Model in Nonequilibrium Argon Plasmas," *Physics of Fluids*, Vol. 30, No. 2, pp. 499-509, February, 1987.

Brokaw, R.S. (1958). "Approximate Formulas for the Viscosity and Thermal Conductivity of Gas Mixtures," *Journal of Chemical Physics*, Vol. 29, No. 2, pp. 391-397, August, 1958.

Brokaw, R.S. (1961). "Estimated Collision Integrals for the Exponential Attractive Potential," *Physics of Fluids*, Vol. 4, No. 8, pp. 944-946, August 1961.

Burton, L. L., and Blades, M. W. (1990). "A Simple Method for Calculating Deviations from Local Thermodynamic Equilibrium in the Inductively Coupled Plasma," *Spectrochimica Acta.*, Vol. 45B, Numbers 1/2, pp. 139-144, 1990.

Butler, G.W., Kashiwa, B.A., and King, D.Q. (1990). "Numerical Modeling of Arcjet Performance, " AIAA Paper 90-1474, AIAA 21st Fluid Dynamics, Plasma Dynamics and Lasers Conference, July 18-20, 1990, Seattle, Washington.

Butler, J.N., and Brokaw, R.S. (1957). "Thermal Conductivity of Gas Mixtures in Chemical Equilibrium," *Journal of Chemical Physics*, Vol. 26, No. 6, pp. 1636-1643, June 1957.

Caledonia, G.E., Wu, P.K.S., and Pirri, A.N. (1975). "Radiant Energy Absorption Studies for Laser Propulsion," NASA CR-134809 (PSI TR-20), March 1975.

Cebeci, T. and Bradshaw, P. (1977). Momentum Transfer in Boundary Layers, Hemisphere Publishing Corporation, Washington, D.C., 1977.

Cebeci, T. and Bradshaw, P. (1984). Physical and Computational Aspects of Convective Heat Transfer, Springer-Verlag, New York, 1984.

Chang C.H. and Pfender, E. (1990). "Nonequilibrium Modeling of Low-Pressure Argon Plasma Jets; Part I: Laminar Flow," *Plasma Chemistry and Plasma Processing*, Vol. 10. No. 3, pp. 473-492, September 1990.

Chapman, S., and Cowling, T.G. (1990). The Mathematical Theory of Non-Uniform Gases, Third Edition, Cambridge University Press, Cambridge, U.K., 1990.

Chen, D.M. (1980). Analytical Modeling of Two-Temperature Argon Arc Plasmas, Ph.D. Thesis, University of Minnesota, 1980.

Chen, D.M., and Pfender, (1981). "Two-Temperature Modeling of the Anode Contraction Region of High-Intensity Arcs," *IEEE Transactions on Plasma Science*, Vol. PS-9, No. 4, pp. 265-274, December 1981.

Chen, K., and Eddy, T. L. (1991). "Composition and Partition Functions of Partially Ionized Hydrogen Plasma in Non-Local Thermal Equilibrium (Non-LThE) and Non-Local Chemical Equilibrium (Non-LChE)," Heat Transfer in Thermal Plasma Processing, HTD-Vol. 161, pp. 177-185, 28th National Heat Transfer Conference, Minneapolis, Minnesota, July 28-31, 1991, American Society of Mechanical Engineers, New York.

Chmieleski, R.M., and Ferziger, J.H. (1967). "Transport Properties of a Nonequilibrium Partially Ionized Gas," *Physics of Fluids*, Vol. 10, No. 2, pp. 364-371, February 1967.

Cho, K.Y. (1988). Nonequilibrium Thermodynamic Models and Applications to Hydrogen Plasma, Ph.D. Thesis, Georgia Institute of Technology, 1988.

Cho, K.Y., and Eddy, T.L. (1989). "Collisional-Radiative Modeling with Multitemperature Thermodynamic Models," *Journal of Quantitative Spectroscopy and Radiative Transfer*, Vol. 41, No. 4, pp. 287-301, 1989.

Dalgarn, A., and Lane, N.F. (1966). "Free-Free Transiti ns of Electrons in Gases," *Astrophysical Journal*, Vol. 145, No. 2, pp. 623-633, 1966.

Devoto, R.S. (1966). "Transport Properties of Ionized Monatomic Gases," *Physics of Fluids*, Vol. 9, No. 6, pp. 1230-1240, June 1966.

Devoto, R.S. (1967a). "Transport Coefficients of Partially Ionized Argon," *Physics of Fluids*, Vol. 10, No. 2, pp. 354-364, February 1967.

Devoto, R.S. (1967b). "Simplified Expressions for the Transport Properties of Ionized Monatomic Gases," *Physics of Fluids*, Vol. 10, No. 10, pp.2105-2112, October 1967.

Devoto, R.S. (1968). "Transport Coefficients of Partially Ionized Hydrogen," *Journal of Plasma Physics*, Vol. 2, Part 4, pp. 617-631, 1968.

Devoto, R.S. (1973). "Transport Coefficients of Ionized Argon," *Physics of Fluids*, Vol. 16, No. 5, pp. 616-623, May 1973.

Devoto, R.S., and Li, C.P. (1968). "Transport Coefficients of Partially Ionized Helium," *Journal of Plasma Physics*, Vol. 2, Part 1, pp. 17-32, 1968.

Dix, D.M. (1964). "Energy Transfer Processes in a Partially Ionized, Two-Temperature Gas," *AIAA Journal*, Vol. 2, N0. 12, pp. 2081-2090, December 1964.

Donskoi, A.V., Klubnikin, V.S., and Salangin, A.A. (1985). "Two-Temperature Modeling of Argon Arc Plasmas in a Channel," *Sov. Phys. Tech. Phys.*, Vol. 30, No. 11, pp.1255-1257, November 1985.

Drawin, H.W. (1969a). "Collisional-Radiative Ionization and Recombination Coefficients for Quasi-Stationary Homogeneous Hydrogen and Hydrogenic Ion Plasmas," *Z. Physik*, Vol. 225, pp. 470-482, 1969.

Drawin, H.W. (1969b). "Influence of Atom-Atom Collisions on the Collisional-Radiative Ionization and Recombination Coefficients of Hydrogen Plasmas," *Z. Physik*, Vol. 225, pp. 483-493, 1969.

Dresvin, S.V. (1977). *Physics and Technology of Low Temperature Plasmas*, Iowa State University Press, Ames, Iowa, 1977.

Eddy, T. L., and Cho, K. Y. (1991). "A Multitemperature Model for Plasmas in Chemical Nonequilibrium," *Heat Transfer in Thermal Plasma Processing*, HTD-Vol. 161, pp. 195-210, 28th National Heat Transfer Conference, Minneapolis, Minnesota, July 28-31, 1991, American Society of Mechanical Engineers, New York.

Eddy, T. L., Grandy, J. D., and Detering, B. A. (1991). "Chemical Equilibrium in an Argon Plasma Torch Plume," *Heat Transfer in Thermal Plasma Processing*, HTD-Vol. 161, pp. 79-88, 28th National Heat Transfer Conference, Minneapolis, Minnesota, July 28-31, 1991, American Society of Mechanical Engineers, New York.

Eddy, T. L., Leger, J. M., Coudert, J. F., and Fauchais, P. (1991). "Nonequilibrium Diagnostics of a Nitrogen Plasma Jet," *Heat Transfer in Thermal Plasma Processing*, HTD-Vol. 161, pp. 67-77, 28th National Heat Transfer Conference, Minneapolis, Minnesota, July 28-31, 1991, American Society of Mechanical Engineers, New York.

Edwards, A.L., and Fleck,Jr., J.A. (1979). "Two-Dimensional Modeling of Aerosol-Induced Breakdown in Air," *J. Appl. Phys.*, Vol. 50, No. 6, pp 4307-4313, June 1979.

Eguiguren, J. V. (1989). *A Steady Two-Dimensional Flow Model for Laser Sustained Plasmas*, M.S. Thesis, University of Illinois at Urbana-Champaign, 1989.

Einstein, A. (1916). "Emission and Absorption of Radiation according to the Quantum Theory," *Verh. Dtsch. Phys. Ges.*, Vol. 18, pp. 318-323, 1916.

Eskridge, R. H., McCay, T. D., and VanZandt, D. M. (1987). "An Experimental Study of Laser-Supported Plasmas for Laser Propulsion - Final Report," NASA Technical Memorandum TM-86583, NASA George C. Marshall Space Flight Center, January, 1987.

Fowler, M.C. and Smith, D.C. (1975). "Ignition and Maintenance of Subsonic Plasma Waves in Atmospheric Pressure Air by CW CO_2 Laser Radiation and Their Effect on Laser Beam Propagation," *Journal of Applied Physics*, Vol. 46, No. 1, pp. 138-150, January 1975.

Frisbee, R.H., Horvath, J.C., and Sercel, J.C. (1985). "Laser Propulsion for the Orbital Transfer Mission," AIAA Paper 85-1224, AIAA/ASME/SAE/ASEE 21st Joint Propulsion Conference, July 1985.

Gamalii, E. G., Kiselev, A. E., Levanov, E. I., Osokin, S. E., and Sotskii, E. N. (1990). "Nonclassical Transport in a Nonequilibrium Laser Plasma," *Journal of Soviet Laser Research*, Vol. 11, Number 2, pp. 172-182, March 1990.

Gambill, W.R. (1958). "To Get Viscosity for a Gas Mixture," *Chemical Engineering*, Vol. 65. No. 23, pp. 157-160, November 1958.

Glumb, R. J., and Krier, H. (1986). "Two-Dimensional Model of Laser-Sustained Plasmas in Axisymmetric Flowfields," *AIAA Journal*, Vol. 24, No. 8, p. 1331, 1986.

Glumb, R.J., and Krier, H. (1988). "Continuous-Wave (CW) Thermal Laser Rocket Propulsion: Designing an Operational Thruster," Final Technical Report, Contract NAS 3-25271, Combustion Sciences Inc., July 1988.

Gomes, A.M. (1983). "Criteria For Partial LTE in an Argon Thermal Discharge at Atmospheric Pressure; Validity of the Spectroscopically Measured Electron Temperature," *Journal of Physics D: Applied Physics*, Vol 16, pp. 357-378, 1983.

Griem, H. R. (1964). Plasma Spectroscopy, McGraw-Hill, New York, 1964.

Griem, H. R. (1974). Spectral Line Broadening by Plasmas, Pure and Applied Physics, Volume 39, Academic Press, Inc., New York.

Grier, N.T. (1962). "Calculation of Transport Properties and Heat-Transfer Parameters of Dissociating Hydrogen," NASA TN D-1406, 1962.

Grier, N.T. (1966). "Calculation of Transport Properties of Ionizing Atomic Hydrogen, " NASA TN D-3186, 1966.

Guckenheimer, J., and Holmes, P. (1983). Nonlinear Oscillations, Dynamical Systems, and Bifurcations of Vector Fields, Springer-Verlag, New York, 1983.

Gupta, P., and Khare, S.P. (1978). "Elastic Scattering of Electrons by Molecular Hydrogen for Incident Energies of 100-2000 eV," *Journal of Chemical Physics*, Vol. 68, No. 5, pp. 2193-2198, March 1978.

Hirschfelder, J.O., Curtiss, C.F., and Bird, R.B. (1954). Molecular Theory of Gases and Liquids, John Wiley & Sons, Inc., New York, 1954.

Holman, J.P. (1984). Experimental Methods for Engineers, Fourth Edition, McGraw-Hill Book Company, New York, 1984.

Incropera, F.P. (1973). "Procedures for Modeling Laminar Cascade Arc Behavior," *IEEE Transactions on Plasma Science*, Vol. PS-1, No. 3, pp. 3-9, September 1973.

Itikawa, Y. (1974). "Momentum-Transfer Cross Sections for Electron Collisions with Atoms and Molecules," *Atomic Data and Nuclear Data Tables*, Vol. 14, No. 1, pp. 1-10, July 1974.

Itikawa, Y. (1978). "Momentum-Transfer Cross Sections for Electron Collisions with Atoms and Molecules, Revision and Supplement," *Atomic Data and Nuclear Data Tables*, Vol. 21, No. 1, pp. 69-75, January 1978.

Jaffrin, M. Y. (1965). "Shock Structure in a Partially Ionized Gas," *Physics of Fluids*, Vol. 8, No. 4, pp. 606-625, April 1965.

Janev, R.K., Langer, W.D., Evans, Jr., K., and Post, Jr., D.E. (1987). Elementary Processes in Hydrogen-Helium Plasmas, Springer-Verlag, New York, 1987.

Jeng, S.M., and Keefer, D.R. (1986). "Theoretical Investigation of Laser-Sustained Argon Plasmas," *Journal of Applied Physics*, Vol. 60, No. 7, 1986.

Jeng, S.M., and Keefer, D.R. (1987a). "A Theoretical Investigation of Laser-Sustained Plasma Thruster," AIAA Paper 87-0383, AIAA 25th Aerospace Sciences Meeting, January 1987.

Jeng, S.M., and Keefer, D.R. (1987b). "Numerical Study of Laser-Sustained Hydrogen Plasmas in a Forced Convective Flow," *Journal of Propulsion and Power*, Vol. 3, No. 3, May-June 1987.

Jeng, S.M., and Keefer, D.R. (1987c). "Influence of Laser Beam Geometry and Wavelength on Laser-Sustained Plasmas," AIAA Paper 87-1409, AIAA 19th Fluid Dynamics, Plasma Dynamics and Lasers Conference, June 8-10, 1987, Honolulu, Hawaii.

Jeng, S.M., and Keefer, D.R. (1988). "Effect of Finite Rate Chemistry on a Realistic Laser Thermal Rocket Performance," AIAA Paper 88-2774, AIAA Thermophysics, Plasmadynamics, and Lasers Conference, June 1988.

Johnson, L.C. (1972). "Approximations for Collisional and Radiative Transition Rates in Atomic Hydrogen", *Astrophysical Journal*, Vol. 174, pp. 227-236, May 1972.

Karzas, W.J., and Latter, R. (1961). "Electron Radiative Transitions in a Coulomb Field," *Astrophysical Journal*, Supplement Series, Vol. 55, pp. 167-211, 1961.

Keefer, D., Welle, R., and Peters, C. (1985). "Power Absorption Processes in Laser-Sustained Argon Plasmas," AIAA Paper 85-1552, AIAA 18th Fluid Dynamics, Plasma Dynamics and Lasers Conference, July 16-18, 1985, Cincinnati, Ohio.

Kemp, N.H., and Krech, R.H. (1980). "Laser Heated Thruster - Interim Report," NASA CR-161666, Physical Science, Inc., Woburn, Mass., September 1980.

Kemp, N.H., and Root, R.G. (1979). "Analytical Study of Laser-Supported Combustion Waves in Hydrogen," *Journal of Energy*, Vol. 3, No. 1, January 1979.

Kemp, N.H., Root, R.G., Wu, P.K.S., Caledonia, C.E., and Pirri, A.N. (1977). "Laser-Heated Rocket Studies," NASA CR-136127, 1977.

Kihara, T., Taylor, M.H., Hirschfelder, J.O. (1960). "Transport Properties for Gases Assuming Inverse Power Intermolecular Potentials," *Physics of Fluids*, Vol. 3, No. 5, pp. 715-720, September-October 1960.

Kovitya, P. (1985). "Physical Properties of High-Pressure Plasmas of Hydrogen and Copper in the Temperature Range 5000-60000 K," *IEEE Transactions on Plasma Science*, Vol. PS-13, No. 6, pp. 587-594, December 1985.

Kozlov, G. I., Kuznetsov, V. A., Masyukov, V. A. (1979). "Sustained Optical Discharges in Molecular Gases," *Soviet Phys. Tech. Phys.*, Volume 49, Number 11, pp. 1283-1287, November 1979.

Kroesen, G.M.W., Schram, D.C., Timmermans, C.J., de Haas, J.C.M. (1990). "The Energy Balance of a Plasma in Partial Local Thermodynamic Equilibrium," *IEEE Transactions on Plasma Science*, Vol. 18, No. 6, pp. 985-991, December 1990.

Kruger, C.H. (1970). "Nonequilibrium in Confined-Arc Plasmas," *Physics of Fluids*, Vol. 13, No. 7, pp. 1737-1746, July 1970.

Kruger, C.H., and Mitchner, M. (1967). "Kinetic Theory of Two Temperature Plasmas," *Physics of Fluids*, Vol. 10, No. 9, pp. 1953-1961, September 1967.

Kunc, J.A. (1984). "Stepwise Ionization in a Non-Equilibrium, Steady-State Hydrogen Plasma," *Journal of Quantitative Spectroscopy and Radiative Transfer*, Vol. 32, No. 4, pp. 311-323, 1984.

Kunc, J.A. (1987). "Role of Atom-Atom Inelastic Collisions in Two Temperature Nonequilibrium Plasmas," *Phys. Fluids*, Vol. 30, No. 7, p. 2255, July, 1987.

Kunc, J.A., and Soon, W. H. (1989). "Radiation of Hot Atomic Hydrogen," AIAA Paper 89-2598, AIAA/ASME/SAE/ASEE 25th Joint Propulsion Conference, July 1989.

Kuo, K.K., (1986). Principles of Combustion, John Wiley & Sons, New York, 1986.

Langdon, A.B. (1980). "Nonlinear Inverse Bremsstrahlung and Heated-Electron Distributions," *Physical Review Letters*, Vol. 44, No. 9, pp. 575-579, March 1980.

Langerman, M.A. and Lemmon, E.C. (1991). "A Multidimensional Finite Element MHD Model of Internal Plasma Flows," Heat Transfer in Thermal Plasma Processing, HTD-Vol. 161, pp. 121-130, 28th National Heat Transfer Conference, Minneapolis, Minnesota, July 28-31, 1991, American Society of Mechanical Engineers, New York.

Lelevkin, V.M., Pakhomov, E.P., Semenov, V.F., and Engel'sht, V.S. (1986). "Calculation of the Characteristics of an Electric Arc in the Initial Section of the Channel Based on the Two-Temperature Model of a Plasma," *Teplofizika Vysokikh Temperatur*, Vol. 24, No. 3, pp. 587-593, May-June 1986.

Litvak, M.M. and Edwards, D.F. (1966). "Electron Recombination in Laser-Produced Hydrogen Plasma," *Journal of Applied Physics*, Vol. 37, No. 12, pp. 4462-4474, November 1966.

Lorenz, E.N. (1963). "Deterministic Nonperiodic Flow," *Journal of The Atmospheric Sciences*, Vol. 20, No. 2, pp. 130-141, March 1963.

Mason, E.A. (1954). "Transport Properties of Gases Obeying a Modified Buckingham (Exp-Six) Potential," *Journal of Chemical Physics*, Vol. 22, No. 2, pp. 169-186, February 1954.

Mason, E.A. and Saxena, S.C. (1958). "Approximate Formula for the Thermal Conductivity of Gas Mixtures," *Physics of Fluids*, Vol. 1, No. 5, pp. 361-369, September-October 1958.

Mason, E.A., Munn, R.J., and Smith, F.J. (1967). "Transport Coefficients of Ionized Gases," *Physics of Fluids*, Vol. 10, No. 8, pp. 1827-1832, August 1967.

Mazumder, J., Rockstroh, T. J., and Krier, H. (1987). "Spectroscopic Studies of Plasma During CW Laser Gas Heating in Flowing Argon," *Journal of Applied Physics*, Vol. 62, No. 12, p. 4712, 1987.

McCay, T. D., Eskridge, R. H., and VanZandt, D. H. (1988). "Experiments on Optical Discharges in Hydrogen," *Journal of Thermophysics*, Vol. 2, No. 4, pp. 317-323, October, 1988.

Merkle, C.L., Molvik, G.A., and Shaw, E.J.-H. (1985). "Numerical Solution of Strong Radiation Gasdynamic Interactions in a Hydrogen-Seedant Mixture," AIAA Paper No. 85-1554, AIAA 18th Fluid Dynamics and Plasmadynamics and Lasers Conference, July 1985.

Mertogul, A. E. (1989). Energy Absorption and Thermal Conversion Efficiency in Argon Laser Sustained Plasmas, M.S. Thesis, Department of Aeronautical and Astronautical Engineering, University of Illinois at Urbana-Champaign, 1989.

Mertogul, A., Zerkle, D., and Krier, H. (1992). "Investigation of CO_2 Laser-Sustained Hydrogen Plasmas," *Journal of Propulsion and Power*, Vol. 8, No. 5, pp. 1123-1125, September-October 1992.

Mertogul, A., Zerkle, D., Krier, H., and Mazumder, J. (1990). "Continuous Wave Laser Sustained Hydrogen Plasmas for Thermal Rocket Propulsion," AIAA Paper 90-2637, AIAA/DGLR/JSASS 21st International Electric Propulsion Conference, July 18-20, 1990, Orlando, Florida.

Miller, E.J., and Sandler, S.I. (1973). "Transport Properties of Two-Temperature Partially Ionized Argon," *Physics of Fluids*, Vol. 16, No. 4, pp. 491-494, April 1973.

Miller, S., and Martinez-Sanchez, M. (1990). "Viscous and Diffusive Effects in MPD Flows," AIAA Paper 90-2606, AIAA/DGLR/JSASS 21st International Electric Propulsion Conference, July 1990.

Mitchner, M., and Kruger, C.H., Jr. (1973). Partially Ionized Gases, John Wiley & Sons, Inc., New York, 1973.

Moder, J.P. (1990). "Analysis and Design of an Ultra-High Temperature, Hydrogen Fueled MHD Generator as an Open Cycle Power Supply," Ph.D. Thesis, Rensselaer Polytechnic Institute, Troy, New York, June 1990.

Molvik, G.A., Choi, D., and Merkle, C.L. (1984). "A Two-Dimensional Analysis of Laser Heat Addition in Converging Nozzles," AIAA Paper 84-0529, AIAA 22nd Aerospace Sciences Meeting, January 1984.

Monchick, L. (1959). "Collision Integrals for the Exponential Repulsive Potential," *Physics of Fluids*, Vol. 2, No. 6, pp. 695-700, November-December, 1959.

Muckenfuss, C., and Curtiss, C.F. (1958). "Thermal Conductivity of Multicomponent Gas Mixtures," *Journal of Chemical Physics*, Vol. 29, No. 6, pp. 1273-1277, December 1958.

Muller, S., and Uhlenbusch, J. (1982). "Theoretical Model for a Continuous Optical Discharge," *Physica C*, Vol. 112, pp. 259-270, 1982.

Niewood, E., and Martinez-Sanchez, M. (1990). "Quasi One-Dimensional Numerical Simulation of Magnetoplasmadynamic Thrusters," AIAA Paper 90-2604, AIAA/DGLR/JSASS 21st International Electric Propulsion Conference, July 1990.

Oppenheim, A.K., Cohen, L.M., Short, J.M., Cheng, R.K., and Hom, K. (1975). "Dynamics of the Exothermic Process in Combustion," Fifteenth Symposium (International) on Combustion, pp. 1503-1513, The Combustion Institute, Pittsburgh, Pennsylvania, 1975.

Patankar, S.V. (1980). <u>Numerical Heat Transfer and Fluid Flow</u>, Hemisphere Publishing Corporation, New York, 1980.

Patch, R. W. (1969). "Components of Hydrogen Plasma including Minor Species," NASA TN-D-4993, 1969.

Patch, R.W. (1971). "Thermodynamic Properties and Theoretical Rocket Performance of Hydrogen to 100,000 K and 1.01325×10^8 N/m^2," NASA SP-3069, 1971.

Potapov, A. V. (1966). "Chemical Equilibrium of Multitemperature Systems," *High Temperature*, Vol. 4, No. 1, pp. 55-58, January-February, 1966.

Raizer, Y.P. (1970). "Subsonic Propagation of a Light Spark and Threshold Conditions for the Maintenance of Plasma by Radiation," *Soviet Physics JETP*, Vol. 31, No. 6, December 1970.

Rhie, C.M. (1986). "A Pressure Based Navier-Stokes Solver Using the Multigrid Method," AIAA Paper 86-0207, AIAA 24th Aerospace Sciences Meeting, January 6-9, 1986, Reno, Nevada.

Rhodes, R. and Keefer D. (1991). "Modeling Arcjet Space Thrusters," AIAA Paper 91-1994, AIAA/SAE/ASME/ASEE 27th Joint Propulsion Conference, June 24-26, 1991, Sacramento, California.

Rhodes, R.P. and Keefer, D. (1990). "Numerical Modeling of an Arcjet Thruster," AIAA Paper 90-2614, AIAA/DGLR/JSASS 21st International Electric Propulsion Conference, July 18-20, 1990, Orlando, Florida.

Schwartz, S., Mertogul, A., Eguiguren, J., Zerkle, D., Chen, X., Krier, H., and Mazumder, J. (1989). "Laser-Sustained Gas Plasmas for Application to Rocket Propulsion," AIAA/ASME/SAE/ASEE 25th Joint Propulsion Conference, July 10-12, 1989, Monterey, California.

Scott, R.K., and Incropera, F.P. (1973). "Nonequilibrium Flow Calculations for the Hydrogen Constricted Arc," *AIAA Journal*, Vol. 11, No. 12, pp. 1714-1719, December 1973.

Sedghinasab, A., and Eddy, T. L. (1991). Nonequilibrium Thermodynamic Properties of Argon," Heat Transfer in Thermal Plasma Processing, HTD-Vol. 161, pp. 187-193, 28th National Heat Transfer Conference, Minneapolis, Minnesota, July 28-31, 1991, American Society of Mechanical Engineers, New York.

Siegel, R., and Howell, J.R. (1981). Thermal Radiation Heat Transfer, Second Edition, Hemisphere Publishing Corporation, New York, 1981.

Smith, F.J., Mason, E.A., and Munn, R.J. (1965). "Classical Collision Integrals for the Repulsive Screened Coulomb Potential," Physics of Fluids, Vol. 8, pp. 1907-1908, 1965.

Stallcop, J.R. (1974a). "Absorption of Infrared Radiation by Electrons in the Field of a Neutral Hydrogen Atom," Astrophysical Journal, Vol. 187, No. 1, pp. 179-183, January 1974.

Stallcop, J.R. (1974b). "Absorption of Laser Radiation in a H-He Plasma. I. Theoretical Calculation of the Absorption Coefficient," Physics of Fluids, Vol. 17, No. 4, pp. 751-758, April 1974.

Sutton, G.P. (1986). Rocket Propulsion Elements, Fifth Edition, John Wiley & Sons, Inc., 1986.

Uman, M. A. (1964). Introduction to Plasma Physics, McGraw-Hill, Inc., New York.

Vakakis, A.F. (1993). Personal communication with Professor Alexander F. Vakakis, 1993.

van der Mullen, J. A. M. (1990). "On the Atomic State Distribution Function in Inductively Coupled Plasmas - II. The Stage of Local Thermal Equilibrium and its Validity Region," Spectrochimica Acta., Vol. 45B, Numbers 1/2, pp. 1-13, 1990.

Vanderslice, J.T., Weissman, S., Mason, E.A., and Fallon, R.J. (1962). "High-Temperature Transport Properties of Dissociating Hydrogen," Physics of Fluids, Vol. 5, No. 2, pp. 155-164, February 1962.

VanZandt, D. M., McCay, T.D., and Eskridge, R. H. (1984). "An Experimental Study of Laser Supported Hydrogen Plasmas," AIAA Paper 84-1572, AIAA 17th Fluid Dynamics, Plasma Dynamics, and Lasers Conference, June 25-27, 1984, Snowmass, Colorado.

Vasil'evskii, S.A., Sokolova, I.A., and Tirskii, G.A. (1984). "Exact Equations and Transport Coefficients for a Multicomponent Gas Mixture with a Partially Ionized Plasma," Zhurnal Prikladnoi Mekhaniki i Tekhnicheskoi Fiziki, No. 4, pp. 15-24, July-August 1984.

Venugopalan, M. (1971a). Reactions Under Plasma Conditions, Volume I, John Wiley & Sons, Inc., New York.

Vlcek, J. (1989). "A Collisional-Radiative Model Applicable to Argon Discharges Over a Wide Range of Conditions. I: Formulation and Basic Data," Journal of Physics D: Applied Physics, Volume 22, pp. 623-631, 1989.

Vriens, L. (1973). "Energy Balance in Low-Pressure Gas Discharges," Journal of Applied Physics, Vol. 44, No. 9, September 1973.

Vriens, L. (1974). "Two- and Three-Electron Group Models for Low-Pressure Gas Discharges," Journal of Applied Physics, Vol. 45, No. 3, March 1974.

Watanabe, T., Tonoike, N., Honda, T., Kanzawa, A. (1991). "Flow, Temperature and Concentration Fields in Reactive Plasmas in an Inductively Coupled RF Discharge - Characteristics in Argon-Oxygen and Argon-Nitrogen Thermal Plasmas," *Journal of Chemical Engineering of Japan*, Vol. 24, No. 1, pp. 25-32, 1991.

Weisheit, J.C., Tarter, C.B., Scofield, J.H., and Richards, L.M. (1976). "The Spectra of Helium-Like Ions in Laser-Produced Plasmas," *Journal of Quantitative Spectroscopy and Radiative Transfer*, Vol. 16, pp. 659-669, 1976.

Welle, R., Keefer, D., and Peters, C. (1986). "Energy Conversion Efficiency in High-Flow Laser-Sustained Argon Plasmas," AIAA Paper 86-1077, AIAA/ASME 4th Fluid Mechanics, Plasma Dynamics and Lasers Conference, May 12-14, 1986, Atlanta, Georgia.

Welle, R., Keefer, D., and Peters, C. (1987). "Laser-Sustained Plasmas in Forced Argon Convective Flow, Part I: Experimental Studies," *AIAA Journal*, Vol. 25, Aug. 1987, pp. 1093-1099.

Wiese, W.L., Smith, M.W., and Glennon, B.M. (1966). Atomic Transition Probabilities, Volume I Hydrogen Through Neon, NSRDS-NBS 4, National Standard Reference Data Series, National Bureau of Standards 4, U.S. Government Printing Office, May 20, 1966.

Wiggins, S. (1990). Introduction to Applied Nonlinear Dynamical Systems and Chaos, Springer-Verlag, New York, 1990.

Wilke, C.R. (1950). "A Viscosity Equation for Gas Mixtures," *Journal of Chemical Physics*, Vol. 18, No. 4, pp. 517-519, April 1950.

Williams, R.H., and DeWitt, H.E. (1969). "Quantum-Mechanical Plasma Transport Theory," *Physics of Fluids*, Vol. 12, No. 11, pp. 2326-2342, November 1969.

Yos, J.M. (1963). "Transport Properties of Nitrogen, Hydrogen, Oxygen and Air to 30,000 K," Avco Corporation, Wilmington, Mass., RAD-TM-63-7, March 1963.

Zerkle, D.K. (1988). Energy Conversion Measurements in Laser-Sustained Argon Plasmas at Elevated Mass Flux and Pressure, M.S. Thesis, Department of Mechanical and Industrial Engineering, University of Illinois at Urbana-Champaign, May 1988.

Zerkle, D.K. (1992a). Non-Local Thermodynamic Equilibrium in Laser Sustained Plasmas, Ph.D. Thesis, Department of Mechanical and Industrial Engineering, University of Illinois at Urbana-Champaign, October 1992.

Zerkle, D.K. (1992b). Personal Communication with Dr. David K. Zerkle, 1992.

Zerkle, D.K., Schwartz, S., Mertogul, A.E., Chen, X., Krier, H., and Mazumder, J. (1990). "Laser-Sustained Argon Plasmas for Thermal Rocket Propulsion," *Journal of Propulsion and Power*, Vol. 6, No. 1, pp. 38-45, January-February 1990.